Developing diagnostic methods for fatigue damage assessment

A thesis submitted for the degree of Doctor of Philosophy

Ву

Maryam Izadi Najafabadi

Brunel Centre for Advanced Solidification Technology (BCAST),
Brunel University London

2025

Copyright

Copyright © 2025 Maryam Izadi. All rights reserved.

The copyright of this thesis rests with the Author. Copies (by any means) either in full, or of extracts, may not be made without prior written consent from the Author.

Abstract

Most of the metal's failure happens because of the fatigue which is associated with metals that is subjected to cyclic loading over time. Fatigue damage detection is one of important technological issues in both academic and industrial fields. Early fatigue damage detection promotes circular economy and sustainability by prolonging the lifespan and durability of metals. In most metals, in low and high cycle fatigue, the stages of fatigue are pre-crack nucleation, crack nucleation, micro and macro crack growth, and final failure. Several techniques have been proposed and developed for detecting fatigue damage in metals. However, comparatively less attention has been given to early fatigue damage detection, specifically targeting the pre-crack nucleation stage. The pre-crack nucleation stage begins with an increase in dislocation density, followed by the formation of dislocation entanglements and ultimately, the development of slip bands. Subsequently, these slip bands induce intrusion and extrusion, serving as nucleation sites for cracks. The identification of these defects plays an important role as it can facilitate the use of appropriate treatment to either eliminate or mitigate the defects, consequently leading to increase in metals lifespan. The use of non-destructive testing (NDT) methods is particularly crucial in this context, given their wide applicability within industrial environments. Thus, in this thesis appropriate NDT methods for early damage detection fatigue in 316L stainless steel had been used. NDT methods enable the detection of fatigue damage without destruction of specimen.

Techniques such as electrical resistivity measurement and nonlinear ultrasonic testing are employed to detect these defects. The electrical resistance method operates on the principles of Ohm's law, whereby a current is applied to the metal and the resulting voltage drop is measured to determine its electrical resistance. The resistivity is then calculated based on the sample's geometry. Structural defects including dislocations, entanglements, slip bands, and cracks contribute to scattering and elevation in electrical resistivity. However, to make this method works effectively, a responsive technique with the capability of $n\Omega$ resolution is needed. The used method in this study is a combination of delta mode and four-probe technique that effectively eliminates thermoelectric voltages resulting from temperature variations in the circuit and minimizes the impact of lead resistance. Another approach that is used in this study is nonlinear ultrasonic. In this technique, a wave is propagated through the metal specimen, and upon interaction with defects, higher frequency waves are generated. By detecting and analysing these signals, the presence of defects can be identified. This unique capability enables the detection of early fatigue defects such as dislocations and slip bands evolution, providing improved sensitivity and precision in defect identification. Findings indicate that both electrical resistivity measurement and nonlinear ultrasonic testing proficiently detect early-stage fatigue defects in 316L stainless steel. These methods reveal significant changes in two distinct regions prior to 10% of the component's fatigue life.

Following the identification of two distinct regions of significant signal variation prior to 10% of the fatigue life, advanced microscopy techniques were employed to investigate the underlying mechanisms responsible for these observations. Optical microscopy and Scanning Transmission Electron Microscopy with High-Angle Annular Dark Field (STEM-HAADF) imaging were utilized to observe the microstructural evolution in 316L stainless steel. These methods confirmed that the detected signals are correlated with early microstructural changes, specifically the increase in dislocation density, the formation of dislocation tangles, and the onset of cellular structure formation.

Acknowledgement

I would like to thank my supervisors Dr. Ebad Bagherpour, Prof. Zhongyun Fan, and Prof. Isaac T. H. Chang for their invaluable support, guidance, and for providing me with the opportunity to pursue my PhD studies at Brunel University London. I extend my special thanks and deepest gratitude to Dr. Ebad Bagherpour for his generous help and support throughout my time as a PhD student. His advice and encouragement have been invaluable throughout my research journey.

I am especially thankful to Prof. Isaac T. H. Chang for his patient supervision and continuous guidance, particularly during the writing phase of this thesis. I am equally grateful to Prof. Zhongyun Fan for his scientific insight and mentorship, which inspired me to explore innovative directions in my work and to push the boundaries of my thinking.

Secondly, I would like to thank my colleagues for their technical support during my PhD studies. I am grateful to Dr. Chamini Mendis and Shubham Sanjay Joshi for their help in operating the transmission electron microscope, capturing images, and assisting with the interpretation of TEM data. For their support in the technical team, I sincerely thank Mr. Stephen Cook, Mr. Peter Lloyd, Mr. Philip Nicola, Miss Loredana Saccone, for their assistance in using laboratory equipment and facilities. I would also like to thank the administrative team, especially Susan Job, for arranging travel and accommodation for the conferences I attended. I also wish to thank the panel members who supported me during my reviews and progress: Prof. Hamid Assadi and Prof. Dmitry Eskin, for their constructive feedback and encouragement during key stages of my project.

I gratefully acknowledge the financial support provided by UKRI/EPSRC grant EP/V011804/1 and Brunel University London, without which this research would not have been possible.

Thirdly, Special thanks are due to my colleagues and friends Samira Mortezai, and Sadegh Jalalian. The discussions, collaborations, and shared experiences with them made this journey intellectually enriching and personally rewarding.

On a personal note, I am deeply grateful to my family for their love, patience, and belief in me. To my partner, Alexandru Negoita—thank you for your constant encouragement and for being my rock during the toughest moments. To my friends, thank you for the laughter, distractions, and emotional support that helped me maintain balance and perspective.

Research Output

- Awarded best poster prize at the Advanced Metallurgy Symposium held at Imperial college London (20205).
- Finalist in the Society of Women Engineers (SWE) Munich poster competition; presented research in materials engineering and was sponsored by Motorola Solutions for full participation in the event.
- Finalist in the Three Minute Thesis (3MT) presentation competition at Brunel University London; also featured in a podcast episode on Spotify's *Circular Metal* channel, highlighting the significance of my research.
- Oral presentation at the 8th Postgraduate Symposium on Ferrous Metallurgy in London, sharing research findings with experts and peers in the field of metallurgy.
- M. Izadi, E. Bagherpour, I. Chang, Zh, Fan." Early-stage fatigue detection in metals: A comparative study between electrical resistivity and nonlinear ultrasound at early fatigue life of 316L stainless steel." 2025, (Under preparation).
- M. Izadi, E. Bagherpour, I. Chang, Zh, Fan, Sh. Sanjay Jashi." Microstructural origins of early-stage fatigue signal peaks: TEM-based analysis of dislocation evolution in 316L stainless steel."2025, (Under preparation).

Table of Contents

	Copyr	ight .		II	
	Abstra	act		!!!	
	Ackno	cknowledgement			
	Resea	rch (Output	1	
Ch	apter	1.	Introduction	6	
	1.1	Bac	kground	6	
	1.2	Res	earch Objectives	7	
	1.3	Out	line of the thesis	8	
Ch	apter	2.	Literature review	9	
	2.1	Intr	oduction	9	
2	2.2	Fati	gue	9	
	2.2.	1	Mechanisms of fatigue	10	
	2.2.	2	Rationale for material choice	14	
	2.2.	3	Evolution of dislocation structure in 316L Stainless Steel during fatigue	15	
	2.2.		Evolution of slip bands and persistent slip markings in 316L stainless steel	23	
	2.2.		Mechanical parameters of the fatigue loading		
	2.2.	6	High cycle fatigue	28	
	2.2.	7	Low cycle fatigue	28	
	2.3	Nor	n-Destructive techniques (NDT) for fatigue damage detection	29	
	2.3.	1	Surface investigation methods	30	
	2.3.	2	Electromagnetic testing	32	
	2.3.	3	Positron annihilation spectroscopy (PAS)	36	
	2.3.	4	Acoustic emission	37	
	2.3.	5	Electromagnetic testing	40	
	2.3.	6	Ultrasound methods	50	
	2.4 nonlin		clusion on chosen NDT methods: Justification for electrical resistivity and	62	
	apter	-	Electrical resistivity (ER) method		
	3.1	Intr	oduction		
	3.2	Fun	damental principle of electrical resistivity	66	
	2 2		or sources in electrical resistivity measurements	66	

	3.3.1		Elimination of thermoelectric voltage	68
	3.3.	2	Elimination of lead and contact resistance errors using the four-wire method	d 74
	3.3.	3	Elimination of non-ohmic Contact error	77
	3.3.	4	Eliminating of device heating	78
3.	4	Exai	mples of error correction techniques in fatigue and metallurgical studies	81
3.	5	Con	clusion	82
Cha	pter	4.	Nonlinear ultrasound testing	83
4.	1	Prin	ciples of second harmonic generation for fatigue damage detection	83
	4.1.	1	Equation of motion	84
4.	2	Con	clusion	91
Cha	pter	5.	Methodology	92
5.	1	Intr	oduction	92
5.	2	Fati	gue instrument	92
5.	3	Surf	ace roughness test with SURFTEST SJ-210	97
5.	4	Equ	ipment requirement for ER:	98
	5.4.	1	Electrical resistivity setup and measurement	102
5.	5	Mea	asurement instruments and procedure for nonlinear ultrasound	106
	5.5.1		Introduction	106
	5.5.2		Equipment for signal generation:	107
	5.5.	3	Experimental procedure:	115
	5.5.4		Signal processing	120
	5.5.	5	Signal processing methods	121
	5.5.		Experimental determination of optimal gain and magnitude for nonlinear	420
			ic testing	
_	5.5.7 5.6 Mic		Measurement procedure for repeatability assessment	
5.			roscopy techniques	
	5.6.		Optical microscope (OM)	
Char	5.6.		Experimental procedure TEM	
	pter 1		Non-destructive method results	
6. 6.			ection of high-cycle fatigue for early-stage damage detection	
o.	6.2.		Effect of probe spacing	
	6.2		Effect of measurement time on electrical resistivity	
	6.2	5	Effect of surface roughness on electrical resistivity	148

6.2.	Repeatability of the electrical resistivity (ER) measurement setup	150
6.2.	Reliability of the electrical resistivity (ER) measurement setup	153
6.2.	Study of fatigue process by ER	154
6.3	Nonlinear Ultrasonic testing method	159
6.3.	Influence of gain and magnitude on accuracy of measurements	159
6.3.	Repeatability of NLP measurement setup	162
6.3	3 Study of fatigue process using NLP	163
6.4	Summary	166
Chapter	7. Microstructural characterization results	168
7.1	Introduction	168
7.2	Optical microscopy study	168
7.3	TEM studies	170
7.3.	1 Comparison of conventional TEM and STEM-HAADF images	170
7.3.	2 STEM-HAADF studies of stainless steel 316L subjected to fatigue	174
7.4	Summary	192
Chapter	8. Discussion	193
8.1	Introduction	193
8.2	Evolution of dislocation during early-stage high cycle fatigue	193
8.3	Changes in ER and NLP in response to dislocation	199
8.3.	1 Effect of dislocation pinning on nonlinear acoustic response	199
8.3.	2 Effect of dislocation dipoles on nonlinear acoustic response	201
8.3.	3 Effect of dislocation features on electrical resistivity	203
8.4	Comparison of ER and NLP method	205
8.4.	Comparison of ER and NLP results during the early-stage HCF	205
8.4	Comparison of NLP results during the early-stage HCF for both sa 208	mple A and B
8.5	Correlation between ER/NLP and TEM/HDDF observations	209
8.6	Summary	217
Chapter	9. Conclusion and prospects	218
9.1	Conclusion	218
9.2	Future work	219
9.2.	1 Extending NDT monitoring further within pre-crack fatigue life	219
9.2 20%	2 Apply TEM/HDDF to study the development of microstructural ch HCF lifetime of 316L stainless steel	

9.2.3	Integration of NDT Techniques for In-Situ Fatigue Monitoring	.220		
9.2.4	Use of ECCI for dislocation mapping over larger areas	.220		
9.2.5	Applying these NDT methods to other engineering alloys	.220		
9.2.6	Implementation for complex-shaped components	.220		
Appendix A.		.221		
References				

Chapter 1. Introduction

1.1 Background

Fatigue has long been recognized as one of the most critical and common mechanisms of material failure in engineering structures. From the earliest failures in rotating shafts and bridges to the modern challenges faced in aerospace and offshore industries, fatigue has posed a persistent threat to the safety and reliability of structural components subjected to cyclic loading [1, 2].

Early investigations into fatigue behaviour primarily relied on destructive techniques, with a focus on fractographic analysis through advanced microscopy methods. Over time, it became evident that fatigue failure is typically initiated by the nucleation and growth of microscopic cracks, which eventually lead to macroscopic fracture [3].

In response, non-destructive testing (NDT) methods emerging as a promising approach as tools for tracking crack formation and growth before catastrophic failure occurs. Techniques such as acoustic emission, ultrasonic testing, and radiography were increasingly employed to monitor the onset and propagation of fatigue cracks. These methods aimed to identify crack initiation time, rate of crack growth, and failure prediction—thus enabling engineers to implement inspection and maintenance strategies before structural integrity is degraded [4].

More recently, the focus has shifted from crack detection to fatigue damage detection—that is, identifying structural changes that occur before any visible cracks have formed. This shift is driven by the realization that a considerable portion of a component's fatigue life may be spent in the so-called pre-crack nucleation phase, which involves dislocation multiplication, slip activity, formation of intrusions and extrusions, and surface roughness changes. Detecting this early-stage damage has the potential to revolutionize fatigue life prediction, enabling preventive action long before crack formation [5, 6].

Various NDT techniques have been explored for this purpose. Some have shown promise in monitoring the entire fatigue process—including the three key stages: pre-crack nucleation, crack initiation, and crack propagation [5]. However, many of the literatures has focused on low-cycle fatigue (LCF) conditions, where the damage mechanisms involve significant plastic deformation and surface changes, making them easier to detect. In contrast, high-cycle fatigue (HCF) typically involves lower stress amplitudes and lower-magnitude microstructural changes, making early damage more difficult to detect.

Moreover, many studies have approached fatigue damage as a generalized fatigue evolution, detecting structural changes at a few widely spaced intervals (e.g., 0%, 50%, and near failure), rather than examining structural behaviour at short intervals. As a result, the first 10–20% of the fatigue life—a critical phase for early diagnostics—remains largely under-investigated, particularly under HCF conditions.

The aim of this research project is to apply appropriate, responsive, and cost-effective NDT methods capable of detecting early fatigue damages in HCF, and correlating findings with microstructural changes.

By enabling the detection of microstructural damage trends within shorter fatigue-life intervals and earlier fatigue stage—such as the first 10%—this work supports sustainability goals in several ways. Early detection allows for timely intervention before cracks form or propagates, which can significantly extend the service life of components. This reduces the need for replacement prior to end-of-life, lowers material and manufacturing demands, and minimizes waste. In turn, it contributes to more resource-efficient maintenance strategies and promotes a circular economy by extending the structural performance lifespan of materials.

1.2 Research Objectives

The main objectives of this research are to validate non-destructive diagnostic methods capable of detecting early-stage fatigue damages—specifically in the high-cycle fatigue (HCF) regime—and to correlate these findings with microstructural changes. The motivation stems from the need to identify damages well before crack initiation, enabling more accurate life predictions and facilitating condition-based maintenance in industrial applications.

This research addresses the following specific objectives:

Objective 1: Evaluation of responsive and reliable NDT techniques for early-stage fatigue damage detection:

Review and select appropriate non-destructive testing techniques—particularly those responsive to dislocation density and related microstructural phenomena—and assess their capability to detect changes associated with early fatigue damage. Two primary NDT methods selected for detailed were study and comparison. While this study does not experimentally assess industrial applicability, the selection of NDT methods was guided by practical considerations, including cost-effectiveness, ease of use, and potential for application in complex geometries and real-world engineering environments. An essential aspect of this research is to evaluate not only the accuracy of the selected non-destructive testing (NDT) methods but also their repeatability and reliability. This involved conducting multiple trials under consistent conditions to verify that the measured responses are stable, reproducible, and consistent. Ensuring high repeatability is critical for establishing the credibility and practical applicability of these methods in detecting early-stage fatigue damage. The insights gained from this evaluation provide confidence in the robustness of the selected techniques for future industrial or research applications.

Objective 2: Microstructural evolution and its correlation with NDT responses in early-stage fatigue damage:

Investigate and document microstructural evolution that occurs in the early stages (e.g., first 10% of fatigue life) under high-cycle fatigue conditions, focusing on dislocation activity, slip band formation, and the onset of cell structures. Then, correlate data obtained from selected NDT techniques with observations from optical and electron microscopy, to validate the diagnostic potential of these methods for early-stage fatigue damage.

1.3 Outline of the thesis

This thesis is structured into nine chapters, each addressing a key component of the research. Following the introduction in this chapter, Chapter 2 provides a comprehensive literature review, focusing on the mechanisms of fatigue with an emphasis on the evolution of dislocation structures in 316L stainless steel. It further discusses existing non-destructive testing (NDT) methods and justifies the selection of nonlinear ultrasonic evaluation and electrical resistivity measurement as the two methods used in this study, along with the rationale for choosing stainless steel as the test material. Chapter 3 elaborates on the principles of the electrical resistivity method, particularly the use of the four-probe technique combined with delta mode. Chapter 4 presents the theoretical foundation of nonlinear ultrasonic testing, and Chapter 5 outlines the experimental methodology, including specimen preparation, fatigue testing procedures, the setup of non-destructive testing (NDT) techniques, the optimized parameters used for each technique in this study, and the microscopy methods applied in this research. Chapters 6 and 7 report the results of nondestructive measurements and microstructural characterization, respectively. In Chapter 8, a detailed discussion is presented, correlating the NDT results with observed microstructural changes to evaluate the effectiveness of each method in detecting early-stage fatigue damage and the success rate of both methods for early damage detection. Finally, Chapter 9 summarizes the key findings, highlights the contributions of the research, and proposes directions for future work.

Chapter 2. Literature review

2.1 Introduction

This literature review is divided into two main sections. The first part explores the mechanisms and microstructural evolution of fatigue, with a focus on 316L stainless steel, which is the material used in this research. The reason for selecting this alloy is explained in Section 2.2.2. This section emphasizes key features such as dislocation structures and slip bands formation before crack initiation. The second part reviews various non-destructive testing (NDT) methods, highlighting the rationale behind selecting electrical resistivity and nonlinear ultrasound for this study. Together, these two parts provide the foundational knowledge for understanding and detecting early-stage fatigue using NDT, which is central to the aim of this research.

2.2 Fatigue

Fatigue is one of the most common modes of failure in metallic components, occurring due to the progressive and localized structural damage that develops when a material is subjected to cyclic loading. Fatigue failures occur under repeated stresses that are often significantly lower than the material's yield strength. This makes fatigue particularly important, as components may appear structurally sound until they fail, often without any visible warning signs. It has been estimated that up to 90% of all metallic failures in service are related to fatigue, underlining its significance in engineering design and maintenance [1, 7]. In addition to conventional mechanical fatigue, other types such as corrosion fatigue—which occurs in corrosive environments—and creep fatigue—which happens under cyclic loading at elevated temperatures—are also important considerations in real-world applications. In this research, fatigue behaviour at room temperature is considered to facilitate experimental control and ease of implementation.

Fatigue is especially critical in high-performance and safety-critical industries such as aerospace, automotive, energy, and civil infrastructure. Aircraft wings, turbine blades, bridges, and vehicle suspensions all experience fluctuating loads during operation, making them vulnerable to fatigue-induced cracks that can propagate over time. The catastrophic consequences of undetected fatigue failures in such contexts highlight the necessity for reliable and early detection methods. In this research, "early detection" refers specifically to the identification of microstructural changes that occur prior to crack nucleation—well before any visible or detectable cracks form.

The process until a component finally fails because of fatigue can be divided into three stages: first, during many cycles, the damage develops on the microscopic level and grows until a microscopic crack is formed. Then, the microcrack grows until it becomes a macroscopic crack and in third stage it reaches a critical length and finally the cracked component breaks because it can no longer sustain the peak load. The details of the last two stages are usually considered within the scope of fracture mechanics. Because the majority of a component's

life is spent before a macroscopic crack becomes observable, most designs aim to prevent the occurrence of such damage [1–3, 7, 8]. This highlights the importance of early damage detection.

By detecting fatigue damage in its earliest stages—prior to crack initiation—it becomes possible to take timely and targeted actions that can significantly extend the service life of critical components. Most existing research focuses on damage assessment after microcrack formation, emphasizing crack growth monitoring and control. In contrast, this project aims to identify microstructural changes that occur before any visible cracks develop, using non-destructive techniques with high sensitivity. This reduces the need for replacement prior to end-of-life, lowers material and manufacturing demands, and minimizes waste. In turn, it contributes to more resource-efficient maintenance strategies and promotes a circular economy by extending the structural performance lifespan of materials.

To enable the detection of these defects, this chapter first discusses the stages and mechanisms of fatigue. This includes how cracks initiate and propagate under cyclic loading. This provides a foundation for understanding how fatigue damage evolves over time in metallic components. Then the role of defects and how they influence fatigue life is mentioned. The concept of early damage, as defined in the context of this research, is introduced in relation to microstructural changes that occur before visible cracks form. Additionally, brief overview of Low Cycle Fatigue (LCF) and High Cycle Fatigue (HCF) is also provided, along with definitions of key fatigue terms commonly used in this research.

2.2.1 Mechanisms of fatigue

Microscopic investigations since the early 20th century have shown that crack nucleation in the fatigue process typically originates from persistent slip bands (PSBs), which form because of localized cyclic plastic deformation. During the crack nucleation stage, dislocation structures evolve into PSBs, leading to intrusions and extrusions at the surface, though no visible cracks are yet detectable at this stage [5–7].

Following crack nucleation stage, microcracks form within or alongside of these PSBs. While initially microscopic and gradually propagating, they mark the beginning of the microcrack growth stage. As cyclic loading continues, microcracks begin to propagate deeper into the material, forming a continuous crack path. Once a critical size is reached, the behaviour transitions into the macrocrack growth stage, which is characterized by accelerated crack propagation. This transition typically occurs during the final 10–20% of the fatigue life. Eventually, the crack reaches a critical length at which the applied stress intensity exceeds the material's fracture toughness, resulting in catastrophic failure. Figure 2-1, shows the stages of the fatigue damage process, from initial cyclic slip and crack nucleation to microcrack and macrocrack growth, and ultimately, failure. This figure also reflects the corresponding stress parameters relevant to each stage—stress concentration factor (Kt) during initiation, stress intensity factor (K) during crack growth, and fracture toughness (Kc or KIC) at the point of failure. From a fatigue life standpoint, these stages follow a well-defined sequence: the

formation of persistent slip bands (PSBs) and crack nucleation generally occur in the early to mid-life region; microcrack growth dominates the transition phase; and macrocrack propagation followed by final failure typically occurs in the later stages of the component's life.

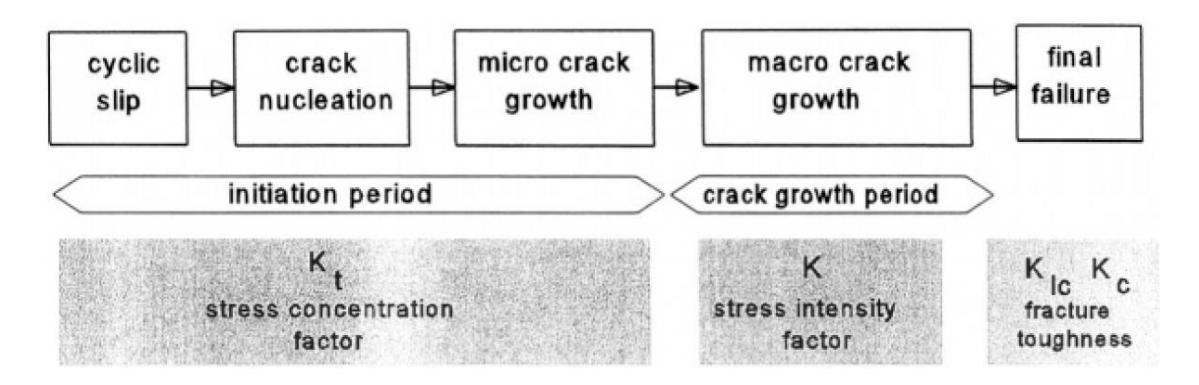


Figure 2-1. Different phases of fatigue life [10, 11]

Under cyclic loading, metals respond by developing a corresponding cyclic strain, which evolves as the material undergoes repeated loading and unloading. This strain response is not constant and reflects changes in the microstructure, such as dislocation movement, accumulation, and rearrangement. To understand this behaviour, the Cyclic Stress-Strain Curve (CSSC) is commonly used, as shown in Figure 2-2. This figure is divided into three primary stages—Stage A, Stage B, and Stage C—each corresponding to distinct microstructural processes that govern fatigue damage progression. The x-axis represents the plastic shear strain (γ_p) on a logarithmic scale, while the y-axis shows the saturation shear stress (τ_{sat}), which reflects the stress level at which the material stabilizes during cyclic loading. In Stage A, material undergoes initial cyclic hardening. This phase is characterized by significant increase in dislocation density as the material responds to the applied loading conditions. The corresponding microstructural image in this stage reveals a highly disordered arrangement of dislocations. As cyclic loading continues, these dislocations begin to interact, multiply, and form complex tangles. This behaviour leads to an increase in saturation stress, reflecting the material's evolving internal resistance to plastic deformation. Stage B represents a plateau phase, where the saturation stress reaches a relatively stable level. During this stage, a significant transformation in the dislocation structure occurs. Dislocations start to reorganize into more defined patterns, forming persistent slip bands (PSBs), which are narrow zones of intense cyclic plastic deformation. The figure includes a curve showing the volume fraction of PSBs increasing significantly during this stage. These PSBs lead to the development of intrusions and extrusions along the surface, particularly near grain boundaries. The schematic illustrations in the figure show how PSBs interact with surrounding grains and act as preferred sites for crack initiation. In Stage C, localized stress continues to increase around persistent slip bands (PSBs), and the microstructure becomes increasingly stabilized, yet remains highly strained.

The dislocations within the PSBs evolve into cell-like structures with thickened walls, indicating a degree of saturation and hardening. This stage marks the onset of crack initiation, typically beginning at PSBs located near grain boundaries where stress concentrations are high. The final schematic representations in the figure for stage C show the mechanisms of crack formation from PSB-induced intrusions and slip transmission across grain boundaries. These microstructural changes result in visible fatigue crack growth, marking the transition from early-stage damage to macroscopic failure. While this study focuses primarily on early-stage fatigue damage, particularly the mechanisms that occur prior to detectable crack formation, it is helpful to briefly review the overall fatigue process to introduce the early indicators of fatigue progression.

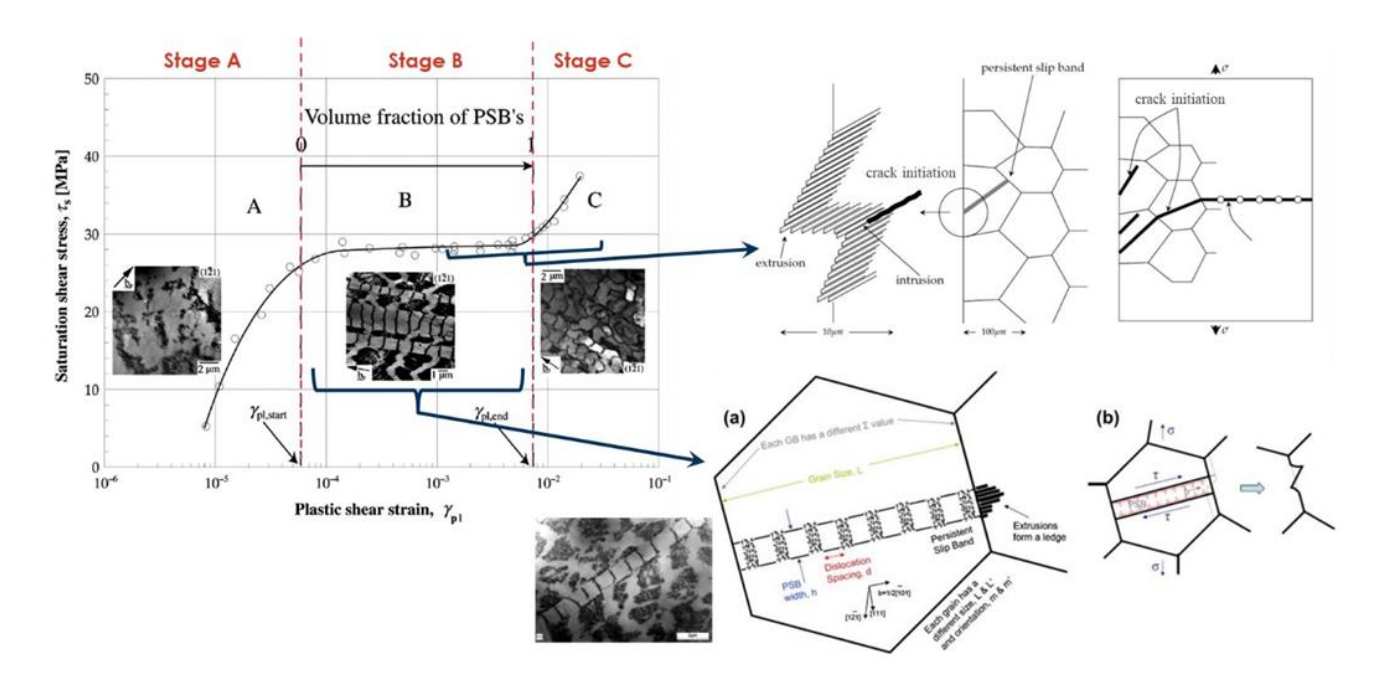


Figure 2-2. A cyclic stress strain curve (CSSC) illustrating the 3 stages of fatigue damage (Figure created by combining and modifying images from [12, 13]

2.2.1.1 Crack initiation

Fatigue crack initiation is often the most prolonged stage in the fatigue life of a component, typically accounting for up to 70–90% of the total fatigue life, especially under low-stress or high-cycle fatigue conditions. This stage is strongly influenced by microstructural features, surface conditions, and local stress concentrations. The process usually begins with localized plastic deformation within individual grains, where cyclic slip accumulates along specific crystallographic planes of maximum shear stress—typically oriented at 45° to the loading axis. This slip activity leads to the formation of intrusions and extrusions on the material surface, which appears as Persistent Slip Marks (PSMs). These surface steps act as micro-notches, intensifying local stress and strain concentration, and thereby serving as primary sites for crack initiation[14]. The critical condition for crack initiation from PSMs is typically associated with a threshold level of slip band density and localized cyclic strain, beyond which microcracks nucleate along persistent slip bands (PSBs) intersecting the free surface.

Experimental studies have correlated surface roughness amplitudes on the order of 0.5–2 μm with the transition to Stage I (crack growth in micron-scale) crack growth. Moreover, the incomplete reversibility of dislocation motion under cyclic loading promotes the gradual build-up of surface steps. This phenomenon has been well documented using transmission electron microscopy (TEM) and scanning electron microscopy (SEM) [15-18]. Stress concentrators such as notches, scratches, or machining marks can significantly accelerate the initiation process. Additionally, material heterogeneities like inclusions, voids or secondphase particles are also common initiation sites. These features promote crack formation primarily by acting as internal stress concentrators, due to differences in elastic modulus, thermal expansion, or interfacial bonding compared to the surrounding matrix. In highstrength steels, fatigue crack nucleation has been observed at oxide or sulphide inclusions ranging from 10–100 μm in size [19]. Similar behaviour has been reported in aluminium alloys, where fatigue cracks often initiate at intermetallic inclusions containing alloying elements such as Fe or Mn [20]. Although surface crack initiation is more common due to environmental interactions and stress localization, subsurface crack initiation can also occur especially when large inclusions or voids are located below the surface. Subsurface cracks are particularly dangerous as they may remain undetected until they reach a critical size.

2.2.1.2 Crack propagation

Once a microcrack has formed, fatigue process enters crack propagation stage. This typically occurs in two sub-stages: Stage I (crack growth in micron-scale) and Stage II (crack growth at macro-scale). In Stage I, cracks propagate along crystallographic slip planes in a shear mode, often at 45° to the principal stress axis, and grow slowly on the order of microns. Microstructural barriers, particularly grain boundaries, play a significant role in influencing this growth, as they can temporarily impede or alter the path of crack propagation [2].

As the crack extends and crosses several grains, it transitions into Stage II, where it grows perpendicular to the maximum tensile stress. This behaviour marks a shift from crystallographic, shear-driven propagation to opening mode crack growth. While Stage I crack growth occurs along slip planes (~45° to the loading axis) due to localized shear and dislocation motion within single grains, Stage II growth reflects the dominance of tensile stress at the crack tip, which drives the crack to open and extend in a direction normal to the maximum principal stress. Here, the crack follows a more stable path, often leaving behind fatigue striations (microscopic features on the fracture surface that correspond to each loading cycle). Stage II growth is generally well-described by linear elastic fracture mechanics (LEFM) using the Paris Law, which relates the crack growth rate to the stress intensity factor range [21].

2.2.1.3 Failure

The final fracture stage occurs when the crack reaches a critical length and the remaining material can no longer support the applied load, leading to rapid, often brittle failure. However, as the focus of this research is on the pre-crack stage, further discussion on fatigue

crack growth and catastrophic failure will not be pursued. Instead, emphasis is placed on understanding the microstructural and mechanical mechanisms leading up to crack initiation[11].

2.2.2 Rationale for material choice

Having discussed the general stages of fatigue—namely crack initiation, propagation, and final fracture—the following section shifts focus to the material used in this study: 316L stainless steel. The discussion will then narrow to the characteristics and mechanisms of early fatigue damage in this specific alloy. The selection of this alloy is based on its widespread industrial use, stable mechanical properties, and extensively studied microstructure. Since this research aims to identify and analyse early indicators of fatigue damage, such as slip band formation and dislocation structures, it is important to use a material in which fatigue behaviour is both representative and experimentally accessible. Steel and aluminium alloys are among the most used materials in fatigue-prone applications. In steels, cracks typically initiate from microstructural defects such as inclusions, slip bands and grain boundaries, whereas in aluminium alloys, intermetallic particles and slip lines play a dominant role in early crack nucleation [20] For the scope of this study, the aim is to narrow down the fatigue initiation mechanisms to slip lines in steels, making 316L stainless. steel an ideal candidate due to its consistent microstructural behaviour and absence of inclusions typically found in this alloy. 316L stainless steel belongs to the austenitic family of stainless steels, which are characterized by a face-centred cubic (FCC) crystal structure.

Grade 316L is the low-carbon version of 316 and contains significant amounts of chromium (~16–18%), nickel (~10–14%), and molybdenum (~2–3%), along with a carbon content of less than 0.03%. The presence of molybdenum enhances resistance to pitting, while the low carbon content prevents sensitization (chromium carbide precipitation at grain boundaries, which can lead to intergranular corrosion, especially in stainless steels during welding) during welding, making it a reliable choice for structural and biomedical applications. Furthermore, 316L shows good formability, weldability, and mechanical stability, making it a popular material in industries ranging from nuclear and chemical processing to medical implants and marine structures. The alloy's ability to form a stable chromium oxide passivation layer at the surface provides it with long-term protection against oxidation and degradation, even in aggressive environments. Given these combined advantages, 316L offers an ideal platform for studying the early stages of fatigue damage, particularly those related to slip activity and dislocations.

Given that, this research focuses on detecting early-stage fatigue damage using non-destructive testing (NDT) techniques, it is crucial to discuss the microstructural evolution that occurs prior to visible crack formation in 316L stainless steel. Most of this material's fatigue life occurs during the pre-crack nucleation phase, marked by a rise in dislocation density, dislocation entanglement and formation of persistent slip bands (PSBs). These early

microstructural changes are key indicators of fatigue damage and serve as important targets for detection using NDT methods.

To effectively understand and characterize early fatigue behaviour, two complementary aspects of microstructural development are considered in the following sections. The first aspect involves the development of dislocation structures within grains, which begins in the very early cycles of loading around 10% of fatigue life even before the appearance of slip bands. These internal dislocation arrangements provide critical insight into subsurface fatigue mechanisms and represent the earliest detectable signs of fatigue-related damage. The second focus is on the formation and evolution of slip bands, which with continued cyclic loading evolve into PSBs and generate surface features known as persistent slip markings (PSMs)—namely intrusions and extrusions that frequently act as crack nucleation sites. Together, these perspectives form the foundation for understanding how early fatigue symptoms appear in 316L stainless steel and how they can be identified using NDT techniques.

2.2.3 Evolution of dislocation structure in 316L Stainless Steel during fatigue

In this section, the evolution of dislocation density and dislocation structures during the fatigue of 316L stainless steel is discussed. Various types of dislocation configurations and their transformation mechanism throughout fatigue life are discussed in detail. This section is particularly important, as the core objective of this research is to use non-destructive testing (NDT) techniques to detect and monitor these microstructural changes, providing an alternative to conventional destructive methods such as Transmission Electron Microscopy (TEM).

The deformation behaviour of AISI 316L stainless steel under cyclic loading is linked to the evolution of its dislocation structures. This occurs because local plasticity can still be activated at stress concentrations—such as grain boundaries, surface imperfections, or inclusions—even under elastic loading conditions. Pham et al. [22], investigated the dislocation structure of 316L stainless steel at room temperature and under low-cycle fatigue (LCF) conditions, where the applied stress amplitudes exceeded the yield strength. Their study revealed a clear correlation between the stages of mechanical response and the corresponding microstructural transformations within the material. These stages are an initial hardening phase, followed by softening, and ultimately a stabilized regime [23].

Initially, the as received 316L stainless steel contains a relatively high dislocation density due to prior processing steps such as hot working, heat treatment or annealing, that occurred before fatigue testing. These dislocations exist predominantly in planar arrangements, including stacking faults particularly close to grain boundaries as shown in Figure 2-3. Such structures are characteristic of FCC metals with low stacking fault energy like 316L, where dislocation motion prefers planar glide.

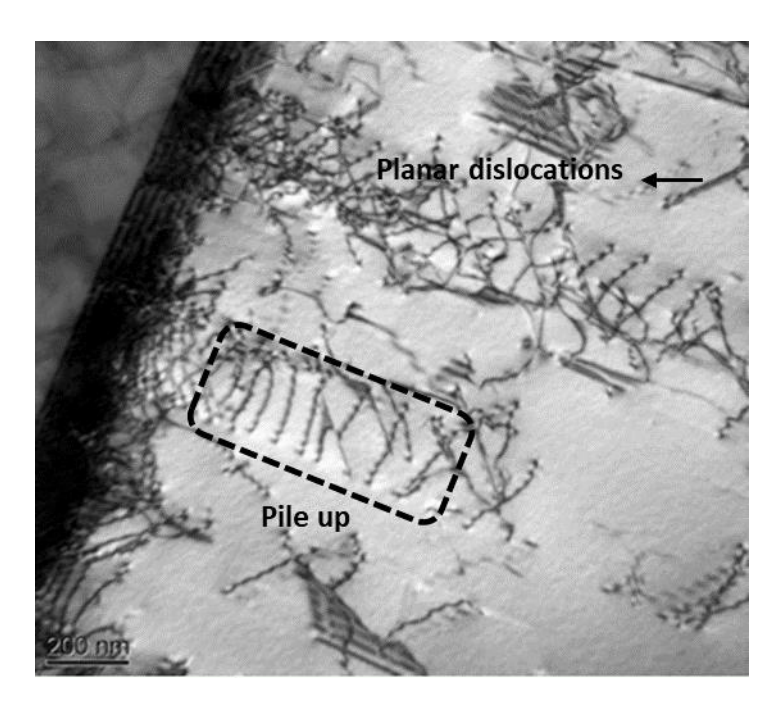


Figure 2-3. Dislocation structures in the as-received (solution treated) condition observed in the <001> beam direction.

Planar structures and dislocation pile-up [23]

As cyclic loading begins, dislocation density rapidly increases, particularly during the early cycles associated with cyclic hardening. Within 8 cycles which is 0.3% fatigue life (the hardening stage), dislocation structures become more tangled and complex, yet still largely maintain a planar character. TEM analysis reveals that while dislocations near grain boundaries are highly dense, the interior of grains maintains clearer planar arrays, indicating heterogeneous activation of slip (Figure 2-4). By the end of the hardening stage (~30 cycles, 1% fatigue life), a homogeneous distribution of dislocations was observed (Figure 2-5a). Repeated dislocation motion along preferred slip planes cause the original grains to break up into smaller regions, called sub-grains, due to internal structural changes (Figure 2-5b).

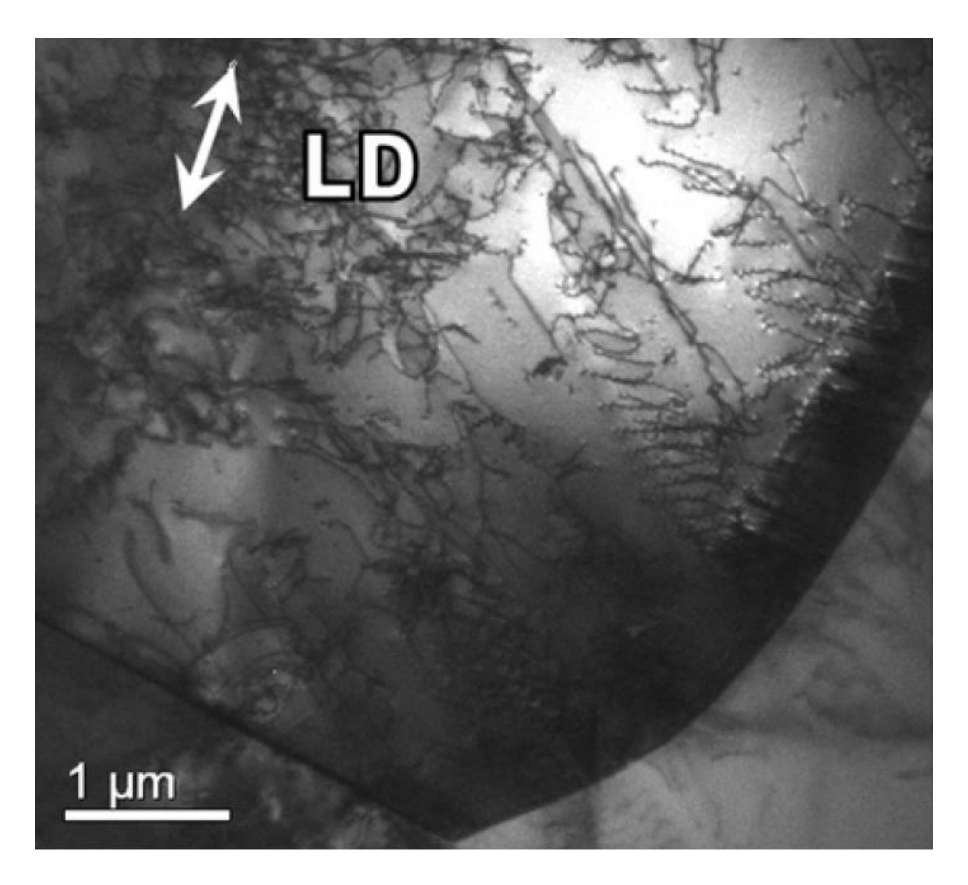


Figure 2-4. Dislocation structures during cyclic hardening with respect to the loading direction (LD) (at 0.3% fatigue life): planar structures of dislocations co-existing with tangled structures of dislocations observed close to grain boundary [23]

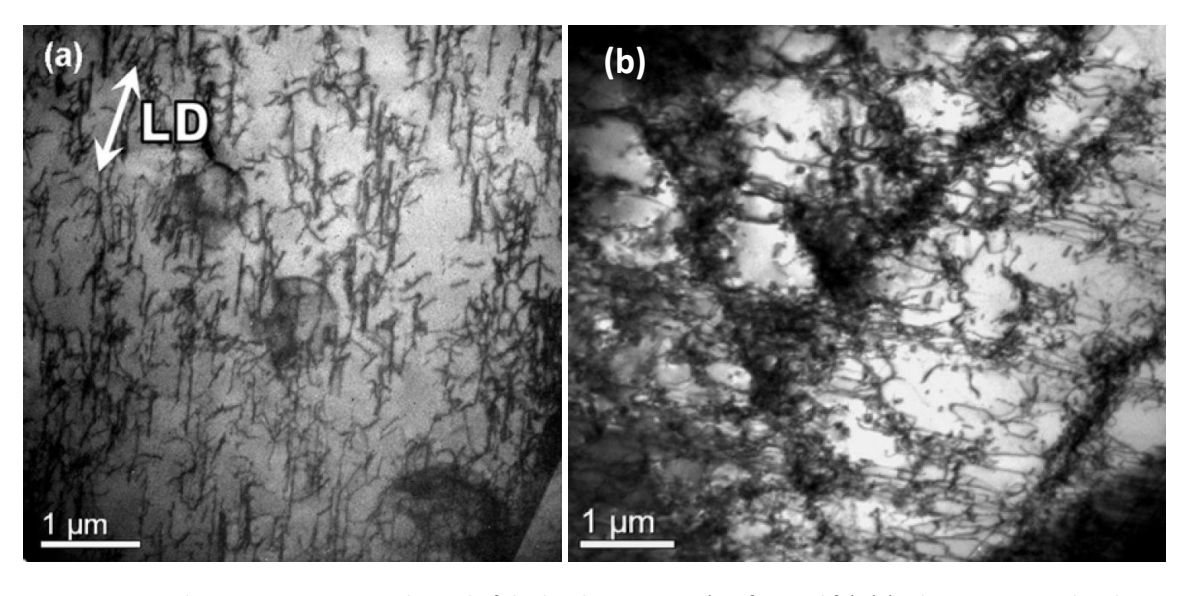


Figure 2-5. Dislocation structures at the end of the hardening stage (1% fatigue life). (a) A homogeneous distribution of dislocations was observed in the <001> beam direction (b) Sub-division of grains by intensely active slip planes observed in the <11 ⁻ 1> beam direction [23]

As fatigue progresses, dislocation interactions become more complex. Between 30–400 cycles (1% to 14% fatigue life), corresponding to the softening phase, the tangled networks begin to reorganize into more structured sub-domains. At this stage, dislocations rearrange into wall-

channel configurations, where dense dislocation walls bound low-density interior regions (Figure 2-6). These walls act as barriers to slip, while the channels provide easier paths for dislocation glide. Over time, these substructures evolve into well-defined equiaxed dislocation cells by the activation of secondary slip systems and cross-slip, promoting annihilation of mobile dislocations and the formation of dislocation-free zones.

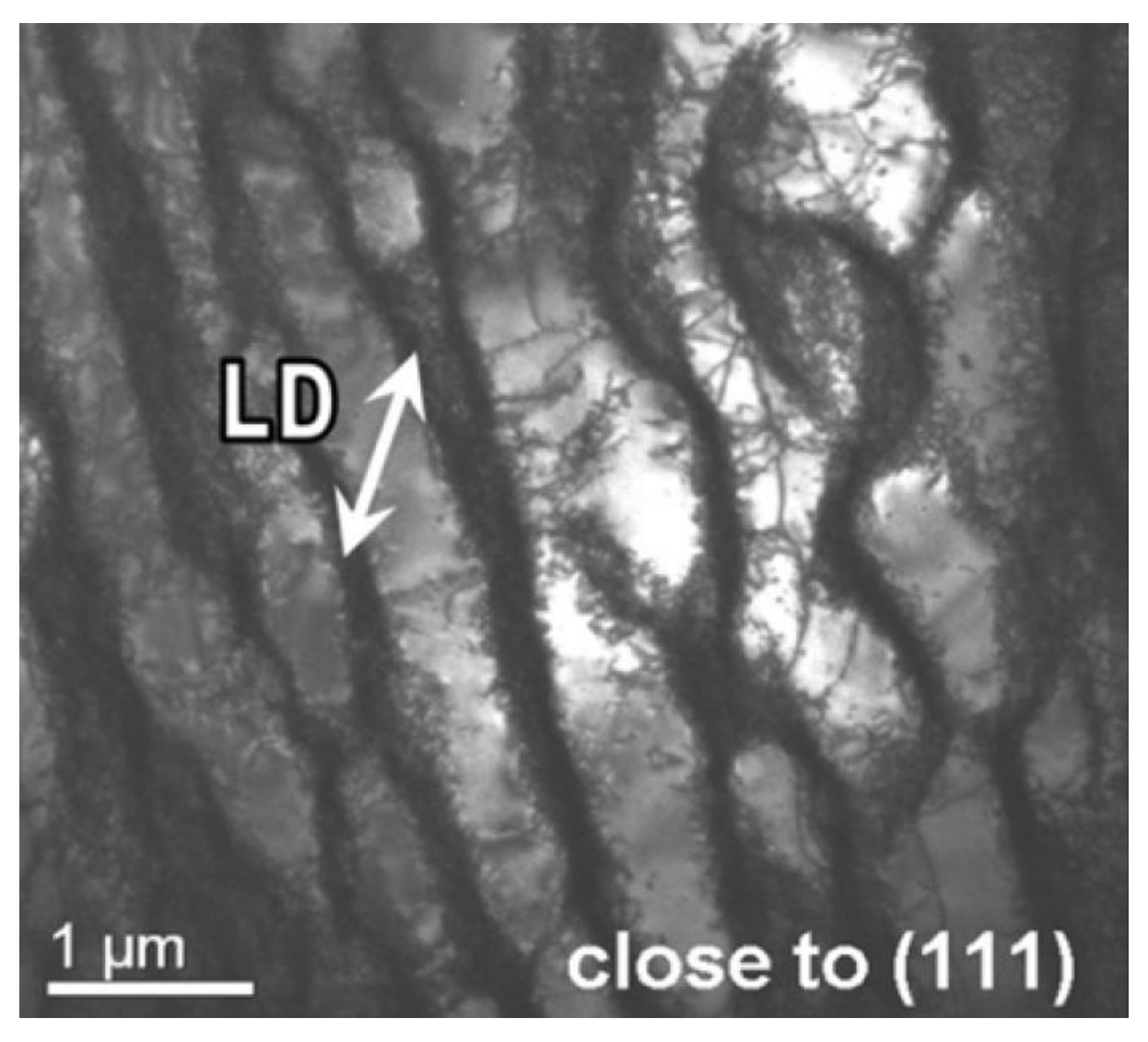


Figure 2-6. Dislocation structures at the midpoint of the softening response phase (1-14% fatigue life). Wall- channel structure is observed in a plane closed to (111) [23]

Interestingly, Pham et al. [22], observed that before fully developed cellular structures appear, a transient yet distinct structure known as the labyrinth structure forms during the mid-to-late softening stage. As reported in their study, the thick dislocation veins visible midway through softening (Figure 2-6), transform into thinner, denser, and more organized walls by the end of the softening regime which is called labyrinth structure showing in Figure 2-7.

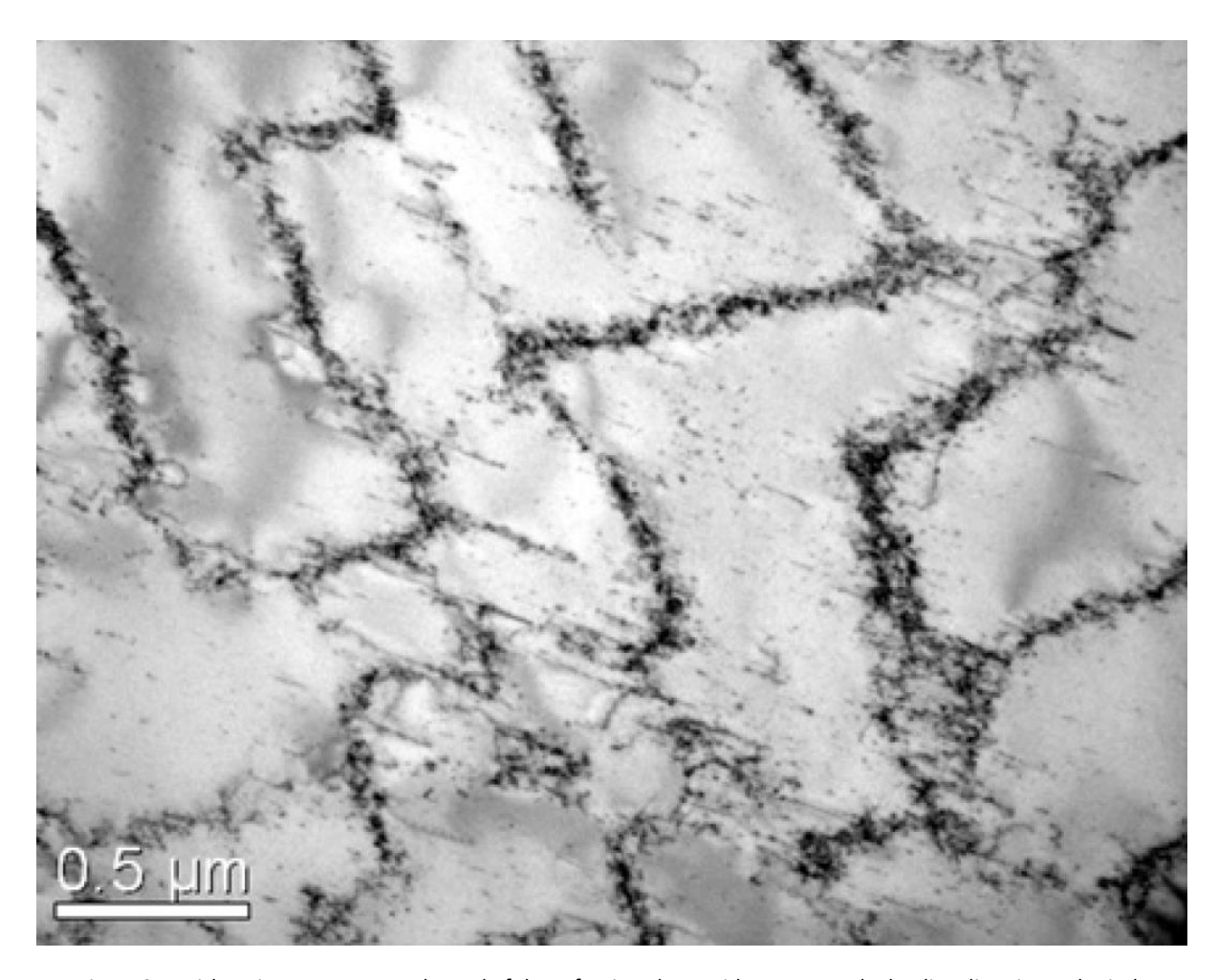


Figure 2-7. Dislocation structures at the end of the softening phase with respect to the loading direction. Labyrinth structure [23]

Boulanger et al. [20], also provided further evidence for the formation and importance of labyrinth structures in dislocation evolution. They studied the development of dislocation structures in 316 stainless steels under cyclic loading. Their work showed that labyrinth-like patterns formed, especially in grains where the [100] crystallographic direction aligned with the applied stress (Figure 2-8). In these grains, dislocation walls formed in two perpendicular planes, creating a well-organized three-dimensional network. These walls were about 50 nm thick and spaced approximately 300 nm apart. Inside these structures, straight screw dislocations moved between the walls, showing that the labyrinth could still support dislocation motion while maintaining its dense and organized shape under fatigue loading.

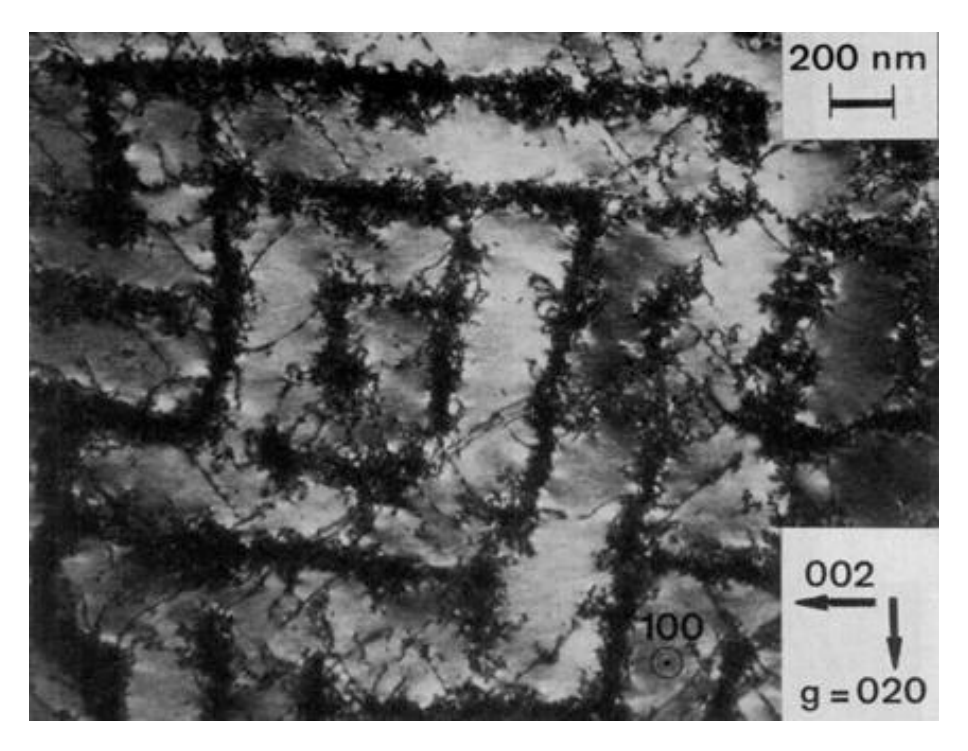


Figure 2-8. Image of labyrinth dislocation structure in thin foil prepared parallel to the stress axis in 316L stainless steel [21]

While Boulanger's observations [24], were made at slightly elevated temperatures (873 K), the dislocation mechanisms—primarily glide and cross-slip—remain valid at room temperature. The resemblance of these structures to those observed by Pham et al. [22], suggests that the labyrinth configuration is a reproducible and orientation-sensitive dislocation feature, emerging prior to or in parallel with cell formation in specific grain orientations. The labyrinth structure likely forms as a transitional stage between early dislocation wall development and the appearance of fully formed dislocation cells or persistent slip bands (PSBs). In some grains, PSBs were observed to cut through the labyrinth structures, forming ladder-like patterns. Although these patterns are less regular than those typically seen in pure metals, they remain clearly visible under TEM (Figure 2-9). This suggests that PSBs may develop at a later stage, building upon the dislocation framework already established by the labyrinth. As fatigue progresses, dislocation motion becomes more concentrated within these PSBs, which accommodate repeated plastic deformation in highly localized regions. These bands are closely linked to the formation of surface features like intrusions and extrusions. In simple terms, cracks often begin to form along these PSBs in the later stages of fatigue.

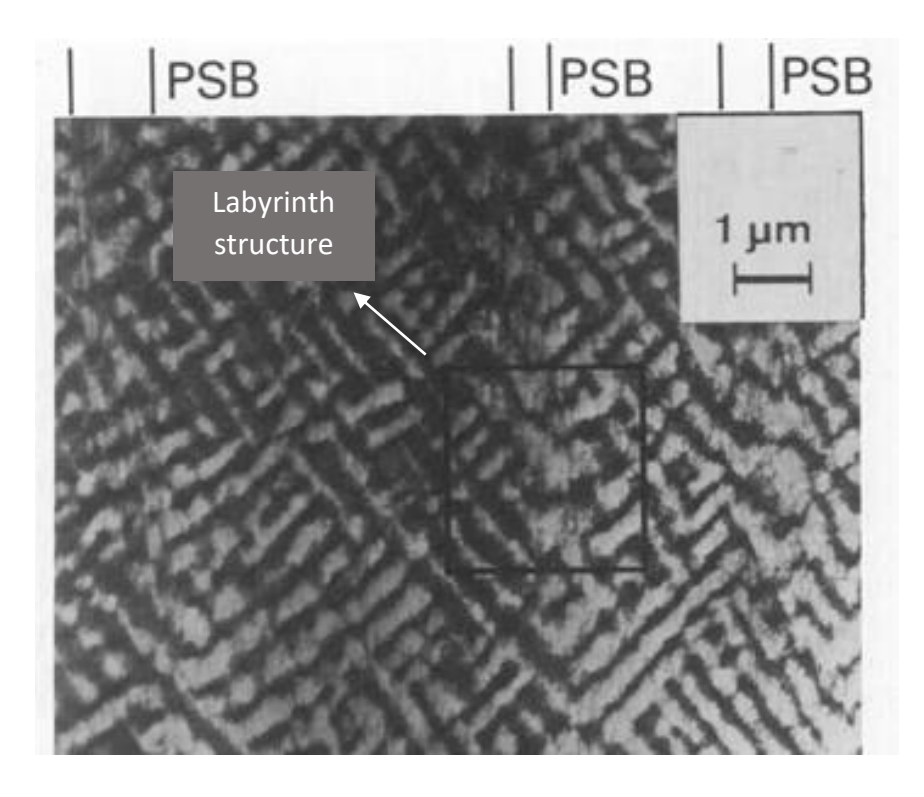


Figure 2-9. This structure composed of PSBs, crossing a labyrinth dislocation structure in 316L stainless steel [21]

Back to Pham et al. [20, 22], they studied another feature of dislocations that is created during the stabilized response stage (Beyond ~400 cycles and continuing until the final 14% of the fatigue life), the microstructure settles into cellular dislocation structures. These consist of equiaxed dislocation cells bounded by high-density walls (Figure 2-10).

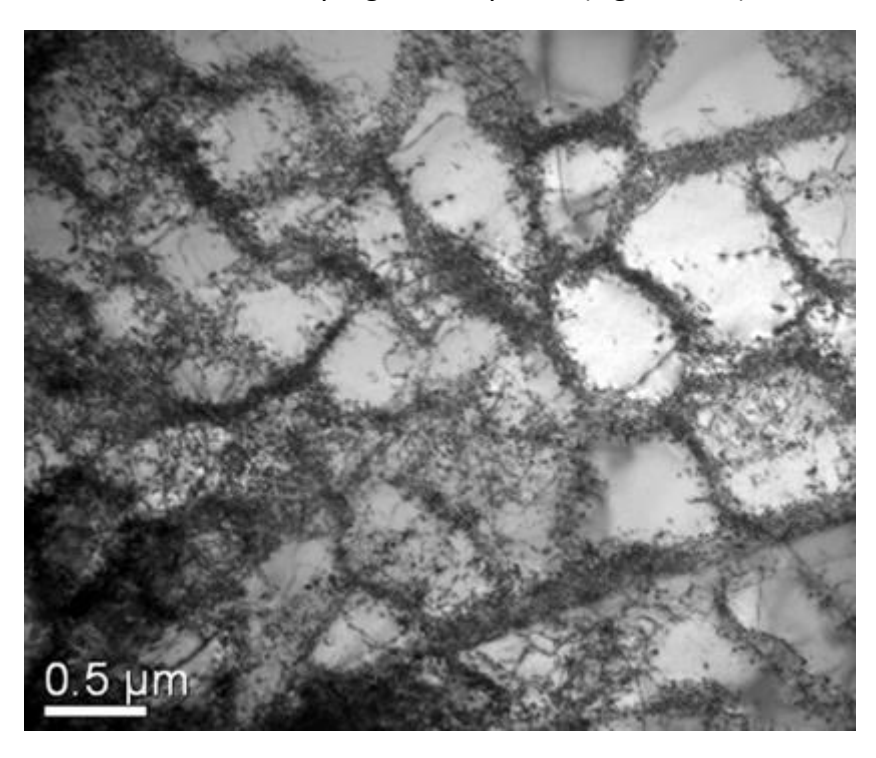


Figure 2-10. Dislocation cell structures near the end life for 316L stainless steel [23]

The comprehensive 3D model proposed by Pham et al.[26], also encapsulates these transitions: from planar dislocation to tangles to wall/channel sub-domains and equiaxed cells. This sequence mirrors the material's mechanical response: initial hardening due to increase in dislocation density and dislocation tangles, followed by softening from rearrangement of dislocations and channel formation, and eventual stabilization through organized cellular networks.

Also, in another work they conclude that in 316L stainless steel, persistent slip bands (PSBs) generally become active toward the end of the softening stage of fatigue, particularly under higher strain amplitudes such as ±0.7%. These bands play a key role in accommodating localized plastic deformation and are strongly associated with surface features like intrusions and extrusions, which are known as onset to fatigue crack initiation. Cracks often nucleate within these PSB regions as fatigue progresses. However, dislocation walls surrounding these structures can also act as barriers to crack propagation, as shown by Pham et al. [23], who observed short cracks terminating or deflecting at these walls. Their work suggests that while PSBs serve as common sites for crack initiation, the surrounding dislocation structures can influence whether cracks will propagate and if so, how they will grow [23].

This microstructural evolution—from dislocation tangles to wall/channel networks, equiaxed cells, and eventually PSBs—not only mirrors the mechanical response of 316L stainless steel but also highlights the interactions between dislocations. While the early stages are driven by an increase in dislocation density, later phases involve significant rearrangement and interaction between dislocations. During these interactions, particularly within walls, channels and PSBs, dislocations of opposite sign can annihilate, especially through mechanisms like cross-slip or dipole collapse. Although dislocation annihilation doesn't directly create stable structures, it helps control dislocation density, lowers internal stress, and supports the development of more organized dislocation patterns during fatigue. In this context, the model proposed by Essmann and Mughrabi [24], remains particularly influential in explaining how the cyclic stabilization of dislocation structures is governed by the balance between dislocation multiplication and annihilation. Dislocation multiplication commonly occurs through mechanisms such as the Frank–Read source, where a pinned dislocation bows out under stress and generates additional dislocations. Annihilation, in contrast, becomes significant as cyclic strain accumulates. Dislocations of opposite signs interact and cancel each other, especially within the walls of persistent slip bands (PSBs). This process becomes increasingly relevant in the later stages of fatigue, when dislocation density is high and microstructures begin to saturate. In 316L stainless steel, where dislocations are densely packed within PSBs and wall-channel structures, such interactions are frequent due to confined geometries. These mechanisms collectively transition the material from early-stage hardening to a stabilized cyclic response, where dislocation density and internal stress reach equilibrium. A second key insight is the mechanism by which screw dislocations undergo annihilation through cross-slip. In FCC metals such as 316L stainless steel, screw dislocations are highly mobile and can cross-slip, meaning they can move from one slip plane to another

nearby. While cross-slip doesn't directly annihilate dislocations, it can bring dislocations of opposite sign onto the same plane, where they can meet and annihilate. This leads to reduction in dislocation density and internal stress. This contributes to the evolution of more stable dislocation configurations, such as vein and cell structures, and aligns well with microstructural observations of cellular domains in 316L during the softening and saturation stages [25, 26].

Experimental studies using Transmission Electron Microscopy (TEM), Electron Channelling Contrast (ECC) imaging, and Electron Backscatter Diffraction (EBSD) have shown that cracks typically nucleate along primary slip bands where strain becomes highly localized. The formation of cellular structures and dislocation walls around these PSBs further intensifies local strain, creating gradients and lattice rotations that concentrate stress and lead to crack formation. Importantly, these dislocation arrangements are not just markers of structural evolution—they actively participate in the damage process. Dislocation walls, for instance, can accumulate stress or act as barriers, influencing how and where cracks begin and grow. In many cases, the interface between PSBs and the surrounding matrix becomes the preferred site for crack nucleation due to the incompatibility in cyclic plastic deformation. While PSBs undergo significant localized plastic strain, the adjacent matrix experiences much lower deformation, leading to strain mismatches and stress concentrations at the interface. This mechanical incompatibility promotes localized accumulation of damage, facilitating microcrack initiation along PSB boundaries. These findings strengthen the understanding that persistent slip bands, dislocation walls, and related strain localization features are the early indicators of fatigue cracks [10, 25, 27, 28]. Therefore, in the context of this research, detecting the evolution of slip bands and dislocation structures at the earliest possible stage is critical. By identifying these microstructural symptoms before cracks formation, this project aims to enable reliable early detection of fatigue damage in 316L stainless steel using nondestructive testing techniques.

2.2.4 Evolution of slip bands and persistent slip markings in 316L stainless steel during fatigue

Under monotonic loading, slip bands form as an early sign of plastic deformation in crystalline materials. In 316L stainless steel, these bands appear when the applied stress exceeds the critical resolved shear stress (CRSS) for dislocation motion. Initially, dislocations move along multiple slip planes, but deformation quickly localizes into specific crystallographic planes that are most favourably oriented with respect to the loading direction. These slip bands are typically narrow, planar features aligned with the active slip systems.

In materials with a face-centred cubic (FCC) structure, such as 316L stainless steel, slip typically occurs on the $\{111\}$ planes in the $\langle 110 \rangle$ directions, resulting in a total of 12 possible slip systems for FCC materials [29]. Initially, dislocation motion occurs broadly across multiple planes, but with continued loading, slip activity begins to concentrate into a few preferred planes—those oriented most favourably with respect to the applied stress (i.e., those with

high Schmid factors). These zones of repeated, concentrated slip eventually stabilize into PSBs, which represent cyclically active and geometrically persistent structures.

Internally, Persistent slip bands (PSBs) consist of organized dislocation structures, often described as ladder-like arrays with walls of immobile dislocations and channels of mobile ones. This arrangement allows the material to accommodate cyclic plasticity in a stable but irreversible way. As PSBs intersect the material's surface, they produce persistent slip markings (PSMs)—visible intrusions and extrusions resulting from non-reversible shear. These markings reflect the underlying dislocation activity and can be observed using high-resolution techniques such as Atomic Force Microscopy (AFM) and Scanning Transmission Electron Microscopy (STEM).

Importantly, these surface markings begin to appear very early in the fatigue life in a low cycle fatigue regime. As shown in the AFM studies by Man et al.[16], in Figure 2-11 and Figure 2-12 intrusions and extrusions in 316L stainless steel can be observed after as few as 10 to 50 cycles, often within the first 0.1% of total fatigue life. These features typically form at angles of 70°-80° to the loading direction. At this stage, most grains show slip activity along a single dominant system. By approximately 500 cycles (~10% of fatigue life), more grains begin to activate secondary slip systems, but beyond this point, the number of grains with multiple active slip systems reaches a steady state—meaning no significant increase in slip system activity is observed across additional grains. This stabilization reflects a saturation in the microstructural response to continued cyclic loading. Meanwhile, surface topography continues to intensify—that is, the amplitude and clarity of persistent slip markings (PSMs), including intrusions and extrusions, become more pronounced and well-defined. This is evident in Figure 2-11 from (a) to (d), and in Figure 2-12, particularly between N = 1000 and N = 3000 cycles. This intensification is driven by increased dislocation accumulation and irreversible plastic shear within the previously activated slip bands, even though no new slip systems are becoming active [16, 18].

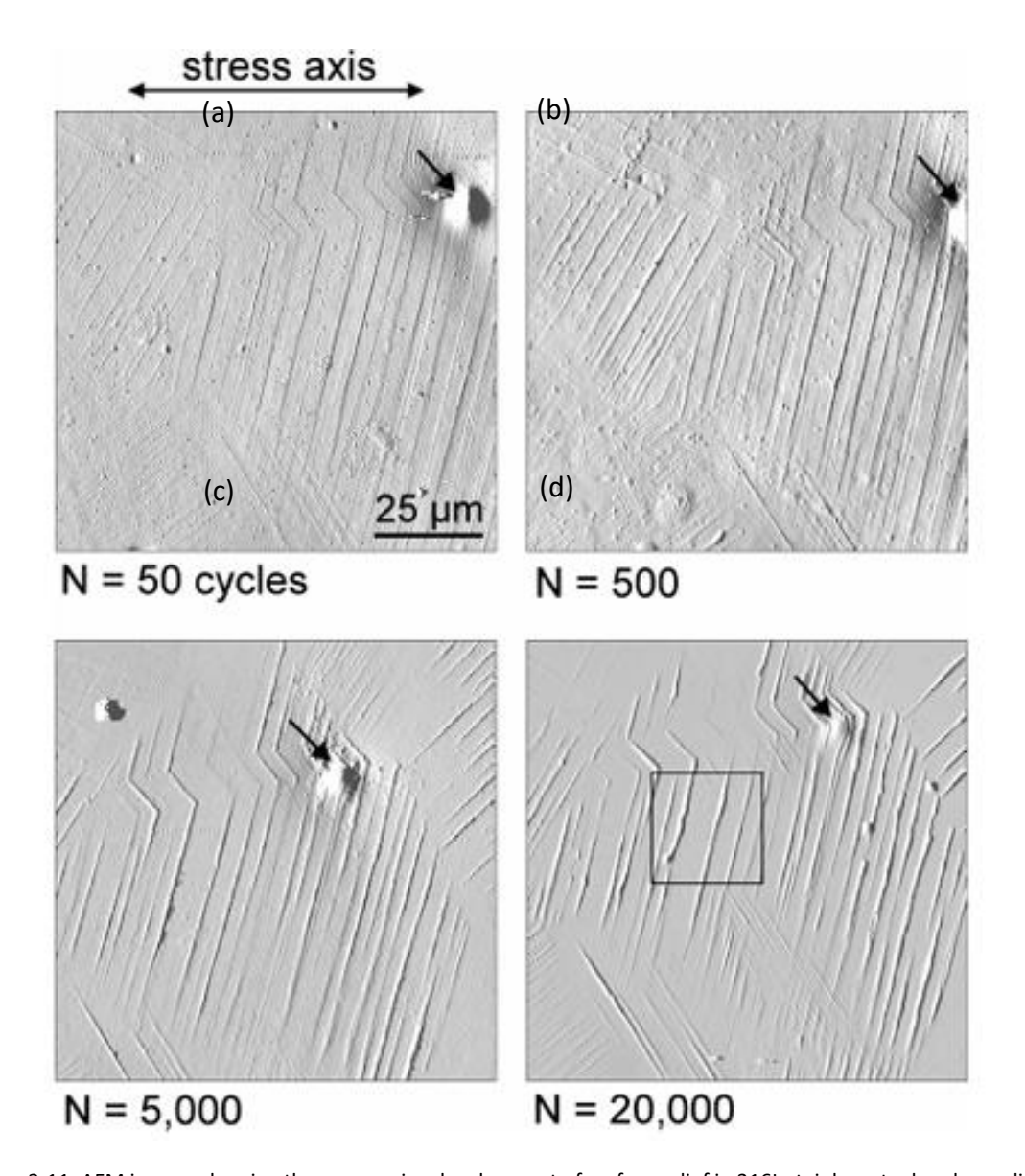


Figure 2-11. AFM images showing the progressive development of surface relief in 316L stainless steel under cyclic loading from 50 to 20k cycles. Persistent slip markings (PSMs) become more pronounced with increasing cycles, indicating the growth of persistent slip bands (PSBs) [16]

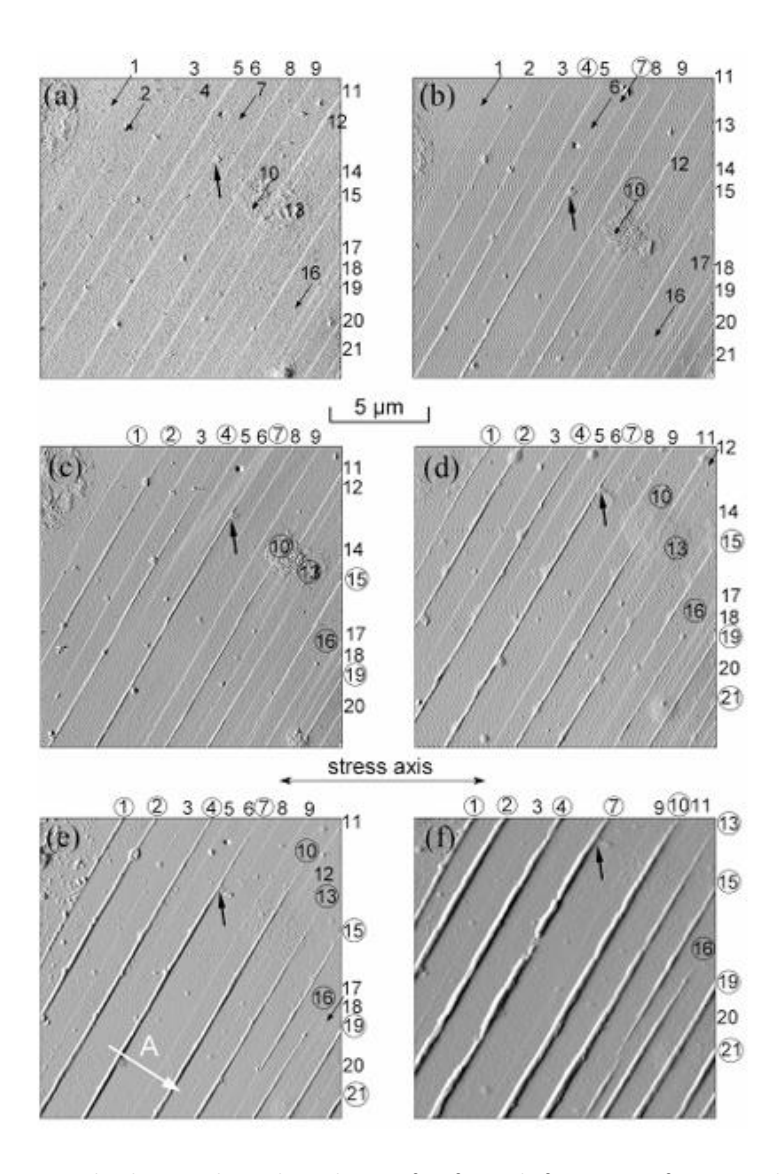


Figure 2-12. AFM micrographs showing the early evolution of surface relief in a grain of 316L stainless steel under cyclic loading at different fatigue cycles. Persistent slip markings (PSMs) begin to appear after only 10 cycles and progressively develop with increasing fatigue life. (a) N=10 cycles (0.02% N_f), (b) N=50 cycles (0.1% N_f), (c) N=100 cycles (0.2% N_f), (d) N=200 cycles (0.4% N_f), (e) N=1000 cycles (2.2% N_f), (f) N=3000 cycles (6.5% N_f) [18]

While both extrusions and intrusions develop together, it is the intrusions that play the more critical role in fatigue crack initiation. According to the model proposed by Polák et al.[18], the width of an intrusion is significantly narrower than that of an extrusion, but its depth is greater, resulting in more severe local stress concentrations. The sharp geometrical discontinuities and subsurface strain accumulation around intrusions make them ideal sites for microcrack nucleation. This has been confirmed in several AFM studies, where the earliest microcracks were almost exclusively associated with deep, narrow intrusions—often measuring between 10 nm to over 500 nm in depth as cycling progressed. Moreover, the evolution of these features follows a predictable pattern. Extrusion height increases rapidly within the first few hundred cycles and then plateaus, while intrusion depth continues to grow steadily and unevenly. By 2000 cycles, most extrusions are accompanied by one or two parallel intrusions with fluctuating depth profiles, and the critical depth at which crack initiation becomes likely has been experimentally observed to be approximately 170 nm in

316L stainless steel. This threshold aligns with findings from EBSD–AFM hybrid studies, which categorized fatigue cracks into grain boundary (GB), twin boundary (TB), persistent slip band (SB), and trans granular (TC) types, confirming that PSB cracks—those initiating at slip bands—are both common and mechanically significant [26].

2.2.5 Mechanical parameters of the fatigue loading

Fatigue loading is commonly idealized as cyclic loading, in which a material is subjected to repeated stress or strain over time. Key parameters used to describe each fatigue cycle include the maximum stress (σ_{max}), minimum stress (σ_{min}), stress amplitude (σ_a) and N is the number of cycles to failure. The mean stress (σ_m) is the average of σ_{max} and σ_{min} , while the stress range ($\Delta\sigma$) is the difference between them. The stress ratio (R) is defined as the ratio of σ_{min} to σ_{max} . Different materials show distinct behaviours in S-N plots. A common stress-life (S-N) curve is depicted in Figure 2-13 [29].

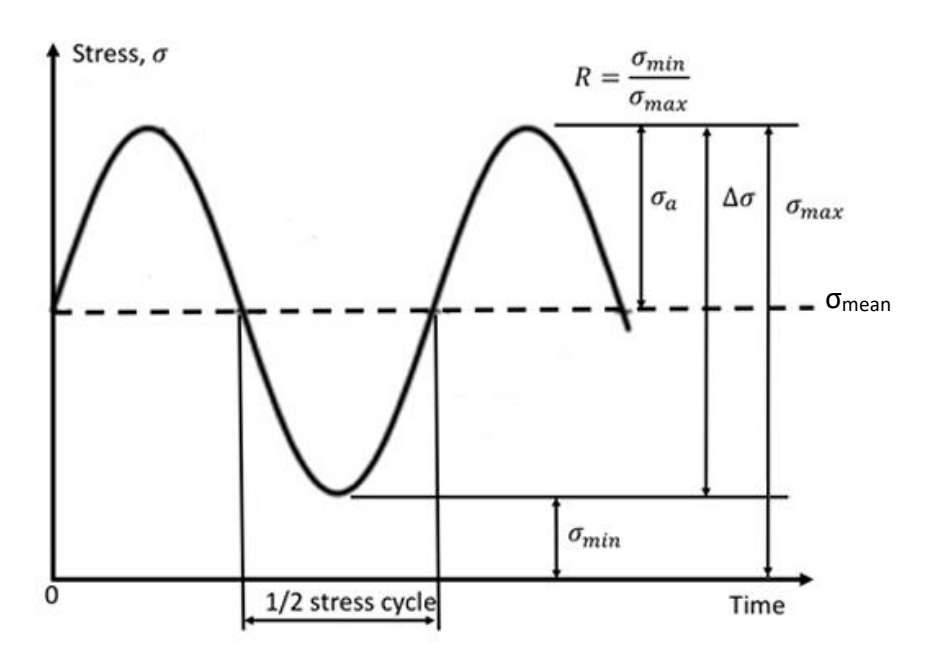


Figure 2-13. S-N curve for cyclic loading [31]

Although S–N curves represent the total fatigue life, they do not distinguish between crack initiation and growth phases. Understanding these mechanical parameters is essential to correlate loading conditions with material response and fatigue behaviour [31], [32].

$$\Delta \sigma = \sigma_{max} - \sigma_{min}$$
 2-1

$$\sigma_m = \frac{\sigma_{max} + \sigma_{min}}{2}$$

$$\sigma_a = \frac{\Delta \sigma}{2}$$

$$R = \frac{\sigma_{max}}{\sigma_{min}}$$

2.2.6 High cycle fatigue

High cycle fatigue (HCF) typically involves low stress amplitude cyclic loading that remains within the elastic range of the material and is characterized by many cycles, often exceeding 10⁵. In this case, stress is typically below the material's yield strength and produces small elastic strains. Repeated cyclic loading generates localized internal stresses, leading to energy dissipation through microplastic deformation and the accumulation of permanent dislocations within slip bands. In most HCF cases, failure is dominated by the crack initiation phase, making it critical to understand how microstructural features—such as slip band formation, surface roughness, and local stress concentrations—contribute to early damage, especially in long-life components. In quick design, a safe design is to have the stress level below the fatigue limit where no failure would take place. The idea of fatigue limit is not ideal because nobody has waited for an infinite number of cycles. Thus, the fatigue limit can be defined objectively, as the maximum stress at large number of cycles (10⁷,10⁸) [33].

2.2.7 Low cycle fatigue

Low cycle fatigue (LCF) occurs under conditions of high stress amplitude, where the material undergoes significant plastic deformation during each loading cycle. This typically results in failure within fewer than 10⁴ to 10⁵ cycles, and LCF tests are usually conducted under straincontrolled conditions. Unlike HCF, where stresses remain below the yield strength, LCF operates at stress levels that exceed the yield point, leading to extensive cyclic plasticity and pronounced hysteresis behaviour in the stress-strain response. With each cycle, the material accumulates plastic strain, causing changes in the dislocation structure, such as multiplication, tangling, rearrangement, and the eventual formation of dislocation cells or persistent slip bands. These evolving structures are closely tied to the material's mechanical response—initial hardening followed by softening and eventual saturation. Because plastic strain is a dominant factor, LCF life is more influenced by the total strain energy absorbed, rather than just stress amplitude. A large portion of the fatigue life in LCF is still consumed by crack initiation, making early detection of microstructural changes such as dislocation rearrangement and localized deformation critical. Predictive models like the Coffin-Manson relation are commonly used to describe the relationship between plastic strain amplitude and fatigue life in this regime, offering useful tools for assessing fatigue performance in materials subjected to severe cyclic loading [34].

2.3 Non-Destructive techniques (NDT) for fatigue damage detection

In the previous section of this chapter, the importance of fatigue and the need for early-stage damage detection—specifically before crack nucleation—was discussed. Detecting early fatigue indicators such as slip band formation and dislocation structures requires effective Non-Destructive techniques (NDT). This chapter presents a literature review of NDT methods relevant to fatigue damage detection, focusing on their capabilities, advantages, and limitations. Special attention is given to techniques suitable for detecting early microstructural changes rather than just visible cracks. The chapter concludes with a rationale for selecting Electrical Resistivity (ER) measurement and Nonlinear Ultrasonic (NLU) as the primary techniques used in this study. NDT techniques for fatigue are generally classified into two main groups: those focused on fatigue crack monitoring and those aimed at detecting fatigue damage. Once a crack initiates, the crack propagation phase is typically brief, meaning that damage can quickly escalate to catastrophic failure if not detected early. Conventional methods relying on crack detection requiring frequent and costly inspection intervals to ensure that a detectable crack does not grow to a critical size between inspections. However, by the time a crack is detectable, the opportunity to intervene and extend the life of the component with minimal risk is significantly reduced. Early detection of fatigue, before macroscopic cracks form, offers the potential to improve maintenance strategies by providing a more accurate and more precise assessment of remaining life. Furthermore, early-stage detection methods enable engineers to monitor and manage fatigue damage during its initiation phase, reducing costs and increasing the safety and reliability of critical components. Therefore, advancing non-destructive methods that can reliably detect and quantify fatigue prior to crack initiation is crucial for enhancing fatigue management and extending the service life of structural components. These NDT methods are classified into electrical resistivitybased methods, electromagnetic radiation testing, ultrasonic testing, acoustic emission, hydrogen as a probe, surface investigation techniques, positron annihilation and electromagnetism-based methods. Each of these categories includes specific techniques, as summarized in the Figure 2-14. Since the primary focus of this project is on damage detection before crack initiation, fatigue crack monitoring techniques will not be discussed. Fatigue damage monitoring refers to methods used during the earlier phase, before any visible crack has formed, with the goal of detecting microstructural changes or early signs of fatigue damage. Among NDT methods, electrical resistivity measurement, hardness-based methods, thermometric and X-ray techniques (which considered as electromagnetic radiation methods), positron annihilation, acoustic emission, magnetic methods and ultrasonic methods are mostly used for damage detection. Each method will be briefly discussed and reasons for selecting the electrical resistivity and nonlinear ultrasonic methods for this project will be explained. A more detailed literature review on these two methods, including their fundamentals and applications, will then be provided in Chapter 3 and Chapter 4.

NDT Methods

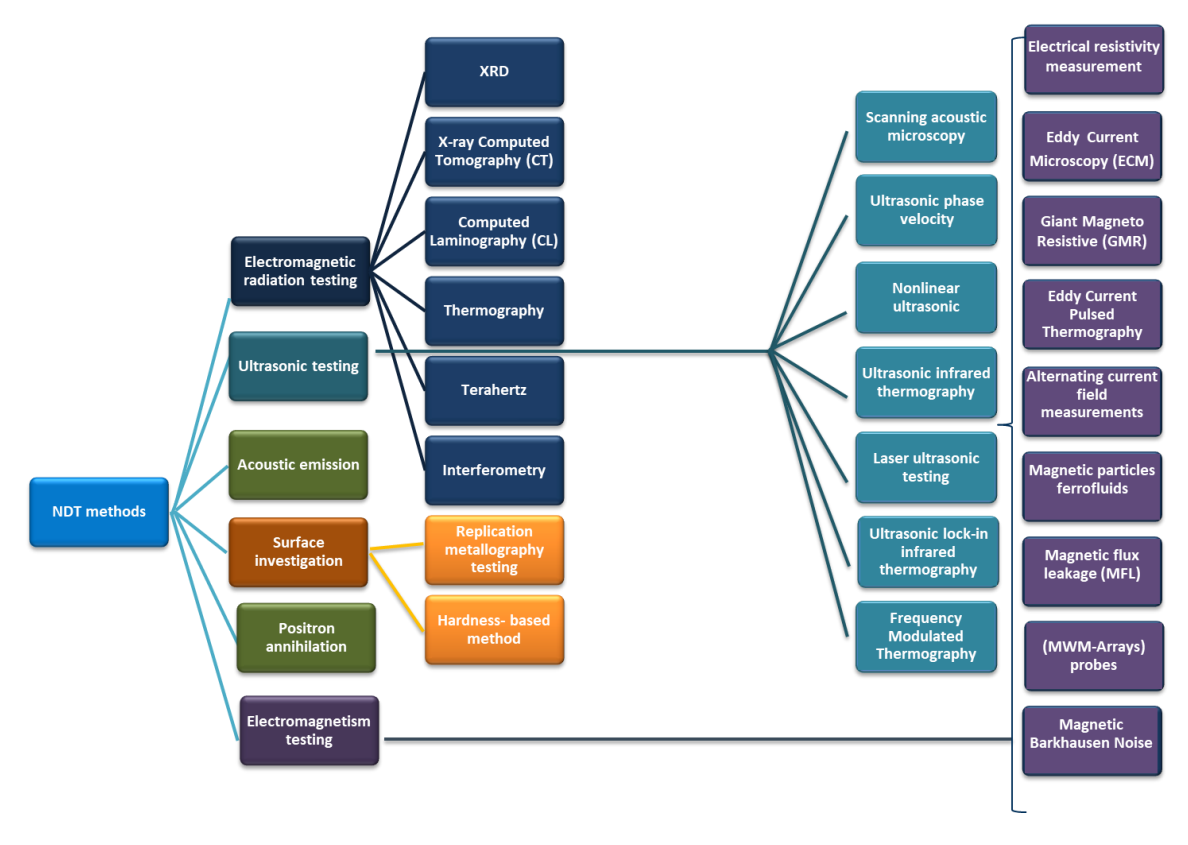


Figure 2-14. Classification of Non-Destructive Testing (NDT) Methods: A comprehensive overview of various NDT methods.

2.3.1 Surface investigation methods

Surface investigation methods are a category of non-destructive testing (NDT) techniques that focus on analysing the material's surface for signs of damage, deformation, or structural changes. These techniques are particularly effective in detecting early signs of fatigue damage, such as surface relief, persistent slip markings (PSMs), microcracks, or oxidation pits, which often develop before larger cracks initiate. Common surface-based methods include Scanning Electron Microscopy (SEM), Atomic Force Microscopy (AFM), Scanning Tunnelling Microscopy (STM), replica techniques, Digital Image Correlation (DIC) and hardness testing. These tools provide high-resolution imaging and precise topographical mapping, allowing for the identification of slip band formation, intrusions, extrusions, and changes in surface morphology associated with cyclic loading. In industrial settings, surface investigation methods are widely used in aerospace, automotive, nuclear, and biomedical fields, where the integrity of structural components is critical. These techniques are particularly suited for metallic materials, especially those prone to surface-dominated fatigue mechanisms, such as austenitic stainless steels (e.g., 316L), aluminium alloys, nickel-based superalloys, and titanium alloys. However, these methods are mostly used in controlled laboratory environments due to their sensitivity, cost, and the need for clean or polished surfaces. Among these, hardness testing stands out as a relatively simple and accessible surface investigation method that has shown potential for monitoring fatigue damage through changes in material hardness during cyclic loading. Although not as sensitive as highresolution imaging techniques, variations in hardness can reflect microstructural changes, such as strain hardening, or local softening, which are indicative of early fatigue damage. For this reason, in the following section, a brief literature review of hardness-based methods and their application in fatigue damage assessment is presented.

2.3.1.1 Hardness – based methods

The use of hardness measurements as a diagnostic tool for fatigue damage detection has been extensively explored in various studies, particularly focusing on microhardness changes during cyclic loading. Several techniques, including Vickers and Brinell hardness tests, have been employed to assess surface layer deformation resistance and microstructural changes throughout the fatigue life of different metals. These studies are typically conducted under high strain amplitude conditions, where plastic deformation is sufficient to induce measurable changes in surface hardness. Ye et al.[35], examined fatigue hardening and softening behaviour in ferrite-pearlite steels through Vickers microhardness measurements. They identified distinct stages of hardness evolution, initial hardening, stabilization and subsequent softening, demonstrating the method's capability to detect localized plastic deformation and dislocation structures near the surface during cyclic loading. As shown in Figure 2-15 The ferritic phase exhibited a more pronounced hardness variation compared to the pearlitic phase, highlighting its lower resistance to plastic deformation. The scatter in microhardness values observed during fatigue damage indicates inhomogeneous dislocation accumulation in the surface grains. An initial increase in hardness is observed up to ~103-104 cycles, attributed to cyclic strain hardening and dislocation multiplication. Beyond this point, a marked decrease in hardness occurs, indicating the onset of cyclic softening and fatigueinduced microstructural degradation, particularly in the ferrite phase. These findings support the potential use of Vickers microhardness as a non-destructive tool for early fatigue damage detection, particularly in the pre-nucleation phase before visible crack formation [36, 37].

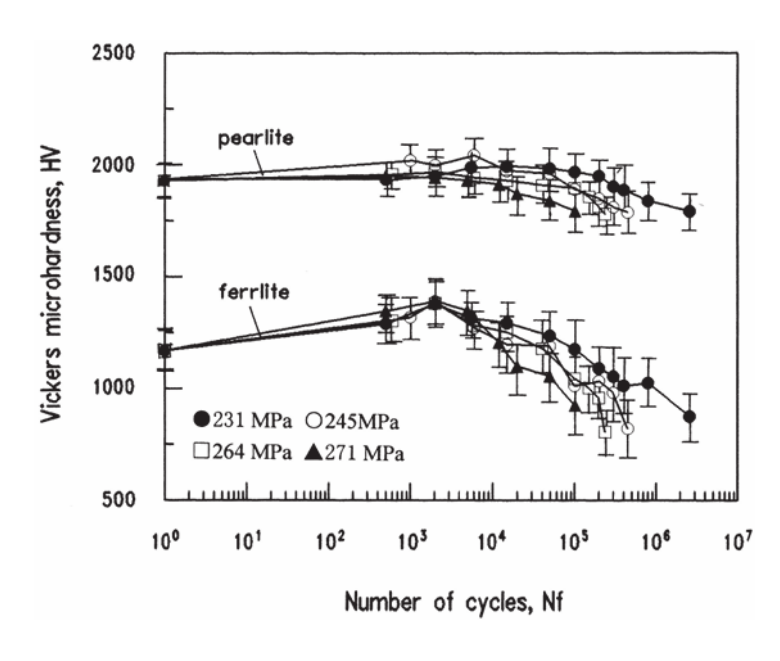


Figure 2-15. Variation in Vickers microhardness with the number of cycles [33]

In another study Pavlou [38], proposed a non-linear cumulative fatigue damage rule based on hardness variations in aluminium alloy 2024-T42. The study observed that surface hardness increased initially due to cyclic hardening and then decreased as fatigue progressed, correlating well with fatigue damage accumulation. A logarithmic relation was derived to link hardness changes with stress amplitude and loading cycles, providing a useful parameter for non-destructive damage assessment.

Drumond et al. [39], conducted extensive research on API 5L X65 steel pipelines, employing Berkovich indentation tests to monitor microhardness changes under high-cycle fatigue (HCF) conditions. Their findings indicated that significant hardness variations occurred within the initial 20% of the material's fatigue life, particularly at depths below 3 μ m. This study underscored the sensitivity of microhardness to early fatigue damage and its applicability for predicting fatigue life before macroscopic cracks appeared. Additionally, Sulko et al. [40], evaluated fatigue damage in steels using both Vickers and Brinell hardness methods. They found that surface hardness measurements could reliably detect fatigue-induced microstructural changes, including persistent slip band formation and microcrack nucleation. The study proposed criteria for an ideal diagnostic method, emphasizing simplicity, minimal invasiveness, and the ability to target surface layers.

Despite this method sensitivity to early-stage fatigue damage and microstructural evolution, hardness-based methods are not considered suitable for the present study. While techniques such as Vickers and Brinell indentation provide valuable insights into surface hardening and softening behaviour, they are inherently semi-destructive and require direct surface access, limiting their applicability for real-time, in-situ monitoring. Additionally, these methods are highly localized and may fail to detect subsurface or distributed microstructural changes, which are particularly relevant in high cycle fatigue (HCF) conditions. In early cycles of HCF, the dominant damage mechanisms are not surface driven, making surface hardness measurements less effective. Since this research focuses on HCF (the rationale for selecting this fatigue regime is discussed in section 6.1), hardness-based methods fall short of the detection capabilities required. Moreover, the resolution and repeatability of these tests are sensitive to surface preparation and operator variability. Given that the objective of this study is to achieve non-invasive, high-resolution detection of early fatigue damage such as slip band formation and dislocation structure evolution, hardness testing is not an appropriate choice for this research.

2.3.2 Electromagnetic testing

Electromagnetic radiation non-destructive testing (NDT) techniques involve the use of electromagnetic waves, ranging from X-rays to infrared radiation, to assess material properties, detect internal changes, or monitor surface conditions. This includes both electromagnetic radiation techniques, such as X-ray and infrared thermography, and electromagnetic induction methods, such as eddy current testing. These methods are widely applied in industries such as aerospace, power generation, and structural health monitoring.

While techniques like radiographic imaging (X-rays), eddy current testing and infrared thermography are highly effective for detecting surface or internal cracks, they are generally less sensitive to early-stage fatigue damage that occurs prior to crack initiation. Since the primary aim of this research is to detect microstructural changes such as dislocation activity and slip band formation in the early stages of fatigue, techniques focused on crack detection fall outside the scope of this study. Therefore, in the following sections, attention is given to X-ray diffraction (XRD) and thermometric methods, which are more applicable to capturing microstructural changes associated with fatigue damage accumulation. These techniques provide insight into internal stress evolution, lattice distortion, and localized heat generation, making them better aligned with the goals of early fatigue damage detection in this work.

2.3.2.1 X-ray diffraction method

The XRD technique is primarily effective in identifying microstructural changes such as dislocation accumulation, microcracks, residual stress variations and strain localization, all of which are early indicators of fatigue crack initiation. Full Width at Half Maximum (FWHM) broadening in X-ray diffraction (XRD) peaks serves as a key indicator of microstructural evolution during fatigue. Specifically, FWHM broadening is associated with two primary mechanisms: (1) a reduction in coherent diffraction domain (crystallite) size, and (2) the introduction of strain due to lattice distortions, often caused by dislocation accumulation and sub-grain formation. This relationship is commonly expressed through the Williamson—Hall equation (2-5), which separates the size and strain contributions to peak broadening [29]:

$$B\cos\theta = \frac{k\lambda}{D} + 4\epsilon\sin\theta$$

where β is the FWHM of the diffraction peak (in radians), θ is the Bragg angle, λ is the X-ray wavelength, K is the shape factor (typically ~0.9), D is the crystallite size, and ϵ is the strain. An increase in dislocation density leads to greater lattice distortion and strain fields, which contributes to an increase in ϵ and, consequently, broadens the diffraction peak. Additionally, dislocation structures introduce stress fields that change the average interplanar spacing, resulting in peak shifts. These shifts can be interpreted using Bragg's Law (Equation 2-6) [29]:

$$2 \operatorname{d} \sin \theta = n\lambda$$

where d is the interplanar spacing. Change in d, caused by tensile or compressive residual stresses, leads to a measurable shift in θ . The corresponding residual stress σ can be estimated by equation 2-7 [29]:

$$\sigma = \frac{E}{1+v} \cdot \frac{\Delta d}{d}$$

where E is Young's modulus, v is Poisson's ratio, and $\Delta d/d$ is the relative change in lattice spacing. Through careful analysis of FWHM and peak position, XRD provides quantitative insight into microstructural features such as dislocation density and residual stress development, all of which are critical for understanding early-stage fatigue damage.

X-ray diffraction (XRD) methods are widely utilized for studying fatigue and creep in crystalline materials due to their high sensitivity to microstructural changes. Pinheiro et al. [41, 42] , focused on fatigue damage in API 5L X60 grade steel pipes under alternating bending loads, using XRD to track micro deformations and residual stresses during the early stages of fatigue damage. In another study, Nagao and Weiss [43], investigated low-cycle fatigue in SAE 1008 plain carbon steel, where XRD line profile measurements provided insight into the cyclic softening behaviour during early fatigue stages. They highlighted a correlation between the reduction in surface residual stress and early crack formation, emphasizing the potential of XRD for continuous fatigue monitoring. In their analysis, XRD detected fatigue damage by tracking shifts in diffraction peak positions, which correspond to changes in interplanar spacing caused by evolving residual stress fields. As plastic deformation accumulates under cyclic loading, the surface layer undergoes stress redistribution, leading to a relaxation of initial compressive residual stress. This stress relaxation reduces the crack initiation threshold and reflects the onset of localized plasticity. Therefore, the observed decrease in compressive residual stress-measured via peak shift-is an indirect but reliable indicator of fatigue damage and early crack initiation. Taira's work [44], extended the application of XRD to both macroscopic and microscopic fatigue behaviour by employing X-ray stress analysis to measure residual stress and micro strain X-ray-diffraction. His findings underscored the technique's ability to detect localized strain and dislocation density changes, making it particularly useful for studying fatigue crack initiation and progression. In this case, increasing micro strain and dislocation density, indicated by FWHM broadening served as markers of fatigue-induced damage accumulation.

While XRD can detect bulk indicators like increased dislocation density through peak broadening (FWHM) and peak shifts, X-ray relies on average over a given volume of material's interaction with X-ray irradiation, hence it is not possible to relate the information to a specific spatial region at sub-micron level. In addition, XRD is primarily a laboratory-based technique, requiring careful sample preparation, precise alignment, and controlled measurement conditions, which limits its practicality for real-time or in-situ monitoring of fatigue damage in operational environments.

2.3.2.2 Thermometric methods

Thermometric methods are a class of non-destructive techniques that detect and monitor fatigue damage by measuring temperature changes associated with internal energy dissipation during cyclic loading. One of the most widely used thermometric techniques is infrared thermography (IRT), which enables real-time, non-contact temperature monitoring of a material's surface. These methods are based on the principle that plastic deformation and microstructural damage generate heat, and changes in surface temperature can be correlated with fatigue damage evolution. Application of thermographic methods for fatigue damage detection has progressed significantly over the years, with initial studies focusing on pre-crack detection and later works developing advanced techniques for fatigue life prediction based on thermal dissipation analysis. Luong et al. [45], introduced infrared

thermography as a real-time, non-contact technique for detecting fatigue damage in metals subjected to low-cycle fatigue. The study highlighted the ability of thermography to measure intrinsic dissipation and localize damage by capturing heat generation patterns on the specimen's surface. This method proved particularly effective in detecting microcrack formation and monitoring failure mechanisms, making it an essential tool for fatigue damage detection. However, most of the research on thermometric methods has primarily focused on predicting fatigue life and determining fatigue limits rather than directly detecting fatigue damage mechanisms such as dislocation movement or slip band formation. For example, the Risitano method proposed by La Rosa and Risitano [46], involves identifying a temperature stabilization point during cyclic loading to estimate the fatigue limit. Similarly, Amiri and Khonsari [47], introduced the temperature-rise angle to estimate remaining fatigue life based on thermal trends during loading. In a more recent study, Teng et al.[48], presented a thermographic method for fatigue damage detection in medium carbon steel (SAE1045), focusing on the correlation between temperature evolution, energy dissipation and microplasticity during cyclic loading. The study used infrared thermography to monitor surface temperature changes in real time, highlighting three distinct phases. It starts with an initial temperature rise, a stabilization phase, and a sharp increase before failure. Figure 2-16 presents the progression of these stages, highlighting the relationship between temperature evolution and damage mechanisms.

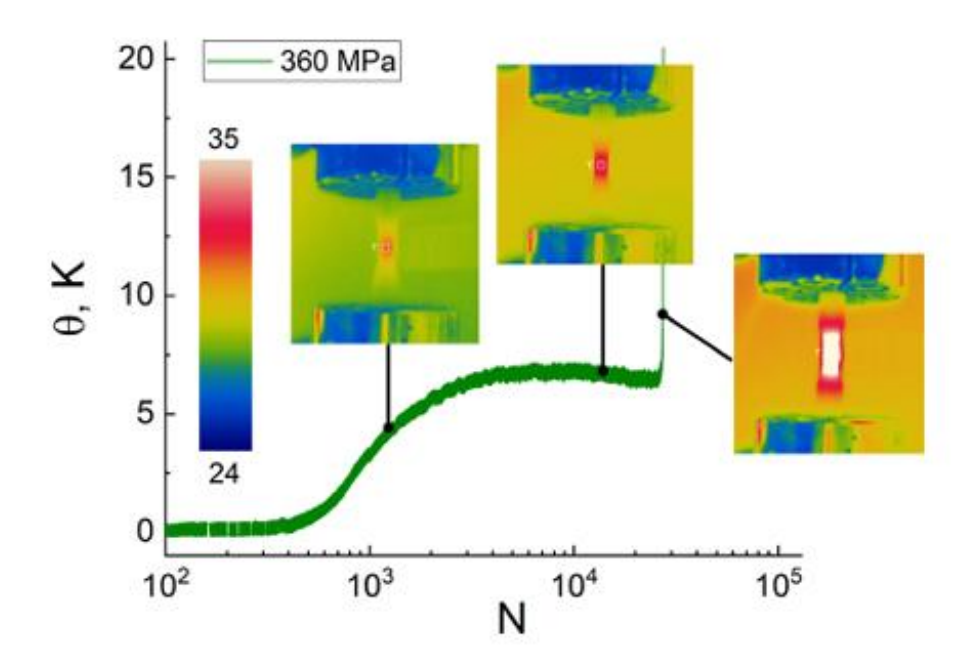


Figure 2-16. Temperature evolution during fatigue testing at 360 MPa showing three distinct phases—initial rise, stabilization, and final sharp increase—captured using infrared thermography at 5, 50, and 100% of fatigue life of SAE1045 Carbon steel [48]

Thermographic methods are useful for assessing fatigue behaviour, particularly for estimating fatigue life and identifying key failure stages, but their sensitivity mainly depends on detecting surface temperature changes caused by heat generated during cyclic loading. This makes them more suitable for detecting bulk material responses rather than specific microstructural

mechanisms such as dislocation rearrangement or slip band evolution. In the context of high cycle fatigue, where plastic deformation is minimal and heat generation is subtle, these methods become less effective for capturing early-stage damage at the microstructural level. For these reasons, thermographic techniques are not considered suitable for this study.

2.3.3 Positron annihilation spectroscopy (PAS)

Positron Annihilation Spectroscopy (PAS) is a non-destructive technique used to study defects and voids in materials by analysing the annihilation of positrons with electrons, revealing information about electron density and momentum distribution. This makes PAS a highly sensitive tool for detecting early microstructural changes such as vacancies, dislocations, and small defects—often before visible fatigue damage occurs. Two main analytical approaches are used in PAS: Positron Annihilation Lifetime Spectroscopy (PALS), which measures the time interval between positron injection and annihilation (linked to the size and type of defect), and line-shape analysis via the S-parameter, which reflects the energy spread of emitted photons and is influenced by the electron environment around defects. Although PAS is generally classified as a non-destructive technique because it does not change the material's crystal structure, it requires very thin samples and specialized facilities, which can limit its practical application as a routine non-destructive testing method. These parameters represent the spatial resolution and penetration depth of the PAS technique — indicating the approximate region of interest (ROI) that can be analysed (up to 1 mm laterally and 2 mm in depth, depending on material density). However, this does not imply that samples of these exact dimensions are required; rather, it defines the effective measurement range within which PAS can characterize defects such as open and closed pores up to 100 nm in size [49, 50].

Positron annihilation spectroscopy (PAS) has shown promising results in fatigue damage monitoring, particularly in detecting early-stage fatigue. Studies by Uematsu et al. [51], showed that Positron Annihilation Lifetime Spectroscopy (PALS) effectively detects crack initiation in 316 stainless steels, whereas line-shape analysis alone was insufficient. In PALS, the positron lifetime (τ) is the time interval between positron implantation and annihilation with an electron in the material. This lifetime is highly sensitive to the local electron density. In regions with defects—such as vacancies, dislocation cores, or micro voids—there is a reduction in electron density, which results in longer positron lifetimes. Specifically, vacancy-type defects trap positrons more effectively due to their open volume and low electron density, while dislocations and their strain fields can also act as shallow traps. By analysing changes in τ , one can infer both the presence and type of defects.

Similarly, Kawaguchi et al. [52, 53], highlighted that the evolution of the S-parameter varies between stress-controlled and strain-controlled loading, underlining PAS's ability to distinguish different fatigue conditions. In particular, for AISI 316L stainless steel, PAS proved effective in identifying early microstructural changes within the first 10% of fatigue life, with significant shifts in PALS data indicating the presence of vacancy-like defects and early

dislocation activity (see Figure 2-17). However, beyond this early phase, both lifetime and S-parameter values tend to stabilize, making it less useful for tracking damage progression during the later stages of fatigue. Figure 2-17 shows the evolution of average positron lifetimes (τ_{av}) as a function of normalized fatigue life (N/N_f) for AISI 316L stainless steel and aluminium alloy 2024. The data show that in AISI 316L (open circles), positron lifetime increases rapidly within the first 10–20% of fatigue life, which indicates the early formation of vacancy-type defects and dislocation structures. This early rise in τ_{av} supports the sensitivity of PALS to microstructural changes occurring well before macroscopic cracks form. In contrast, the lifetime values plateau in the mid to late fatigue life range, suggesting that the defect population reaches a relatively stable state [54, 55].

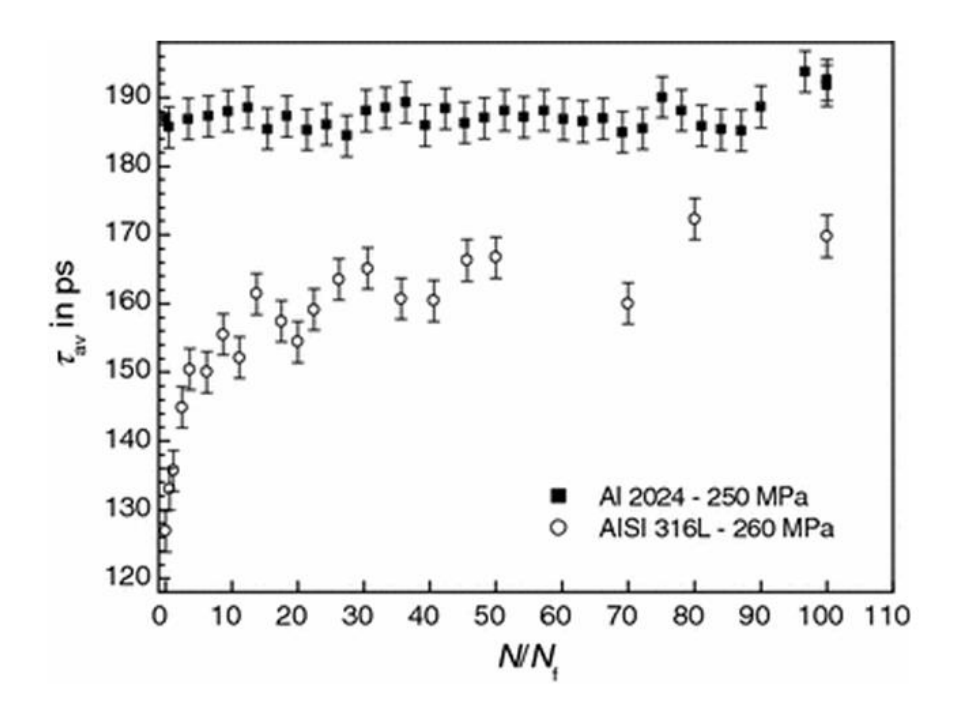


Figure 2-17. Evolution of average positron lifetimes (τ_{av}) as a function of normalized fatigue life comparing stainless steel AISI 316L and aluminum alloy 2024 [52]

Despite its early-stage sensitivity, PAS is limited by its laboratory-based setup, need for highly specialized equipment, and its inability to characterize complex dislocation structures or evolving slip band morphology—features central to this research. Therefore, although PAS provides valuable insights into vacancy-type defects and increase in dislocation density monitoring, it is not considered appropriate for this study, which focuses on non-invasive techniques capable of tracking progressive dislocation and slip band evolution throughout high-cycle fatigue life.

2.3.4 Acoustic *emission*

Acoustic emission (AE) is a well-established non-destructive testing (NDT) method widely used for real-time monitoring of structural health and material fatigue. It operates on the principle of detecting transient elastic waves generated by sudden localized structural changes, such as dislocation movement, microcrack initiation and phase transformations

during mechanical loading. The core idea behind AE monitoring is to capture and analyse high-frequency acoustic signals emitted from the material during mechanical loading, which are recorded by surface-mounted piezoelectric sensors. AE sensors detect these elastic waves and signal parameters such as amplitude, energy, duration and frequency are recorded for further analysis. Each type of microstructural activity (e.g., dislocation motion, slip band formation, microcrack nucleation) produces distinct AE signals, which can be used to characterize the damage mechanisms. For example, Figure 2-18 presents a conceptual model of AE signal evolution during fatigue damage progression, constructed based on patterns reported in the literatures [55, 56]. Dislocation movement produces low-amplitude, long-duration signals with moderate energy. Dislocation entanglement shows a decrease in rise time and duration, with slightly lower energy. Crack initiation is marked by a notable increase in amplitude and energy, while rise time and duration decrease further and crack growth results in the highest amplitude and energy signals, with the shortest rise time and duration.

On the left side of this figure AE waveforms pattern is shown related to each damage—starting from dislocation movement and entanglement to slip line formation, crack initiation, and eventual crack growth. On the right side, a comparison table summarizes how key AE parameters—rise time, amplitude, duration, and energy—vary with each damage stages.

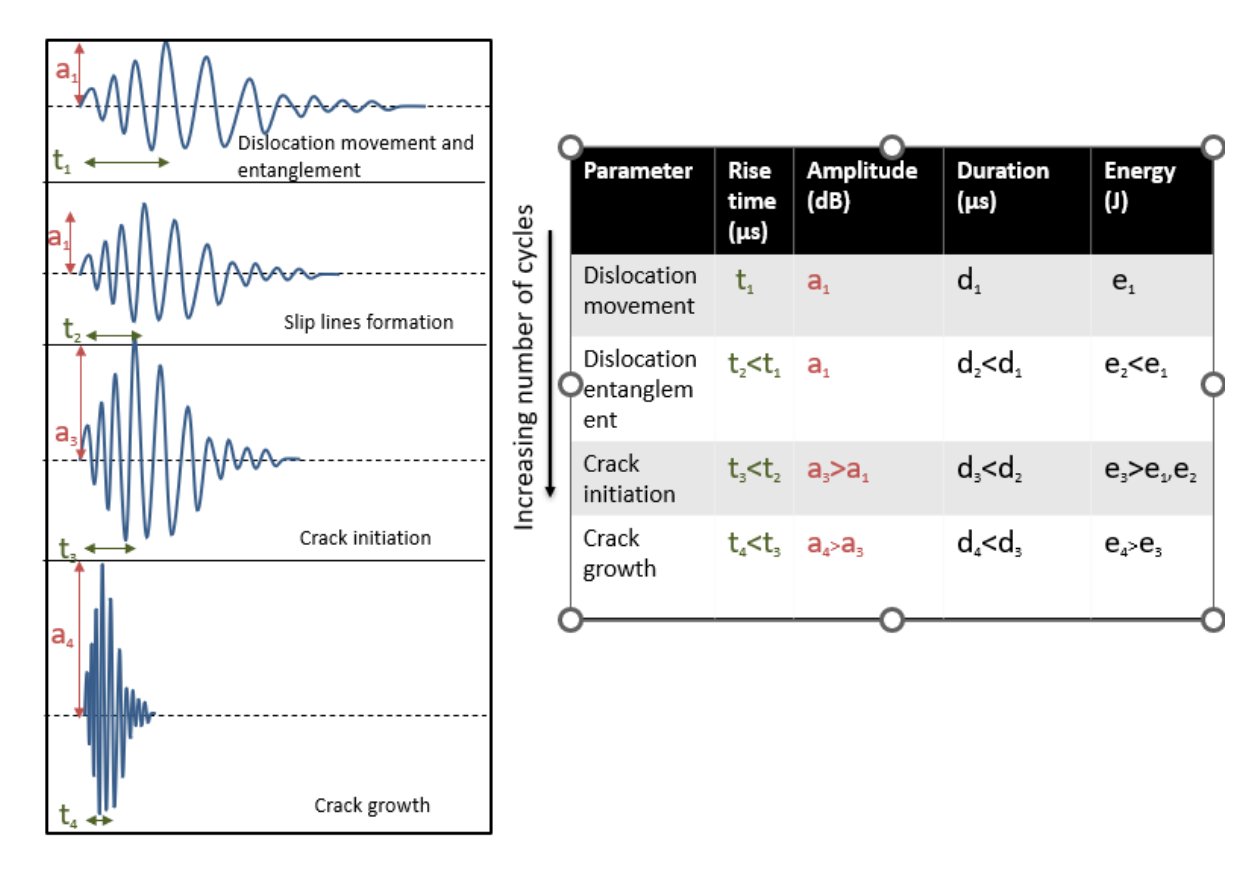


Figure 2-18. Hypothetical representation of acoustic emission (AE) signal patterns and associated parameters across different stages of fatigue damage. AE waveform characteristics—rise time, amplitude, duration, and energy—are shown to evolve with increasing fatigue cycles, corresponding to dislocation activity, slip line formation, crack initiation, and crack growth.

Numerous studies have demonstrated AE's effectiveness in detecting early-stage fatigue damage. Research on stainless steel and aluminium alloys has shown that AE activity increases significantly during the initial stages of fatigue life, correlating with microstructural changes such as slip band formation and microcrack nucleation. Chai et al. [56–59], investigated fatigue damage in stainless steel, observing that AE signals could differentiate between different stages of fatigue damage. Distinct changes in AE amplitude and frequency components were recorded long before the appearance of macroscopic cracks as observed in Figure 2-19. Their study highlighted AE's ability to detect microstructural changes associated with dislocation movement and early crack nucleation. Similarly, Lai et al[59], performed stress-controlled fatigue tests on stainless steel and demonstrated that AE signal characteristics strongly correlate with loading conditions and microstructural behaviour. They concluded that AE monitoring offers a reliable tool for real-time fatigue damage detection, capable of identifying microstructural damage well before crack initiation.

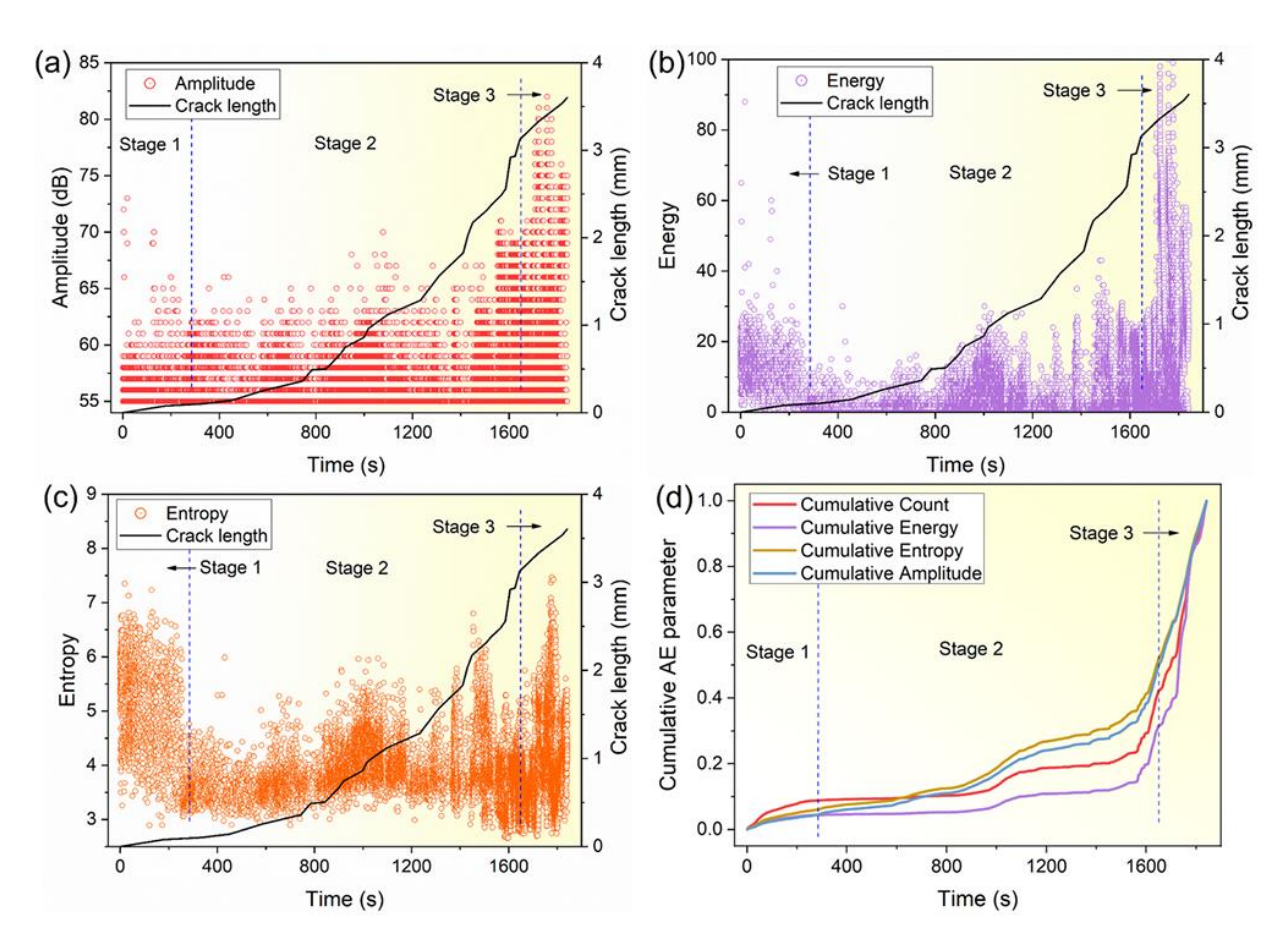


Figure 2-19. The variation of different AE parameters with respect to the fatigue loading time of 316LN stainless steel under stress ratio of 0.1: (a) amplitude, (b) energy, (c) entropy, (d) cumulative AE parameter showing three stages of fatigue life [58].

Vanniamparambil et al. [60], focused on the use of AE to monitor fatigue in aluminium 2024-T3 alloy. Their study demonstrated that AE signals could reliably capture the onset of dislocation activity and crack nucleation, correlating well with different damage stages. Their work emphasized the importance of multi-parameter AE analysis, noting that combining amplitude and energy data provides a more comprehensive understanding of fatigue damage progression. Recent advancements in AE techniques have focused on improving the accuracy of damage detection and life prediction. Seleznev et al.[61], developed a wireless AE monitoring system for high-cycle fatigue (HCF) behaviour in AlSi9Cu3 (EN AC 46000). Their study employed information to evaluate fatigue damage and demonstrated the potential of AE for industrial applications requiring accurate fatigue life prediction. Vlasic et al. [62], compared AE signals with X-ray diffraction results during fatigue loading of aluminium alloys EN AW-2017/T4 and EN AW-6082/T6. Their results showed that AE activity was highly sensitive to microstructural changes before visible cracks appeared, underscoring the capability of AE to detect early fatigue damage mechanisms such as dislocation rearrangement.

Given its high sensitivity to microstructural changes and its proven ability to detect early-stage fatigue mechanisms such as dislocation motion, slip band activity, and microcrack nucleation, Acoustic Emission (AE) appears to be a highly promising technique for this project. Its real-time monitoring capability and ability to capture dynamic damage evolution before visible cracks emerge align closely with the goals of this research, which focuses on early fatigue damage detection. AE's application to austenitic stainless steels like 316L further strengthens its relevance. However, despite its potential suitability, a detailed discussion at the end of this chapter is explained the practical considerations and limitations that ultimately led to the exclusion of AE from the selected methods in this study.

2.3.5 Electromagnetic testing

Electromagnetic-based non-destructive testing (NDT) methods involve the interaction of materials with electrical and magnetic fields to detect changes in their physical or structural properties. These methods differ from electromagnetic radiation-based techniques—such as X-ray or infrared thermography—which rely on the propagation of electromagnetic waves and their interaction with matter via absorption, emission, or scattering. In contrast, field-based methods operate through directly induced material responses, such as eddy currents or magnetization, generated by applied electric or magnetic fields at lower frequencies. This distinction makes field-induced techniques particularly effective for detecting surface and near-surface anomalies in a wide range of engineering materials. These methods are typically categorized into two main groups: magnetic methods and electrical resistivity-based methods.

Magnetic methods, such as Barkhausen Noise and Magnetic Flux Leakage, utilize the sensitivity of magnetic domain structures to changes in material microstructure, making them effective for monitoring fatigue damage in ferromagnetic materials. During magnetization, domain walls move through the material but are impeded by microstructural features such as dislocations, precipitates, and residual stress fields. These interactions cause sudden, discrete jumps in domain wall positions, which generate Barkhausen signals.

On the other hand, electrical resistance methods measure changes in the electrical resistivity of a material, which can be correlated with microstructural damage such as dislocation accumulation and plastic strain. Both categories have been successfully applied in the detection of fatigue damages.

In the following sections, a focused review of these two electromagnetism-based approaches is presented. Their principles, applications and effectiveness in fatigue damage detection—particularly with respect to early-stage microstructural evolution—are discussed to evaluate their relevance to the objectives of this research.

2.3.5.1 Magnetic methods

Magnetic methods are a category of non-destructive testing (NDT) techniques that analyse changes in the magnetic properties of ferromagnetic materials to detect or assess internal microstructural changes. These techniques are particularly sensitive to the movement and interactions of magnetic domain walls, which are influenced by features such as dislocations, grain boundaries and inclusions. As a result, magnetic methods are widely used for evaluating stress, strain and fatigue damage in ferromagnetic alloys. Common techniques in this category include Magnetic Barkhausen Noise (MBN), Magnetic Flux Leakage (MFL) and Magneto acoustic emission technique. Among them Barkhausen Noise (BHN) is widely used for fatigue damage detection in ferromagnetic materials [63, 64]. BHN is based on detecting sudden, discrete changes in magnetization as domain walls move through a ferromagnetic material during magnetization. These domain wall movements are impeded by microstructural barriers such as grain boundaries [65, 66], inclusions [67] and dislocations [68-69].

Numerous studies have explored the utility of BHN in fatigue monitoring. Lindgren and Lepistö [70], developed a novel BHN sensor capable of continuous fatigue monitoring. Their experiments on mild steel under cyclic bending revealed that BHN measurements in a single direction could lead to misinterpretation of damage, as the most prominent changes were observed at approximately 45° to the loading direction. This finding emphasized the need for multi-directional BHN monitoring for accurate fatigue damage assessment. Soultan et al. [71], evaluated the mechanical Barkhausen noise of iron specimens, demonstrating that the root mean square (RMS) of BHN varied throughout the fatigue life. They identified three distinct stages: 1) an initial transient stage with increasing noise, (2) a linear increase in BHN during the stable fatigue phase, and (3) a final reduction stage corresponding to crack formation. These findings highlighted that BHN is particularly sensitive to stress amplitudes near the fatigue knee-point, making it a valuable tool for identifying fatigue damage thresholds. Palma et al. [72], explored the BHN signals in 8620 steels under rotating bending fatigue and axial loading. They found no significant BHN signal changes below the knee-point stress amplitude but recorded distinct increases just above it. However, once the stress exceeded the yield strength, method's sensitivity diminished, suggesting that BHN is most effective in the early elastic regime. Furthermore, Sagar et al. [73], combined BHN monitoring with Transmission electron microscopy (TEM) to study low-carbon structural steel, identifying three distinct phases of fatigue damage progression. As it is observed in Figure 2-20, the variation in peak voltage of Magnetic Barkhausen Emission (MBE), denoted as $M_{\rm max}$, reflects changes in microstructural activity during fatigue. MBE refers to the voltage signals generated by sudden, discontinuous movements of magnetic domain walls as they interact with microstructural features like dislocations and grain boundaries during magnetization. The peak voltage ($M_{\rm max}$) corresponds to the highest amplitude of this signal during a magnetization cycle and serves as a sensitive indicator of domain wall mobility. In this study, the initial rise in $M_{\rm max}$ was attributed to dislocation rearrangement, enhancing domain wall activity. The subsequent drop corresponded to the formation of dislocation cells and slip bands, which increased pinning and reduced domain wall motion. Finally, $M_{\rm max}$ increased again due to crack initiation and propagation, which locally relieved stress and allowed more domain wall movement. This work confirmed the effectiveness of BHN in capturing microstructural evolution and fatigue progression through domain wall dynamics.

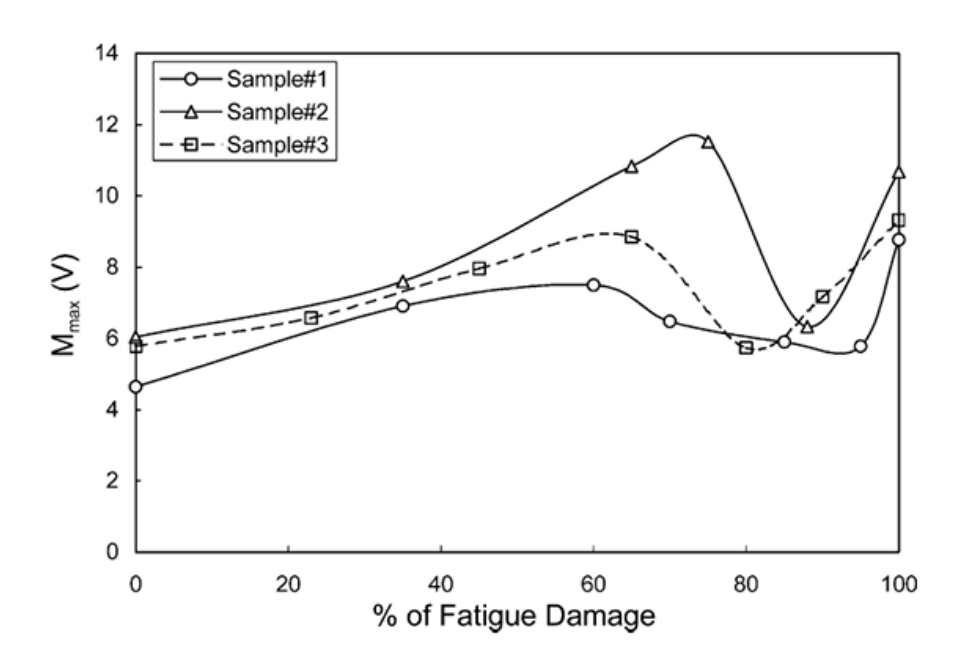


Figure 2-20. Variation of peak voltage of MBE (M _{max}) with % of fatigue damage during online monitoring in three specimens having C=0.16wt% [73]

Despite these promising findings, magnetic methods, especially BHN, have key limitations in the context of the current research. Most important one is that they are only applicable to ferromagnetic materials, and the material of interest in this study, 316L austenitic stainless steel, is non-ferromagnetic. Furthermore, the application of BHN often requires direct surface access and is best suited to simple geometries and early-stage surface damage within plastic loading conditions. Given this study's focus on detecting microstructural fatigue like dislocation evolution and slip band formation in high-cycle fatigue conditions for 316L stainless steel—where plasticity is minimal and changes may be sub-surface—magnetic techniques are not well-aligned with the research objectives.

2.3.5.2 Electrical resistivity method

Electrical resistivity is a fundamental property of materials that quantifies their ability to resist the flow of electric current. It is the material's natural resistance to electrical current and is strongly influenced by its atomic structure, defect and impurities. The electrical resistivity of a material is influenced by factors such as temperature, material composition and structural changes. In metals, resistivity primarily arises from electron scattering due to lattice vibrations, impurities and defects. Due to its sensitivity to these structural variations, electrical resistivity has been widely used in materials science for characterizing phase transitions, detecting defects and monitoring microstructural changes, particularly in fatigue studies. several methods are available for measuring electrical resistivity, each suited to different types of materials and applications. The two-probe method, commonly used for high-resistivity materials, measures the voltage drop across a sample while applying a known current, though it is prone to contact resistance errors. The four-probe method mitigates lead resistance effects by using separate current and voltage probes, making it ideal for lowresistivity materials and high-precision measurements. Other advanced techniques include the van der Pauw method, used for thin films and irregularly shaped samples. Schematic and more details about 2-probe and 4-probe method has been explained in 3.2. Considering this study objectives van der Pauw method is not discussed further but information about this method can be found in reference [74]. The Montgomery method is commonly used for measuring resistivity in pellets and bulk materials. Additionally, modern approaches incorporate pulse-probe techniques and non-contact measurement methods to enhance accuracy. Another widely studied technique is the drop method, which involves monitoring sudden changes in resistivity due to microstructural evolution during cyclic loading. This method is particularly useful for detecting discontinuities such as crack formation and propagation in metallic materials. In the next section, a detailed literature review will be presented on how both the four-point method and the drop method have been utilized for fatigue damage detection, highlighting their effectiveness and limitations in monitoring microstructural changes [72].

2.3.5.3 Electrical resistivity in fatigue damage detection

Electrical resistivity is a widely researched parameter for fatigue damage monitoring due to its sensitivity to microstructural changes in a material under cyclic loading. The methodology for using electrical measurements in damage monitoring shares fundamental principles with crack monitoring, but the focus shifts from detecting existing cracks to tracking changes in resistivity as an early indicator of fatigue damage [75]. These changes in resistivity can be attributed to various factors, including dislocations, point defects and both micro and macro crack propagation. However, other external factors, such as specimen elongation, temperature variations and reduction in cross-sectional area, can also influence resistivity measurements. Therefore, it is crucial to eliminate or account for these influences to ensure accurate monitoring [76, 77]. The relationship between change in electrical resistivity and number of fatigue cycles in copper, as shown in Figure 2-21, shows how resistivity evolves

during cyclic loading under different amplitudes of mean shear strain. This figure highlights that for copper, resistivity initially remains stable, followed by a gradual increase and then a sharp rise as the material approaches failure. This behaviour underscores this method's sensitivity to progressive fatigue damage and its potential for early detection of microstructural changes before macroscopic crack formation [76].

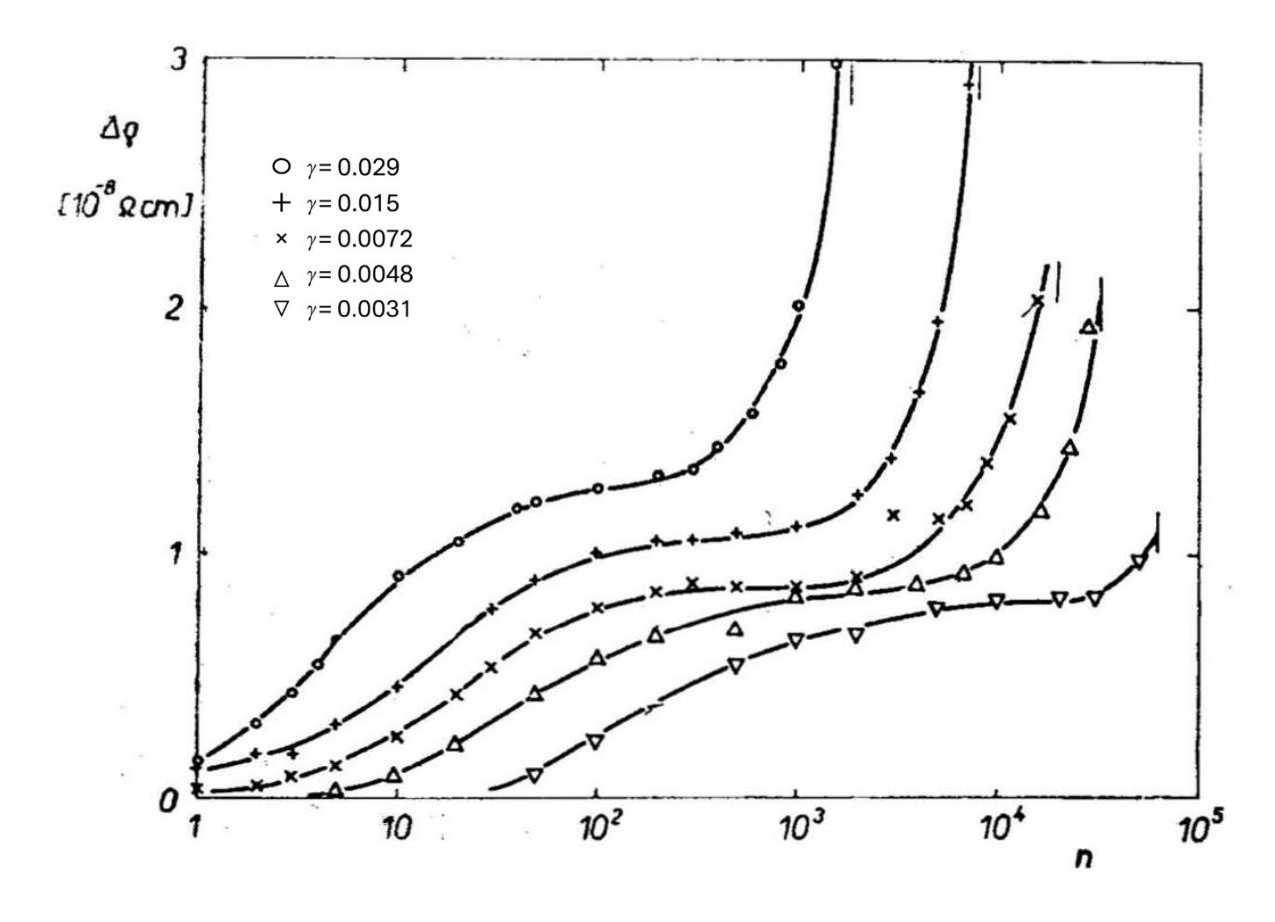


Figure 2-21. Change in electrical resistivity and the number of fatigue cycles in copper under different amplitudes of mean shear strain [76]

In another study, Charsley and Robins [78], investigated the electrical resistance changes in polycrystalline copper foil subjected to cyclic bending deformation at room temperature using a direct current (DC) two probe resistivity measurement method. The study aimed to understand the relationship between fatigue damage and resistivity evolution by varying parameters such as strain amplitude, grain size and cycling frequency. The results in Figure 2-22 showed a steady increase in electrical resistance during the early stages of cyclic loading, attributed to the accumulation of dislocations and the formation of persistent slip bands. Near the point of failure, a sharp rise in resistance was observed, corresponding to microcrack formation. Optical and electron microscopy revealed that grain boundary cracks and intense slip activity contributed significantly to the resistivity changes. This study demonstrated that electrical resistivity measurements are highly sensitive to fatigue-induced microstructural changes, making them a reliable tool for early detection of fatigue damage before visible cracks appear [79].

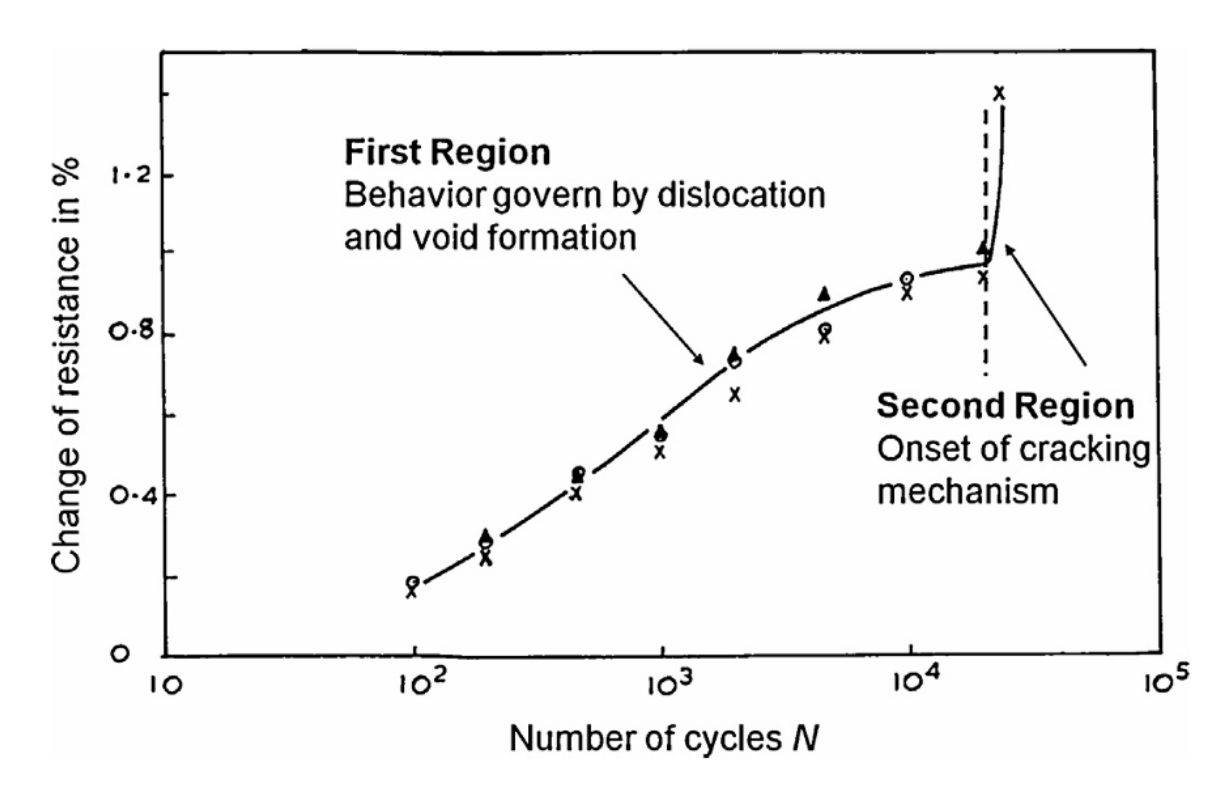


Figure 2-22. Typical resistance changes in polycrystalline coper due to fatigue cycling [78]

In another study, Starke et al. [80, 81], demonstrated that electrical resistivity can reveal the initial condition of materials within a group of specimens made from the same alloy. Their findings showed that specimens with higher initial resistivity tended to have a greater density of pre-existing defects. Furthermore, this initial resistivity was found to correlate with the number of cycles to failure, indicating its potential as a predictive parameter for fatigue life. Further investigations by Germann et al. [82, 83], focused on resistance monitoring during fatigue tests on steels (SAE 4140, EN-GJS-600) and cast irons (EN-GJL-250, EN-GJV-400), using Direct Current Potential Drop (DCPD) method in a two-probe setup, along with temperature and magnetic field sensors. In 2012, they extended their work to include nodular and vermicular cast irons and with varying graphite morphologies and matrix structures, introducing a multi-sensor monitoring approach. This integration significantly enhanced the sensitivity and reliability of fatigue damage detection by distinguishing resistivity changes caused by fatigue from those due to thermal effects, while also capturing magnetic signatures associated with dislocation density and stress-induced phase transformations. The DCPD technique detected resistivity changes as small as 0.5-2 μΩ·cm during early fatigue stages corresponding to less than 1% relative change—even before surface cracks appeared. For instance, in EN-GJS-600, a 1.8 $\mu\Omega$ ·cm increase was recorded after 10⁴–10⁵ cycles. The refined multi-sensor setup enabled resolution down to 200–500 n Ω , allowing for more precise attribution of changes to microstructural damage rather than external noise. Figure 2-23 shows the progression of electrical resistance change (ΔR) during fatigue testing of EN-GJL-250 cast iron, with micrographs(b-e) showing crack evolution. Early microstructural changes and crack initiation occur in (b), followed by crack propagation in (c), significant crack growth in (d) and rapid crack propagation leading to failure in (e)[83]. Initially, at N = 50 cycles (Figure 2-23b), localized stress at graphite lamella tips leads to graphite-matrix debonding and early micro-crack initiation, causing a slight increase in ΔR . However, during further cycling up to around N = 200 (Figure 2-23c), micro-pinholes and cracks partially close, increasing the effective electrical cross-section and resulting in a decrease in ΔR . As cycling continues (Figure 2-23d), reopening of closed cracks and initiation of new micro-cracks begins to dominate, reversing the trend and causing ΔR to rise again. Eventually, at N = N_f (Figure 2-23e), macroscopic crack growth and severe matrix damage occur, leading to a sharp increase in ΔR until failure. This study highlighted that the magnitude of resistance change, both in the initial decrease and the subsequent sharp increase, depended on the applied stress amplitude, offering valuable insights into stress-dependent fatigue behaviour.

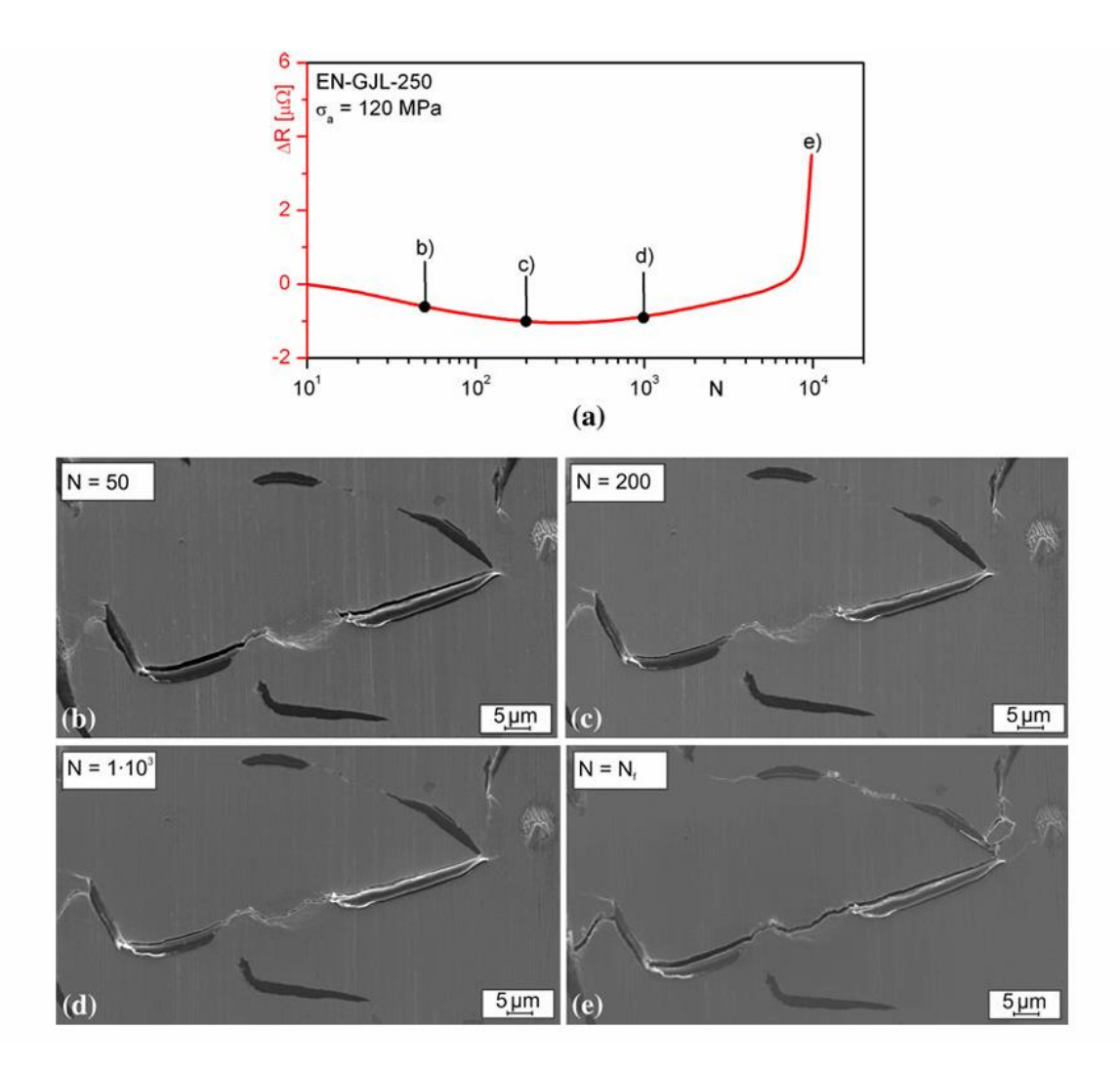


Figure 2-23. Eelectrical resistance change (ΔR) vs. fatigue cycles (*N*) for EN-GJL-250 cast iron at a cyclic stress amplitude of 120 MPa (a). Micrographs (b–e) illustrate the progression of fatigue cracks at different stages: (b) early-stage crack initiation at N=50, (c) mid-stage crack propagation at N=200, (d) late-stage crack growth at N=1×10³ and (e) final fracture at N=N_f [83]

Similarly, Smaga et al. [84], utilized electrical resistance measurements to characterize fatigue damage in austenitic steels across a wide temperature range, highlighting its sensitivity to defect density, dislocation arrangements, and phase transformations during cyclic loading shown in Figure 2-24.

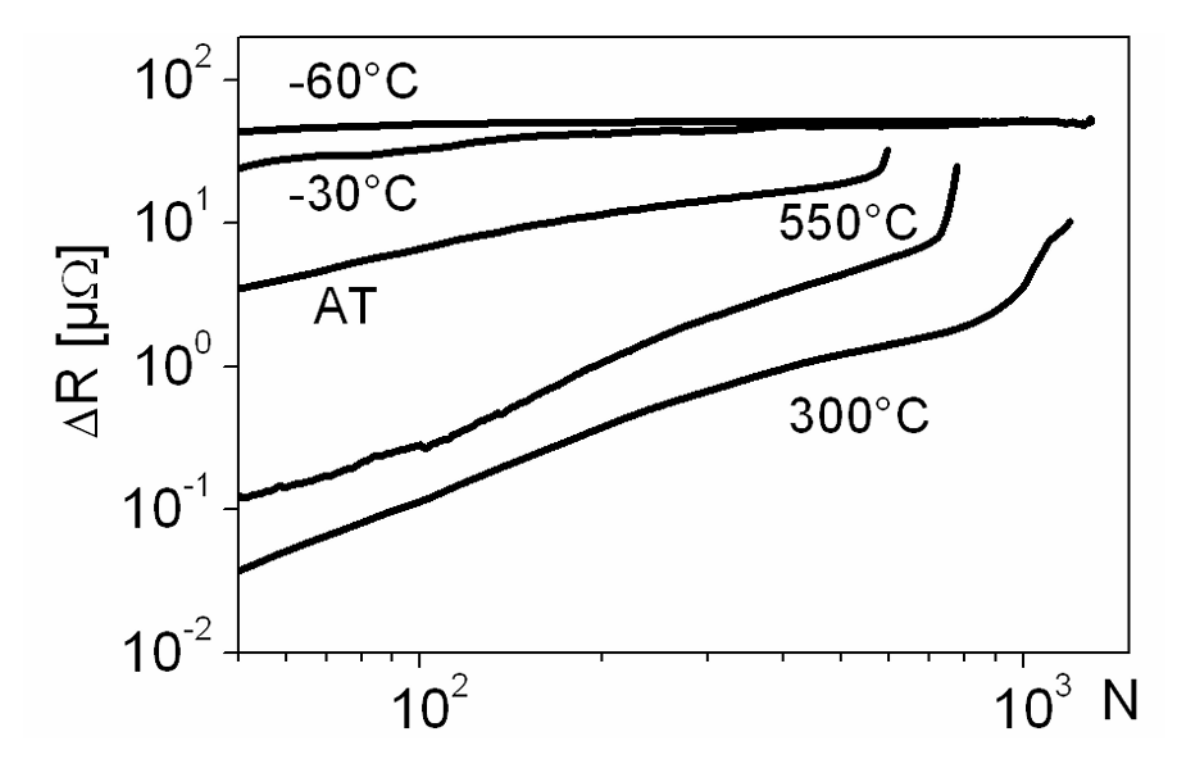


Figure 2-24. Changes in electrical resistance in fatigue tests for AISI 348 at -60°C and -30°C as well as AISI 321 at AT (ambient temperature) \leq T \leq 550°C [84]

The use of resistivity in fatigue damage monitoring has also led to the development of predictive models. Sun et al. [85, 86], proposed an accumulative damage model based on resistance changes, though this model was not tested under variable amplitude loading, leaving room for further investigation. They developed an electrical resistivity measurement technique for detecting high-cycle fatigue damage by monitoring direct current (DC) resistance changes, employing a four-probe method to improve accuracy by eliminating contact and lead resistances. Their method involves measuring electrical resistance in real-time during rotary bending fatigue tests of structural steels. This technique demonstrated high sensitivity to micro-crack initiation and fatigue damage, with precise measurements in the range of 10^{-8} to 10^{-5} Ω . This high sensitivity allows for early detection of fatigue damage and accurate lifetime prediction.

In another study, Omari and Sevostianov [87], investigated fatigue damage in 304 stainless steels using a four-probe electrical resistivity measurement technique to monitor resistivity changes during fatigue loading. They developed a formulation to estimate dislocation density based on the measured resistivity changes over multiple fatigue cycles. To validate their resistivity-based dislocation density estimates, they performed SEM imaging with 6000x

magnification of the specimens at different stages of fatigue loading. Interestingly, they found that the dislocation density calculated from SEM images was approximately three times lower than that obtained using their resistivity-based formulation, which is derived from the following equation:

$$\Delta R = R - R^0 = \frac{\Delta \rho R^d}{N}$$

Solving for dislocation-related resistivity increase gives:

$$\Delta \rho = \frac{N(R - R^0)}{R^d}$$

where R and R⁰ are the measured and initial resistances, Δp is electrical resistivity, N is the number of cycles, and R^d is a constant related to the dislocation network. This formulation assumes an isotropic distribution of dislocations and directly links the macroscopic resistivity increase to dislocation density evolution. The discrepancy with SEM measurements was attributed to the limited spatial resolution and surface sensitivity of SEM, which may miss fine-scale or subsurface dislocation structures that significantly affect electron scattering and, therefore, electrical resistance. Wu et al. [88], investigated the fatigue behaviour of steel by combining electrical resistivity measurements with X-ray diffraction (XRD) and TEM. They used a DC-based resistivity measurement method, specifically applying the potential drop technique on the central section of the fatigue specimen, where the most significant microscopic changes occur. Their study demonstrated that resistivity changes correlates well with dislocation density during fatigue, especially in the early stages where micro-crack formation is minimal. The sensitivity of their DC-based method was highlighted in detecting dislocation-driven fatigue damage well before observable cracks appeared. They concluded that resistivity is a viable tool for early fatigue damage detection in ductile steels [88].

Nobile and Saponaro [89, 90], explored the application of in-situ electrical resistance change (ERC) for predicting fatigue damage in AISI 316L stainless steel. They employed a four-probe method to measure resistivity during cyclic loading. The study found that resistivity variations reliably indicated fatigue progression, with distinct resistance behaviour change observed before crack initiation. Figure 2-25 presents the relationship between Percentage of change of electrical resistance versus fatigue cycles. They observed that electrical resistance initially decreases 3% in the early stages of fatigue life. They attributed this drop to the reorganization of dislocations into more stable configurations, such as dislocation cells and walls, which reduces electron scattering. Around 30 to 40% of the fatigue life, the change of resistance starts to increase sharply, which they linked to irreversible fatigue damage, including significant plastic deformation and the initiation of micro-cracks. The authors noted that the rate of resistance change was inversely proportional to the applied stress amplitude, meaning that higher stresses resulted in a smaller resistance increase because of the larger plastic zone size. A larger plastic zone leads to a smaller resistance change because the strain and microstructural damage (such as dislocation accumulation or microcracking) are distributed over a wider area. This distribution reduces the local concentration of defects, which are the

primary contributors to electron scattering and, consequently, changes in electrical resistance. In contrast, when the plastic zone is small, deformation and damage are localized, leading to a higher density of defects per unit volume, which has a more pronounced effect on resistivity. Therefore, the same amount of overall damage causes less change in resistance when spread over a large plastic zone. Finally, just before complete failure, the resistance rises rapidly due to the propagation of cracks [75].

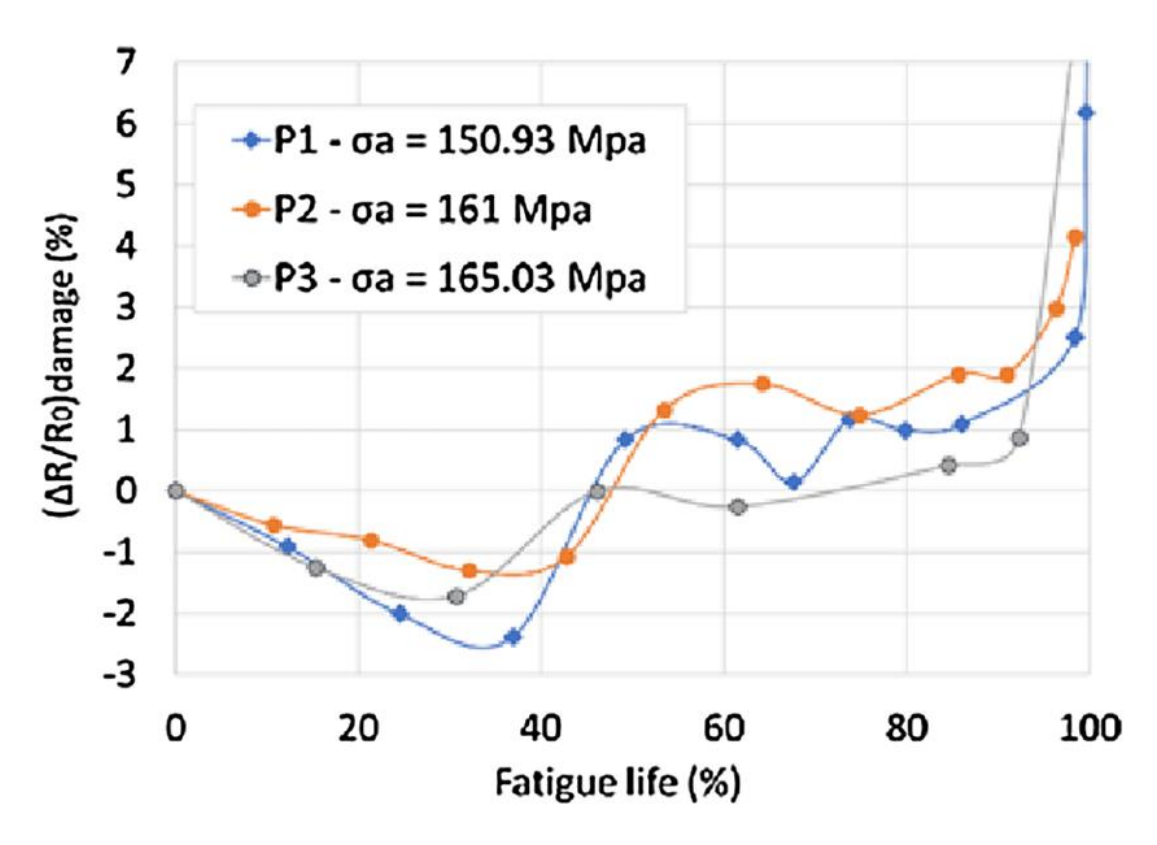


Figure 2-25. Percentage of change of electrical resistance associated to damage versus fatigue life [90]

Saberi et al.[91], introduced a novel coupled electro-mechanical four-point method for in situ measurement of electrical resistivity during plastic deformation, offering significant advancements over existing techniques. This innovative approach allows continuous, real-time resistivity monitoring under various deformation conditions, including uniaxial tensile and plane strain tests. Unlike earlier methods, which were typically restricted to isotropic materials, their method effectively handles anisotropic strain paths and diverse deformation histories, making it a valuable tool for characterizing complex metal forming processes. In addition to monitoring deformation, the method can detect critical microstructural defects such as dislocations, voids and crack initiation sites. By capturing variations in resistivity linked to dislocation density and lattice distortions, it facilitates early detection of fatigue damage and material degradation.

Based on the reviewed literature, it is evident that electrical resistivity measurements—particularly when implemented using the four-probe method—offer a highly sensitive and non-invasive approach for detecting early-stage fatigue damage. This technique has

demonstrated effectiveness across a wide range of metals, including stainless steels. Given these advantages, electrical resistivity measurement using the four-probe technique aligns closely with the aims of this research and in next chapters will be discussed with more details.

2.3.6 Ultrasound methods

Ultrasound-based techniques are a widely used class of non-destructive testing (NDT) methods that rely on the propagation of high-frequency sound waves through a material to detect internal changes, discontinuities, or evolving damage. When ultrasonic waves travel through a solid, their interaction with the microstructure—such as grain boundaries, dislocations, voids, and cracks—alters wave parameters like velocity, amplitude, and attenuation. By analysing these changes, ultrasonic methods can provide insights into the material's internal state, often without the need for disassembly or surface preparation. Due to their high sensitivity and depth penetration capabilities, ultrasonic techniques are extensively used in industries like aerospace, nuclear, and manufacturing for defect detection, quality assurance, and fatigue monitoring.

2.3.6.1 Linear ultrasound

Linear ultrasonic testing is the most used ultrasonic approach and involves the use of high-frequency longitudinal or shear waves to detect geometric discontinuities such as cracks, voids and inclusions. It is based on the principles of reflection, transmission, and attenuation of ultrasonic waves as they encounter interfaces or flaws within a material. Linear ultrasound is highly effective for locating and sizing visible defects and for evaluating crack propagation and fracture progression under fatigue loading. This method is generally more applicable to the later stages of fatigue, once macroscale defects have formed. Its application in detecting early microstructural fatigue features—such as dislocation movement or slip band formation—is limited. Therefore, while linear ultrasound is a powerful tool for conventional defect detection, it is not within the scope of this project, which focuses on the early, precrack stage of fatigue damage. Instead, the attention in this study is directed toward nonlinear ultrasonic methods, which have shown greater promise for capturing subtle microstructural changes before crack initiation [92].

2.3.6.2 Nonlinear ultrasound

Ultrasonic testing uses high-frequency sound waves to inspect structures for flaws. Nonlinear ultrasound (NLU) is a non-destructive testing (NDT) technique that has gained significant attention for early detection of fatigue damage in different materials. Unlike conventional linear ultrasound methods, which detect defects by measuring wave reflection, attenuation, and sound speed, NLU focuses on the generation of harmonic waves caused by nonlinear interactions between the ultrasonic wave and microstructural features of the material. The presence of dislocations, slip bands, microcracks and other forms of microstructural damage causes nonlinear distortion in the ultrasonic wave, producing higher-order harmonics that can be measured and analysed. This makes NLU particularly effective in detecting early-stage fatigue damage before macroscopic cracks are visible. The key parameter in NLU is the

nonlinear coefficient (β), which quantifies the ratio of the second harmonic amplitude to the square of the fundamental wave amplitude. An increase in this coefficient indicates the accumulation of microstructural damage. Details about this parameter and how to measure it will be discussed in Chapter 4. Nonlinear ultrasonic testing methods can broadly be classified into three main categories:

2.3.6.2.1 Harmonic generation measurement

Harmonic generation is one of the most widely used nonlinear ultrasonic techniques for early damage detection. It involves the measurement of higher-order harmonics—typically the second harmonic—that are generated as an ultrasonic wave propagates through a material with nonlinear elastic properties. More detail about harmonic generation and how they form is discussed with detail in Chapter 4. These nonlinearities are caused by microstructural changes such as dislocations, micro voids, grain boundary sliding, and other early fatigue-related defects. The presence and amplitude of the second harmonic are direct indicators of material degradation, making this method highly sensitive to damage well before macrocracks appear. Additionally, wave mixing techniques, which involve the interaction of two incident waves to create a third wave at a combination frequency, can further enhance sensitivity to localized changes [93, 94, 95].

2.3.6.2.2 Nonlinear spectroscopy

Nonlinear acoustic spectroscopy includes techniques that analyse a material's frequency response under ultrasonic excitation to evaluate its nonlinear characteristics. Unlike harmonic generation, which typically employs broadband excitation to detect harmonics, nonlinear spectroscopy focuses on frequency shifts, amplitude modulation, and spectral distortions at specific points or regions of interest. This approach necessitates sophisticated equipment and signal processing but is highly effective in detecting early damage precursors, such as incipient microcracks, delamination particularly in composite and layered materials. Nonlinear spectroscopy is especially suited for point-based damage characterization, making it ideal for applications requiring precise defect localization, though it may be less practical for wide-area monitoring due to its complexity and time demands [96].

2.3.6.2.3 Nonlinear ultrasonic phased array imaging

Nonlinear ultrasonic phased array imaging represents an advanced category of nonlinear ultrasonic testing. It combines the beam-forming and steering capabilities of phased array systems with nonlinear signal analysis to image non-classical nonlinearities, such as tightly closed fatigue cracks, kissing bonds and microstructural distortions that are challenging to detect using linear methods. These systems utilize multiple transducers and complex signal processing algorithms to reconstruct high-resolution images of internal features. The integration of nonlinear analysis enables the detection of subtle or closed defects that may not reflect or scatter linear ultrasonic waves. While these techniques are highly effective, they require specialized equipment, advanced operator expertise, and substantial computational resources. Table 2-1 summarizes a brief review of different nonlinear ultrasound methods,

their sensitivity to damage, advantages and disadvantages. It is evident that second harmonic generation stands out as the most promising technique for the scope of this project [97, 98].

Table 2-1. Summary of a comparative study for existing nonlinear ultrasonic techniques [95, 99, 100]

Method	Damage sensitivity	Advantages	Disadvantages	
Second harmonic	Plasticity, creep,	Sensitive to a broad	- Provides only a spatially	
Generation	low	range of	averaged measurement across	
	and high cycle	microstructural	the bulk material	
	fatigue damage,	damage	-Double sided access in most	
	thermal aging		cases but single-sided access has	
			been achieved using focused	
			transducers	
Wave mixing	Plasticity, kissing	-Volumetric	-Complicated	
	bond and fatigue	localisation of	experimental setup	
	crack	nonlinear source.	-primarily a laboratory-based	
		-Separation of	technique as requires precise	
		instrument and	control over input signals	
		material nonlinearity		
Nonlinear elastic	Partially closed	Long range inspection	-Only surface	
wave spectroscopy	crack and		measurements	
	delamination		-Complicated	
			experimental setup	
Nonlinear time	Partially closed	Imaging of nonlinear	-Only surface	
reversal	crack and	scatters over large	measurements	
spectroscopy	delamination	area	-Complicated	
			experimental setup	
Subharmonic array	Partially closed	Through depth	-Complicated	
imaging	crack	imaging. Single-sided	experimental setup	
		access	-Better suited for detecting	
			cracks than early fatigue damage	
Fundamental	Partially closed	-Through depth	-Requires complex	
amplitude	crack	imaging	instrumentation	
modulation imaging		-Single-sided access	- less sensitive to early damages	
Nonlinear	Partially closed or	-Highest sensitivity to	More suitable or laboratory	
ultrasonic diffuse	closed crack	elastic nonlinearity	measurements and needs	
energy imaging		-Through depth	complex experimental setup	
		imaging.		
		-Single-sided access		

In the next section, a focused literature review on the application of second harmonic generation for early fatigue damage detection will be presented. This review will highlight how the technique has been utilized across different materials, loading conditions and fatigue stages, and will establish its relevance and effectiveness as a diagnostic tool in this study.

2.3.6.3 Second harmonic nonlinear ultrasonic in fatigue damage detection

Kyung-Young Jhang [100], demonstrated the effectiveness of nonlinear ultrasonic (NLU) in detecting early-stage material degradation by measuring the nonlinear parameter β , which quantifies second harmonic generation during ultrasonic wave propagation. The study assessed fatigue damage and aging degradation in various metals, particularly mild steel (SS41, SS45) and Cr-Mo-V steel (used in turbine rotors). Key findings of this research show that the nonlinear parameter β increased significantly with mechanical degradation, showing a strong correlation with dislocation accumulation and microstructural evolution. Unlike traditional ultrasonic parameters (attenuation, sound velocity), β can effectively reflected early fatigue damage. In Cr-Mo-V steel, β correlated well with the Fracture Appearance Transition Temperature (FATT), validating its use in monitoring long-term material aging in high-temperature environments. While the study did not include direct microscopy, it suggested that the observed nonlinear effects stem from dislocation interactions and microstructural changes. The authors recommended further research to correlate nonlinear ultrasonic (NLU) findings with microscopy techniques such as SEM and TEM to better understand the underlying degradation mechanisms [101]. In 2006 Palit Sagar et al. [102], introduced a nonlinear ultrasonic (NLU) technique for assessing fatigue damage in low-carbon structural steel. The study introduced Total Harmonic Distortion (THD), defined as the ratio of the amplitude of the second harmonic to the fundamental frequency, as a key parameter to monitor fatigue progression. They demonstrated that NLU parameters could sensitively detect early fatigue damage stages. Their experiments revealed that THD increased significantly during early fatigue due to dislocation accumulation, stabilized as dislocation cells formed, and sharply rose again near failure when micro-cracks initiated as it is shown in Figure 2-26 and Figure 2-27. This study established the potential of NLU for real-time fatigue monitoring by correlating ultrasonic parameters with microstructural changes.

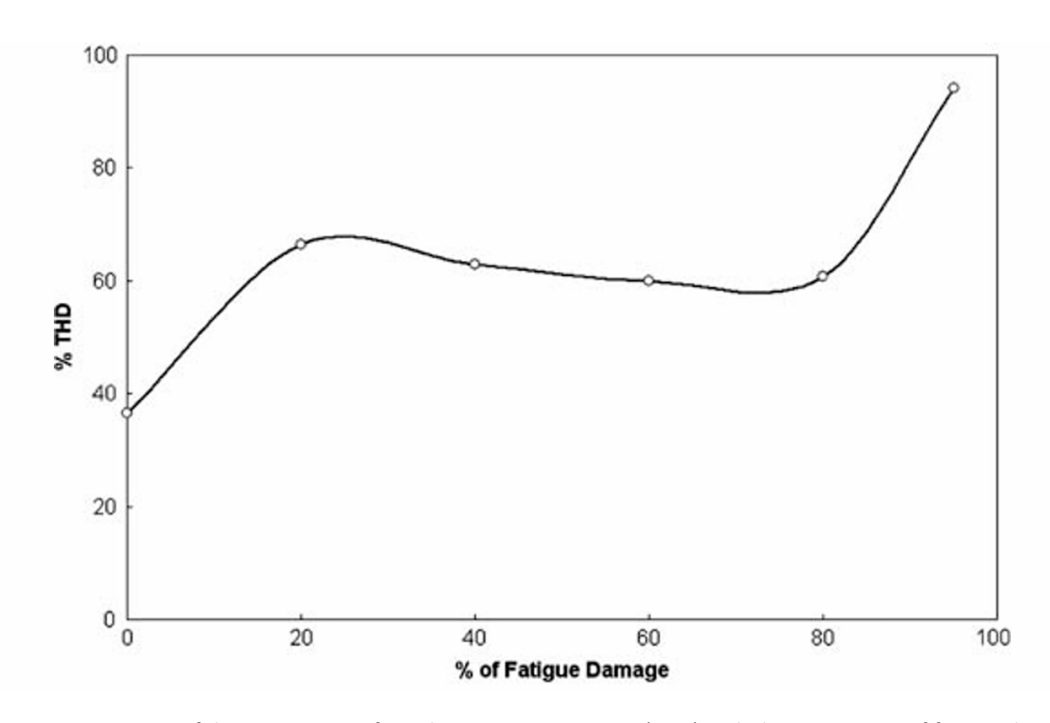


Figure 2-26. Variation of the percentage of Total Harmonic Distortion (THD) with the percentage of fatigue damage (expressed as % of total fatigue life) showing three stages of fatigue life in low-carbon structural steel [102]

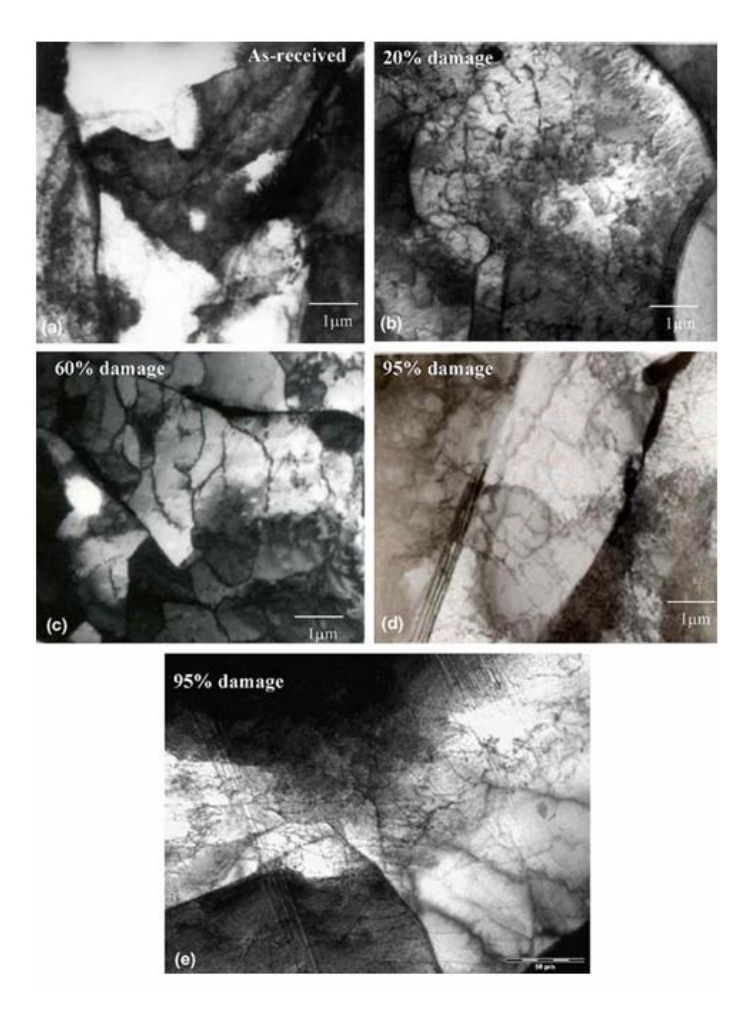


Figure 2-27. TEM micrographs of different % fatigue damaged specimen showing the correlation between microscopy and THD parameter in low carbon structural steel [102]

Sagar et al. [103], extended their previous research on nonlinear ultrasonics (NLU) to investigate low-cycle fatigue (LCF) in pearlitic steel with 0.3 wt.% carbon. This study focused on how microstructural changes, particularly dislocation evolution and cementite shearing, influence the second harmonic generation in ultrasonic waves. They introduced a normalized nonlinearity parameter (β) and observed distinct phases of fatigue damage, including dislocation multiplication, stabilization and micro-crack nucleation as observed in Figure 2-28. This progression highlighted the improved sensitivity of NLU techniques to complex microstructures. Together, these studies demonstrated that NLU is a reliable method for early fatigue damage detection and microstructural monitoring across different steel types.

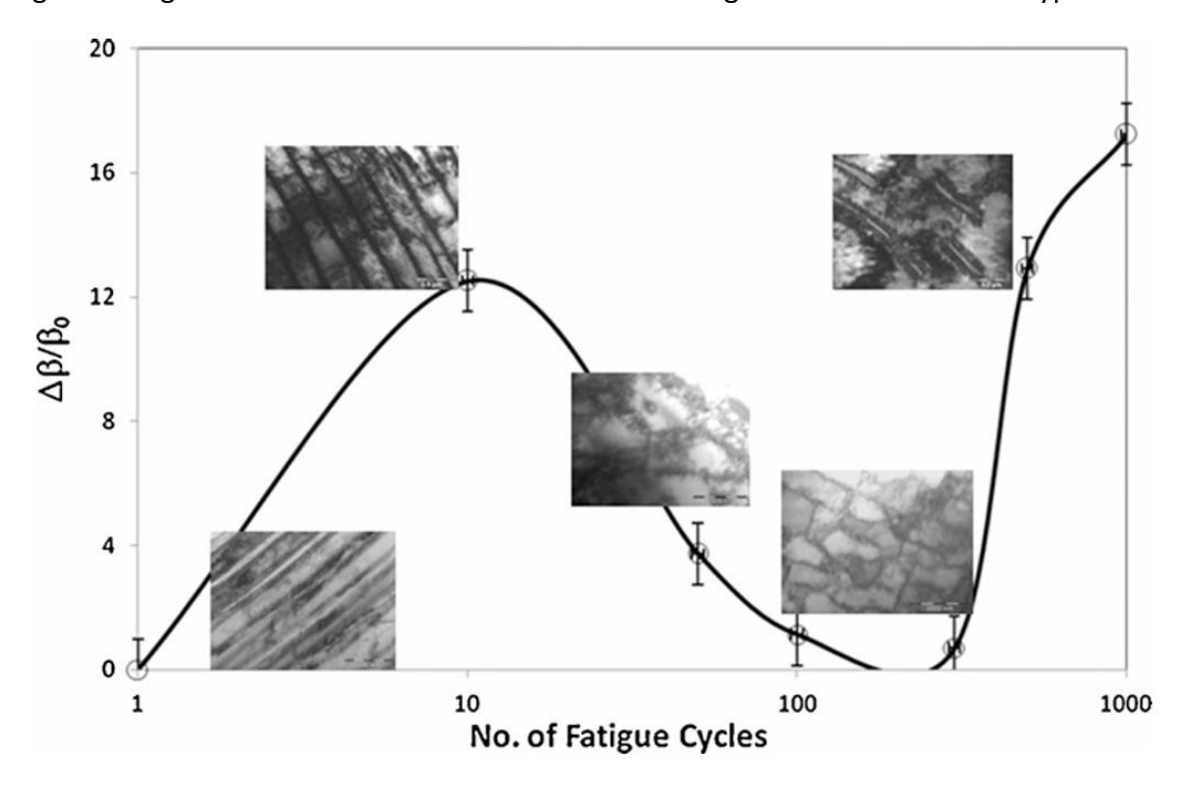


Figure 2-28. Variation of normalized NLU parameter with number of fatigue cycles in pearlite steel showing three stages of fatigue [103]

In another study Kim et al [104], investigated the evolution of fatigue damage in a nickel-based superalloy using the acoustic nonlinearity parameter (β) to track changes in microstructure during high- and low-cycle fatigue (LCF and HCF). The study provided a repeatable, robust measurement system that isolated material nonlinearity from instrumentation effects. Overall, these nonlinear ultrasonic results indicate that the fatigue damage associated with HCF is relatively localized, whereas the damage in LCF is more evenly distributed across the material. The ability to track these differences through nonlinear ultrasonic measurements underscores the potential of this technique as a robust tool for fatigue life prediction and structural health monitoring.

Additional work focused on the relationship between dislocation density and the ultrasonic nonlinearity parameter β in P91 steel had been done by Cai et al. [105], using X-ray diffraction (XRD) to estimate dislocation density and nonlinear ultrasonic testing. They established a

monotonic increase in β with increasing dislocation density, demonstrating that NLU techniques can effectively assess mechanical degradation. Their findings revealed distinct stages of dislocation evolution as follows, at low strains, β increased rapidly due to dislocation multiplication; at moderate strains, it stabilized as dislocations reorganized into cell structures; and at higher strains, β increased sharply again, indicating the formation of voids and microcracks. These results suggest that nonlinear ultrasonic can serve as an early-stage diagnostic tool for fatigue damage, allowing real-time monitoring of material degradation [105].

While Cai et al.[105], provided strong experimental evidence for the correlation between dislocation density and ultrasonic nonlinearity, a more refined theoretical framework was developed by Xiang et al.[106], who introduced a model incorporating mixed dislocations (edge and screw dislocations). Their theoretical framework is based on dislocation line energy and variable line tension, accounting for the orientation of the dislocation line relative to the Burgers vector. They assume that mixed dislocations can be treated as a combination of edge and screw components and derive a total line energy expression dependent on this orientation. The model also incorporates a back-stress term, representing internal stresses from dislocation interactions, and uses a Taylor series expansion to express the strain induced by ultrasonic waves. A key assumption is that the dislocation bow-out follows a circular arc under stress, allowing for an analytical solution of strain-stress relations up to third order. This leads to a nonlinear acoustic parameter (β) that depends on dislocation density, segment length, back stress, and the fractions of edge vs. screw dislocations. The model's accuracy was validated experimentally, showing excellent agreement with measured data, and outperforming earlier models like Hikata et al. [93], by more accurately capturing the behaviour of mixed dislocations and their contributions to acoustic nonlinearity. Their findings indicated that β is more sensitive to edge dislocations, particularly in materials with a higher Poisson's ratio due to their stronger elastic interactions because of non-symmetric strain field, higher pinning behaviour, and their greater impact on wave propagation as captured in the model equations. This explains why materials with higher fractions of edge dislocations show larger nonlinear ultrasonic responses. By validating their model with coldrolled 304 stainless steel and martensitic stainless steel, they demonstrated that edge dislocations interact more strongly with nonlinear acoustic waves, causing greater harmonic distortion than screw dislocations. This research bridges the gap between theoretical predictions and experimental observations, refining the application of nonlinear ultrasonic for dislocation-sensitive material evaluation.

Moving beyond static deformation, Zhang and Xuan [107], examined the evolution of nonlinear ultrasonic parameters during low-cycle fatigue (LCF) in 304 austenitic stainless steel. Their study introduced a "mountain-shaped" correlation between β and change to number of cycles as shown in Figure 2-29, where β initially increased until reached a peak at 10% fatigue life and then gradually decreased. This behaviour was attributed to the cyclic evolution of dislocation structures. Figure 2-30 provides direct microstructural evidence

supporting this behaviour. In early fatigue stage (8–10% fatigue life), rapid increase in β is observed due to dislocation multiplication and the formation of tangled dislocation structures, dislocation walls and veins, which significantly contribute to elastic nonlinearity. As the material enters the mid-life stage, dislocation structures become more organized. Dislocations rearrange into stable configurations such as cells and persistent slip bands (PSBs). This reorganization reflects a state of maximum microstructural nonlinearity, leading to the peak of the β parameter. In the later stages of fatigue life, the β parameter begins to decline. This reduction is attributed to the saturation and coarsening of dislocation structures, which become more energetically stable and less responsive to further cyclic deformation. By "coarsening" of dislocation structures, this study didn't refer not to increased tangling, but to the transformation of fine, highly mobile dislocation networks into more stable, lowerenergy, and spatially coarser cell-like substructures with thicker walls and fewer mobile segments. The notion of "energetic stability" is supported by transmission electron microscopy (TEM) observations in the late fatigue stages, which show thicker and more uniformly spaced dislocation cell walls. These morphologies suggest reduced internal stress gradients and dislocation mobility, indicating a transition toward lower internal energy states. This process reduces the density of dislocation intersections and dynamic interactions. As dislocations settle into well-defined cellular arrangements, the capacity for generating new nonlinearity diminishes, resulting in a gradual decrease in second harmonic amplitude. TEM analysis in this stage confirms a more uniform and less dynamic microstructure, consistent with the declining β trend. This does not mean that β is entirely unresponsive to static microstructures, but rather that its sensitivity is significantly higher when the microstructure is undergoing active evolution. The β parameter is influenced by both the presence and the behaviour of dislocations—specifically their mobility, multiplication, and interactions. When dislocations are actively moving, forming tangles or reorganizing, they create non-uniform internal stress fields that strongly modulate the material's nonlinear elastic response, thereby increasing β. However, once dislocations become stabilized into low-energy configurations (e.g., cells or walls), these dynamic interactions decrease, reducing their contribution to acoustic nonlinearity. Thus, the key microstructural feature influencing β is not merely the presence of dislocations, but their configuration and dynamic activity. A static, well-organized dislocation structure contributes less to second harmonic generation than a disordered, evolving one.

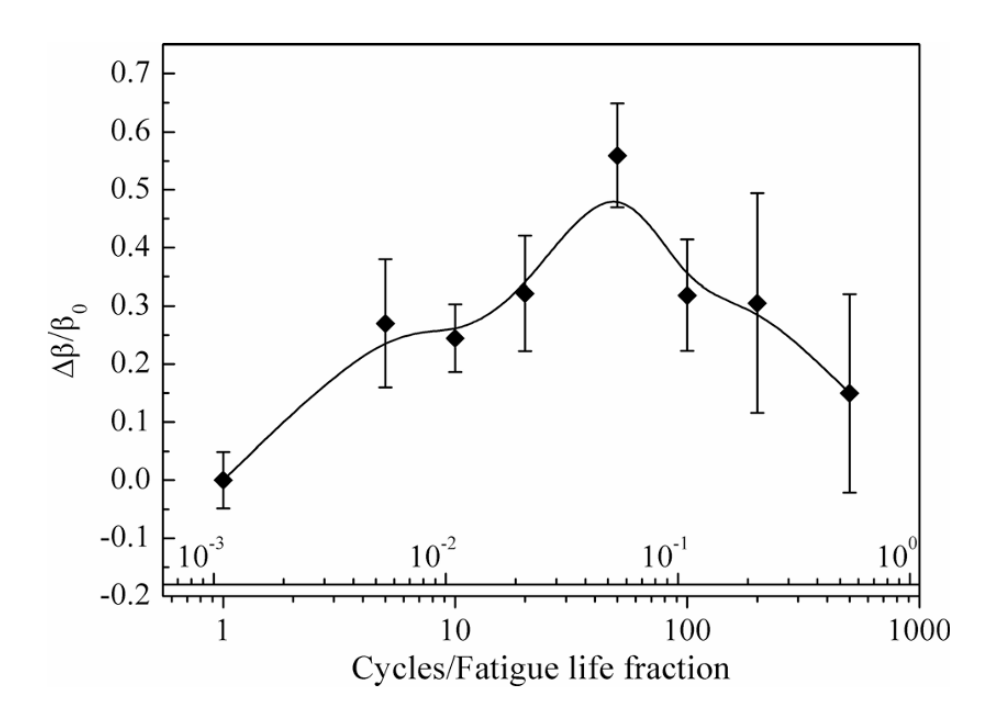


Figure 2-29. Correlation of normalized nonlinear acoustic parameter with fatigue cycles of 304 SS [107]

This mountain-shaped profile of the nonlinear parameter shows the capability of nonlinear ultrasonic techniques to sensitively monitor fatigue-induced microstructural changes. It highlights their effectiveness in detecting early-stage fatigue damage—before the initiation of visible cracks—by capturing the evolving dislocation dynamics throughout the fatigue life.

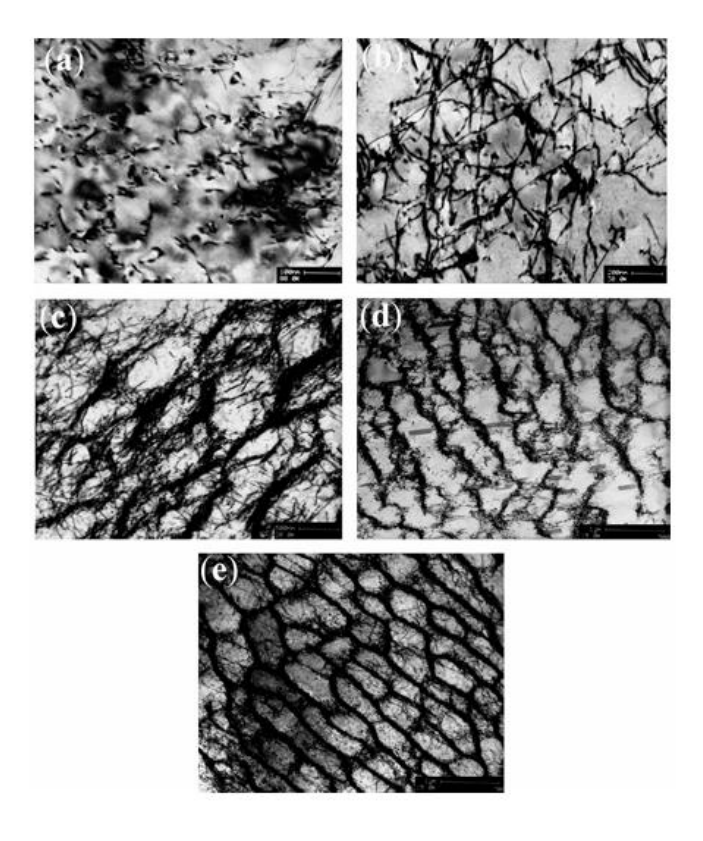


Figure 2-30. TEM micrographs of different fatigued specimens: (a) as received, (b) 5 cycles, (c) 50 cycles, (d) 100 cycles, and (e) 500 cycles [107]

The nonlinear ultrasonic parameter (NLP) method has also been applied to 316L stainless steel produced by selective laser melting (SLM) to investigate fatigue damage. Due to the unique microstructural characteristics of SLM materials—such as porosity, residual stress, and rapid solidification microstructures—fatigue behaviour can differ significantly from conventionally processed alloys. Qiao and Yan [108], investigated the use of high-order harmonic nonlinear ultrasonic testing to monitor the evolution of fatigue damage in SLM 316L stainless steel. By correlating nonlinear ultrasonic parameters with scanning electron microscopy (SEM) and transmission electron microscopy (TEM) observations, they provided insights into the microstructural mechanisms governing fatigue failure in additively manufactured metals. Their findings demonstrated a progressive increase in second harmonic generation (A₂) with fatigue cycles, while the fundamental wave amplitude (A₁) decreased, leading to a rise in the nonlinear parameter β (Figure 2-31). The frequency-domain plots in Figure 2-31 (b) and (d) show the growth of the second harmonic peak, confirming enhanced nonlinearity from 10,000 to 50,000 cycles. The corresponding time-domain waveforms shown in Figure 2-31 (a) and (c), also show a change in waveform shape and attenuation, consistent with increased dislocation activity. This behaviour correlated with distinct fatigue damage stages. As shown in Figure 2-32 in the early stages (0 –20K cycles), dislocation multiplication dominated, causing a slow increase in β . As fatigue cycles increased to 20K-50K cycles, dislocations evolved into tangled networks, veins, and walls, resulting in a rapid rise in nonlinearity. In the late stages (>50K cycles), microcrack initiation and propagation further enhanced harmonic generation, reaching a peak before declining due to macrocrack formation and material failure[108].

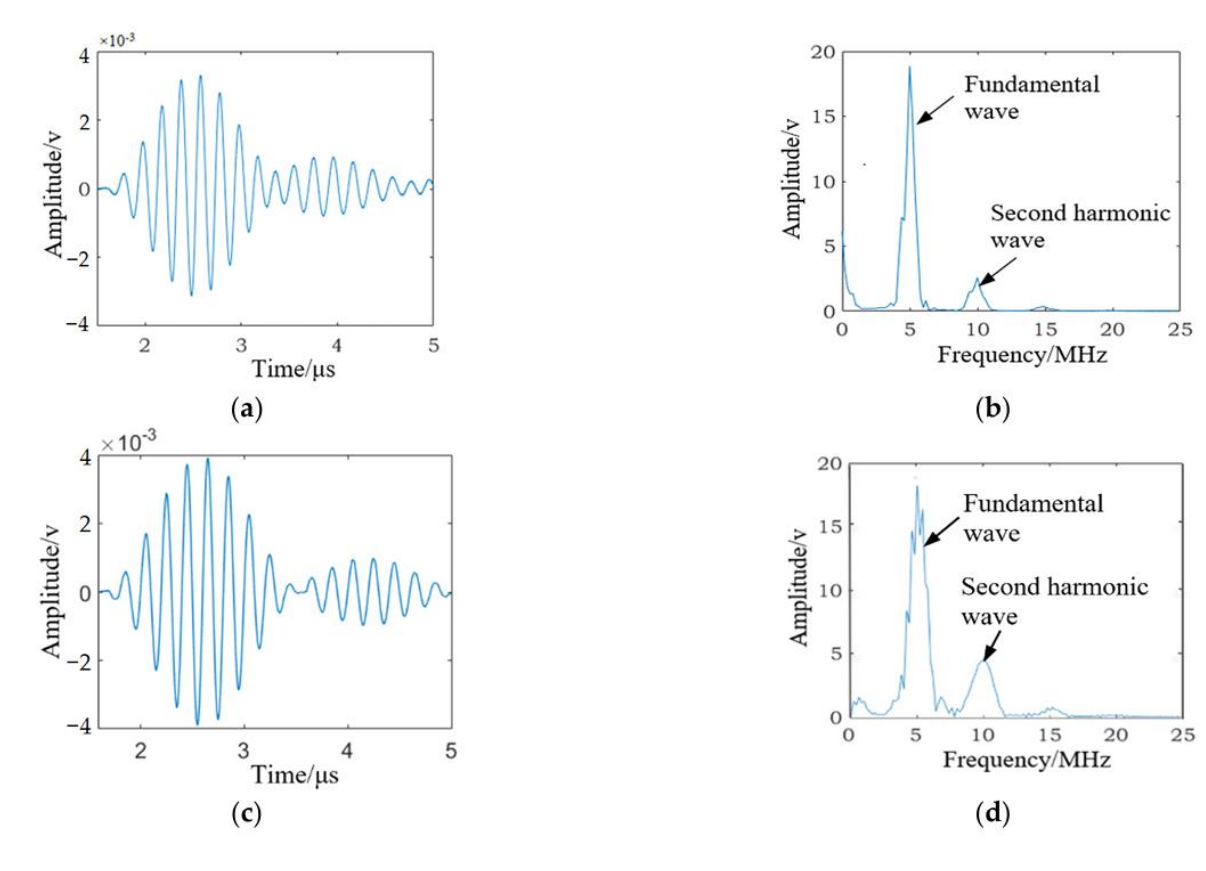


Figure 2-31. The SLM316Lstainless steel specimen subjected to different fatigue cycles. (a) The received time-domain signal subjected to 10,000 fatigue cycles. (b) The frequency spectra of the received signal subjected to 10,000 fatigue cycles. (c) The received time-domain signal subjected to 50,000 fatigue cycles. (d) The frequency spectra of the received signal subjected to 50,000 fatigue cycles [108]

SEM and TEM analyses confirmed these trends by revealing a microstructural evolution from planar dislocations to dislocation walls and eventually crack formation. The study highlighted the "breathing effect", where ultrasonic waves cause microcracks to open and close under alternating stress, further amplifying nonlinear wave interactions. This phenomenon significantly contributed to harmonic wave generation, making it an effective indicator of fatigue progression.

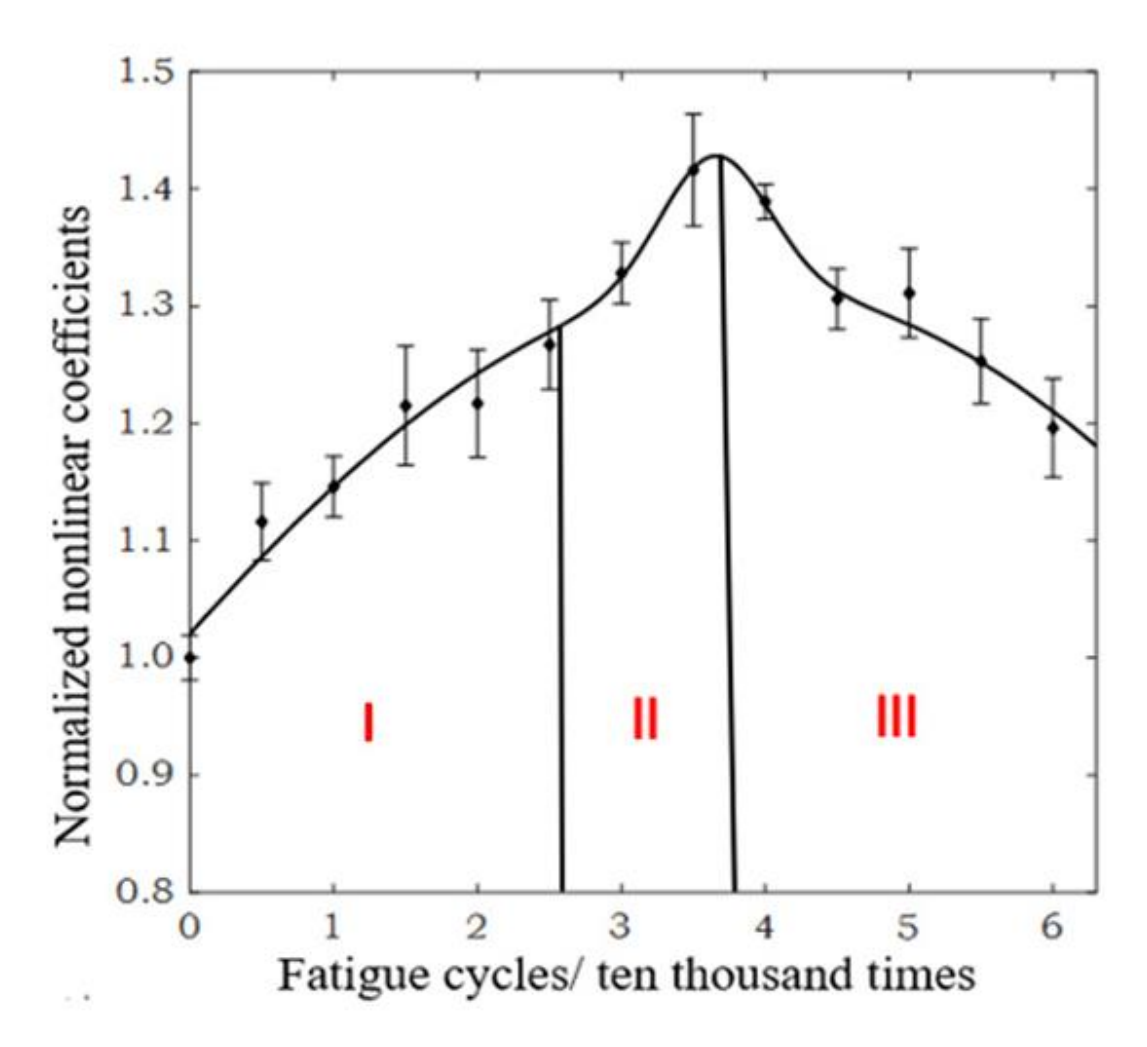


Figure 2-32. The normalized ultrasonic nonlinear coefficients vary with the fatigue cycles [108]

The study concluded that nonlinear ultrasonic harmonic generation is a reliable non-destructive tool for tracking fatigue damage in SLM metals.

Based on the reviewed studies, it is evident that nonlinear ultrasonic techniques—particularly second harmonic generation—are highly effective for detecting early-stage fatigue damage across a range of metallic materials, including conventional steels, stainless steels, nickel-based superalloys, and selectively laser melted (SLM) alloys. The consistent correlation between the nonlinear parameter β and microstructural features such as dislocation multiplication, wall and cell formation and microcrack initiation strongly supports the applicability of this method for tracking fatigue progression from its earliest stages. These findings align closely with the objectives of this research, which aims to identify non-invasive and highly sensitive methods for early fatigue damage detection in 316L stainless steel under high-cycle fatigue. Therefore, the nonlinear ultrasonic parameter method is considered highly suitable for this study, and in the following chapters, a more detailed explanation of the fundamental principles, experimental setup and implementation of this method will be provided.

2.4 Conclusion on chosen NDT methods: Justification for electrical resistivity and nonlinear parameters:

Among numerous methods reviewed, it became evident that while several techniques offer significant insights into fatigue behaviour, not all are equally suited for early damage detection. Surface investigation methods (hardness-based techniques) have demonstrated their utility in monitoring surface plasticity and deformation during fatigue damage. Techniques such as Vickers and Brinell hardness tests have been widely used to assess microhardness changes and localized plasticity in the surface layers of metals. However, a significant limitation of these methods is their confinement to surface-layer damage, which may not fully represent the fatigue behaviour of the entire component. Furthermore, the requirement for polished specimens prior to testing introduces a key discrepancy regarding their classification as truly non-destructive. Polishing removes a portion of the surface material, potentially altering the microstructural features that are critical for fatigue damage analysis.

Electromagnetic radiation-based methods, particularly X-ray diffraction (XRD), excel in detecting residual stress, dislocation accumulation, and strain localization, making them effective for identifying early fatigue damage. However, these methods face several significant challenges. First, XRD and similar techniques are costly, not only in terms of equipment but also due to the need for highly specialized operators and maintenance. Furthermore, these methods are generally limited to crystalline materials, meaning they are not universally applicable to all material types. Another major drawback is their limited suitability for industrial applications—specifically for in-situ, real-time monitoring in operational environments and requires significant time for data collection. X-ray machine also needs to comply with the health & safety due to the use of ionising radiation in the X-ray diffractometer unit. XRD equipment is typically bulky, requires precise alignment, and is sensitive to vibrations and environmental disturbances, making it difficult to deploy in manufacturing or field settings. Consequently, while XRD offers high sensitivity and accuracy in laboratory conditions, its practicality in industrial fatigue monitoring remains constrained.

Thermographic methods, while effective for real-time monitoring and fatigue life prediction, are primarily suited for evaluating damage at the crack initiation stage, where the most significant thermal changes occur. However, detecting earlier microstructural changes—such as dislocation motion or slip band formation—remains challenging due to the relatively low levels of heat generated during these initial phases of fatigue. Additionally, thermographic methods are highly dependent on thermal boundary conditions and external environmental factors, such as ambient temperature and airflow, leading to inconsistencies in measurements, particularly in uncontrolled industrial environments. Based on the literature review, it is also evident that most of the work on thermographic methods has focused on fatigue life prediction rather than on detecting different stages of fatigue damage. Therefore, while these methods are valuable for crack detection and fatigue life assessment, their

broader application in early-stage damage detection and in-situ monitoring remains limited. Another limitation of these methods is that they primarily detect surface-level damages.

Positron annihilation spectroscopy (PAS) and magnetic methods like Barkhausen noise (BHN) have shown potential in detecting early microstructural changes. However, PAS is very sensitive to the type of material, meaning it works better with certain compositions than others, and it becomes less effective in later stages of fatigue when the damage is more advanced. Additionally, PAS is not commonly used in industrial applications because it requires complex, advance equipment and is difficult to apply in real-world settings or for insitu monitoring. Moreover, positron annihilation spectroscopy must comply with strict health and safety regulations related to radiation, as the method uses positron-emitting radioactive sources (such as ²²Na or ⁶⁴Cu), which produce ionizing radiation, including positrons and 511 keV gamma photons. On the other hand, BHN is only useful for ferromagnetic materials, limiting its range of applications. Since one of the main goals of this project is to develop methods that can be applied easily in industrial environments and potentially used in-situ, these limitations reduce the practicality of PAS and BHN for such purposes.

While AE has proven to be a valuable tool for detecting fatigue damage, several challenges still limit its broader application. One of the key difficulties lies in discriminating between various AE signal sources, such as signals generated by dislocation motion, crack initiation, crack growth, or even friction between contact surfaces. These events often produce overlapping or similar frequency content, making it difficult to isolate the specific damage mechanism responsible for each signal. Additionally, environmental and operational noise—from machinery, vibrations, or electromagnetic interference—can compromise signal clarity, especially in industrial settings. This reduces the signal-to-noise ratio and makes reliable interpretation more difficult. To overcome these limitations, future research should focus on advanced signal processing techniques such as machine learning-based classification, time-frequency analysis, and pattern recognition to improve source identification and reduce false positives. Moreover, proper sensor placement, coupling, and calibration are essential for capturing accurate AE data, as incorrect sensor orientation or poor coupling may lead to signal attenuation or missed events.

Table 2-2 summarizes the advantages, limitations, best applications and smallest detectable defect size (in terms of order of magnitude) of each reviewed method. Base on this table and explained reasons, nonlinear ultrasonic (NLU) technique and electrical resistivity (ER) measurement emerged as the most promising techniques for early fatigue damage detection.

Table 2-2. Comparative Summary of NDE Methods [109 –113]

NDE Method	Advantages	limitations	Best application	Smallest detectable
				defect size
Surface Investigation methods	Simple and sensitive to surface plasticity	-Limited to surface layer -Requires polished surface	-Surface deformation and persistent slip marking band detection	~ 1μm
X-Ray Diffraction (XRD)	Highly sensitive to dislocation density and residual stresses	-Expensive equipment -Limited to crystalline materials -Less practical for insitu and industrial applications	Residual stress and dislocation density monitoring	~ 5-10 μm
Thermographic Methods	Real-time monitoring, non-contact, effective in detecting microcrack formation	-Affected by thermal boundary conditions -Load frequency dependent, -Mostly suited for fatigue life prediction not detailed damage stages detection	Fatigue life prediction and crack initiation detection	100-300 μm
Positron Annihilation Spectroscopy (PAS)	High precision in detecting early microstructural changes	-Limited to early stages and laboratory based -Not applicable in industry -Requires complex equipment and expert analysis	Early microstructural fatigue damage detection	~ 1 nm
Magnetic Methods	Sensitive to dislocations, grain boundaries, inclusions	Effective only for ferromagnetic materials	Fatigue damage detection in ferromagnetic materials	~ 10 μm
Acoustic Emission (AE)	Real-time monitoring, sensitive to microcrack nucleation and dislocations	-Requires advanced signal processing and proper sensor placement	Real-time fatigue damage monitoring in metals	~ 10 μm
Nonlinear Ultrasonic (NLU)	Sensitive to dislocation density, early microstructural changes	-Complex signal interpretation -Requires calibration and specialized equipment	Early fatigue damage detection and microstructural monitoring	~ 100 nm
Electrical Resistance (ER)	High sensitivity to microstructural changes, early crack detection	-Influenced by temperature -Requires proper calibration	Early fatigue damage detection and life prediction	~ 1-10 μm

Next chapters, a more comprehensive review of electrical resistivity (ER) and nonlinear ultrasonic (NLU) methods will be provided. These methods were selected based on their high sensitivity to microstructural changes, including dislocation accumulation and slip band formation, which are critical for detecting fatigue damage before crack initiation. The challenges associated with these techniques will be thoroughly discussed. Furthermore, strategies and methodologies to overcome these challenges will be explored to enhance the accuracy, reliability and industrial applicability of these methods. This detailed analysis will lay the groundwork for the experimental framework presented in subsequent chapters, where the integration of ER and NLU techniques will be investigated for fatigue damage detection.

Chapter 3. Electrical resistivity (ER) method

3.1 Introduction

Based on the literature review and the objectives of this study, one of the non-destructive evaluation techniques employed is the measurement of electrical resistivity during the early stages of fatigue. This chapter begins by outlining the fundamental physical principles of electrical resistivity, followed by a detailed discussion of the challenges and error sources commonly encountered in resistivity measurements. Then techniques and strategies used to eliminate these errors are introduced, including both instrument-based and methodological approaches. Furthermore, a comparative analysis of error magnitudes is presented to identify which sources contribute most significantly to measurement uncertainty. Finally, examples of error correction methods applied in previous fatigue and metallurgical studies are provided to demonstrate their practical relevance and to relate this work to the broader context of materials research.

3.2 Fundamental principle of electrical resistivity

Electrical resistivity ($\rho(\Omega \cdot m)$) is a fundamental material property that describes how strongly a material resists the flow of electric current. It is defined by the equation 3-1[114]:

$$p = R \cdot \frac{A}{l}$$

where electrical resistance ($R(\Omega)$) is the measured resistance. It is calculated using Ohm's Law, $R = \frac{V}{I}$, where V is the applied voltage in volts (V) and I is the current in amperes (A), A is the cross-sectional area in square meters (m²), and L is the length of the material through which the current flows in meters (m). The physical origin of resistivity lies in the scattering of conduction electrons by various features within the material. In pure metals, electron scattering is primarily due to phonons (lattice vibrations), especially at elevated temperatures. However, in real engineering materials, microstructural features such as dislocations, grain boundaries, second-phase particles, solute atoms, and precipitates act as additional electron scattering centres, leading to a measurable increase in resistivity. Dislocations disrupt the regular lattice, producing localized strain fields that scatter electrons. Grain boundaries act as barriers to electron flow, particularly in fine-grained or deformed metals. Second phases and precipitates introduce compositional and structural discontinuities, contributing to resistivity increases. Solute atoms create local distortions in the crystal lattice and increase scattering, especially in solid solution-strengthened alloys. These structural features evolve during plastic deformation and fatigue, making resistivity highly sensitive to microstructural changes [29].

3.3 Error sources in electrical resistivity measurements

Several models and techniques have been proposed for measuring electrical resistivity, each varying in precision and suitability depending on factors such as contact resistance, sample

geometry, and material type (e.g., single crystal, thin film, powder pellet, or small crystallite). Among the commonly used methods, the two-probe technique is typically applied to high-resistance materials—those with resistivity values above $10^4~\Omega\cdot\text{cm}$, such as certain ceramics and insulators. In contrast, the four-probe technique is more accurate for low-resistance materials—generally below $10^{-2}~\Omega\cdot\text{cm}$ —such as metals and highly conductive materials, as it minimizes errors caused by lead and contact resistance[29].

A typical DC measurement method is based on Ohm's Law, which states that V=IR where V is the voltage, I is the current and R is the resistance. In practice, to measure resistance, the method involves applying a DC stimulus current to the sample and measuring the resulting DC voltage drop across it. But in practice, this is not as straightforward as it is in theory. Low-resistance measurements are subject to numerous sources of errors and noises, which are discussed further.

One of the sources of error is common-mode current which happens when there's a difference in voltage between the instrument's ground (LO terminal) and the building's ground (earth). This difference causes a small unwanted current to flow between them which can also affect low-resistance measurement accuracy. Similarly, lead resistance in a twoprobe setup can contribute to significant error, while contact resistance, especially when it becomes non-ohmic due to surface contamination or oxidation, can further distort results. Another error is device heating, the applied current during measurement can heat the device, causing its resistance to change—especially if the material has a significant temperature coefficient of resistance, which refers to the rate at which a material's resistance changes with temperature. For materials with a high positive temperature coefficient (e.g., metals), resistance increases with temperature, while materials with a negative coefficient (e.g., some semiconductors) show decreasing resistance as temperature rises. Moreover, offsets in the chosen instrument's voltmeter input circuit are another source of error. This is a type of 1/f noise (also known as drift noise), which refers to a form of electronic noise whose power spectral density is inversely proportional to frequency (f). In other words, the noise becomes more significant at lower frequencies. This type of noise arises due to imperfections in the voltmeter's internal circuitry, leading to an inherent input offset that can directly add to the measured voltage and distort the resistance calculation.

There are also some errors that are from external sources like offsets generated by Rectification of Radio Frequency Interference (RFI). The reason for this type of error is high-frequency signals from external sources (e.g., nearby electronic equipment) can be rectified by non-linear elements in the measurement circuit, producing DC offsets and leading to incorrect resistance readings. Another external source of errors are magnetic fields and ground loops that can interfere with low-resistance measurement accuracy. Magnetic field error occurs when nearby magnetic fields induce unwanted voltages in the measurement wires, especially if the wires form loops like two probe method. Ground loop error happens when there are multiple grounding paths in the circuit, resulting in small circulating currents

that interfere with the measurement. These can be minimized through shielding, proper grounding, and reducing loop areas in the measurement setup.

Noise refers to any unwanted signal that interferes with the desired measurement or causes fluctuations between data points over time. In electrical measurements, noise can significantly affect accuracy, particularly in low-resistance applications. It typically consists of three main components:

- 1. 1/f Noise (Drift Noise): This low-frequency noise arises from DC offset voltages and is often caused by imperfections in electronic components or slow-changing thermal effects.
- 2. White Noise (Johnson or Thermal Noise): This is a random, unpredictable noise with a Gaussian distribution, caused by the thermal agitation of electrons in a conductor. Even in the absence of current, the natural motion of electrons due to temperature generates small voltage fluctuations.
- 3. Thermoelectric voltage/Thermoelectric EMFs (Electromotive Forces): These offsets are produced by temperature differences at junctions of dissimilar metals—commonly found at connections between leads and the device under test. Thermoelectric voltages can be particularly problematic in low-resistance measurements, as they may be of similar magnitude—or even larger—than the actual signal voltage. Small thermal voltages, often in the range of a few microvolts, can result from minor temperature gradients in the test setup, such as those caused by fluctuating ambient conditions or air drafts near sensitive components.

By addressing these error sources with the appropriate techniques, low-resistance measurements can be made more accurate and reliable. In the following, methods to specifically address these errors and more detail about each error is discussed [115].

3.3.1 Elimination of thermoelectric voltage

One of difficulty during measuring low resistance is thermoelectric voltages (thermoelectric EMFs) which can cause error offset and drift in voltage readings. In the past, it was possible to increase the test current until the response voltage of the device under test became much larger than the errors. This approach is no longer viable. Increasing the test current can lead to device overheating, altering its resistance, or even damaging it. The crucial factor for achieving accurate and consistent measurements is to eliminate the error. There are three measurement techniques that can be used to overcome this unwanted offset: the current-reversal method, delta mode, and the offset-compensated ohms method. More information about each method is provided below [115, 116].

3.3.1.1 Current-reversal method

The current-reversal method helps overcome this issue by applying current in opposite directions and averaging the resulting voltage measurements to cancel out the thermoelectric

EMFs. In this method, a known current is first applied in one direction (positive polarity), and the resulting voltage (V_{M+)} across the device under test (DUT) is measured. This measured voltage includes two components, the thermoelectric voltage (V EMF) caused by temperature gradients and the true voltage (IR) across the DUT due to the applied current. Next, the current polarity is reversed (negative polarity), and the voltage (V_{M-}) is measured again. In this case, the thermoelectric voltage remains unchanged, but the voltage due to the current (IR) has the opposite sign. The two voltage measurements are then combined by averaging them, which effectively cancels out the thermoelectric EMFs since they are independent of current direction. The resulting averaged voltage is in Figure 3-1. This leaves only the true voltage across the DUT, which can be used to accurately calculate the resistance using Ohm's law (R= V_M/I). For the current-reversal method to be effective, it is essential that the voltmeter used has a fast response time, ideally faster than the thermal time constant of the DUT. If the response time is too slow, changes in the thermoelectric voltage during the measurement process may not be fully cancelled, resulting in residual errors. Additionally, using a low-noise voltmeter further enhances the accuracy of the method by reducing random noise in the measurements.

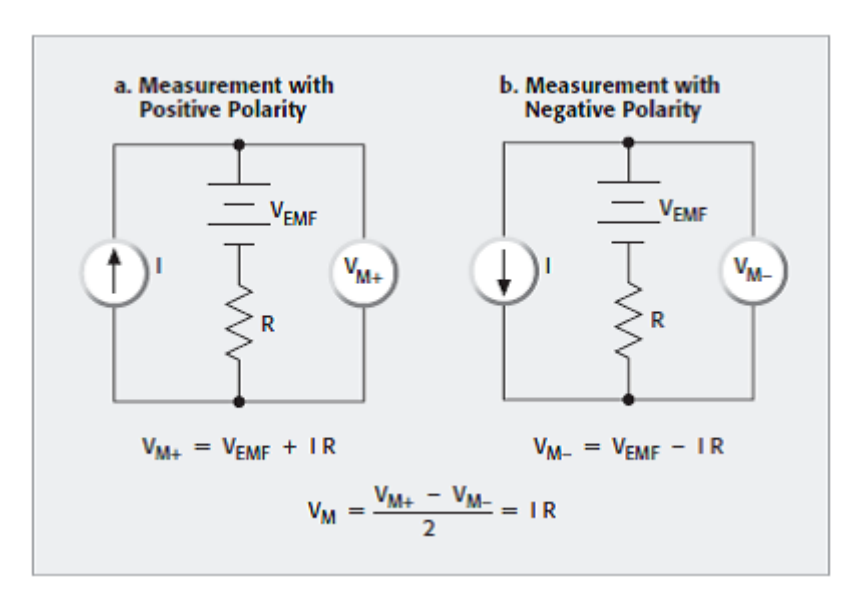


Figure 3-1. Illustration of the Current-Reversal Method for Cancelling Thermoelectric EMFs. (a) Measurement with positive current polarity. (b) Measurement with negative current polarity [116]

3.3.1.2 Offset compensated ohms method

The offset-compensated ohms method is an effective technique for cancelling thermoelectric offsets (V_{EMF}) in low-resistance measurements, ensuring high precision. This method, commonly built into advanced instruments like Keithley Source Meters (e.g., Models 2450, 2460, and 2461), alternates between applying a fixed source current and no current during the measurement cycle. This approach allows the thermoelectric voltage to be isolated and subtracted, leaving only the true voltage across the device under test (DUT). How the method works is based on the following steps. First a fixed source current (I) is applied to the device under test (DUT) and the resulting voltage (V_{M1}) is measured which includes two components [115, 116].

 $V_{M1}=V_{EMF}+IR$ 3-2

Then the source current is set to zero and the voltage is measured. In this state, the only voltage is thermoelectric EMF:

$$V_{M2}=V_{EMF}$$
 3-3

The thermoelectric voltage measured in latter step is subtracted from the voltage measured in first step.

$$V_{M}=V_{M1}-V_{M2}$$
 3-4

Substituting the expressions for V_{M1} and V_{M2} is as follows:

$$V_{M}=(V_{EMF}+IR)-V_{EMF}=IR$$
 3-5

Once the true voltage is obtained, the resistance calculated using Ohm's law:

$$R = \frac{V_{M}}{I}$$

This process cancels out thermoelectric offset, providing precise resistance value. Figure 3-2 shows the offset-compensated ohms method.

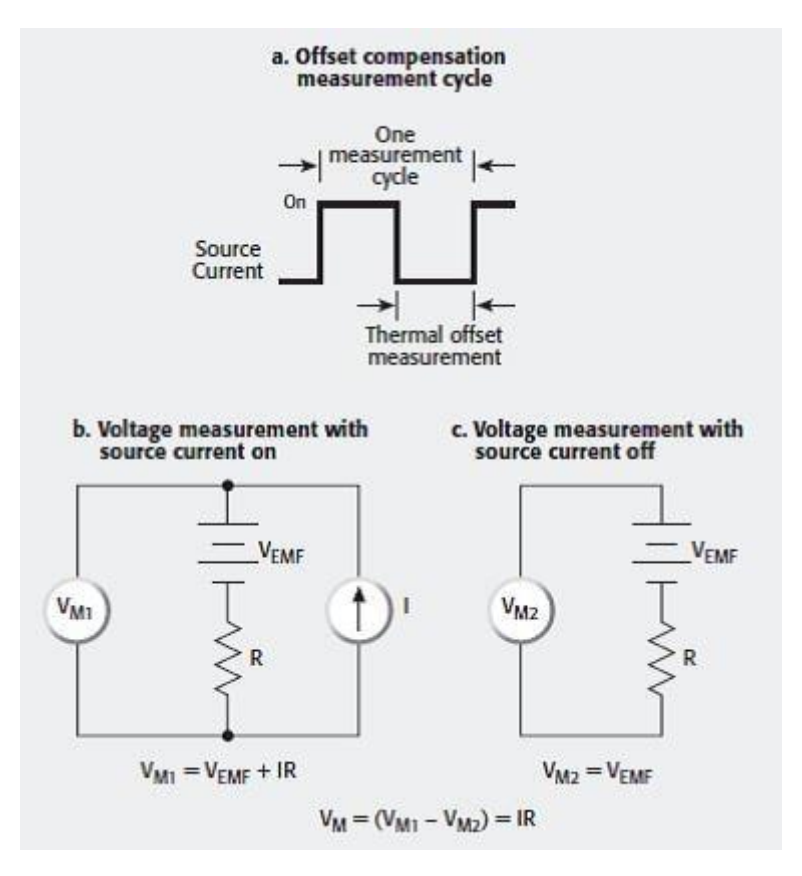


Figure 3-2. Offset-Compensated Ohms Method. (a) The measurement cycle alternates between applying a source current and measuring thermal offsets. (b) With the source current on, the measured voltage includes both the thermoelectric offset and the true voltage. (c) With the source current off, only the thermoelectric offset is measured. Subtracting cancels the thermoelectric offset, leaving the true voltage for accurate resistance calculation [116]

3.3.1.3 Three step delta mode (Three-point current reversal technique)

While the other two methods effectively cancel constant offsets, the delta method uses three voltage measurements per cycle to better handle fluctuating thermoelectric voltages. This makes it ideal for achieving precise results in unstable thermal environments. The delta method is more accurate than the offset-compensated or current-reversal methods when thermoelectric voltages are changing during the measurement cycle.

As it is known in Figure 3-3 the thermal voltage plot demonstrates the fluctuating nature of thermoelectric voltages over time, which arise from temperature gradients and drift within the measurement system. This figure shows specific region where the thermoelectric drift follows a linear trend, illustrating the behaviour that can be approximated and compensated for using the three-step delta method. This linear approximation is crucial because it allows for the effective cancellation of both constant thermoelectric offsets and linearly changing voltages. By alternating the test current quickly and taking precise voltage measurements, the slope (rate of change) of the thermal drift can be accurately calculated and removed.

How delta mode works is first a known current is applied to DUT with alternating polarity. Thermoelectric voltages can be cancelled by taking voltage measurements at both positive and negative test currents, a process known as a delta reading. At each polarity change, voltage measurements (V_{M1} , V_{M2} , V_{M3}) are taken. Each voltage measurement includes a constant thermal offset (V_{EMF}), caused by thermoelectric effects, a linearly changing voltage offset (δV) as shown in Figure 3-4 , caused by slow thermal drift in the circuit and the true voltage drop (IR) across the DUT. For the linear approximation to be valid, the current source must alternate quickly, and the voltmeter must make accurate voltage measurements within a short time interval. If these conditions are met, the three-step delta technique yields an accurate voltage reading of the intended signal unimpeded by thermoelectric offsets and drifts. Finally, by taking three voltage measurements and applying a moving average, the delta method cancels out the constant thermoelectric offset, the linearly changing thermal drift offset (δV), and the final averaged result provides the true voltage (IR) across the DUT[116, 117].

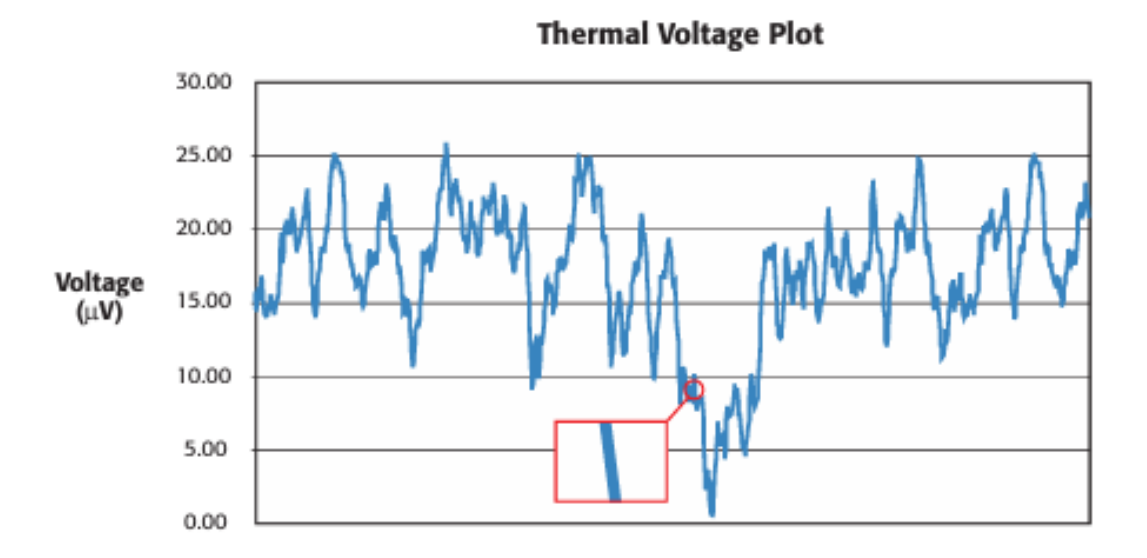


Figure 3-3. Thermal Voltage Plot showing fluctuations and linear drift in thermoelectric voltages [117]

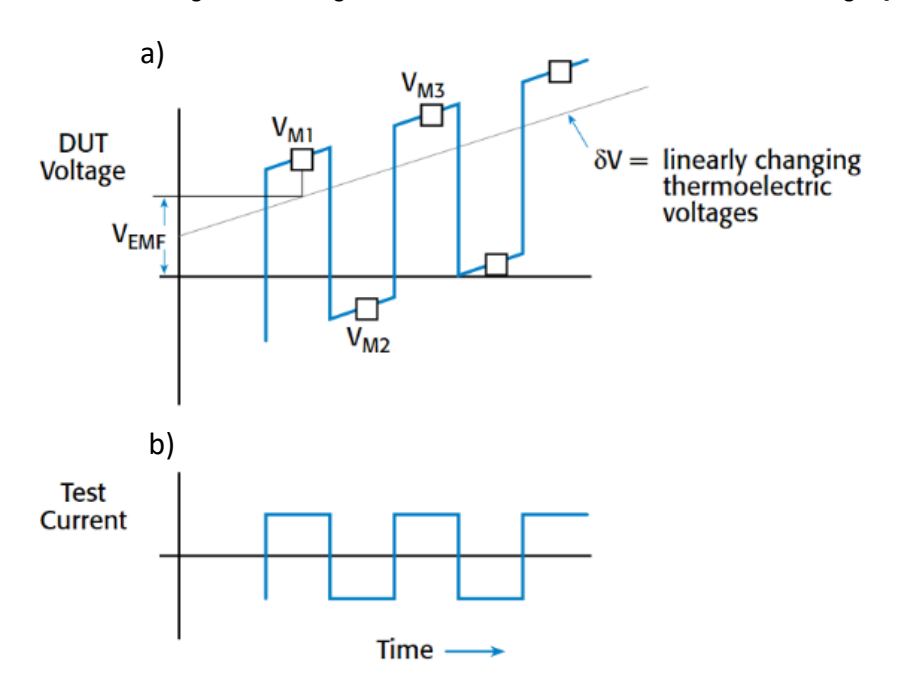


Figure 3-4. Delta Mode Measurement Process. (a) Thermal effect is considered. (b) no thermal effects are present [115]

Calculations for this measurement are as follows:

$$V_{M1} = V_1 + V_{EMF}$$
 3-7

$$V_{M2} = V_2 + V_{EMF} + \delta V \tag{3-8}$$

$$V_{M3} = V_3 + V_{EMF} + 2\delta V 3-9$$

where: V_{M1}, V_{M2}, and V_{M3} are voltage measurements

 V_{M1} is presumed to be taken at time = 0

V₁, V₂, and V₃ are the voltage drop of the DUT due to the applied current

 V_{EMF} is the constant thermoelectric voltage offset at the time the V_{M1} measurement is taken δV is the thermoelectric voltage change

Both the thermoelectric voltage offset (V_{EMF})and the thermoelectric voltage change (δV) can be eliminated through mathematical calculations involving three voltage measurements. First, take one-half the difference of the first two voltage measurements and call this term V_A :

$$V_{A} = \frac{(V_{M1} - V_{M2})}{2} = \frac{V_{1} + V_{EMF} - (V_{2} + V_{EMF} + \delta V)}{2} = \frac{(V_{1} - V_{2})}{2} - \frac{\delta V}{2}$$
 3-10

Next, calculate V_B by taking half the difference between the second (V_{M2}) and third (V_{M3}) voltage measurements.

$$V_{B} = \frac{(V_{M3} - V_{M2})}{2} = \frac{(V_{3} + V_{EMF} + 2\delta V) - (V2 + V_{EMF} + \delta V)}{2} = \frac{(V_{3} - V_{2})}{2} + \frac{\delta V}{2}$$
 3-11

The final voltage reading is the average of V_A and V_B and is calculated as follow:

$$V_{Final} = \frac{(V_A + V_B)}{2} = \frac{V_1 + V_3 - 2V_2}{4}$$
3-12

For linear devices:

 $|\mathbf{v}_1| = |\mathbf{v}_2| = |\mathbf{v}_3| = \mathbf{v}_R$ = voltage across resistor induced by stimulus current

Thus:

$$v_1 = \frac{1}{4}(4v_R) = v_R$$
 3-13

Note that both the V_{EMF} and δV terms are eliminated in the final voltage calculation. To understand the calculations better there is an example in appendix A.

The delta mode technique is the best choice for high-accuracy resistance measurements. Figure 3-5 compares 1000 measurements of a $100-\Omega$ resistor made with a 10-nA test current taken over approximately 100 s. In this example, the rate of change in thermoelectric voltage is no more than 7 V/s. As shown, the current-reversal technique fluctuates 30% as the thermoelectric error voltage drifts. In contrast, the delta mode technique has much lower noise [118, 119, 120].

1000 Delta Resistance Readings 100 Ω Resistor, 10nA Source Current Max. Thermal Voltage Rate of Change $< 7\mu V/s$

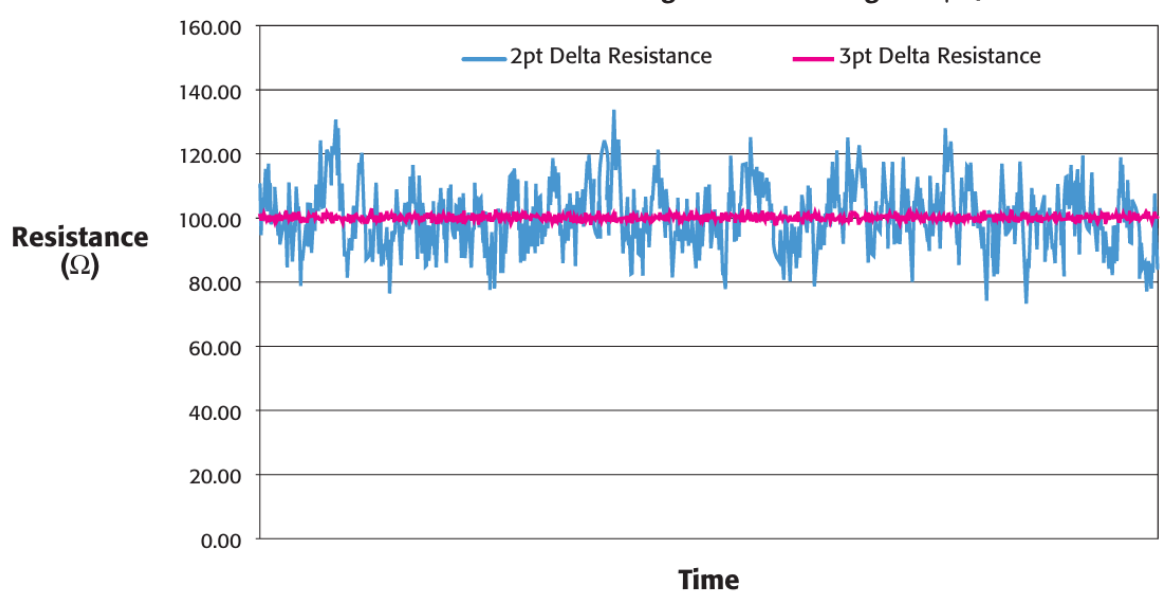


Figure 3-5. Comparison of current reversal and delta mode techniques accuracy measurements for 1000 measurements [120]

Even though the experiments in this project are conducted at room temperature in a controlled lab environment, minor temperature fluctuations can still occur due to HVAC systems. These small temperature changes can cause thermoelectric voltages in the circuit during the measurement process, leading to inaccuracies. Therefore, the use of delta mode is recommended for removing thermoelectric voltage for this project, as it provides greater accuracy.

3.3.2 Elimination of lead and contact resistance errors using the four-wire method

Measuring low resistance value around 1Ω or lower presents several technical challenges, one of the most significant challenges is lead resistance. Inaccurate results can occur because the resistance of the measuring leads(cables), adds extra resistance to the system. This issue is particularly problematic in the two-point method, where both current and voltage are measured through the same leads, making it impossible to avoid the impact of lead resistance on the measurement. As shown in the Figure 3-6, in the two-point method, the test current flows through both the measurement leads and the sample and the resistance (R) being measured. The meter measures the voltage across the resistance using the same test leads and calculates the corresponding resistance value. This causes the resistance of the leads (R_{LEAD}) to add to the measurement, leading to errors form the voltage drops across the leads, generated by the measurement current, can affect the accuracy of the reading, as the voltage measured by the voltmeter (V_M) may differ from the actual voltage across the test resistance (V_R). However, this error becomes significant only when the lead resistance is comparable to

the sample resistance. Since typical lead resistance ranges from 10 to 100 m Ω , it introduces minimal error when measuring specimens with resistances above 10 Ω . For instance, a 100 m Ω lead resistance contributes only 1% error when measuring a 10 Ω sample, and even less for higher resistances. Therefore, lead resistance primarily becomes problematic when dealing with very low-resistance samples (below 1 Ω), where the lead resistance may become a non-negligible fraction of the total resistance [121].

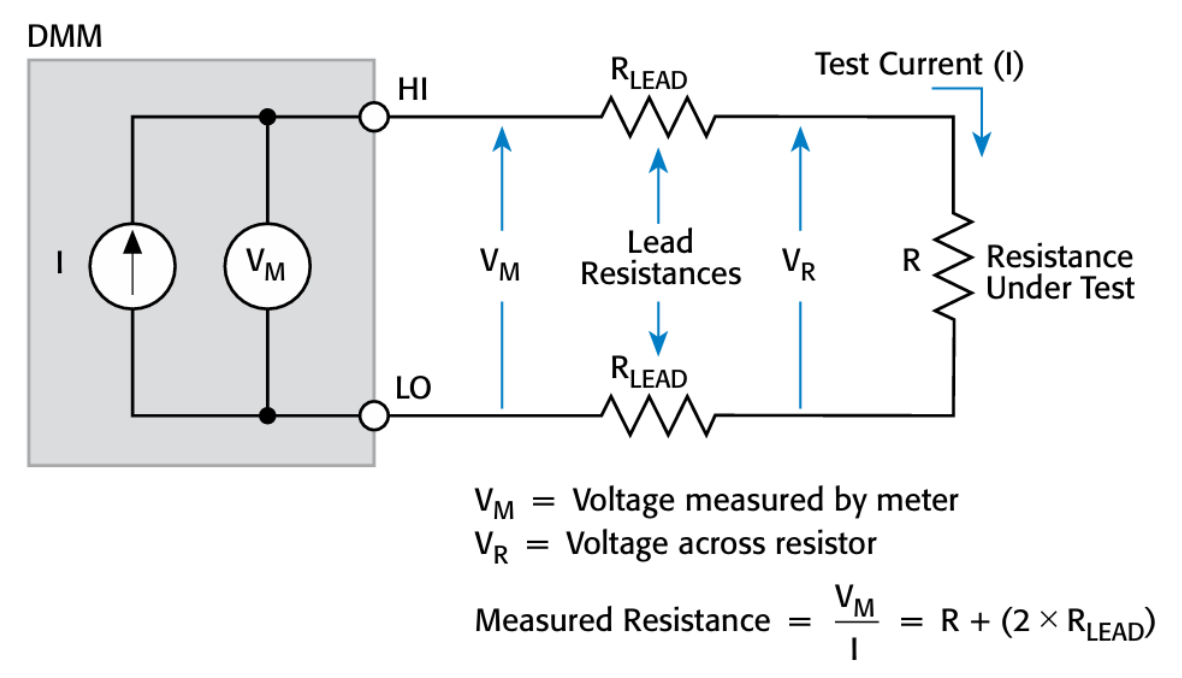


Figure 3-6. Effect of Lead Resistance in Two-Probe Low-Resistance Measurements [121]

To eliminate the effect of lead resistance, the four-point method with probes in co-linear configuration as shows in Figure 3-7 is recommended. The key aspect of this method is that it uses separate leads for carrying the test current and measuring the voltage drop, ensuring that the voltage measurement is not affected by the resistance of the current-carrying leads. As shown in the Figure 3-8, this setup, the test current (I) flows through the test resistance (R) using one pair of leads, while a separate pair of leads (the sense leads) measures the voltage (V_M) across the resistor. The current in the sense leads is very small near to 0.1 μA, allowing to ignore its effect on the voltage measurement. Since the voltage drop across the sense leads is negligible, the measured voltage (V_M) is nearly identical to the voltage across the resistor (V_R) [120, 122]. In the four-probe (Kelvin) configuration, the measurement system uses four separate terminals as shown in Figure 3-8. Source HI, Source LO, Sense HI, and Sense LO. The Source HI and Source LO terminals are responsible for supplying the test current through the sample. Source HI delivers the current into the high-potential end of the sample, while Source LO returns the current from the low-potential end, completing the circuit. In parallel, the Sense HI and Sense LO terminals are connected across the sample to measure the voltage drop independently of the current path. This separation is crucial because it ensures that the voltage measurement is not affected by the voltage drops across the current-carrying leads, which may have non-negligible resistance. Since the sense circuit draws an extremely small current—often in the nanoampere range—the voltage drop across the sense leads is negligible. This allows the voltmeter to accurately measure the voltage directly across the resistance under test, thereby improving precision in low-resistance measurements.

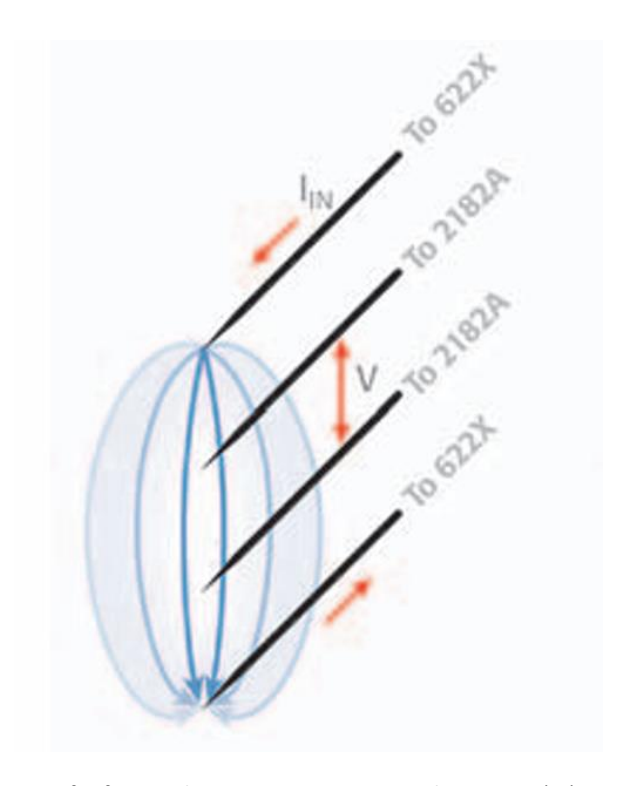


Figure 3-7. Co-linear configuration for four-probe measurement setup. The current (I_{IN}) is supplied using Keithley 622X source, while the voltage (V) is measured using a Keithley 2182A nanovoltmeter [122]

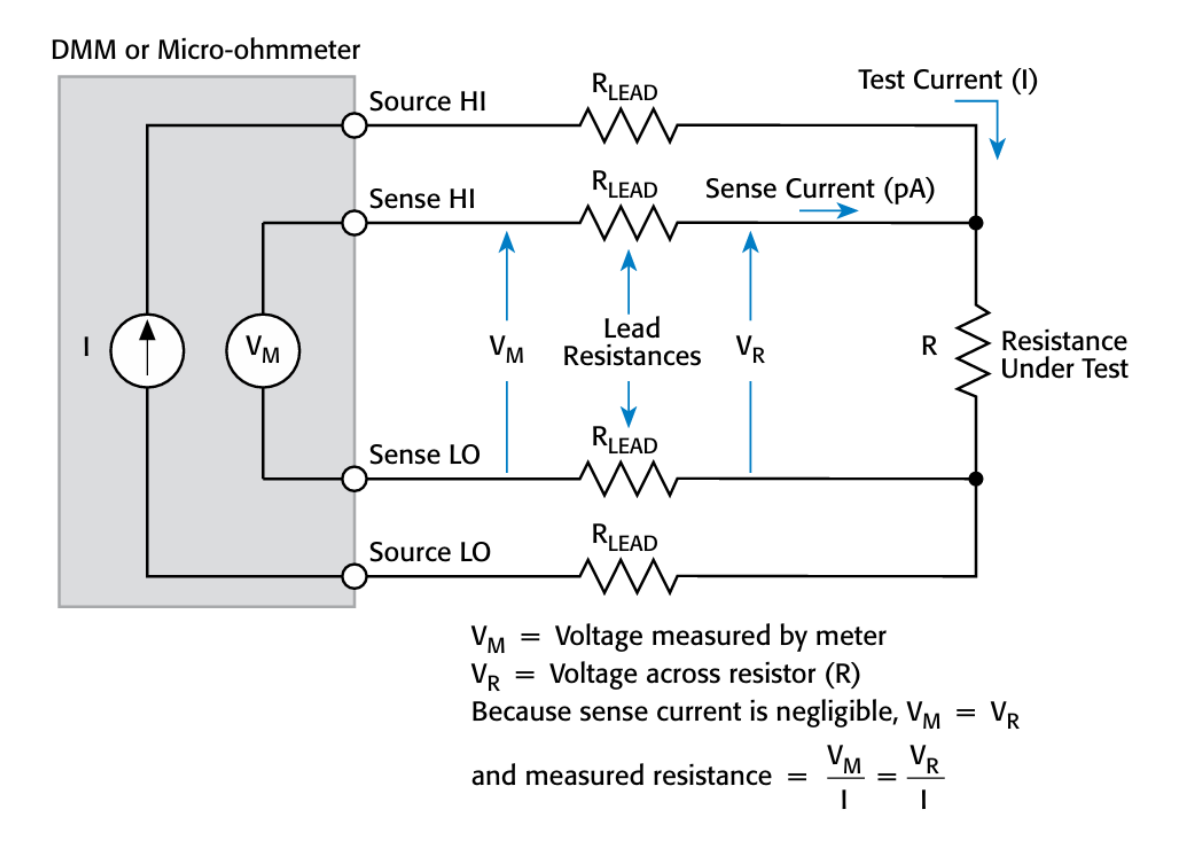


Figure 3-8. The four-wire (or Kelvin) connection method [121]

3.3.3 Elimination of non-ohmic Contact error

Non-ohmic contacts occur when the voltage across the contact between the measurement lead (or probe) and the test specimen does not increase proportionally with the current. This can happen due to oxide layers or other irregular connections in low-voltage circuits. They may also convert radio frequency signals into unwanted offset voltages, causing errors in the measurement. One method to check for non-ohmic contacts when using a digital mustimeter (DMM) to measure low resistances is by changing the measurement range on the DMM. When the range changes (e.g., from $m\Omega$ to Ω), the DMM also changes the test current it applies to the device under test (DUT) so the resistance reading should stay the same since the contact is ohmic (linear), regardless of the range or test current, but with different resolution (higher or lower precision). If the contact is non-ohmic (non-linear), the reading may change significantly because non-ohmic contacts behave differently depending on the current level. To check for non-ohmic contacts when using a separate current source and voltmeter to measure low resistances, current should be applied in both positive and negative directions (reverse the polarity) and observe the compliance voltage (the voltage required to maintain the set current). If the contact is non-ohmic, the compliance voltage will change significantly when the current polarity is reversed, indicating a problem with the current source's contact. Non-ohmic contacts in the voltmeter can rectify AC signals (like interference from external sources) and create a DC offset in the measurement, leading to incorrect resistance values. In this case, use the offset-compensated ohms method instead of the

current-reversal method is more effective. To better show the difference, a schematic V–I plot can be used (see Figure 3-9). An ohmic contact shows a straight-line V–I relationship (linear behaviour), while a non-ohmic contact shows curvature or asymmetry in the V–I plot, indicating current-dependent resistance behaviour. This method alternates between applying current and no current, allowing to measure and subtract the offset. Also, to prevent non-ohmic contact ensuring good contact quality, cleaning the contact surfaces to remove any oxide layers or contaminants that could introduce non-linear behaviour, applying consistent and sufficient pressure to the contact points to ensure a stable electrical connection and properly shield and ground the measurement setup to reduce AC pickup from external sources to minimize the risk of rectification at non-ohmic contacts is of high importance[119].

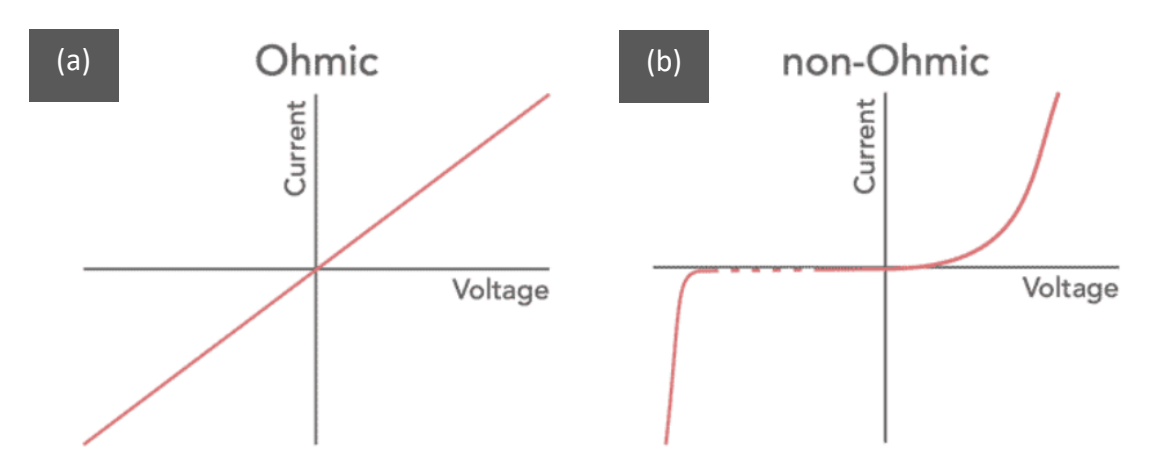


Figure 3-9. (a) Ohmic and (b) Non-Ohmic Conductors schematic [123]

3.3.4 Eliminating of device heating

Device heating is a significant consideration in low-resistance measurements, especially when working with temperature-sensitive devices such as thermistors, superconductors, or conductors with a high temperature coefficient. This phenomenon occurs due to power dissipation in the device under test (DUT) during the measurement process. Since low-resistance measurements typically require much higher test currents compared to high-resistance measurements, the resulting power dissipation (P=I²R) can lead to a noticeable increase in temperature. As the temperature of the DUT rises, its resistance may change, which introduces errors in the measurement and reduces the accuracy of the results. As the DUT's temperature increases, its resistance can also change, introducing errors and reducing measurement accuracy. For metals, this occurs because their electrical resistance generally increases linearly with temperature over a moderate range. This relationship is described by the equation 3-14 [75]:

$$R(T) = R_0 (1 + \alpha \cdot (T - T_0))$$
 3-14

where R(T) is the resistance at temperature T, R_0 is the resistance at reference temperature T_0 , and α is the temperature coefficient of resistance (TCR), typically a positive value for metals (e.g., around 0.003–0.006 °C⁻¹ for copper, aluminium, etc.). Therefore, even a modest

rise in temperature due to self-heating can lead to a measurable increase in resistance, resulting in an overestimation of the actual value if not properly compensated. For temperature-sensitive devices, even a slight increase in temperature can cause significant deviations in resistance, making device heating an important factor to address. In standard digital mustimeters (DMMs), the test current level is generally determined automatically by the selected measurement range and there is often no manual control over the current level. This limitation makes it difficult to prevent heating in the DUT during low-resistance measurements. Consequently, alternative methods must be employed to minimize the effect of device heating on the measurement. One effective approach is using the instrument's oneshot trigger mode, in which only a brief current pulse is applied to the DUT during the measurement cycle. This minimizes the total energy delivered to the DUT, thereby reducing the risk of heating errors. For example, the Keithley 2400 Source Meter allows current pulse widths as short as 100 microseconds, though typical durations for resistance measurements range from 1 to 10 milliseconds, which is sufficient for most single, high-precision readings with minimal thermal impact [119]. Another technique to mitigate device heating is offset compensation. In this method, the test current is applied for only 50% of the total measurement time. By alternating between periods when current is applied and periods when it is not, the total power dissipation in the DUT is reduced, which helps control the temperature rise. Offset compensation is particularly useful in applications where consistent current levels are required over longer periods, but heating needs to be minimized. Since accurate low-resistance measurements are critical to achieving the desired results, mitigating device heating is essential to ensure precision. Furthermore, if the DUT includes materials or devices with a high sensitivity to temperature, employing strategies such as one-shot triggering or offset compensation becomes even more important[119]. Table 3-1 shows a summary of methods to address these errors and the typical error magnitude.

Table 3-1.Error Sources and typical magnitudes in Low-Resistance Measurements and their Correction Methods [119, 120, 121, 124]

Error Source	Correction Method	Typical Error Magnitude
Thermoelectric	Use Current-Reversal	1–100 μV (may exceed signal voltage)
EMF Offsets	method, Delta mode or Offset	
	Compensated Ohms method	
RFI Rectification	Shielding, grounding, low-	~10 μV to several mV (environment-
	pass filtering	dependent)
Voltmeter Input Offsets	Proper Calibration	~1–100 μV depending on device specs
Johnson Noise	Minimize temperature	1–10 nanovolts of noise per VHz at
	fluctuations, use low and	room temperature
	controlled temperature	
	environments	
Magnetic Fields & Ground	Four probe, short leads,	1–10 nanovolts of noise per VHz
Loops	proper grounding	
Common-Mode Current	Choose an instrument with a	Up to several mV if poorly managed
	high CMRR (Common-Mode	
	Rejection Ratio) or use	
	differential measurement	
	techniques (which measure	
	only the difference between	
	two points and ignore	
	common signals)	
Lead Resistance	Use four-point measurement	10–100 mΩ, may cause >1% error for
	method	<1 Ω DUT
Non-Ohmic Contacts	Use the offset-compensated	Can cause 10–30% deviation from true
	ohms method ensuring good	resistance
	contact quality	
	Use high-quality contact	
	materials	
Device Heating	One-shot trigger mode	~0.3–0.6%/°C for metals
	Offset compensation	

According to Table 3-1 and magnitudes of errors, certain sources of error are particularly critical and large in low-resistance measurements and must be carefully controlled to ensure accurate results. Among these, thermoelectric EMF offsets, non-ohmic contacts, and device heating are the most significant. These issues are especially relevant when measuring low-resistivity materials such as 316L stainless steel, which has a typical resistivity of around 70–75 $\mu\Omega$ ·cm. In such cases, the magnitude of these errors can be comparable to—or even exceed—the actual signal voltage.

To address these major sources of error, this study employs a combination of the four-probe (Kelvin) method and the delta mode technique. The four-probe configuration effectively eliminates the influence of lead and contact resistance by separating the current and voltage paths. Meanwhile, the delta mode significantly reduces thermoelectric offsets and compensates for small thermal drifts that may occur during measurement. This combination

is particularly suited to high-accuracy low-resistance applications and has been implemented throughout the experimental procedures described in Chapter 5.

For the remaining error sources—such as Johnson noise, voltmeter input offsets, and common-mode currents—although their impact is generally smaller, they still require attention. These have been addressed in the methodology section, where it is explained how environmental parameters such as temperature have been stabilized, contact quality ensured through cleaning and consistent pressure, and electrical interference minimized using proper shielding and grounding. Together, these steps help to maintain stable and repeatable measurement conditions throughout the study.

3.4 Examples of error correction techniques in fatigue and metallurgical studies

To support the accurate low-resistance measurement techniques for this study, several recent studies have demonstrated the use of electrical resistivity monitoring in different metallurgical applications—each implementing specific error correction strategies regarding to their aim. Table 3-2 provides a summary of the alloys, types of deformation, error elimination techniques, and the measurement resolution achieved in these studies. In Rafefi's study [125], on CO2-induced corrosion of thin-film AISI 1010 carbon steel, a combination of the offset-compensated ohms and four-wire method plus thermal management (using watercooled copper blocks and thermal pads) was applied. This setup effectively mitigated thermoelectric offsets and reduced voltage noise to below 11 µV, enabling sub-micron resolution in metal loss detection. In another study, Saberi et al.[126], investigated the use of electrical resistivity (ER) as a tool for monitoring plastic deformation and strain in Aluminium 6062, Copper CW024A, and Steel DC04 during multiaxial tensile testing. Using a four-probe setup combined with magnetic flux sensors, Pt1000 temperature sensors, and digital low-pass Bessel filters, they maintained high thermal and electrical stability. Their system achieved $\mu\Omega$ level resolution and reliably detected up to 30% increases in ER correlated with plastic strain, validating the method as a sensitive and reliable approach for in-situ strain and damage monitoring. In a study by Nobile and Saponaro [127], fatigue behaviour of AISI 316L stainless steel was evaluated under cyclic loading. A high-precision four-probe method was used to eliminate lead and contact resistance. To further improve accuracy, the setup included surface insulation using glued tabs to prevent electrical interference, real-time temperature monitoring with three T-type thermocouples, and calibration of the thermal coefficient of resistance (0.002 m Ω /°C) to correct for resistance changes due to temperature fluctuations. With a 3000-mA test current, their setup achieved 0.004% accuracy and clearly resolved resistivity changes throughout fatigue life—capturing early damage (20-40%) and crack propagation stages (80-90%).

Table 3-2. Summary of the alloys, testing conditions, error elimination techniques, and measurement resolution achieved in different studies used electrical resistivity technique [125, 126, 127]

Study	Alloy/	Testing	ER error elimination	ER
	Material	condition	method	measurement
				accuracy
Rafefi	AISI 1010	CO ₂ -induced	Offset-compensated ohms;	<11 μV voltage
(2021)	carbon steel	corrosion (TLC	four-probe method; thermal	noise; sub-
	(thin film, 50	condition)	stabilization (cooling block +	micron metal
	μm)		thermal pads); current pulse	loss detection
			method	
Saberi et al.	Al 6062, Cu	Plastic	Custom four-probe method;	ER sensitivity
(2021)	CW024A, Steel	deformation	magnetic flux sensor;	~30%; μΩ range
	DC04 (sheet, 1	via uniaxial &	Pt1000 temp. sensor; digital	resolution
	mm)	plane strain	low-pass filter; surface	
		tension	cleaning	
Nobile &	AISI 316L	Fatigue under	Four-probe method; surface	μΩ accuracy
Saponaro	stainless steel	tension-	insulation; 3x T-type	
(2022)	(U-notched	tension	thermocouples; thermal	
	specimens)	loading	coefficient calibration and	
			correction	

3.5 Conclusion

Given that the present research focuses on early-stage damage detection, minimizing sources of measurement error is critical. A combination of techniques has been used in this study, including the three-step delta mode and the four-probe method, which together have proven effective in eliminating key sources of error such as thermoelectric voltages, lead resistance, and contact resistance. Additionally, thermal shielding and precision current control were employed to minimize further error sources, including device heating and temperature-induced offsets. This integrated approach enables our set-up to achieve $n\Omega$ level resolution, making it highly suitable for tracking microstructural changes during the initial stages of fatigue. Chapter Chapter 5 will provide a detailed discussion of the equipment requirements necessary to implement these techniques simultaneously.

Chapter 4. Nonlinear ultrasound testing

4.1 Principles of second harmonic generation for fatigue damage detection

Second Harmonic Generation (SHG) is a nonlinear ultrasonic technique used in this study to evaluate early-stage fatigue damage in metallic materials. The method is grounded in the physics of acoustic wave propagation and its interaction with microstructural features such as dislocations, precipitates, and voids, which can alter the local mechanical response of the material. The process begins with the generation of acoustic waves using a piezoelectric transducer, which converts electrical signals into mechanical vibrations at a specific fundamental frequency. These waves then propagate through the material, interacting with its internal microstructure. In an ideal, perfectly elastic (linear) medium, the wave travels without distortion and retains its original frequency. However, in materials used in practical applications, the presence of microstructural defects leads to dynamic nonlinear elastic behaviour—an effect that is not observed in quasi-static tensile tests, where stress-strain curves typically remain linear and appear to obey Hooke's Law. Under the influence of highfrequency ultrasonic waves, these defects interact with the stress field in a nonlinear manner, distorting the propagating wave and causing part of its energy to shift from the fundamental frequency to its harmonics—most notably the second harmonic. This phenomenon, referred to as spectral energy migration, is a direct indicator of nonlinear elastic behaviour and is particularly sensitive to subtle microstructural changes associated with early-stage fatigue damage. In this thesis, materials showing such dynamic nonlinear elastic responses under ultrasonic excitation are referred to as nonlinear materials. To describe this behaviour mathematically, the classical elastic wave equation is extended to include not only the linear elastic constants (such as Young's modulus, which governs the second-order, linear response), but also higher-order elastic constants (typically third- and fourth order). These nonlinear elastic constants are distinct from Young's modulus and are essential for modelling the additional complexity introduced by defect-induced nonlinearity. The intensity of second harmonic generation is quantified using the nonlinear acoustic parameter, commonly denoted as β , which serves as a valuable metric for characterizing material nonlinearity and fatigue damage. By solving the nonlinear wave equation, the second harmonic amplitude can be predicted and used for diagnostic purposes. This chapter provides a foundational overview of the theoretical concepts relevant to this research. It begins by introducing the mathematical formulations necessary for understanding wave propagation problems within the scope of this study. The discussion starts with the fundamental equations of motion for a linear, isotropic material, expressed in terms of displacement. The focus then shifts to plane harmonic waves propagating in a linear elastic medium, setting the stage for a deeper exploration of nonlinear effects. In the latter part of the chapter, the assumption of linear elasticity is dropped, and the fundamental principles of nonlinear wave propagation are introduced. Given that most of the equations presented are formulated in three-dimensional

space, different notations are used to ensure clarity. In some cases, it is more practical to express equations using vector notation, while in others, index notation proves to be more efficient. To maintain consistency and avoid confusion, vectors are represented using bold letters (e.g., **u**), whereas variables in index notation are written in regular letters with subscripts (e.g., u_i) [106, 128].

4.1.1 Equation of motion

This section presents the fundamental equations governing wave propagation in elastic solids. The derivation starts with the balance of linear momentum, which leads to Cauchy's equation of motion. Assuming the material is linear, homogeneous, and isotropic, the stress-strain relationship is defined by Hooke's law. This assumption allows the equations to be further simplified into the Naiver equations, which describe elastic wave behaviour and form the basis for analysing nonlinear wave phenomena.

4.1.1.1 Balance of Linear Momentum

A detailed derivation of the equations of motion and an in-depth introduction to linear wave propagation can be found in [129]. A brief overview is provided here to outline the physical and mathematical principles underlying wave propagation. The analysis begins with the balance of linear momentum for a body with volume V and surface S, subjected to both surface traction forces (t_i) and external body forces (f_i) per unit volume (as illustrated in Figure 4-1). This fundamental principle forms the basis for understanding how mechanical waves propagate through materials and interact with their internal and external environments [130].

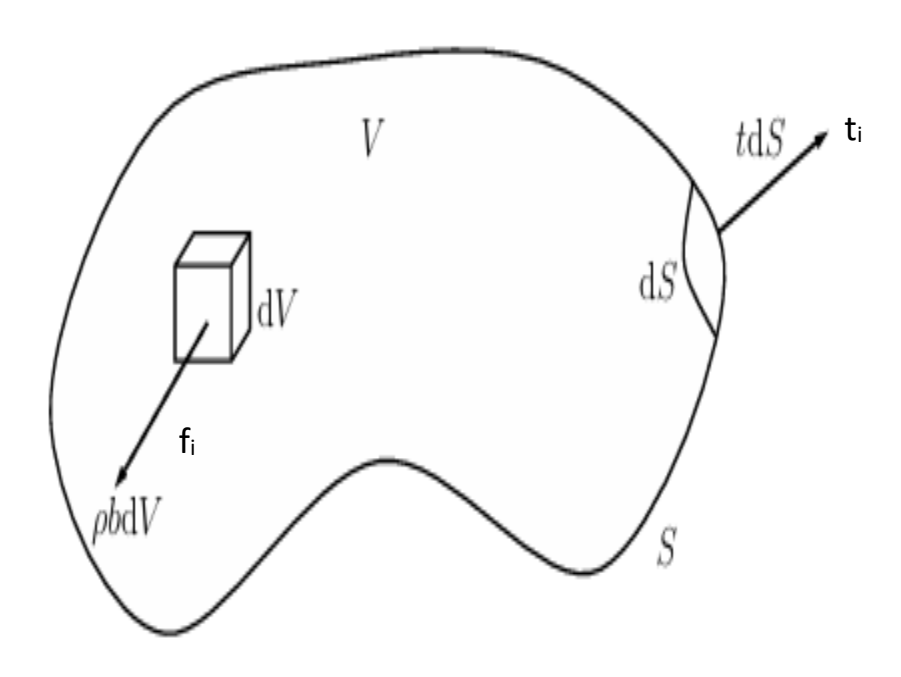


Figure 4-1. Momentum balance [130]

$$\int\limits_{S} t_{i} \, dS + \int\limits_{V} \rho f_{i} \, dS = \int\limits_{V} \rho \ddot{u}_{i} \, dV \eqno(4-1)$$

Here, ρ denotes the material density, and \ddot{u}_i represents the i-th component of the displacement vector, while t_i corresponds to the traction forces acting on the material's surface. To relate these surface forces to internal stresses, Cauchy's stress formula is applied, which expresses traction in terms of the stress tensor [130].

$$\mathbf{t_i} = \mathbf{\sigma_{ii}} \mathbf{n_i}$$
 4-2

 σ_{ij} is the stress tensor and n_j is the j-th component of the outward normal vector. Gauss' theorem is applied to convert the surface integral into a volume integral. This transformation leads to the volume form of the balance of linear momentum, expressed as [130]:

$$\int\limits_{V}\left(\sigma_{ij,j}+\;\rho f_{i}-\rho\ddot{u}_{i}\right)=0 \tag{4-3}$$

Because this condition must be satisfied for any arbitrary volume element within the material, the integral form can be eliminated, yielding the local (differential) form of the equation of motion, commonly known as Cauchy's Equation of Motion [130]:

$$\left(\sigma_{ii\,i} + \rho f_i - \rho \ddot{\mathbf{u}}_i\right) = \mathbf{0} \tag{4-4}$$

For the remainder of this thesis, the body force f_i will be neglected to simplify the analysis. To express the equation of motion using displacement components and material properties, the material is assumed to be linear, homogeneous and isotropic. Under these conditions, the relationship between the stress σ_{ij} and strain ϵ_{ij} (ϵ_{ij} is the strain component in the i-th direction due to a displacement gradient in the j-th direction) and ϵ_{kk} (total volumetric strain) are related by Hooke's law [130].

$$\sigma_{ii,i} = \lambda \, \delta_{ii} \, \epsilon_{kk} + 2\mu \epsilon_{ii} \tag{4-5}$$

 λ and μ are Lamé's constants, which are material-specific elastic constants. strain is defined by:

$$\epsilon_{ij} = \frac{1}{2} \left(\mathbf{u}_{i,j} + \mathbf{u}_{j,i} \right) \tag{4-6}$$

Using Equations 4-5 and 4-6 to eliminate 4-4 and neglecting f_i, the Navier equation is obtained:

$$(\lambda + \mu)u_{i,ii} + \mu u_{i,ij} = \rho \ddot{\mathbf{u}}_{i}$$
 4-7

Or in vector form:

$$\mu \nabla^2 \mathbf{u} + (\lambda + \mu) \nabla \nabla \cdot \mathbf{u} = \rho \ddot{\mathbf{u}}$$
 4-8

These partial differential equations describe govern the propagation of waves within a solid material. To simplify the solution, the Helmholtz decomposition theorem is employed. According to this theorem, the displacement field u can be represented as a combination of scalar potential φ and vector potential φ , allowing the wave motion to be separated into longitudinal and shear components. This decomposition is expressed as:

$$\mathbf{u} = \nabla \mathbf{\Phi} + \nabla * \mathbf{\Phi}$$
 4-9

In this representation, $\nabla \Phi$ corresponds to longitudinal wave motion (also known as compressional waves) while $\nabla * \Phi$ accounts for shear wave motion (or transverse waves). To ensure the uniqueness of the solution, the divergence of the vector potential Φ must satisfy the following condition:

$$\nabla \cdot \Phi = 0$$

By substituting these potentials into 4-7, the system reduces to two uncoupled wave equations, each representing a distinct mode of wave propagation.

Longitudinal wave equation:

$$(\lambda + 2\mu)\nabla^2 \Phi = \rho \ddot{\Phi}$$
 4-11

And Shear wave equation:

$$\mu \nabla \cdot \Phi = \rho \ddot{\Phi}$$
 4-12

These equations independently describe the behaviour of compressional (longitudinal) and shear (transverse) waves in an elastic medium, facilitating the analysis of wave propagation in complex materials [130].

4.1.1.2 Linear Wave Propagation

A plane wave is defined as a wave which constant-phase surfaces are normal to the direction of propagation, represented by a unit vector p. While an ideal plane wave cannot be generated in practice, it provides a highly useful approximation for many real-world wave propagation scenarios. For instance, longitudinal waves emitted from a transducer with a flat surface such as those used in this research, closely resemble plane waves, assuming practically valid. This approximation significantly simplifies the mathematical analysis of wave propagation, which is why the derivations in this chapter are based on plane wave behaviour. Mathematically, the displacement field (u) in an elastic medium due to a plane wave propagating with velocity (c) in the direction of (p) as a function of time (t) can be expressed as [131]:

$$\mathbf{u} = \mathbf{f}(\mathbf{x} \cdot \mathbf{P} - \mathbf{c}\mathbf{t})\mathbf{d} \tag{4-13}$$

where x is the position vector in the medium, and f is an arbitrary function that defines the shape or profile of the wave. Substituting this equation into the Navier equation (4-8) results in the expression:

$$(\lambda - \rho c^2)d + (\lambda + \mu)(p.d) = 0$$
4-14

This equation can be satisfied under two distinct conditions:

1- Longitudinal Waves (P-Waves)

If $\mathbf{d} = \pm \mathbf{p}$ (i.e., the displacement direction is aligned with the wave propagation direction), the wave is classified as a longitudinal wave (P-wave). In this case, the wave velocity is given by:

$$c = c_l = \left(\frac{\lambda + 2\mu}{p}\right)^2$$

2- Shear waves(S-waves)

If **p·d=0** (i.e., the displacement direction is perpendicular to the wave propagation direction), the wave is classified as a shear wave (S-wave). Depending on the orientation of displacement: If the displacement remains in the propagation plane, it is called an SV-wave (shear vertical wave). If the displacement is perpendicular to the propagation plane, it is referred to as an SH-wave (shear horizontal wave). In both cases, the wave velocity is given by:

$$c = c_{T} = \left(\frac{\mu}{p}\right)^{2}$$

Since $c_L > c_T$ always holds, longitudinal waves propagate faster than shear waves.

3- Time-Harmonic Plane Waves

A specific category of plane waves is time-harmonic plane waves, for which the original equation for the displacement (2.13) written as [131]:

$$\mathbf{u} = \mathbf{Ad} \, \exp[\mathbf{i}\mathbf{k}(\mathbf{x} \cdot \mathbf{P} - \mathbf{c}\mathbf{t})] \tag{4-17}$$

where:

- A is the complex amplitude of the wave, independent of x and t.
- $k = \frac{w}{a}$ is the wave number.
- $w=2\pi f$ represents the angular frequency (f is the linear frequency, indicating how many complete cycles the wave undergoes per second).

This formulation expresses wave propagation in terms that directly incorporate both frequency and wave number, which is especially valuable for analysing wave interactions in elastic media. Up to this point, the discussion has assumed of an infinite, homogeneous medium with no discontinuities, allowing for simplified derivations of wave velocities and displacement fields. However, in real materials, when a wave encounters a discontinuity such as a boundary between two different media—new wave phenomena arise. At such interfaces, part of the wave is reflected, while the remaining portion is transmitted into the second medium. In the context of this study, the most relevant boundary condition is the interface between a metallic test sample and air, which functions as a free boundary. Due to the large contrast in acoustic impedance between the metal and air, nearly all the incident wave energy is reflected, and the transmitted energy into air is negligible. Therefore, refraction effects can be ignored in this scenario. When a longitudinal wave (P-wave) encounters a free boundary, it typically produces both reflected P-waves and shear vertical waves (SV-waves) as shown in Figure 4-2. The propagation angles of these reflected waves are governed by the angle of incidence θ_0 of the incident wave. A special case arrives when the wave hits the boundary perpendicularly ($\theta_0 = 0$) in this situation, only a reflected P-wave is generated, and no SV-wave is produced [130].

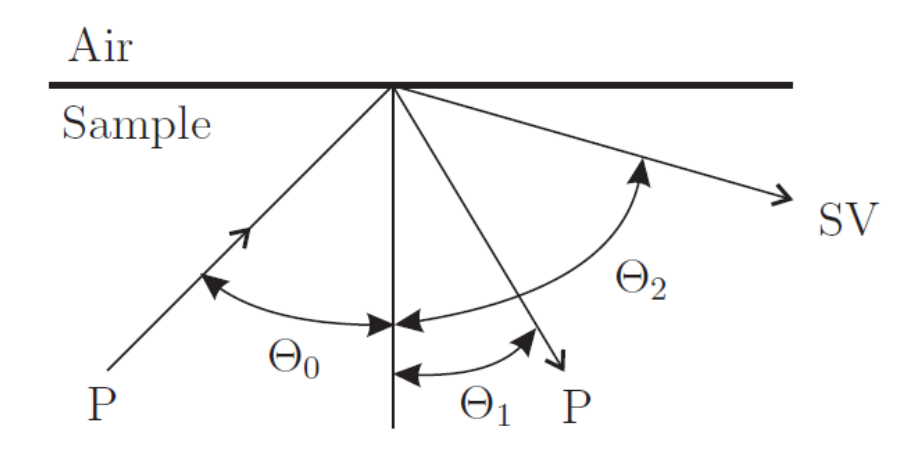


Figure 4-2. Reflection of a P-wave at a free boundary [130]

In this study, the transducers are consistently placed on two opposing parallel surfaces, which are configured to generate only longitudinal waves (P-waves). Consequently, the wave propagation within the test structure is limited to P-waves, as outlined in Table 4-1. Shear vertical waves (SV-waves) shows a similar reflection behaviour where both reflected SV-waves and P-waves can be generated upon interaction with a boundary. However, in the case of shear horizontal waves (SH-waves), the reflection behaviour is distinct. When an SH-wave encounters a boundary, it does not convert into other wave types; instead, only SH-waves continue to propagate, maintaining their original mode of motion.

Table 4-1. Angle relations for reflection at a free boundary [130]

incident P-wave	e reflected P-wave	reflected SV-wave
θο	$\theta_1 = \theta_0$	$\sin \theta_2 = \sin (c_T/c_L) \sin \theta_0$

4.1.1.3 Nonlinear Wave Propagation

Although linear wave theory is sufficient for most cases, there are specific cases where nonlinear approaches are necessary. A key application, which is central to this research, is the application of nonlinear acoustics for non-destructive evaluation. Of particular interest is the generation of higher harmonics because of material nonlinearity. In a nonlinear material, an initially pure wave with a single frequency ω undergoes distortion as it propagates. Consequently, the resulting signal is not limited to the original frequency ω but also contains higher harmonic components, which appear at integer multiples of the original frequency (such as 2ω , 3ω , etc.). This harmonic generation is crucial for detecting early-stage material damage, as the presence and intensity of these harmonics can provide insights into the microstructural changes within the material [131].

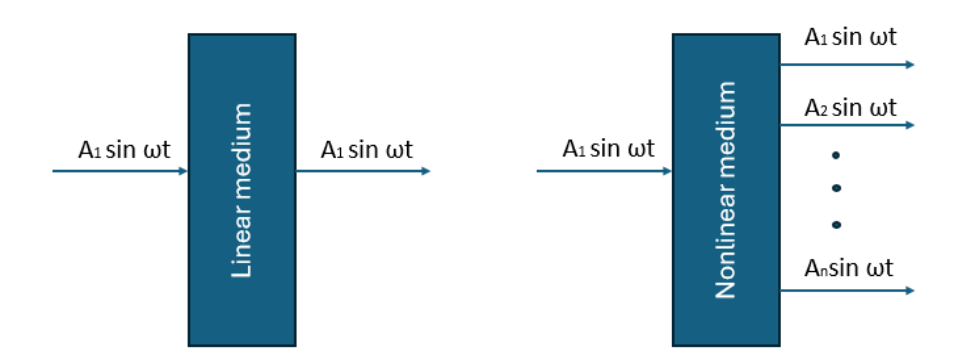


Figure 4-3. Linear and Nonlinear Wave Propagation.

The generation of higher harmonics is fundamentally attributed to the nonlinear elastic behaviour of a material, as illustrated in Figure 4-3. This nonlinearity emerges from deviation in the conventional stress-strain relationship, where stress (σ) is no longer directly proportional to strain (ϵ), as assumed in linear elasticity. Instead, the material exhibits a more complex response under deformation. This behaviour is commonly describing as the nonlinear extension of Hooke's law, which, for a simplified one-dimensional form, is mathematically expressed in Equation 4-18 [130, 131].

 $\sigma = \operatorname{E}\varepsilon \left(1 + \beta\varepsilon + \cdots\right)$ 4-18

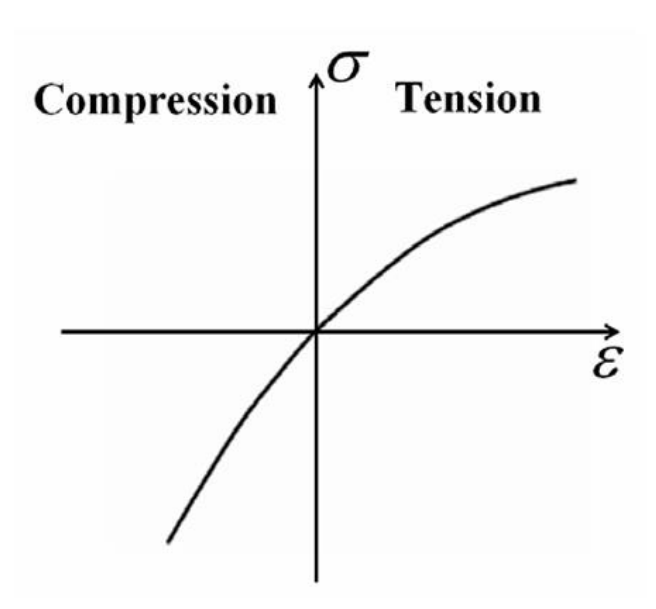


Figure 4-4. Nonlinear relationship between stress and strain [131]

Where E represents Young's modulus, and β is the second-order nonlinear elastic coefficient, which will be referred to as the nonlinear parameter in this thesis. To understand the mechanism behind higher harmonic generation, consider a scenario where a single-frequency ultrasonic longitudinal wave is introduced on one surface of a flat plate-shaped specimen, propagates through the material, and is detected on the opposite surface. Assuming attenuation effects are negligible, the equation of motion governing the behaviour of longitudinal plane waves in the flat specimen can be expressed as follows:

$$\rho_0 \frac{\partial^2 u}{\partial t^2} = \frac{\partial \sigma}{\partial x} \tag{4-19}$$

Where ρ represents the density of the medium, x denotes the wave propagation distance, σ is the stress, and u refers to the displacement. By utilizing Equations 4-18 and 4-19 in combination with the standard relationship between strain and displacement, the nonlinear wave equation for displacement u(x,t) can be derived and expressed as follows:

$$\rho \frac{\partial^2 u}{\partial t^2} = E \frac{\partial^2 u}{\partial x^2} + 2E\beta \frac{\partial \sigma}{\partial x} \frac{\partial^2 u}{\partial x^2} \tag{4-20}$$

Here, Equation 4-18 is considered up to the second-order term. To solve the resulting nonlinear wave equation, perturbation theory is employed. For this approach, the displacement field u is assumed as expressed in Equation 4-21.

$$\mathbf{u} = \mathbf{u_0} + \mathbf{u}' \tag{4-21}$$

Here, u₀ represents the initially excited wave, which corresponds to the fundamental linear response, while u' corresponds to the first-order perturbation solution, accounting for the

nonlinear effects. If u_0 is defined as a sinusoidal wave with a single frequency, then the displacement can be expressed as:

$$\mathbf{u} = \mathbf{A}_1 \cos\left(\mathbf{k} \mathbf{x} - \mathbf{w} \mathbf{t}\right) \tag{4-22}$$

This equation describes a wave of amplitude A_1 , moving in the positive x-direction, oscillating at frequency f, and propagating with wave speed c. ω is angular frequency — defined as $\omega=2\pi f$ where f is the frequency (in Hz). It determines how fast the wave oscillates in time. K is Wavenumber — defined as $k=2\pi/\lambda$ and λ is the wavelength. It describes how many wave cycles occur per unit length.

And then the perturbation solution up to the 2nd order can be obtained as follows:

$$u = u_0 + u' = A_1 \cos(kx - wt) - A_2 \sin 2(kx - wt)$$
 4-23

With:

$$A_2 = \frac{\beta}{8} A_1^2 k^2 x \tag{4-24}$$

The second term in Equation 4-23 represents the second harmonic frequency component, whose amplitude is directly influenced by the nonlinear parameter β . This relationship indicates that β can be determined by measuring the magnitude of the second harmonic frequency component (A_2), as expressed in Equation 4-25.

$$\beta = \frac{8}{k^2 x} \frac{A_2}{A_1^2}$$
 4-25

The magnitude of harmonic waves is influenced by the material properties of the medium. As a result, evaluating the extent of higher harmonic wave generation in the transmitted ultrasonic wave can provide insight into the degradation of the material's elastic behaviour. Such analysis can be used to detect early-stage changes in microstructure, indicating the onset of damage or fatigue [131].

4.2 Conclusion

This chapter introduced the theoretical principles of the nonlinear ultrasonic method, focusing on Second Harmonic Generation (SHG) for early fatigue damage detection. Starting from the classical equations of motion, the discussion progressed to nonlinear wave behaviour caused by microstructural defects. The nonlinear parameter β was defined as a key indicator of material nonlinearity, directly related to the amplitude of the second harmonic wave. This parameter enables the detection of early-stage fatigue damage with higher sensitivity than linear methods. The foundation laid in this chapter supports the experimental work to follow. In the next chapter (Chapter 5), the experimental setup, equipment, and key parameters used to apply this method in practice will be presented.

Chapter 5. Methodology

5.1 Introduction

This chapter presents the experimental procedures and equipment used throughout the study. It begins with a description of the fatigue testing machine and the applied fatigue loading regimes used across different test series in the thesis. Details on surface roughness measurements and specimen dimensions are also provided. The chapter then introduces the electrical resistivity (ER) measurement system and its associated equipment, followed by a description of the equipment used for nonlinear ultrasonic measurements.

Subsequently, the signal processing techniques employed for nonlinear parameter (NLP) analysis are explained in detail. The characterization techniques used in this research are then discussed, including optical microscopy and transmission electron microscopy (TEM). For the TEM analysis, the application of scanning transmission electron microscopy with high-angle annular dark-field (STEM-HAADF) imaging is addressed, along with the rationale for its selection in this study. Finally, the material preparation procedures specific to each characterization method are described.

5.2 Fatigue instrument

Cyclic mechanical tests provide information about stress-strain changes in the material studied during cycling. Various loadings can be tested, which can be uniaxial or multiaxial, tension (on cylindrical or flat part), torsion, internal pressure (on tubular useful part) or any combination of these loadings. Servo controlled machines allow for precise control and measurements during mechanical tests. A servo-valve controls electronically the movement of an actuator. The specimen is fixed between the actuator and the load cell. The section of the specimen's gauge length must be constant, and its length must be sufficiently large to assume that strains and stresses are uniform in the gauge length.

The uniaxial testing machine used in this study was a servo-hydraulic INSTRON machine of type 8501 as shown in Figure 5-1. It is equipped with a load cell of capacity ±100 kN. The movement of the actuator can be controlled in displacement, load, or strain. Control and data acquisition were conducted using wave mix software. Fatigue tests were performed at room temperature (20 °C) and in air. Load and strain were recorded simultaneously at imposed frequency during cycling.



Figure 5-1. Instron 8501 fatigue testing machine.

The standard geometry and dimensions of specimen used in this study for fatigue tests are shown in Figure 5-2.

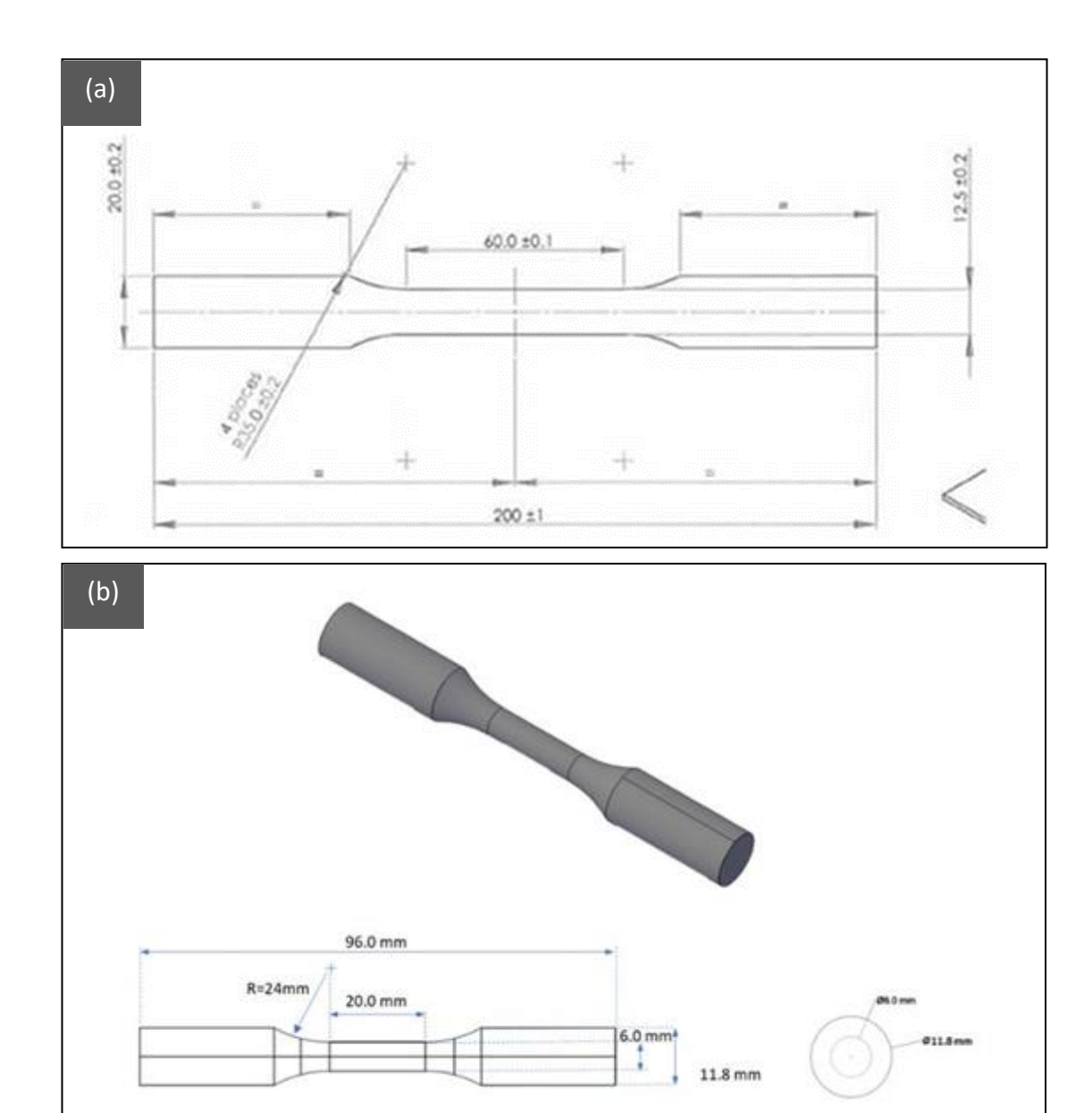


Figure 5-2. Geometry of (a) flat tensile test-shaped fatigue specimen and (b) cylindrical tensile test-shaped fatigue specimen, based on ASTM E606 standards.

In this study the samples that used for fatigue testing were cylindrical and flat specimens with dimensions shown in Table 5-1 for flat samples and Table 5-2 for cylindrical samples. The sample geometry was designed to facilitate consistent application of cyclic loads and ensure accurate measurement of fatigue life under varying conditions. These standardized dimensions also allowed for reproducible testing and reliable comparison of results between different fatigue regimes and treatment conditions.

Table 5-1. Flat tensile test-shaped fatigue specimen dimensions

L	Length (mm)	Gauge length (mm)	Gauge width (mm)	Thickness (mm)	
	200	60	12.5	2	

Table 5-2. Cylindrical tensile test-shaped fatigue specimen dimensions

Length (mm)	Diameter (gauge section) (mm)	Diameter (mm)	Gauge length (mm)	
96	6	11.8	20	

As discussed in section 2.2.2, 316L stainless steel was used because it is widely utilized in various industries due to its excellent mechanical properties, corrosion resistance and relatively predictable fatigue behavior. Additionally, for the purpose of this project, which focuses on using NDT methods to detect early-stage fatigue damage with an emphasis on dislocation density and dislocation arrangements, 316L stainless steel is a more suitable choice. Compared to aluminum alloys, where fatigue is influenced by factors such as inclusions, precipitates, and secondary phases, the fatigue process in 316L stainless steel is often more straightforward cause fatigue primarily involves dislocation slip and arrangement patterns (e.g., persistent slip bands, dislocation walls, and dislocation cells). There are no strong second-phase particles that significantly impact fatigue crack initiation (except for minor carbide formations at grain boundaries in solution-annealed 316L) and cracks initiate from intrusions and extrusions. This makes it easier to study how NDT methods respond specifically to dislocation structures, rather than being affected by other microstructural features. The 316L stainless steel used in this study was supplied from Berkley precision engineering company in the form of extruded bars for both flat and cylindrical specimens. The chemical composition of the material is detailed in Table 5-3. The as-received microstructure of the extruded bar, observed using optical microscopy prior to any fatigue loading, is shown in Figure 5-3 and Figure 5-4. It shows an austenitic structure with an average grain size of 50 μm (Figure 5-3) and 60 μm (Figure 5-4) , and twin boundaries are also visible in the microstructure.

Table 5-3. The composition of SS316L stainless steel used in a study, represented in weight percent (wt.%).

Eleme nt	Carbon (C)	Silicon (Si)	Manga nese (Mn)	Phosp horus (P)	Sulfur (S)	Chromi um (Cr)	Nickel (Ni)	Nitrog en (N)	Molyb denum (Mo)	lron (Fe)
wt.%	0.022	0.51	1.11	0.031	0.001	16.7	10.1	0.022	2.01	Balanced

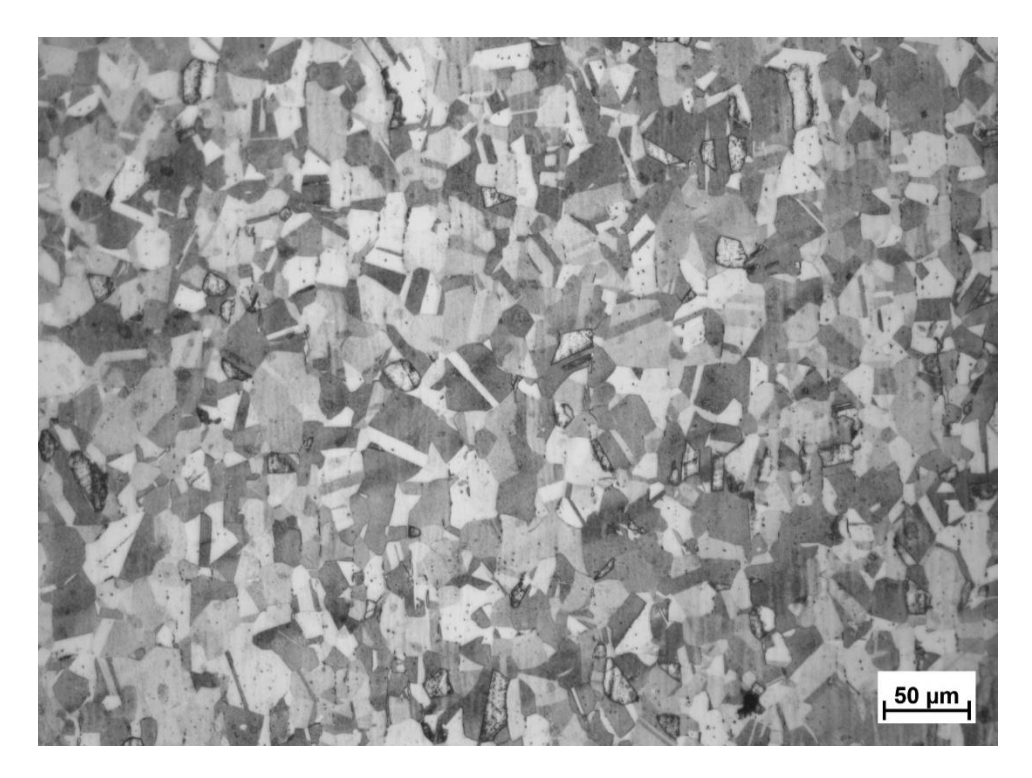


Figure 5-3. Optical microscopy image of the as received SS316L sample flat specimen.

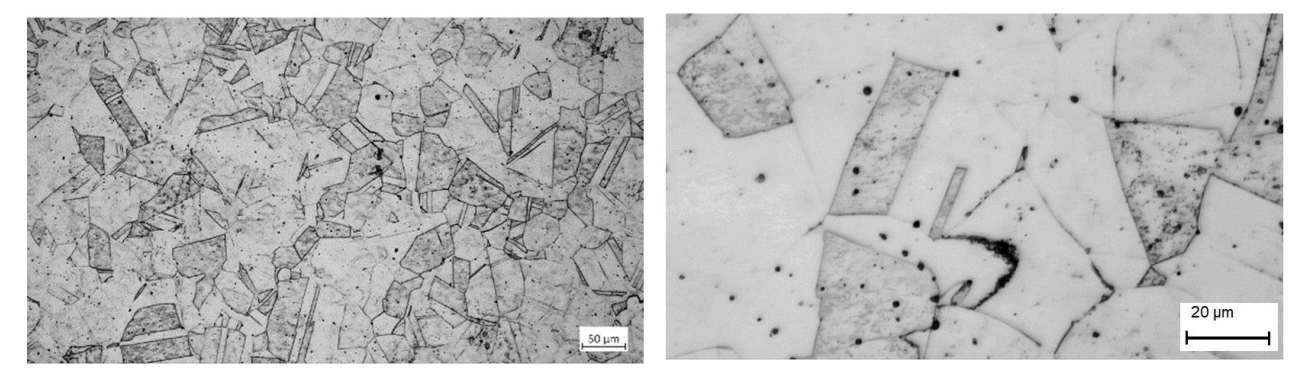


Figure 5-4. Optical microscopy image of the as received SS316L sample cylindrical specimen.

For the fatigue testing in this study, an initial tensile test was performed to determine the yield strength, which was essential for selecting an appropriate maximum load for the fatigue samples. The yield strength of the flat-surfaced samples was measured as 263 ± 7 MPa. Fatigue tests were then carried out on both cylindrical and flat specimens under cyclic loading using different stress ratios and control modes according to the experimental requirements. The tests were conducted in load-controlled mode at room temperature with sinusoidal loading waveforms. Specifically, cylindrical samples were tested under tension—tension loading with a maximum load of 310 MPa, a stress ratio (R) of 0.5, and a frequency of 10 Hz, up to 2×10^6 cycles. Flat samples were tested under two different loading conditions: one set under tension—tension loading with R = 0.1, a maximum load of 290 MPa, and a frequency of 1 Hz up to 4×10^5 cycles; and another set under tension—compression loading with R = -0.4, a maximum load of 260 MPa, and a frequency of 10 Hz up to 5×10^6 cycles. A summary of the fatigue loading regimes, specimen geometries, and their corresponding applications in the thesis is provided in Table 5-4.

Table 5-4. Fatigue loading parameters and specimen types used in various experiments, along with corresponding sections of the thesis where each configuration was applied.

Sample type	Maximum load (MPa)	Stress ratio (R value)	Frequency (Hz)	Fatigue regime (cycles)	Section of thesis using this Sample
Cylindrical	310	0.5	10	$2 \times 10^6 \pm 1$ × 10^5 cycles	6.2.6 (Figure 6-14)
Flat	290	0.1	1	4× 10 ⁵ ± 2 × 10 ³ cycles	6.1 (Figure 6-1 to Figure 6-7)
Flat	260	-0.4	10	5× 10 ⁶ ± 2 × 10 ⁵ cycles	6.2.6 (Figure 6-15, Figure 6-16) 6.3.2 (Figure 6-20, Figure 6-21, and Figure 6-22) 7.3.1, 7.3.2

For all tests related to probe spacing optimization (Section 6.2.1), the effect of measurement time (Section 6.2.2), the surface roughness method (Section 6.2.3), and repeatability assessment (Section 6.2.4) in the electrical resistance method, as well as for determining the optimal gain and magnitude settings (Section 6.3.1) and repeatability (Section 6.3.2) in the nonlinear ultrasonic method, flat tensile test specimens were used.

5.3 Surface roughness test with SURFTEST SJ-210

The Surftest SJ-201, manufactured by Mitutoyo Corporation (Japan), is a shop-floor-type surface roughness measuring instrument designed to trace the surfaces of machined parts, calculate surface roughness based on established standards, and display the results digitally. A pickup stylus attached to the SJ-201P detector scans the surface irregularities of the specimen, with the vertical displacement during the trace digitally processed and displayed on an LCD screen. This device has a maximum measurement range of 350 μm (-200 μm to +150 µm) and provides surface texture characterization using parameters such as Ra (average roughness), Rq (root mean square roughness), and Rz (average maximum height). These parameters are essential for evaluating the influence of surface characteristics on material properties. More detailed information regarding the operating principles of this device is provided in Figure 5-5. In this study, surface roughness measurements were used to (1) assess the effect of surface texture on electrical resistivity, and (2) ensure consistent initial surface conditions across samples used in electrical resistivity (ER) and nonlinear ultrasonic parameter (NLP) measurements during fatigue testing. To achieve this, all specimens underwent a standardized surface preparation process involving mechanical polishing using SiC papers up to 1200 grit to ensure uniform initial roughness.

Measurements were conducted at room temperature, using the following test settings: a cut off length of 0.8 mm, evaluation length of 4 mm, and a traversing speed of 0.5 mm/s, consistent with ISO 4287 standards. For each specimen, 10 to 12 measurements were taken, primarily at the centre of the gauge length—where maximum deformation typically occurs—following established protocols to minimize variability [132, 133].

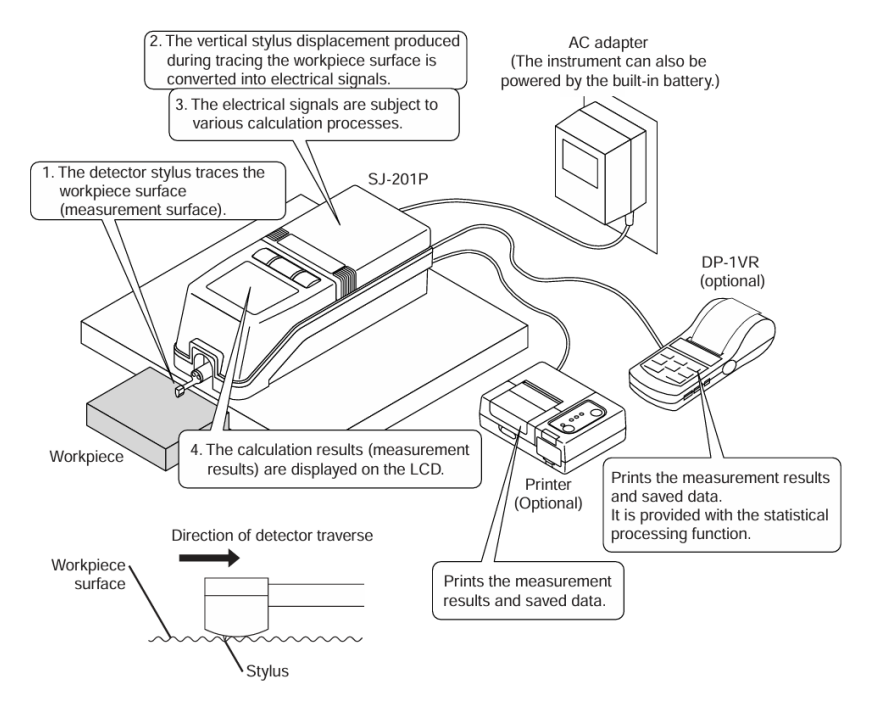


Figure 5-5. Surface roughness measurement principles [134]

5.4 Equipment requirement for ER:

As discussed in Chapter 3 electing appropriate measurement equipment is crucial for minimizing noise and eliminating errors in electrical resistivity measurements. A combination of the delta mode and the four-probe method has been shown to be effective in addressing these issues, ensuring higher accuracy and reliability. In the following section, the necessary equipment that meets these criteria is described in detail.

The effectiveness of the three-step delta method relies on the assumption that thermal drift behaves in a linearly approximal manner when observed over a short period. This linear approximation allows for the cancellation of drift-induced errors, thereby enhancing the accuracy of the measurement. To ensure the success of this method, specific performance criteria must be met by both the current source and the voltmeter, particularly in terms of speed, synchronization, and stability. First, the measurement cycle time should be faster than the thermal time constant of the test system. This imposes certain requirements on the current source and voltmeter used. The current source needs to switch quickly at evenly spaced intervals, allowing for a fast measurement cycle. Consistent spacing between current steps ensures that the thermoelectric voltage changes at a steady rate between measurements.

In parallel, the voltmeter must be tightly synchronized with the current source and capable of making accurate measurements in a short time interval. Synchronization relies on instrument coordination, ensuring that the voltmeter takes voltage measurements only after the current source has stabilized, and the current source switches polarity only after the voltage measurement is completed.

The measurement speed of the voltmeter is critical in determining total cycle time; faster voltage measurements mean shorter cycle times. For reliable resistance measurements, the voltmeter must maintain this speed without sacrificing low noise characteristics.

Finally, in low-power applications, the current source must be capable of outputting low values of current so as not to exceed the maximum power rating of the device. By meeting these criteria, the delta method becomes a powerful tool for achieving highly accurate and thermally stable resistance measurements [120].

Selecting appropriate measurement equipment is critical to the three-step delta method. Keithley has designed the Models 6220 and 6221 Current Sources and the Model 2182A Nanovoltmeter to perform resistance measurements using the three-step delta technique. This equipment provides high resolution and low noise for precise low current sourcing. This combination is ideal for making low resistance measurements (down to $10n\Omega$).

The Keithley Models 6220/6221 Current Source and the Model 2182A Nanovoltmeter are designed to work together to achieve up to 48 delta readings per second at an integration time of 1 PLC (16.67 ms at 60 Hz power line frequency or 20 ms at 50 Hz). These instruments are interconnected using the Keithley Trigger Link bus, enabling the test to be conducted completely independently of a computer.

For low-power applications, the current source must deliver low current values to avoid exceeding the maximum power rating of the device under test. This is particularly important when working with moderately high- or high-impedance devices. Both the Model 6220 and 6221 Current Sources can provide currents as low as 100 fA. When paired with the Model 2182A Nanovoltmeter, this setup enables highly accurate measurements with a sensitivity of 1 nV.

The use of a pulsed current source allows the test current to be increased without exceeding the device's power rating. The Model 6221 distinguishes itself from the 6220 by supporting pulsed delta measurements, capable of generating pulses as short as 50 μ s, with amplitudes ranging from 100 fA to 100 mA. This feature makes the Model 6221 particularly well-suited for applications requiring precise and controlled pulsed currents [117].

The essential characteristics of a high-quality current source including High resolution, a broad range of compliance settings, rapid output settling time, low noise levels and high output impedance. While many power supplies can deliver current to a device by simply setting the output voltage and allowing the device to draw whatever current it needs, this approach is often insufficient for accurately characterizing device behaviour. In many

scenarios, it is more informative to describe a device's performance in terms of the current passing through it, rather than the voltage across it. Consequently, sourcing a constant current is generally preferable to sourcing a constant voltage. Constant current sources ensure a specified current flow through the device under test (DUT) and automatically adjust the voltage as needed to maintain that current. Advanced models, such as the Keithley Model 6220 and 6221, provide the capability to establish a "compliance limit," which regulates the maximum voltage applied while sourcing the specified current. The Model 6220 and Model 6221 share most of the same functions and capabilities, but the Model 6221 adds AC current sourcing, waveform generation, and pulsing functions, as well as a built-in Ethernet interface so model 6221 had been used for this research. The Model 2182A Nanovoltmeter is the natural measurement partner for either Model 622X current source for measuring resistance and creating I-V curves. In resistance measurements, lower test currents produce lower voltages across the devices, which can be challenging to measure. By integrating the Model 2182A with a Model 6221 Current Source as shown in Figure 5-6 and Figure 5-7, these challenges can be effectively addressed within an efficient and user-friendly setup. The Model 2182A Nanovoltmeter offers low noise, thermoelectric EMF cancellation, high measurement speed, and 2ppm accuracy, making it ideal for challenging low voltage tasks such as analysing the electrical properties of power-sensitive materials, highly conductive metals, and superconductors at both high and low temperatures. When used in combination with a current source (in modes like delta) the current source configures and controls the nanovoltmeter via the RS-232 and Trigger Link interfaces, then collects data over the RS-232 interface for further processing. Once the instruments are connected properly, starting the test is simply pressing the source's Delta button and then the Trigger button. The delta mode automatically triggers the current source to alternate the signal polarity and then triggers a nanovoltmeter reading at each polarity. These high-speed current reversals cancel out both constant and drifting thermoelectric offsets, reducing measurement noise and increasing voltage and resistance measurement accuracy [135].

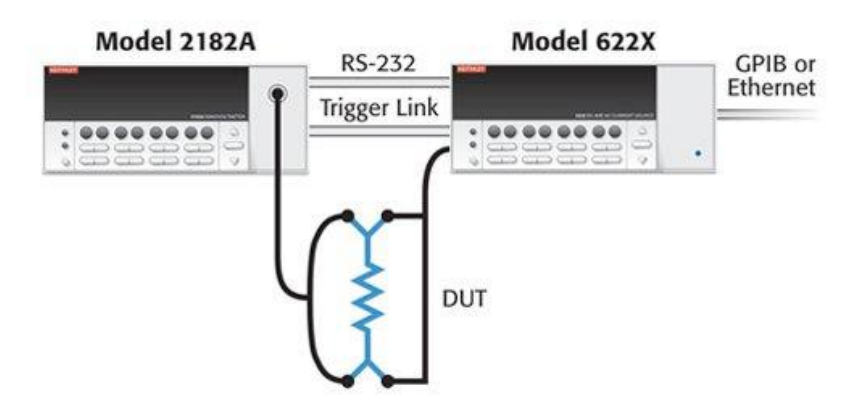


Figure 5-6. The Model 622X controls the Model 2182A. The pair act as a single instrument for trouble-free programming and operation [135]

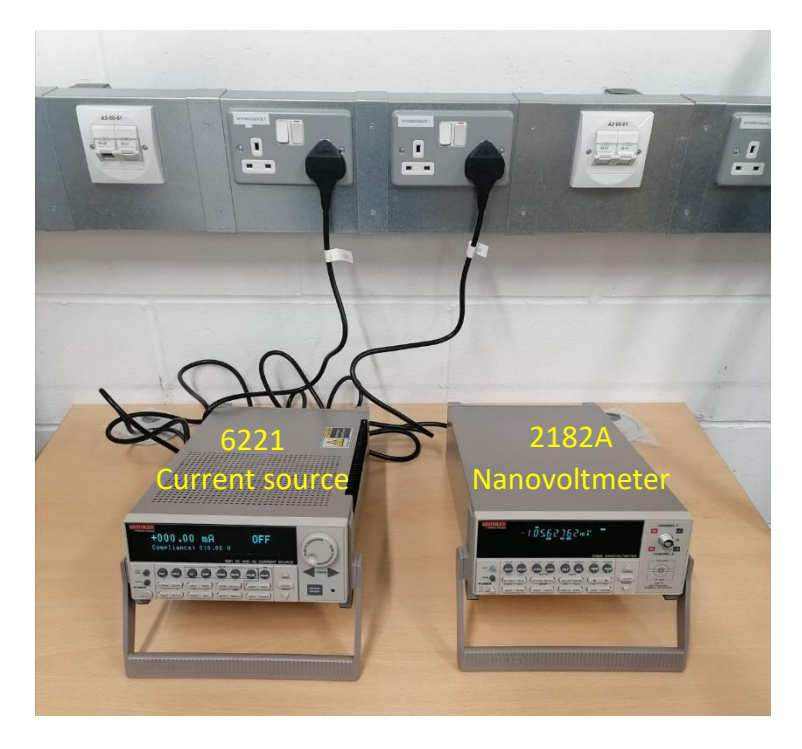


Figure 5-7. The Model 6221 current source and Model 2182A nanovoltmeter

In Table 5-5 a summary of the features and benefits of this combination is provided.

Table 5-5. A summary of the features and benefits of model 6221 AC and DC Current Source integrating with model 2182A nanovoltmeter [136]

Features	Benefits
Measure resistances from $10n\Omega$ to $100M\Omega$	Covers an extremely wide measurement range and
	specializes in ultra-low resistance measurements for
	characterizing high conductivity materials,
	nanomaterials, and superconducting materials.
Synchronized current-pulsed source and	Limits power dissipation in components such as
measurement times as short as 50μs	nanodevices and nanomaterials that can be easily
	destroyed unless tested at very low power levels.
Delta mode current reversal, resistance	Makes accurate ultra-low resistance measurements by
measurement technique	eliminating the effects of thermal offsets and reduces
	noise down to 30nV p-p noise (typical) for one reading.
	Multiple readings can be averaged for greater noise
	reduction.
Differential conductance measurement	Offers speeds ten times faster and lower noise than
	other conductance measurement techniques. Good
	measurements are made without the need to average
	the results of multiple sweeps.
Nanovoltmeter and current source interface to work	Both instruments can be operated like a single
together seamlessly	instrument when making differential conductance and
	resistance measurements.
Delta, differential conductance, and pulse modes	Allows characterizing devices that can be easily disrupted
generate minimal current transients	by current spikes.

5.4.1 Electrical resistivity setup and measurement

Electrical resistivity (ER) measurements of the low-resistance materials were performed using a Keithley 6221 Current Source and a Keithley 2182A Nanovoltmeter configured in a delta mode setup, which ensures highly accurate and low-noise readings. The experimental setup and measurement procedure followed the manufacturer's guidelines for the instrument.

5.4.1.1 Instrument setup

The experimental setup involved connecting the Keithley 6221 and Keithley 2182A using the Model 8501 Trigger Link cable for synchronization and a CA-351 null-modem (Figure 5-8) serial cable for communication. The 6221 was responsible for supplying a precise current, while the 2182A measured the corresponding voltage drop across the sample. All connections were made using low-thermal input cables equipped with spade lugs to minimize thermoelectric noise and ensure accurate low-resistance measurements.

For the electrical resistivity measurements, the sample was securely attached using copper tape to prevent movement and ensure stable electrical contacts. A 237-ALG-2 triax cable (Figure 5-9), terminated with alligator clips, was used to connect the current source output to the sample. The trigger circuit was established by following the recommended wiring scheme using copper wire to ensure consistent triggering between the instruments [136, 137, 138, 139].

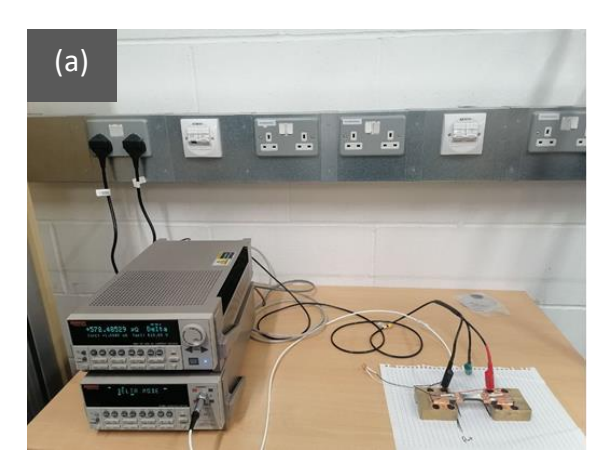


Figure 5-8. CA-351 null-modem serial cable



Figure 5-9. 237-ALG-2 Triax cable terminated with alligator clips on one end

The final setup for the electrical measurement is illustrated in the Figure 5-10.



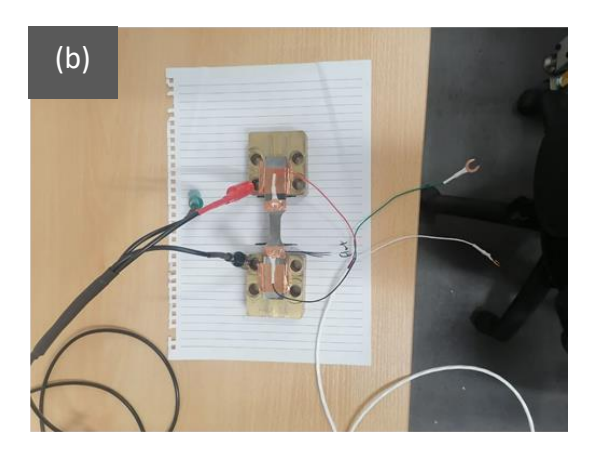


Figure 5-10. Electrical resistance measurement set up (a) showing overall setup and (b) showing the test specimen setup

5.4.1.2 Measurement procedure

The procedure for measuring electrical resistivity is as follows:

1. Both the Keithley 6221 and Keithley 2182A instruments were powered on, and the delta mode was initiated on the 2182A Nanovoltmeter by pressing the "Delta" button on the front panel.

- 2. The trigger button on the 2182A was pressed to begin the measurement sequence.
- 3. Probes were connected to the sample, with the current applied from the 6221, and the voltage drop was recorded by the 2182A across the sample.
- 4. The electrical resistivity (ρ) was calculated from the measured resistance (R) using the relation: ρ=R.A/L where A is the cross-sectional area of the sample, and L is the distance between the voltage probes. (The most accurate value for the probe space is the distance between the centres rather than the closest distance between the probes).
- 5. The distance between all the four points should be equal also. When measuring electrical resistance (ER) for samples with more complex geometries, it's essential to apply correction factors based on the sample's shape. This is because irregular geometries can significantly affect current distribution and resistance readings. However, when equal spacing is used between the probes, the calculations for ER become simpler and more straightforward. By maintaining the same distance between probes, the impact of geometric variations is minimized, allowing for easier application of mathematical relationships to calculate resistivity or conductivity. This consistency reduces the need for complex corrections, leading to more accurate and reliable measurements.
- 6. While resistance and resistivity are related properties, they are not synonymous. Resistivity is a property of the material itself, so it's independent of the geometry of a particular sample. In contrast, resistance depends not only on the material but on the length and cross-sectional area of the sample being measured [140].

The readings were displayed on the screen of the Keithley 6221 and recorded using Kickstart software, interfaced with a connected computer for data acquisition. All measurements were conducted with appropriate personal protective equipment (PPE)—including safety glasses, gloves, and lab coats—to maintain operator safety and prevent sample contamination.

5.4.1.3 Measurement procedure for assessing the effect of probe spacing

This experiment aimed to investigate the influence of varying the spacing between probes on electrical resistivity (ER) measurements. An AA6082 aluminium bar, with dimensions based on Figure 5-2a, was used as the test specimen. ER measurements were conducted at different probe spacing: 10 mm, 15 mm, 20 mm, and 30 mm. Based on the results discussed in Section 6.2.1,a probe spacing of 20 mm was selected as the standard configuration for all subsequent experiments.

5.4.1.4 Measurement procedure for assessing the effect of measurement duration

Additionally, the effect of measurement duration was evaluated to ensure that no significant differences in electrical resistivity (ER) readings occurred across varying measurement times.

The ER of a flat fatigue sample made from stainless steel 316L, with dimensions specified in Figure 5-2a, was measured at different durations: 10 seconds, 20 seconds, and 30 seconds. This test aimed to confirm that the length of the measurement period does not significantly influence the results.

5.4.1.5 Measurement procedure for assessing the effect of surface roughness

Next, the effect of surface roughness on ER was measured, revealing that rougher surfaces can increase ER, suggesting this factor should be considered in future investigations. To assess the influence of surface roughness on electrical resistivity, a 316L stainless steel bar (200 mm × 20 mm × 1.97 mm) was prepared and subjected to different surface treatments. These included the as-received condition, grinding with 80-grit paper to make the surface rougher, grinding with 1200-grit paper, and final polishing with a polishing disk to have a final smooth surface. Surface roughness was measured using a SurfTest profilometer, and electrical resistivity (ER) was measured five times per condition using the Keithley 6221/2182A setup in delta mode.

5.4.1.6 Measurement procedure for repeatability assessment

In the preliminary stages of the electrical resistivity (ER) measurement procedure, several factors were analysed to ensure the accuracy and consistency of the setup prior to conducting measurements across different fatigue cycles. One of the steps is investigating the repeatability of the Keithley 6221/2182A measurement setup. It was evaluated to assess how consistently the instrument and setup could record the ER of the same sample across multiple trials, with minimal variation in results. Two specimens were used for this purpose: one flat fatigue sample stainless steel 316L, and one AA6802 standard fatigue specimen with dimensions mentions in Figure 5-2a. For each sample, five measurements were performed, with each measurement lasting 10 seconds and consisting of approximately 70 data points. The results of these repeatability tests are presented in Figure 6-12 and Figure 6-13.

5.4.1.7 Measurement procedure for reliability assessment

Reliability refers to the ability of a measurement setup to consistently perform its intended function without failure or significant deviation over time. To evaluate the reliability of the setup used in this study, the electrical resistance of various alloys was measured and compared to values reported in the scientific literature. The materials tested included annealed stainless steel 316L, non-annealed stainless steel 316L, AA6802 aluminium alloy, and a pure copper bar. The close alignment between the measured values and those found in literature indicates that the setup performs consistently and accurately. Table 6-4shows the results related to this measurement.

Based on the findings from the preliminary evaluations of probe spacing, measurement duration, surface roughness, repeatability, and reliability, a standardized procedure was established for the fatigue study on electrical resistivity (ER). For each fatigue cycle, ER was

measured three times to ensure data consistency and account for any variability. Between each measurement, the probes were carefully removed and reattached to simulate realistic experimental handling and to evaluate contact stability. Each individual measurement was conducted over a duration of 10 seconds with probe spacing 20mm, capturing approximately 70 data points per trial. A constant electrical current of 1 mA was applied during all measurements to maintain uniform testing conditions across all samples and fatigue stages.

5.5 Measurement instruments and procedure for nonlinear ultrasound

5.5.1 Introduction

The primary objective of the nonlinear ultrasound measurements in this study is to evaluate the sensitivity of the nonlinear parameter (β) to microstructural changes, particularly those related to dislocation and slip bands structures. This measurement approach aims to detect early-stage fatigue damage by analysing the generation of higher harmonic components in ultrasonic wave propagation. The key goal is to measure nonlinear parameter β in different cycles and investigate if it can detect early fatigue damages (before 20%) of fatigue life, which serves as an indicator of microstructural evolution under cyclic loading.

The experimental methodology follows a structured approach to ensure reliable measurement of nonlinear ultrasound signals. The process begins with sample preparation, ensuring that all specimens have consistent surface conditions and geometrical dimensions to minimize variations in signal propagation. A piezoelectric transducer is used to introduce an ultrasonic wave of with fundamental frequency into the material. Due to the inherent material nonlinearity, a second harmonic component (2f) is generated as the wave propagates through the specimen.

To capture and analyse these signals, a high sensitivity receiving transducer is placed on the other side of sample. The transmitted wave is then amplified and digitized using a high-resolution data acquisition system (DAQ). The acquired signal undergoes signal processing where the amplitude of the second harmonic (A_2) is extracted and compared to the fundamental harmonic (A_1). The nonlinear parameter β is subsequently computed using the relationship:

$$eta \sim rac{A_2}{A_1^2}$$

The procedure is repeated for two samples under the same fatigue conditions to establish a correlation between β and material defects. Nonlinear acoustic techniques are highly sensitive to external influences, particularly the inherent nonlinearity of the equipment used. Therefore, each component must be carefully selected. To establish a precise and reliable experimental setup, various options were considered. This chapter provides a detailed description and evaluation of all components used to obtain nonlinear acoustic measurements, ensuring that each fulfils its specific requirements.

5.5.2 Equipment for signal generation:

In nonlinear measurements, short, high-power tone burst signals are required to accurately assess material nonlinearity. To ensure precise measurements, the input signal must be as clean as possible, ideally consisting of only a single frequency. The RITEC RAM-5000 is specifically designed to generate such signals while providing high-power output, making it suitable for nonlinear ultrasonic applications.

5.5.2.1 RITEC RAM-5000 high-power ultrasonic system

Beyond maintaining signal purity, another crucial requirement for the generated signal is a high-power output. In metallic materials, nonlinearity is relatively weak, meaning that the second harmonic amplitude is significantly smaller than that of the fundamental frequency. Consequently, a high-power input signal is necessary to detect the second harmonic and maintain an adequate signal-to-noise ratio (SNR). Additionally, the material nonlinearity parameter exhibits higher values at low amplitudes but declines rapidly until it stabilizes at a certain input level [141, 142].

The RITEC RAM-5000 (Figure 5-11) is specifically designed to meet the demands of nonlinear ultrasonic measurements. It generates a clean output signal and can deliver power outputs of up to 1.5 kW RMS. Further technical specifications of the RITEC RAM-5000 are summarized in Table 5-6.

Frequency Range for Gated Amplifier	250 kHz to 17.5 MHz
Maximum Pulse Width	200 microseconds
Nominal Output Impedance of Gated	50 Ω
Amplifier	
Typical Gated Amplifier RMS Output	1.5 KW between 0.25 and 7 Mhz

Table 5-6. Specifications of RITEC RAM-5000 [141]

Here is a brief explanation that why each of these specifications are beneficial for the purpose of this research.

- Frequency Range for Gated Amplifier: 250 kHz to 17.5 MHz

A broad frequency range allows for flexibility in selecting the optimal frequency for different materials and applications. Lower frequencies (e.g., 250 kHz - 1 MHz) penetrate deeper into materials, making them suitable for bulk material analysis and internal defect detection while, higher frequencies (up to 17.5 MHz) provide finer resolution, which is essential for detecting early-stage fatigue damage and microstructural changes near the surface. The wide frequency coverage enables the study of multiple nonlinear phenomena, such as harmonic generation and wave mixing.

Maximum Pulse Width: 200 Microseconds

A longer pulse width increases the energy delivered to the material, improving the signal-tonoise ratio (SNR) and enhancing detectability of weak nonlinear responses. Longer pulse durations allow higher excitation energy, which is beneficial when measuring second or higher harmonic signals that are typically weak. The adjustable pulse width ensures that experiments can be tailored based on the required resolution and penetration depth.

- Nominal Output Impedance of Gated Amplifier: 50 Ω

A 50 Ω impedance is the standard for high-frequency RF circuits, ensuring maximum power transfer and minimal signal loss between the amplifier and transducer. This impedance matching helps reduce reflection and distortion in the transmitted signal, improving measurement accuracy. It allows for efficient coupling between the amplifier and ultrasonic transducers, leading to cleaner and more reliable signals.

- Typical Gated Amplifier RMS Output: 1.5 kW between 0.25 and 7 MHz

A high-power output (up to 1.5 kW RMS) is essential for detecting weak nonlinear responses, such as second harmonic generation, by ensuring sufficient excitation energy. Higher power enhances the detectability of small nonlinearities in metals, which is crucial for early fatigue detection before visible cracks form. The power output is particularly useful in low-frequency applications (below 1 MHz), where high-energy signals are required for deeper material penetration. By covering 0.25 to 7 MHz, the system is ideal for studying various materials, from metals to composites, each requiring different excitation conditions.



Figure 5-11. RITEC SNAPRAM-5000 High-Power Ultrasonic System [141]

5.5.2.2 RITEC low-pass and high-pass filters (RLPF-5 and HPF-10)

Although the RITEC RAM-5000 is designed to generate pure signals, unwanted higher harmonics can still appear. To minimize these, an additional Low Pass Filter (LPF) is used. The FD-5-10 system includes a 5 MHz Low Pass Filter and a 10 MHz High Pass Filter (HPF). The LPF is a Chebyshev filter with a 50 Ω input impedance, ensuring proper matching between the amplifier output and the 200 MHz output impedance, which approximates the impedance of a piezoelectric transducer. This impedance matching is crucial because mismatched impedances can distort the signal. The HPF in the FD-5-10 system can also be used to measure

the second harmonic, but in this study, it is primarily used to validate signal processing results by improving signal clarity.

5.5.2.3 RITEC RA-31, RA-32 and RT-50 High power attenuator

The RITEC RA-31 and RA-32 High Power Attenuators are essential components in nonlinear ultrasonic testing systems, specifically designed to control and optimize the transmitted signal power. These attenuators allow precise adjustment of signal amplitude by inserting a defined level of attenuation into the transmit (Tx) line during experiments.

The RA-31 and RA-32 attenuators help regulate signal power by gradually reducing the amplitude in controlled steps. This is crucial for ensuring accurate and repeatable measurements, especially when investigating second harmonic generation (SHG) and other nonlinear ultrasonic effects. By integrating these attenuators into the system, users can systematically modify the excitation level, ensuring that the nonlinearity parameter is measured consistently across different drive amplitudes.

The attenuation level is adjustable in 1 dB increments, allowing precise control over the power levels reaching the transducer. During a User-Defined scan, attenuation values are incrementally increased (e.g., from 0 dB to 20 dB) while the system records the corresponding fundamental and second harmonic amplitudes. The attenuation switches on the RA-31 and RA-32 units are manually toggled after each scan point to set the desired level of attenuation. The total attenuation inserted is the sum of all selected values.

Figure 5-12 presents a comparison of the second harmonic of the signal immediately after the amplifier and after passing through the attenuator and filter. In both cases, the amplifier generates a 30-cycle 5 MHz tone burst at 95% output level. The recorded signals are subsequently normalized relative to their fundamental frequency peak. It is clearly visible that the second harmonic portions of the signal are successfully filtered out by the LPF.

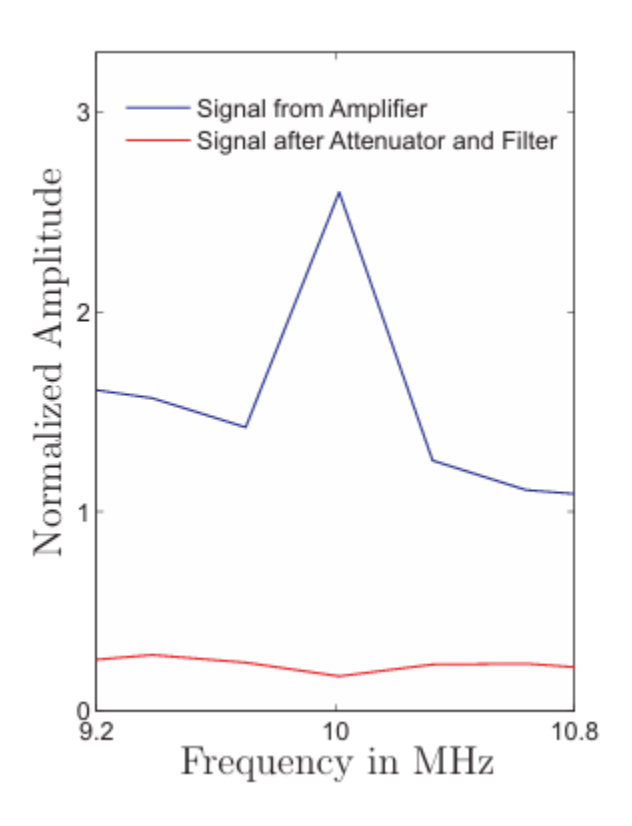


Figure 5-12. Comparison between Second Harmonic of Signal from Amplifier and Signal after Attenuator and Filter [143]

5.5.2.4 Transducers

Ultrasonic transducers play a crucial role in nonlinear ultrasonic measurements by converting electrical signals into mechanical waves and vice versa. Their performance directly influences the accuracy of measurements, making them one of the most critical components in the experimental setup. Even with a perfectly clean electrical input signal, the measurement results can be significantly distorted if the transducers introduce nonlinearities. To ensure accuracy, the transducers must exhibit minimal signal distortion and should not generate unwanted higher harmonics. In addition to maintaining linearity, the transmitting transducer should operate with high efficiency, meaning it should convert as much electrical energy into mechanical waves as possible. Similarly, the receiving transducer must efficiently convert mechanical waves back into electrical signals.

One of the most widely used transducer types is the piezoelectric ceramic transducer, commonly made from materials such as lead zirconate titanate (PZT) or lead meta-niobate. These transducers exhibit high electromechanical coupling efficiency, making them suitable for both linear and nonlinear ultrasonic applications. However, due to their material properties, PZT transducers can introduce internal harmonic distortion, which must be accounted for in nonlinear measurements. Alternatively, single-crystal transducers, such as quartz and lithium niobate transducers, are often preferred in high-precision nonlinear experiments. These transducers exhibit lower intrinsic nonlinearity, meaning they generate fewer unwanted harmonics and provide cleaner signals. Lithium niobate transducers are particularly effective in nonlinear ultrasonic testing due to their higher energy conversion

efficiency compared to quartz transducers. However, despite these advantages, single-crystal transducers are less commonly available, more expensive, and require specialized fabrication, making them less practical for many experimental setups. Another type of ultrasonic transducer is the electromagnetic acoustic transducer (EMAT), which operates through electromagnetic induction rather than direct contact with the material. EMATs are particularly useful in applications where coupling mediums cannot be used, such as high-temperature testing or rough surface inspections. However, their low efficiency and limited signal strength make them less suitable for nonlinear ultrasonic studies that require high-powered excitation signals. A more recent advancement in ultrasonic technology is the capacitive micromachined ultrasonic transducer (CMUT), which is based on MEMS (microelectromechanical systems) technology. CMUTs offer broad bandwidth and miniaturized transducer designs, making them ideal for high-frequency acoustic sensing applications. However, they typically have a lower signal-to-noise ratio (SNR) than piezoelectric-based transducers, which limits their effectiveness in nonlinear ultrasonic experiments.

In this study, PZT-based ultrasonic transducers have been chosen as the primary transducers for nonlinear ultrasonic measurements. While single-crystal transducers such as quartz and lithium niobate may provide lower intrinsic nonlinearity, several factors justify the use of PZT transducers in this research. First, PZT transducers are the industry standard for nonlinear ultrasonic testing and non-destructive evaluation. Their high availability, affordability, and ease of integration make them practical for experimental setups. Unlike single-crystal transducers, which are often more expensive and difficult to obtain, PZT transducers provide a reliable and cost-effective solution for nonlinear studies. Second, PZT transducers exhibit high electromechanical efficiency, allowing them to effectively generate and detect nonlinear ultrasonic waves. The efficiency of lithium niobate transducers in converting electrical energy to acoustic waves is often highlighted in literature, but PZT transducers also demonstrate strong energy conversion capabilities, making them effective in detecting second harmonic signals in nonlinear measurements. Although PZT transducers inherently introduce some nonlinearity, this issue can be corrected and accounted for through experimental calibration techniques. Baseline measurements of transducer-generated harmonics can be performed on reference samples, allowing the intrinsic nonlinearity of the transducer to be separated from the material's nonlinear response. Additionally, the experimental setup includes attenuators (RA-31, RA-32) and filtering techniques (RLPF-5 and HPF-10), which help minimize unwanted harmonic distortions, ensuring that the measured second harmonic signals originate primarily from the material under investigation. Furthermore, the high sensitivity and signal-to-noise ratio (SNR) of PZT transducers support their effectiveness in nonlinear ultrasonic testing. The selected 5 MHz transmitting transducer and 10 MHz receiving transducer provide sufficient excitation power and reliable second harmonic detection, making them suitable for the objectives of this research. Since second harmonic amplitudes are strongly dependent on the fundamental frequency wave amplitude, the high powerhandling capability of PZT transducers ensures adequate signal strength for nonlinear characterization. Finally, experimental repeatability and practical considerations further support the use of PZT transducers. Many previous nonlinear ultrasonic studies have successfully utilized PZT-based transducers, demonstrating their ability to accurately detect material nonlinearity. Additionally, using identical transducers for transmitting and receiving ensures consistent conditions, which improves measurement repeatability and reduces uncertainty [143].

In this study, the input signal for the transducer is a 5 MHz tone burst, which means the transmitting transducer is specifically designed to have its resonant frequency at 5 MHz Since this research focuses on detecting second harmonic generation, the receiving transducer is selected to have a resonant frequency at 10 MHz, which corresponds to twice the fundamental frequency of the transmitter. For the contact condition, oil was applied between both transducers and coupling the specimen.

5.5.2.4.1 Types of Transducers Used in This Research

This study utilizes two different types of straight-beam ultrasonic transducers one for transmitting signals and one for receiving, selected based on their frequency characteristics and application in nonlinear ultrasonic testing. Specifications of these transducers are in Table 5-7.

Table 5-7. Specifications of the 5 MHz Transmitting Probe and 10 MHz Receiving Probe Used in Nonlinear Ultrasonic Measurements

Specifications	5 MHz Ultrasonic Transducer (Transmitting Probe)	10 MHz Ultrasonic Transducer (Receiving Probe)
Centre Frequency	5 MHz	10 MHz
Chip Size	8 mm	8 mm
Sensitivity	44 dB	48 dB
Signal-to-Noise Ratio (SNR)	26 dB	29 dB
Initial Wave Width	14 mm	15 mm
Operating Temperature Range	-10°C to ~50°C	: -10°C to ~50°C

The selection of these transducers ensures high measurement accuracy in second harmonic generation experiments. The 5 MHz transmitter efficiently excites the material at its fundamental frequency, while the 10 MHz receiver is optimized to detect the second harmonic component, ensuring reliable characterization of material nonlinearity (Figure 5-13). Their low noise levels, high sensitivity, and temperature stability make them suitable for high-precision nonlinear ultrasonic testing in varied experimental conditions.



Figure 5-13. 10 MHz Ultrasonic Transducer (Receiving Probe)

5.5.2.5 Fixture

The measurement method used in this study requires that each transducer can be mounted independently without altering the bonding conditions of the other transducer. Additionally, both transducers must be positioned precisely opposite each other on either side of the sample. These requirements are met by the fixture illustrated in Figure 5-14. The fixture is adjustable, accommodating flat samples with different dimensions. The minimum sample size is constrained by the dimensions of the transducers themselves.



Figure 5-14. Fixture setup used in this study

5.5.2.6 Oscilloscope

The RIGOL MSO5104 oscilloscope was used to visualize and save the incoming signals from the received transducer, 10MHz. The oscilloscope captures average of 512 waveforms over one time-domain signal and the sampling rate is 500Ms/s. Once the signal is visualized by the oscilloscope, it was saved as csv. file for further signal processing.



Figure 5-15. RIGOL MSO5104 - Four Channel, 100 MHz Digital / Mixed Signal Oscilloscope

5.5.3 Experimental procedure:

The calibration process was conducted within the company, and after that, the device was used as follows:

The first step involved securely clamping the specimen in the fixture. It was important to ensure that the specimen was held firmly to prevent any changes in the coupling conditions when attaching the transmitter later, particularly in terms of the force applied to the transducers. However, excessive tightening was avoided to prevent surface damage or unnecessary stress on the specimen. Once the specimen was properly positioned, a small drop of oil was applied to the receiving transducer and the transducer was carefully secured to the specimen. To maintain consistency across multiple measurements, the exact position of the transducers was recorded to replicate the same coupling conditions in all tests. Additionally, the amount of oil applied on each side of the sample and the timing of the test were kept consistent to ensure reliable and repeatable measurements.

A thin couplant layer like oil enhances the efficient transmission of ultrasonic waves while minimizing harmonic generation caused by the coupling medium. Once the transducer is securely attached, the experimental setup is finalized. The Block Diagram for the Measurement of the Second or Third Harmonics using the Ritec SNAP system is showing in Figure 5-16 and Figure 5-17 and the set up that been used in this study is illustrated in Figure 5-18. The signal from the gated amplifier is initially attenuated by 20 dB and then low pass filtered before reaching the transmitting transducer. After propagating through the sample, the signal is captured by the 10 MHz receiving transducer.

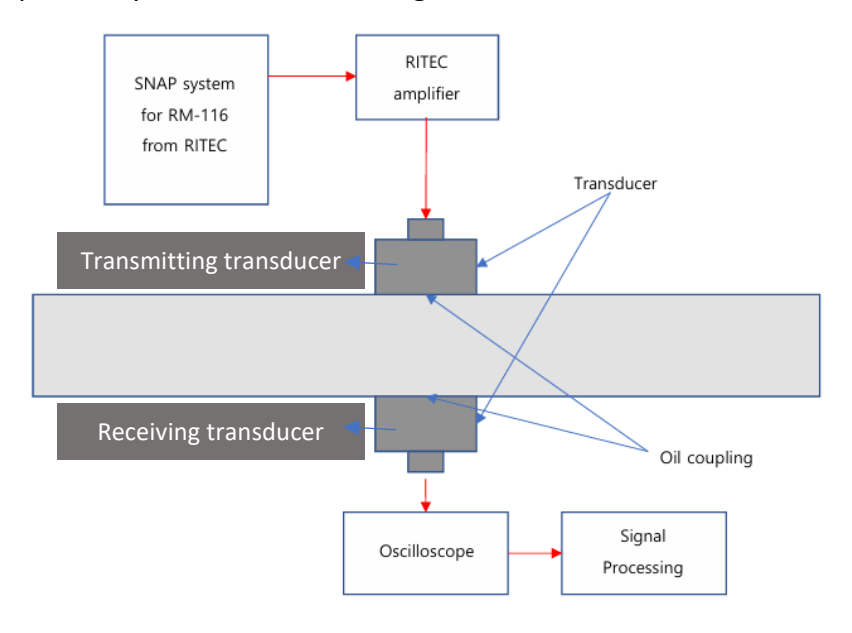


Figure 5-16. Longitudinal wave measurement setup schematic [144]

Block Diagram for Measurement of the Second and/or Third Harmonics

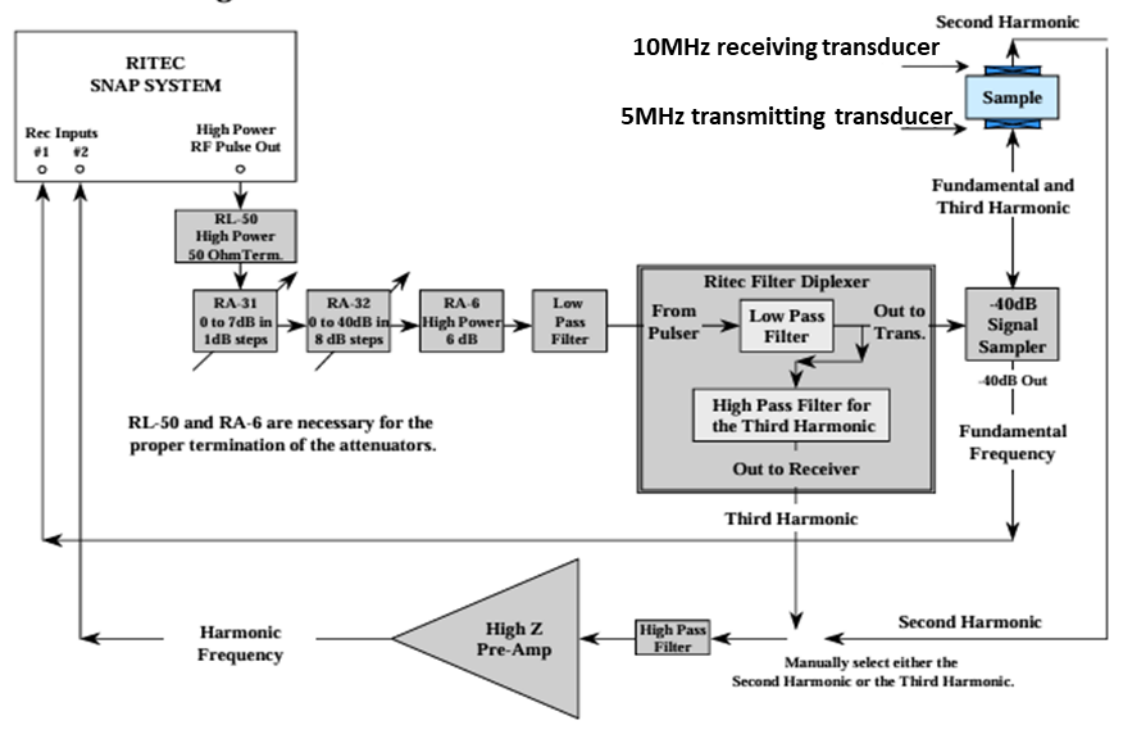


Figure 5-17. Block Diagram for the Measurement of the Second or Third Harmonics using the Ritec SNAP system [141]

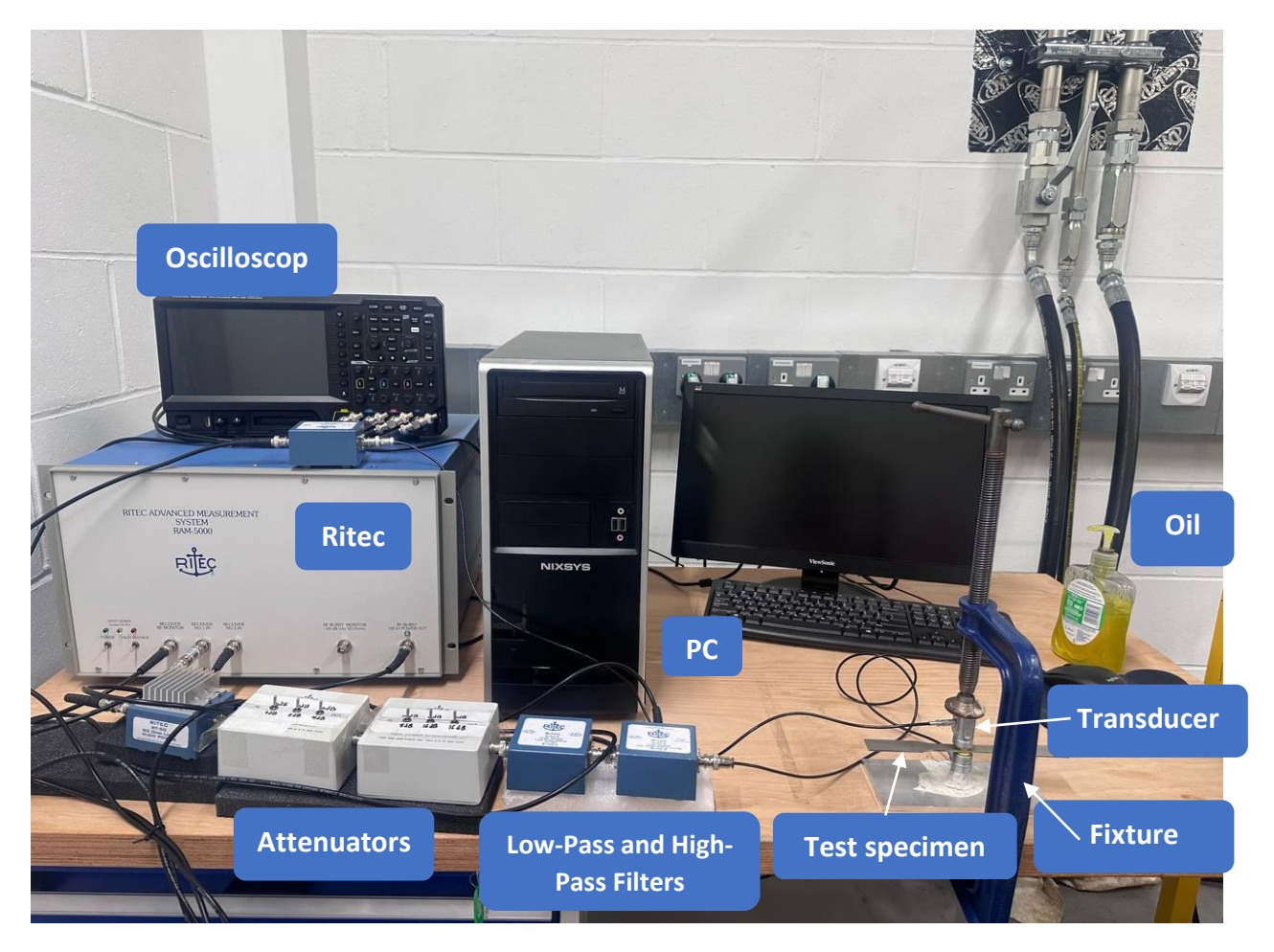


Figure 5-18. Experimental Setup for nonlinear acoustics measurements in this study

5.5.3.1 Input and output signal parameters for SHG measurement

In the Second Harmonic Generation (SHG) measurement setup, various input and output signal parameters must be carefully adjusted to ensure accurate detection of the nonlinear response. These parameters influence the excitation conditions, wave propagation, signal acquisition, and the measurement of the nonlinear parameter (β or NLP).

5.5.3.1.1 Input Signal Parameters

The input parameters define how the excitation signal is generated and transmitted into the sample. The key adjustable parameters include:

Source Frequency (MHz): Determines the fundamental frequency of the input wave, typically set at 5 MHz for the transducer used in this setup. Adjusting this parameter affects the wavelength, penetration depth and nonlinear interactions.

Burst Width (μ s): Defines the duration of the excitation pulse. A longer burst width improves frequency resolution, whereas a shorter burst width enhances time resolution. To avoid overlapping of signals, the burst width should follow the relation d/v, where d is the sample thickness and v is the wave velocity. For 316L stainless steel with a thickness of 2 mm and a longitudinal wave velocity of approximately 5800 m/s, the calculated optimal burst width is about 0.345 μ s. However, due to equipment limitations, the machine only offers a discrete

set of selectable burst widths. Among these options, the closest available value is 2.5 μ s, which was selected for all experiments.

Burst Cycles: Specifies the number of oscillations in the transmitted pulse. A higher number of cycles ensures better excitation at the transducer's resonance frequency.

Burst Cycles=Burst Width × Frequency

The important settings are the source frequency and burst width. A longer burst improves accuracy by providing better frequency resolution; however, if it is too long, the incident and reflected waves will overlap at the receiver, making it difficult to extract the incident wave separately. The rest of these settings can be considered fine adjustments and can influence the resolution.

Amplitude (% FS): Controls the excitation power of the transducer. Higher amplitudes enhance nonlinear effects but may introduce unwanted distortions if too high.

RF Level Control (V): Adjusts the voltage applied to the transducer, affecting the transmitted wave energy. A higher RF level leads to increased harmonic generation.

Gate Delay (\mus): Determines when the system starts acquiring the received signal. Proper adjustment ensures that only the desired portion of the wave is captured, avoiding noise from reflections.

Gated Amplifier Output: Controls whether the amplifier is active. It must be turned ON to apply the amplified excitation pulse to the transducer.

High-Pass and Low-Pass Filters (MHz): Low-pass filters (such as the RLPF-5) remove unwanted harmonics from the excitation signal, ensuring a pure fundamental wave is transmitted. High-pass filters (such as the HPF-10) remove the fundamental frequency in the receiver, allowing the detection of only the second harmonic (10 MHz). Table 5-8 presents all the selected parameters for the output signals used in this experiment.

Table 5-8. Selected input signal parameters and their corresponding values for the SHG measurement experiment. These parameters define the excitation conditions, ensuring proper wave propagation and harmonic generation

Input signal parameters	Value
source Frequency	5 MHz
Burst Width	2.5 μs
Burst Cycles	12.5 cycles
Amplitude	100 % FS
RF level control	2.797 V
Gate Delay	2.5 μs
Gated Amplifier Output	ON
High-Pass Filter	10 MHz
Low-Pass Filter	5 MHz
Multi-Frequency Tracking	Enabled

5.5.3.1.2 Output Signal Parameters

The output signal parameters control how the received signals (fundamental and second harmonic components) are processed and measured. Key parameters include:

Receiver Gain (dB): Adjusts the amplification of the received signal. The gain must be optimized to prevent overloading the receiver while maintaining a high signal-to-noise ratio.

Tracking Frequency: The receiver must be tuned to capture the fundamental frequency (5 MHz) on Signal Set 1 and the second harmonic frequency (10 MHz) on Signal Set 2.

Integrator Rate (V/V_{ms}): Defines how the received signals are averaged over time to improve measurement stability. A properly adjusted integrator rate ensures that the signal remains within the 2 - 4 V range, preventing overdriving of the receiver (Figure 5-19).

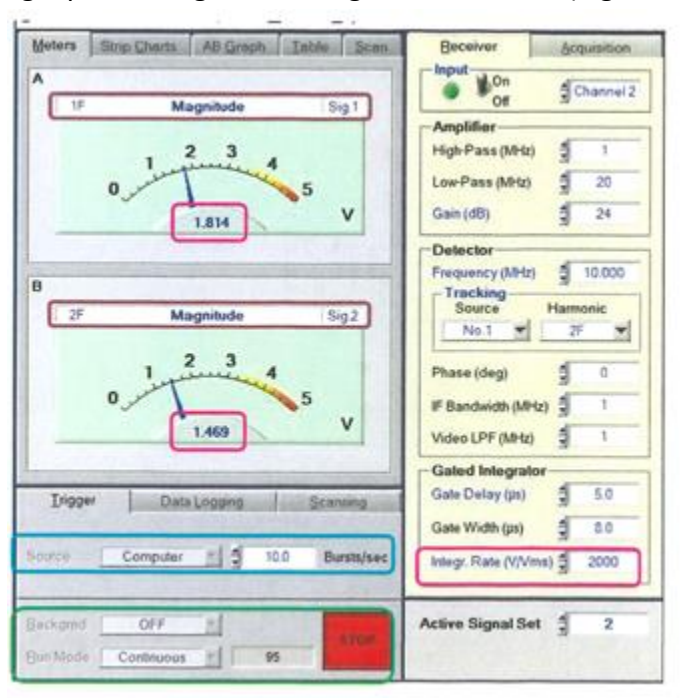


Figure 5-19. Properly adjusted integrator rate to avoid overdriving of receiver $\,$

Signal Sets: The system records two signal sets: Signal 1 for the fundamental component (5 MHz) and Signal 2 for the second harmonic (10 MHz). These settings ensure accurate measurement of the nonlinear response.

Multi-Frequency Tracking: Used to track different frequency components in real-time, ensuring accurate differentiation between the fundamental and harmonic signals.

Table 5-9 presents all the selected parameters for the output signals used in this experiment.

Table 5-9. Configured output signals parameters for Channel 1 and 2 for SHG measurement experiment

Output signal parameters	Value channel 1	Value channel 2
Receiver Gain	64 dB	30 dB
Tracking Frequency	Fundamental: 5 MHz	Second Harmonic: 10 MHz
Integrator Rate	196 V/V _{ms}	2000 V/V _{ms}
Gate Delay	2.0 μs	5.0 μs
Gate Width	8.0 μs	8.0 μs
Active Signal Sets	2 (Fundamental and Second Harmonic)	
Multi-Frequency Tracking	Enabled	
Acquisition Mode	Differential (0°/90°/180°/270°)	
Averaging Mode	OFF (can be enabled to improve signal-to-noise ratio)	

5.5.4 Signal processing

5.5.4.1 Raw data acquisition and visualization

The first stage in the signal processing workflow involves capturing and visualizing the raw time-domain data from the received transducer. The RIGOL MSO5104 oscilloscope is used to collect the signal transmitted through the specimen, with an averaging of 512 waveforms to minimize noise and enhance the clarity of the received data. The raw data consists of an amplitude-modulated waveform that represents the ultrasonic wave propagating through the material. Figure 5-20 shows the type of signal that is observed in oscilloscope.



Figure 5-20. Time averaged base signal measured from transducer

The fundamental component at 5 MHz and the second harmonic at 10 MHz are extracted from the spectrum. The magnitudes of these two frequency components serve as the primary parameters for computing nonlinearity.

5.5.4.2 Attenuation levels and their role in measurement

To systematically investigate the nonlinear response, different levels of attenuation are introduced into the transmitted signal. The RITEC RA-31 and RA-32 high-power attenuators are used to control the signal amplitude by inserting incremental attenuation steps (1 dB per step) into the transmit line. The purpose of using different attenuation levels is reducing the transmitted signal gradually, it ensures that the fundamental signal remains within a linear operating range, preventing overdriven signals that might lead to artificial harmonic generation. Additionally, improving Signal-to-Noise Ratio (SNR) Considerations can happens. As attenuation increases, the signal amplitude reduces, affecting the SNR. At lower excitation levels, increased fluctuations in the nonlinear parameter NLP are observed due to noise dominance. Averaging techniques are applied to mitigate these effects. During the experiment, the attenuation is increased from 0 dB to 32 dB while measuring the corresponding fundamental and second harmonic amplitudes at each step. This allows a comprehensive dataset that accounts for different levels of input excitation energy.

5.5.4.3 Extracting nonlinear parameter (NLP)

Once the fundamental and second harmonic magnitudes are extracted from the frequency domain data, Figure 5-21 can be generated and the nonlinear parameter (NLP) is calculated. This figure shows the relationship between square of the first harmonic amplitude and second harmonic amplitude over the changes in amplitudes. From this we can easily think that the slope of the plot is the and by dividing by x which is sample thickness the relative nonlinearity can be calculated.

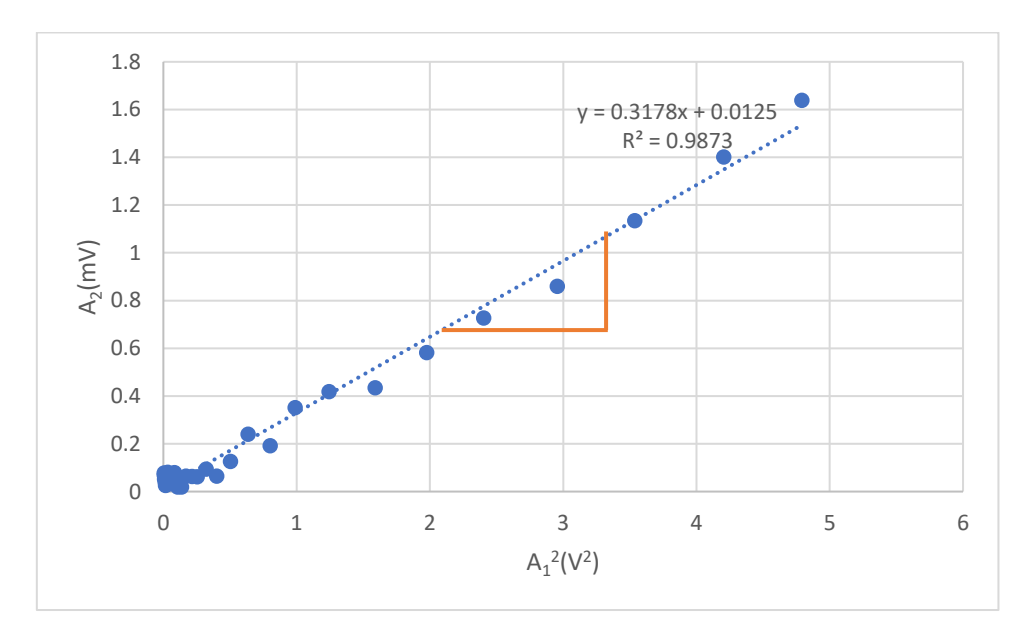


Figure 5-21. Relationship between square of first harmonic and second harmonic amplitudes

5.5.5 Signal processing methods

Signal processing methods are essential tools for analysing and interpreting complex data in various fields. Among the commonly used techniques are the Fast Fourier Transform (FFT), Short-Time Fourier Transform (STFT), and Wavelet Transform. Each of these methods has its

strengths and limitations. For instance, the FFT is powerful for frequency analysis but does not provide time-localized information. The STFT addresses this by dividing the signal into shorter segments, though it still faces a trade-off between time and frequency resolution. Wavelet Transform provides a more flexible approach by offering multi-resolution analysis, but it can be computationally intensive. For further details on these methods, please refer to [145], In this research, however, we will focus on the superheterodyne receiver method for signal processing, which will be discussed in detail in the following sections [145].

5.5.5.1 Superheterodyne receiver

While Wavelet Transform (WT) improves upon Short-Time Fourier Transform (STFT) by providing adaptive time-frequency resolution, it still has limitations when applied to nonlinear ultrasonic testing. Choice of wavelet basic function is of high importance. WT relies on predefined basis functions (e.g., Morlet, Daubechies, Haar) and the accuracy of the signal decomposition depends on selecting an appropriate wavelet, which is not always straightforward also, If the wrong wavelet function is chosen, it may not accurately represent the frequency components of the signal. WT still suffers from spectral leakage, meaning some frequency components spread into adjacent frequencies, reducing accuracy. Edge effects occur when the wavelet does not fully cover the beginning or end of the signal, leading to artefacts in the time-frequency representation and WT requires complex mathematical transformations and is computationally expensive, making real-time signal analysis challenging. These limitations highlight the need for an alternative approach. The RITEC SNAP device employs a superheterodyne receiver with quadrature phase-sensitive detection to analyse signals in the frequency domain. This technique does not require a full FFT transformation but instead relies on frequency scanning and phase detection to extract meaningful data [142].

Nonlinear ultrasound analysis requires highly sensitive detection techniques capable of isolating weak nonlinear signals from background noise. The Ritec SNAP system achieves this through several advanced techniques. First, it employs superheterodyne frequency conversion, which shifts the received signal to an intermediate frequency (IF), improving the signal-to-noise ratio. Second, it utilizes quadrature phase-sensitive detection, which separates the signal into real and imaginary components, enabling precise measurement of both amplitude and phase information. Additionally, gated integrators selectively process desired signal components while rejecting irrelevant noise. Finally, multiple frequency synthesizers allow precise control over transmission and reception frequencies, facilitating advanced nonlinear measurements. These methods provide enhanced signal clarity and measurement precision, making them superior for applications such as harmonic analysis, difference frequency generation, and high-resolution nonlinear ultrasound studies. Furthermore, while Fourier and Wavelet methods are designed for broad signal analysis, the SNAP system is specifically engineered for detecting harmonic generation, difference frequencies, and phase-sensitive nonlinear interactions.

5.5.5.1.1 Signal processing

Utilizing superheterodyne receive is a method commonly employed in radio communication (Figure 5-22), to improve the detection and processing of nonlinear ultrasound signals.

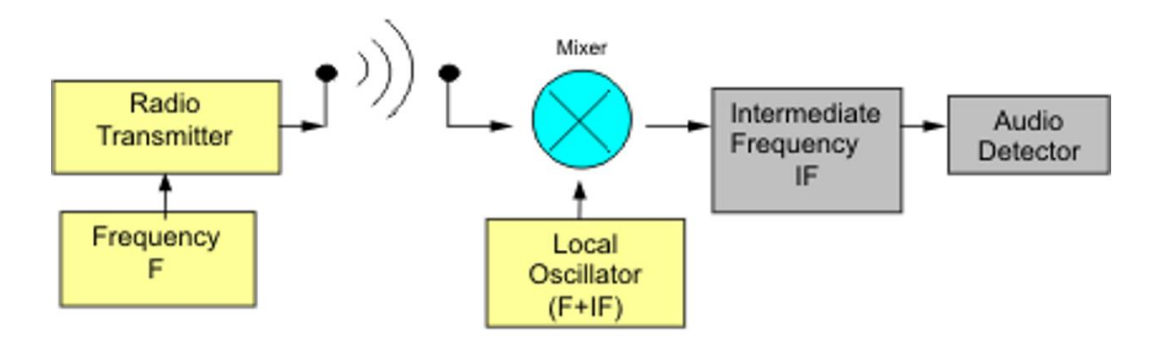


Figure 5-22. A block diagram showing the arrangement of Superheterodyne receiver used in radio transmission and reception[142]

This approach involves shifting the received high-frequency ultrasound signals to an intermediate frequency (IF), facilitating more precise analysis while enhancing signal-to-noise ratio. The superheterodyne system in the SNAP unit requires three distinct frequencies for operation: the ultrasonic transmission frequency (F), the intermediate frequency (IF), and the local oscillator frequency (LO). When a signal is received, it is mixed with the local oscillator frequency, generating two new frequency components: a sum frequency and a difference frequency. The system filters out the sum frequency while amplifying and analysing the difference frequency, which corresponds to the intermediate frequency (IF). This method enables the use of narrow band tuned IF amplifiers, which remain stable across different operating frequencies and require minimal adjustment. One of the challenges at very low operating frequencies is that both the sum and difference frequency components may fall within the bandwidth of the IF filter, causing signal ripples in the output. To address this issue, low-pass filters are implemented to suppress unwanted fluctuations, and gated integrators further reduce residual noise by averaging the detected signal over time. These additional processing steps enhance the reliability and precision of nonlinear ultrasound measurements. By implementing a superheterodyne detection system, the Ritec SNAP system provides significant advantages over traditional ultrasound detection techniques. It enables better noise rejection, stable signal amplification, and improved phase-sensitive detection, making it an essential tool for high-precision nonlinear ultrasound studies.

This section details how the superheterodyne receiver shifts received ultrasound signals to an intermediate frequency (IF) for better processing and phase-sensitive detection allows the system to extract both amplitude and phase information, which is crucial for analysing nonlinear acoustic properties and then Several techniques are implemented to minimize errors, including low-pass filtering, phase synchronization, and digital signal calibration.

Figure 5-23 shows the diagram of the instrumentation approach used in RAM-5000 SNAP system.

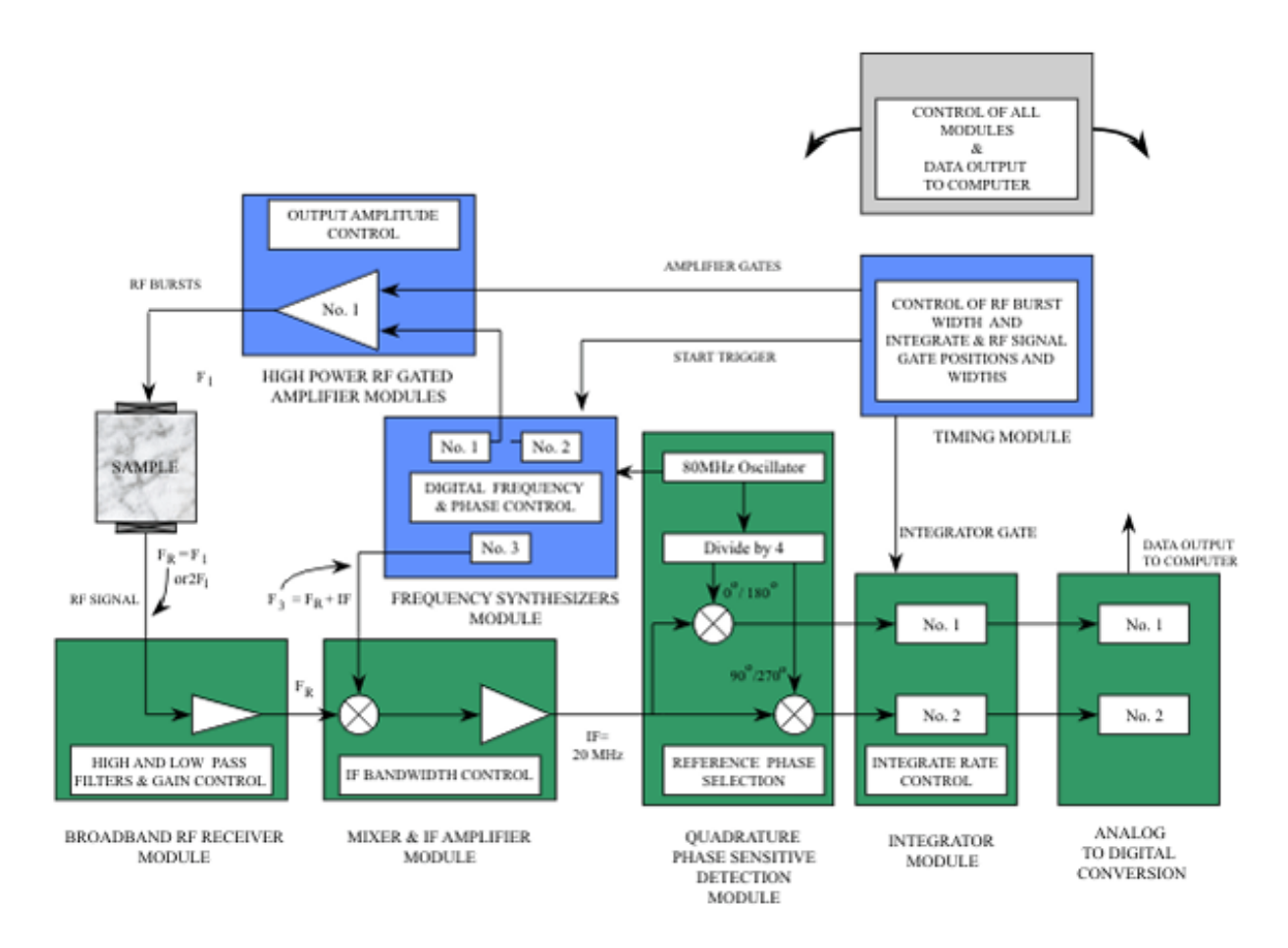


Figure 5-23. Block diagram of RAM system [142]

The primary input to the gated amplifier is derived from Synthesizer No. 1, which generates the signal used in the system. In some cases, Synthesizer No. 2 may also contribute to the output, but for the sake of discussion, we assume that only Synthesizer No. 1 is used. The transmitted signal can be mathematically represented as:

Transmitted signal = $A_{S1}\cos(2\pi F_{S1}t)$

5-2

 A_{S1} is the amplitude of the transmitted signal and F_{S1} is the frequency of the transmitted signal, t represents time, which is taken as zero at the beginning of each transmission burst when the synthesizers are activated.

5.5.5.1.2 Superheterodyne receiver and phase-sensitive detector

The superheterodyne receiver in the Ritec SNAP system is designed to process ultrasonic signals by shifting their frequencies to an intermediate frequency (IF) for improved filtering and analysis. This process helps maintain the phase relationships of the received signals, allowing for more accurate detection of nonlinear acoustic properties [142].

How the Superheterodyne receiver works is that the received ultrasonic signal is multiplied by a reference signal using an RF multiplier circuit. This shifts the signal to an intermediate frequency (IF) for better processing. The IF signal is amplified and passed through filters to remove noise. The filtering process improves signal clarity and measurement precision. The

IF signal is mixed again to bring it down to zero frequency (baseband). This is done using phase-sensitive detectors, which extract key signal components. These detectors are driven by two reference signals at the same frequency but shifted by 90°. The system multiplies the received signal with the two 90°-shifted reference signals. This method, called quadrature phase detection, separates the real and imaginary parts of the signal. The extracted signals are filtered and integrated to remove unwanted high-frequency components. The final signal is converted into digital format using a 16-bit analog-to-digital (A/D) converter. A computer processes the digital signal to determine amplitude and phase information.

To better understand the operation of the superheterodyne receiver, the received ultrasonic signal can be described as a narrow-band function that varies in amplitude and phase. This signal f(t) is first amplified by a wide-band RF amplifier with a gain range of 78 dB, ensuring the signal is strong enough for processing. Once amplified, the signal is multiplied with the synthesizer's output signal (V_{S3}) at frequency ($IF + F_r$) using an analog multiplier (mixer). Mathematically, this step is represented as:

$$V_{S3}=A_{S3} \sin (2\pi (IF+F_r) t)$$
 5-3

where: A_{S3} is the amplitude and shape of the synthesizer signal, IF is the intermediate frequency, F_r is the received signal frequency, t is time.

This assumes that Synthesizer 3 has been configured to generate the expected receive frequency plus IF (20 MHz). As a result of this multiplication, the system produces a new signal at an intermediate frequency (IF). Since the received ultrasonic signal may have different frequency components than the transmitted signal (F_{S1}), the phase term ϕ_{Ir} is directly related to the transmission phase at time zero. Therefore, the received signal at the pre-amplifier input is given by:

$$f(t) = A_r(t)\sin(2\pi F_r t + \phi_r)$$
5-4

Where, $A_r(t)$ is the time-dependent amplitude and ϕ_r accounts for phase shifts in the transducers and sample including the effects of acoustic transit time.

After amplification, the signal undergoes another multiplication process with the synthesizer reference output. This results in a mixed voltage signal:

$$V_{\text{Mixer}} = g_2 A_r(t) \cos(2\pi I F t - \phi_r) + \text{High Frequency.Term}$$
 5-5

Where, g_2 accounts for the RF gain, reference signal amplitude A_{S3} , and conversion efficiency of the multiplier. Any high-frequency components, such as those at (IF + 2F_r), are filtered out by the IF amplifier, which operates at a fixed centre frequency of 20 MHz with selectable bandwidths of 0.4 MHz, 1 MHz, and 4 MHz. To ensure phase accuracy, the IF reference signal is obtained by dividing the synthesizer clock to generate a reference phase with a fixed starting point near 0°:

Reference₀= $A_{Ref} \sin(2\pi IFt)$

5-6

The remaining portion of the signal, which contains the phase information of the ultrasonic wave, is amplified and then multiplied by two reference signals that are 90° apart in phase. This process is known as quadrature phase-sensitive detection and is performed using analogue multipliers. The outputs are:

PhaseDet.No.1=
$$g_3A_r(t)\sin\phi_r$$
+High Frequency. Term

5-7

PhaseDet.No.2=g3Ar(t)cos ϕ_r +High Frequency. Term

5-8

Where g₃ includes total system gain and efficiency factors.

The high-frequency components are effectively removed using integrators and low-pass filters, leaving only the baseband phase components of the received signal. This ensures that the extracted signal accurately represents the phase shifts caused by nonlinear acoustic interactions. If the local oscillator synthesizer (Synthesizer 3) is not set to the correct frequency, unwanted terms may appear in the phase detector output, leading to frequency discrepancies between the transmission and reception signals [142].

5.5.5.1.3 Analog integration in phase detection

The analogue integration process is a crucial step in signal processing that allows for accurate measurement of amplitude and phase while eliminating high-frequency noise components. If the high-frequency terms from the phase detection equations (5-8 and 5-7) are completely filtered out, the amplitude and phase (ϕ_r) can be calculated after measuring the instantons value of the phase detector at the centre of its waveform or under stable conditions. However, if the signal bursts contain only a few cycles, the low-pass filters struggle to completely remove the high-frequency components without affecting the integrity of the detected signal. In such cases, it becomes difficult to determine where exactly to take the instantaneous value for accurate phase measurement. Figure 5-24 illustrates a typical detection scenario. In this example the upper trace represents the RF signal, which contains more than two oscillation cycles. The lower trace shows the detected signal, processed to align with a 0° phase reference. It is evident that removing the RF components from the detected outputs without introducing distortion is a challenging task. To resolve this, phasedetected signals are passed through an analogue integration circuit, which provides the following benefits: Removes high-frequency RF components without distorting the baseband signal. Makes gate position non-critical, allowing for more flexible signal processing. Enhances the signal-to-noise ratio, improving measurement accuracy.

Detection & Integration Phase Angle = 0 deg RF Signal 0 Unfiltered 90 deg Phase Detector (M2) 0 90 deg Integrator (I2) Unfiltered 0 deg Phase Detector (M1) 0 deg Integrator (I1) 0 0 2 8 10 20 12 14 16 18 Time

Figure 5-24. RF receiver, Quadrature phase sensitive detector and integrator outputs for a typical signal with $\phi_r=0^\circ[142]$

The integration process in the Ritec SNAP system is controlled by the integrator gate, which determines the time limits for signal integration. The rate of integration (r₁) is managed by the computer, ensuring precise timing. The integrator gate is positioned so that integration begins before and ends after the signal, ensuring a complete signal capture. A sample-and-hold circuit retains the integrated signal value until it is digitized and recorded by the computer for further processing. The system uses two integrators (No.1 and No.2) to extract the quadrature components of the received signal. Their outputs are expressed:

$$I_1 = r_1 g_3 \cos \varphi r \int\limits_{t1}^{t2} A_r(t) dt$$

$$I_2 = r_1 g_3 \sin \varphi r \int\limits_{t1}^{t2} A_r(t) dt$$
 5-10

 I_1 and I_2 are the outputs of Integrator No.1 and No.2, respectively. t_1 and t_2 are the start and stop times defined by the integrator gate. After integration, the phase angle of the received signal is determined using the ratio of the two integrator outputs:

$$\Phi_{r} = tan^{-1} \left(\frac{I_{2}}{I_{1}}\right)$$
 5-11

This equation shows that the phase angle is obtained by computing the arctangent (inverse tangent) of the ratio between the two integrated signals [142].

5.5.6 Experimental determination of optimal gain and magnitude for nonlinear ultrasonic testing

To determine the optimal criteria for gain and magnitude, a series of tests were conducted using a sample with 0 fatigue cycles, ensuring that the material's response remained stable throughout the measurements. The experiment was performed in two stages:

- 1- The magnitude for both Channel 1 and Channel 2 was kept constant, while different gain values were applied to analyse their effect on the measurement.
- 2- The gain and the magnitude of channel 1 was kept constant and the magnitudes for Channel 2 were varied to observe how changes in signal amplitude affected the results.

These tests helped to identify the most suitable gain and magnitude settings for achieving accurate and repeatable nonlinear ultrasonic measurements while minimizing signal distortion and noise amplification.

For first experiment, the magnitude of both Channel 1 (fundamental frequency, A_1) and Channel 2 (second harmonic, A_2) was kept constant, while the gain values were varied from 38 dB to 24 dB to observe their effect on the nonlinear ultrasonic measurements. Results related to this is reported in 6.3.2.

5.5.7 Measurement procedure for repeatability assessment

An important aspect to consider for nonlinear ultrasound method, like electrical resistivity, is ensuring the repeatability of the setup to guarantee that the experiment can be reliably reproduced. In this study, measurements were taken four times on the same material under identical conditions using an as-received sample. Between each measurement, the transducers were removed, the sample was cleaned, and the transducers were reattached to assess repeatability. Results regarding this experiment can be found in section 6.3.2.

5.6 Microscopy techniques

5.6.1 Optical microscope (OM)

For optical microscopy, flat samples were sectioned from the middle of the gauge length of the flat fatigue specimens, as this region experiences the most significant cyclic deformation. The samples were cut using a precision abrasive cutting machine (Struers Secotom-15) with continuous water-based cooling to minimize thermal damage and preserve the microstructure. The cut samples were mounted in thermosetting epoxy resin using a Buehler SimpliMet hot mounting press, then subjected to standard metallographic preparation procedures. Surface grinding was performed sequentially using silicon carbide (SiC) abrasive papers with grit sizes of 320, 600, 800, 1200, and 2400, under constant water flow to prevent overheating and clogging.

After grinding, the specimens were polished using with a 0.05 μ m alumina suspension on a soft cloth pad to achieve a mirror-like finish suitable for microstructural observation. For microstructure revelation, the polished surfaces were etched using Adler's etchant, a common solution for revealing features in austenitic stainless steels such as 316L. The etchant consisted of 10 ml hydrochloric acid (HCl), 15 ml nitric acid (HNO₃), and 10 ml glycerol (C₃H₈O₃). Due to its strong reactivity, each sample was etched for 2 to 5 seconds, allowing features such as grain boundaries, deformation bands, and twin structures to become clearly visible under the optical microscope. The prepared specimens were examined using a Zeiss Axioscope optical microscope (OM), which provided high-resolution imaging for detailed microstructural characterization.

5.6.2 Experimental procedure TEM

Sample preparation for microstructural characterization using transmission electron microscopy (TEM) involved sectioning plates parallel to the loading axis from the gauge length and the middle section of the flat fatigue test specimen. The discs were marked to indicate the loading direction. Samples were cut from the gauge area using precision cutting machine, and the slices and were mechanically ground using SiC paper up to grit size 4000 until the thickness of 100 µm was obtained. Then thin discs of 3 mm in diameter were extracted using a punch hole device. Next, these discs were electropolished by the Struers Tenupol-5 electrolytic polish apparatus at a DC potential of 35 volts, using the solution of 5% perchloric acid and 95% methanol. The polishing temperature was set to be -35 °C. This polishing voltage was obtained by scanning at various values to obtain an optimal value. The best polishing current range was achieved to 135 to 170 mA, and the electrolyte flow rate is set to 20. The total polishing time is about 20~30 sec. This step induces a hole formation in these thin discs ensuring electron transparency. This polishing time was obtained by considering an optimum size of hole achieved by luminosity sensor whose value was set to be 45. If the polishing voltage is too low, the electro-polishing effect will be minimal during polishing and the corrosion will be the dominant process, which has no polishing and thinning effects on the sample.

Then specimens were observed using a double tilt holder in a Thermo Fisher Talos F200i S-FEG TEM, equipped with EDS, STEM imaging, HAADF capabilities. The acceleration voltage condition for STEM imaging was 200 kV. Initially, the area around the thin hole in the centre of the TEM sample was examined to select approximately 10 grains that best represented the microstructural condition. For each cycle all grains have been investigated and the structures that representing the dominant structures were reported. To maintain consistency in the loading direction (LD) during observations, the samples were aligned along the holder β axis with tilting limited to approximately 0 to ± 2 degrees.

The (110) beam direction is selected for imaging because it aligns with the slip direction in FCC crystals, like stainless steel 316L, which is being investigated in this study. Dislocations in FCC materials preferentially move along directions with the highest linear atomic density. In

this context, the $\langle 110 \rangle$ direction, when combined with the $\{111\}$ slip planes (the planes with the highest atomic packing density), forms the most favourable slip system for dislocation motion. Imaging along the $\langle 110 \rangle$ beam direction provides an optimal projection of the $\{111\}$ planes and facilitates clear visualization of dislocation arrangements within these active slip systems. For each cycle multiple grains were analysed and 2 to 3 grains that shows dominant structures is reported.

5.6.2.1 Common techniques for observation of dislocations by TEM:

Transmission electron microscopy techniques are powerful and versatile tools in the direct characterization of dislocations at multiple scales. Since the initial direct studies of TEM on dislocations, various diffraction contrast techniques such as Bright Field, Dark Field, Weak-Beam and Convergent Beam, two beam condition and STEM-HAADF have been developed to observe and analyse dislocations' properties, including Burgers vectors, interactions, configurations and distributions across numerous crystalline materials under diverse loading conditions. The structure of a typical TEM is showed in Figure 5-25. A standard TEM comprises an electron gun that generates incident electrons. These emitted electrons are focused as they pass through two condenser lenses and subsequently travel in a straight path onto a thin specimen. Upon interacting with the crystal structure, the electron beam is diffracted at specific orientations in accordance with Bragg's law. The objective lens, positioned directly beneath the specimen, focuses the diffracted beams onto the back focal plane. At this plane, electron beams exiting the thin specimen at the same angle converge at the same point, forming the diffraction pattern of the specimen. In TEM's diffraction mode, the diffraction pattern can be visualized by correctly operating the subsequent lenses in the image below a ray diagram for making an image with a conventional TEM is shown. All transmitted and diffracted beams leaving the specimen are combined to form an image at viewing screen but in this mode the specimen shows little contrast. By tracing the rays in Figure 5-26, each point in the objective lens's back focal plane contains rays from all parts of the specimen. This means not all rays in the back focal plane are needed to form an image. An image can be created with only the rays passing through a single point in this plane. The points in the back focal plane are unique because all rays entering a given point are scattered by the specimen at the same angle. By placing an "objective aperture" at a specific spot in the back focal plane, an image is formed using only the electrons diffracted at a particular angle. This results in two imaging modes, bright filed and dark field imaging mode which is discussed in next part [23].

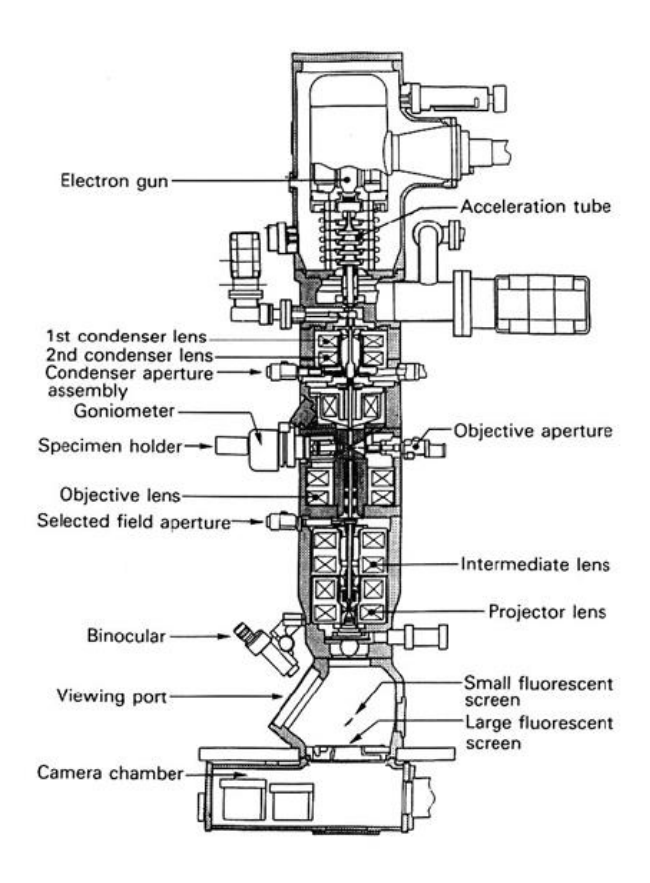


Figure 5-25. The structure of a typical TEM [23]

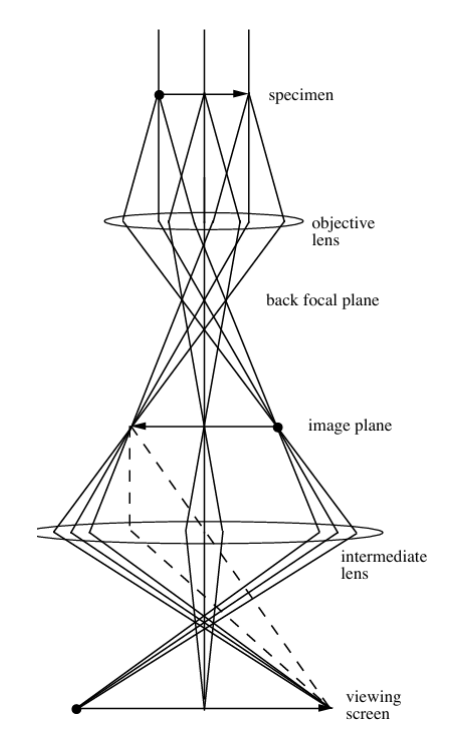


Figure 5-26. Ray diagram of electron beam in TEM, image mode [146]

5.6.2.1.1 Two beam condition - Bright field and Dark field imaging

The two-beam condition is achieved by tilting the crystal so that only one strong diffracted beam (g) and the direct beam (un-scattered beam) are significantly excited. Bright-field image is an image that is produced by the transmitted wave (the wave that undergoes no diffraction) in a diffraction pattern formed on the back focal plane of the objective lens, using the objective aperture. In the image, a location where diffraction takes place appears dark, whereas a location where diffraction does not take place appears bright. The bright-field image, together with the dark-field image, is used for analysis of lattice defect and measurement of specimen thickness. When the aperture is set to allow only the transmitted (un-diffracted) electrons to pass through, a bright-field (BF) image is created. When the aperture is set to allow only the diffracted electrons to pass through, a dark-field (DF) image is created. Figure 5-27a show the BF and Figure 5-27b shows the DF mode.

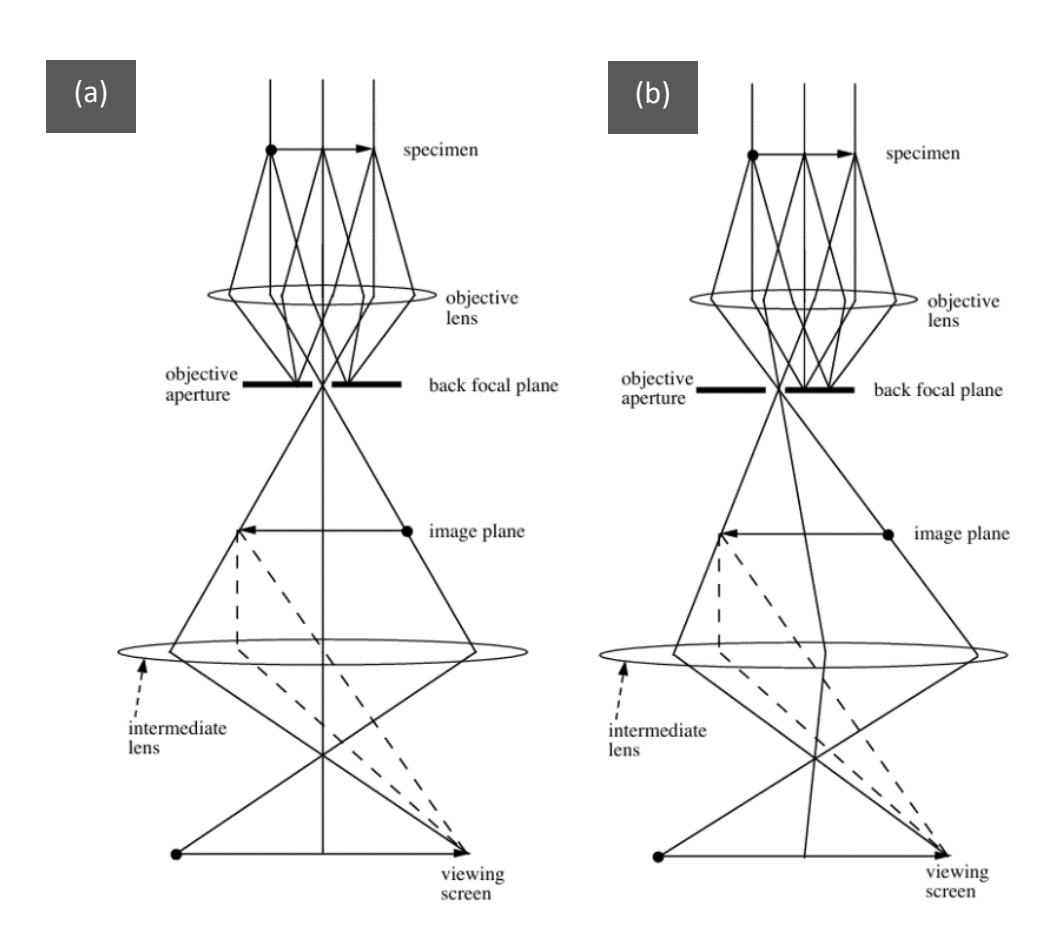


Figure 5-27. (a) bright-field (BF) mode. (b) dark-field (DF) mode [146] $\,$

In Figure 5-28 an example of diffraction under two beam condition and its corresponding dark field and bright field imaging can be seen [22].

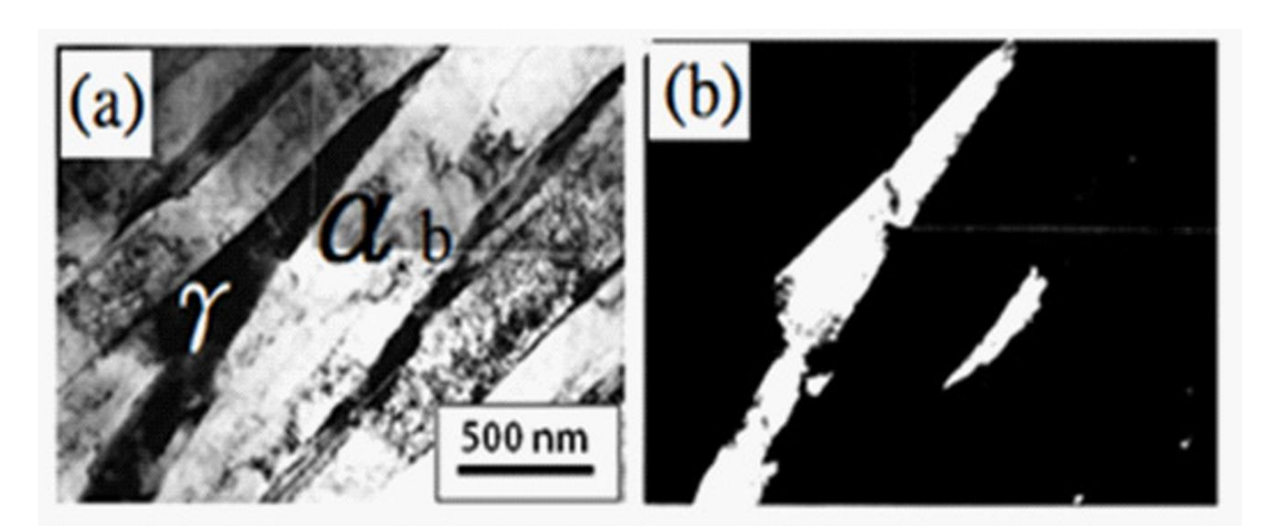


Figure 5-28. Bright-field (a) and dark-field (b) TEM images of austenite and bainite ferrite in 1C-2Ti-2Mo steel aging at 550 °C for 60 min [147]

For crystalline materials, BF-TEM and DF-TEM images are mainly dominated by diffraction contrast that is highly sensitive to the direction of the incident beam. Therefore, it is very difficult to obtain these techniques to get images with clear contrast through the entire tilt range.

5.6.2.1.2 Selected area electron diffraction

To image the diffraction pattern of a specimen using Transmission Electron Microscopy (TEM), the intermediate lenses are adjusted to focus on the back focal plane of the objective lens. A second aperture, known as the "intermediate aperture," is then placed in the image plane of the objective lens to isolate the diffraction pattern of a specific area. This method, called Selected Area Electron Diffraction (SAED), follows a series of steps (Figure 5-29). Initially, the specimen is inspected to locate an area of interest. The intermediate aperture is then positioned to illuminate this selected area exclusively. Switching the microscope to diffraction mode allows for capturing the diffraction pattern of the chosen area (Figure 5-30. This diffraction pattern is important for obtaining information about the crystallographic orientation of the selected area, relative to a specific orientation, such as the loading direction (LD) [148].

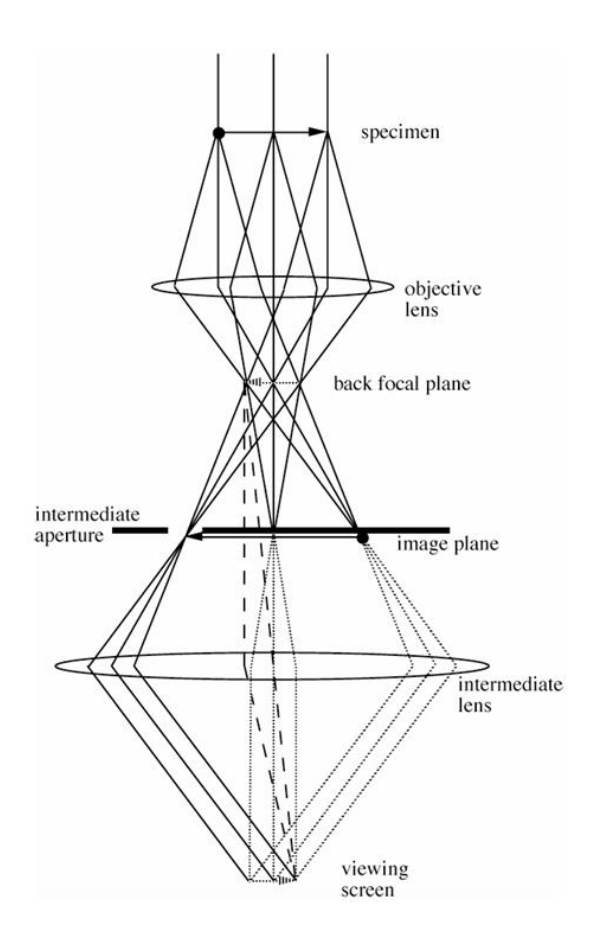


Figure 5-29. Selected Area Diffraction (SAD) mode [146]

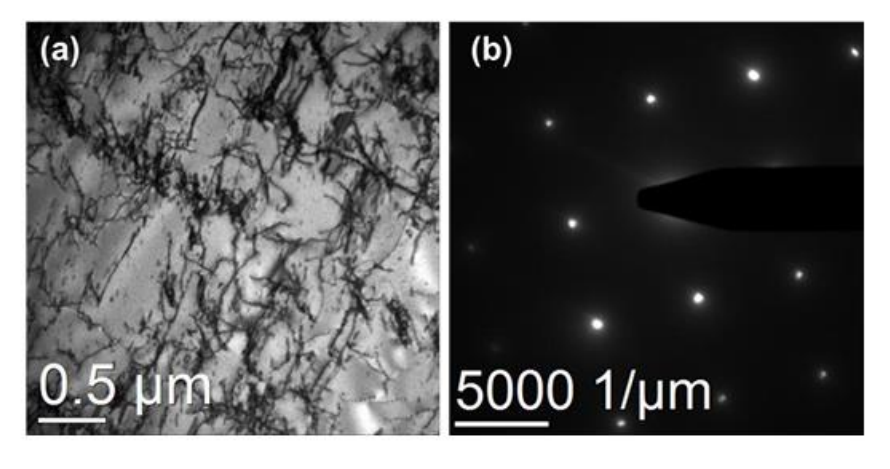


Figure 5-30(a) BF image of dislocations and (b) its corresponding SAED (the diffraction pattern of the <001> beam direction) - AISI 316L [146]

5.6.2.1.3 High-Angle Annular Dark-Field (HAADF) – Scanning Transmission Electron Microscopy (STEM)

The fundamental principle of conventional TEM relies on electron diffraction patterns, which are produced when electrons interact with the crystalline structure of a sample. By focusing the electron beam, TEM enables detailed examination of microscopic regions, including single crystals. These diffraction patterns serve as a critical tool for investigating structural features such as defects, interfaces, and other microstructural properties within materials.

Scanning transmission electron microscopy (STEM) works by focusing a highly concentrated electron beam into a small probe and systematically scanning it across the sample, like the operation of a scanning electron microscope (SEM). The image is constructed pixel-by-pixel by detecting the electrons transmitted through the sample at each scanned point. The sample requirements are like those in conventional TEM, as enough electrons must pass through the specimen to generate a clear image. As in Figure 5-31 STEM electrons interact with the sample in three main ways: Some electrons pass through the sample without being scattered, traveling between the atoms. Other electrons interact with the electron cloud of an atom, losing energy by knocking electrons out of their shells. This process is known as inelastic scattering. Electrons traveling near the atomic nucleus are scattered to high angles by the Coulomb field, a process known as elastic scattering. The scattering intensity increases with the atomic number (Z), making this property useful in STEM for analysing materials with atomic number contrast, such as copper precipitates in an aluminium matrix [149, 150].

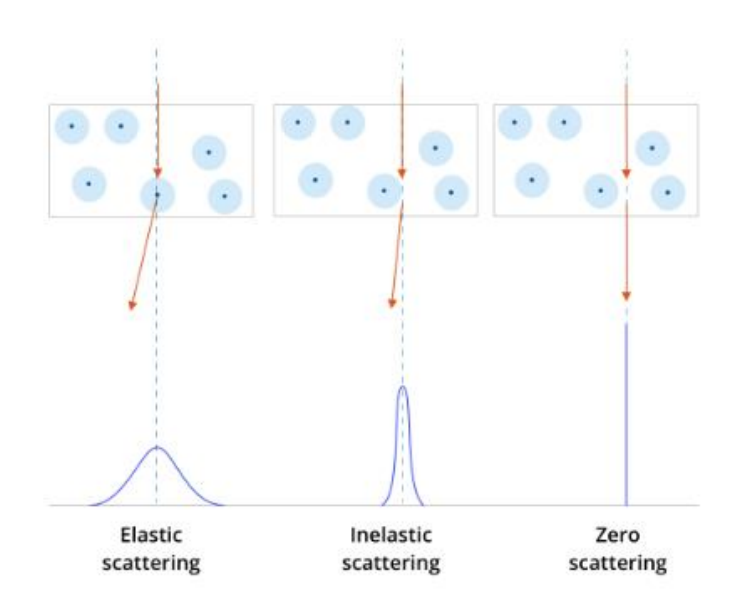


Figure 5-31.Interaction of electrons with specimen in TEM [151]

In STEM mode, several detectors are used to capture electrons scattered at different angles simultaneously, and the resulting intensity is displayed as micrographs of the scanned region, as shown in Figure 5-32. These detectors include:

Bright Field (BF): A disc-shaped detector that collects electrons transmitted directly along the microscope's optical axis.

Annular Dark Field (ADF): A ring-shaped detector positioned around the BF detector. It allows the BF signal to pass through while detecting diffracted or scattered electrons.

High-Angle Annular Dark Field (HAADF): A larger annular detector that captures electrons scattered at very high angles. HAADF relies on elastic scattering at high angles, where the scattering intensity increases with the atomic number (Z).

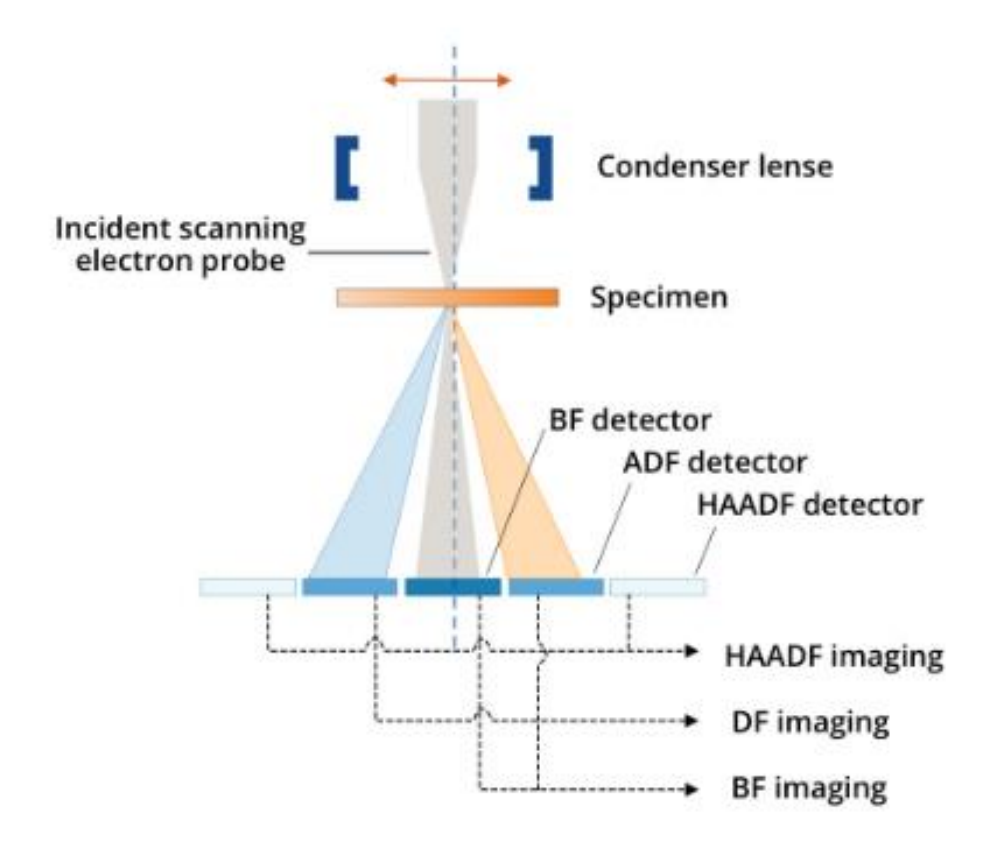


Figure 5-32. STEM detectors [151]

In this project, STEM-HAADF has been selected due to its effectiveness in analysing dislocation structures and patterns. Unlike conventional TEM imaging, HAADF minimizes wave interference effects, such as phase contrast and diffraction artefacts, resulting in the near absence of bending contours. These contours, which typically occur in TEM due to variations in crystal orientation or thickness, can obscure or complicate the interpretation of dislocation structures. By eliminating such artefacts, HAADF produces a clear and direct image, enhancing the clarity and accuracy of dislocation analysis. A key advantage of STEM-HAADF is its high spatial resolution. The finely focused electron probe in STEM scans across the sample, achieving atomic-scale resolution. This allows for precise detection and mapping of individual dislocation lines and the surrounding atomic arrangements. Furthermore, like conventional TEM, HAADF imaging is sensitive to thickness variations and strain fields introduced by dislocations. These structural changes affect the scattering of electrons, and HAADF effectively captures these variations due to its sensitivity to high-angle elastic scattering.

Some examples of TEM and STEM-HAADF of 316L stainless steel in this study is reported in section 7.3.1 showing the difference between these two methods.

This chapter presented a comprehensive overview of the experimental procedures, equipment, and characterization techniques employed in this study. These methodologies collectively establish the foundation for evaluating early-stage fatigue damage in 316L stainless steel. The key novelty of this work lies in the integration of two highly sensitive nondestructive evaluation techniques — electrical resistivity (ER) and nonlinear ultrasonic parameter (NLP) measurements — within a single, well-controlled fatigue testing framework. A systematic calibration and error-mitigation strategy was developed using the four-probe delta-mode configuration for ER and an optimized second harmonic generation setup for NLP. This dual-technique approach, combined with high-repeatability testing under identical fatigue regimes, enables a direct correlation between electrical, acoustic, and microstructural responses — a capability rarely reported in the literature. Additionally, the implementation of a nano-ohm– $n\Omega$ resolution resistivity measurement system and the precise synchronization of acoustic signal processing provide a new level of accuracy in capturing microstructural changes during the very early fatigue stages (<10% of life). These methodological innovations form a solid experimental foundation for the subsequent chapters, where the results and sensitivity of both ER and NLP methods will be evaluated in detail.

Chapter 6. Non-destructive method results

In this chapter, the rationale for selecting high-cycle fatigue for this study is first presented. This is followed by the results of electrical resistivity and nonlinear ultrasonic measurements. For each method, the repeatability and optimized setup parameters are discussed prior to addressing their application in fatigue damage monitoring.

6.1 Selection of high-cycle fatigue for early-stage damage detection

As mentioned in 2.2.6 and 2.2.7, there are two types of fatigue tests: high-cycle fatigue (HCF) and low-cycle fatigue (LCF). In this study, high-cycle fatigue (HCF) was chosen to investigate early-stage fatigue damage detection. Initially, preliminary tests were conducted using low-cycle fatigue (LCF) to assess its suitability for studying the early stages of fatigue damage. However, optical microscopy (OM) analysis of both the surface and cross-sections of LCF-tested samples revealed that even after 10 cycles, a significant number of slip bands were already visible, and the surface had become considerably rough. These observations indicated that LCF induces plastic deformation after a few cycles, making it less applicable for studying the initial stages of dislocation activity and patterns before significant microstructural changes occur. The corresponding optical microscopy images supporting these observations are presented in the following section.

To support this investigation, fatigue tests were performed under a low-cycle fatigue (LCF) regime using flat specimens and fatigue life of 400,000 cycles. The tests were carried out under load-controlled tension-tension loading with a stress ratio (R) of 0.1, a maximum stress of 290 MPa, and a frequency of 1 Hz at room temperature (Details of this fatigue condition are provided in Table 5-4). Fatigue condition are Surface roughness measurements at the early stages of fatigue can indicate the presence of surface intrusions and extrusions, which are typically associated with the development of macro-slip bands. However, it is important to note that slip bands—particularly micro-slip bands—can form well before any detectable surface roughness appears. Therefore, while surface roughness changes may correlate with slip activity, the formation of slip bands can also be confirmed independently through optical microscopy at earlier stages. Figure 6-1 shows surface roughness versus the number of cycles. As can be seen, there is an increase in surface roughness after 10 cycles. To ensure a uniform microstructure with minimal pre-existing dislocations and no visible slip bands, specimens were annealed at 900 °C for 1 hour under an argon atmosphere, followed by cooling in air. Optical microscopy was performed on specimens in the annealed condition, as well as after 2, 5, and 10 cycles of fatigue. The corresponding changes can be observed in the optical microscopy images.

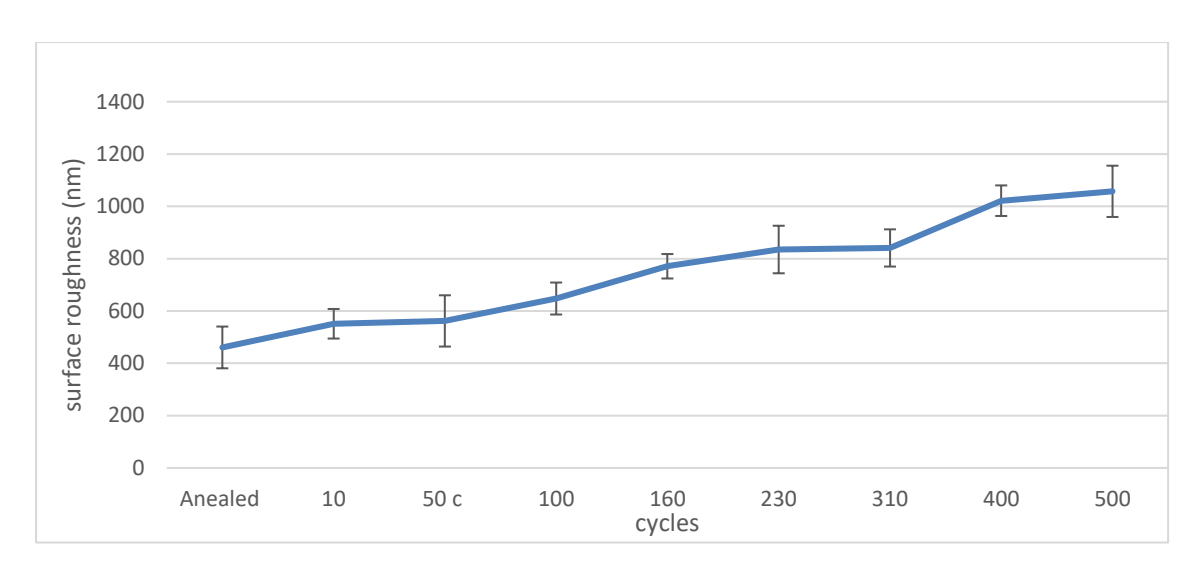


Figure 6-1. Surface roughness measurement at early cycles of fatigue to predict the initiation of slip lines and then validate it by optical microscopy

Based on the surface roughness analysis, optical microscopy was employed to capture images from both the centre and edges of the specimen in the annealed condition, as well as after 2, 5, and 10 fatigue cycles. These images, presented in Figure 6-2 through Figure 6-5 reveal the progressive evolution of surface features associated with cyclic loading. Notably, after 10 cycles, distinct slip bands become clearly visible at the edges of the specimen, as indicated by the arrows in Figure 6-5. This observation suggests that plastic deformation has begun to localize, leading to the formation of slip bands—a key microstructural indicator of fatigue damage. The presence of slip bands at such an early stage (the 10th cycle) indicates that fatigue-induced microstructural changes initiate rapidly under the loading conditions applied. However, it is important to note that while slip bands are clearly observable after 10 cycles, their absence in earlier cycles cannot be definitively concluded from optical microscopy alone. It is possible that slip bands had already begun to form at a finer scale undetectable by optical microscopy. To accurately determine the onset of slip band formation, more advanced characterization techniques such as Scanning Electron Microscopy (SEM) or Transmission Electron Microscopy (TEM) would be required. Nevertheless, this level of microstructural analysis falls outside the scope of the current study. These findings have significant implications for the choice of fatigue regime in this research. The early appearance of visible slip bands suggests that low-cycle fatigue may not provide a sufficiently broad window to investigate the progressive evolution of microstructural changes using non-destructive testing (NDT) methods. Since one of the aims of this study is to evaluate the potential of electrical resistivity and nonlinear ultrasonic for monitoring fatigue damage, a regime that allows for more gradual damage accumulation is preferable. Consequently, high-cycle fatigue is selected as the more appropriate focus for this project, as it enables a more detailed and extended examination of fatigue-related dislocation activity and microstructural evolution over time.

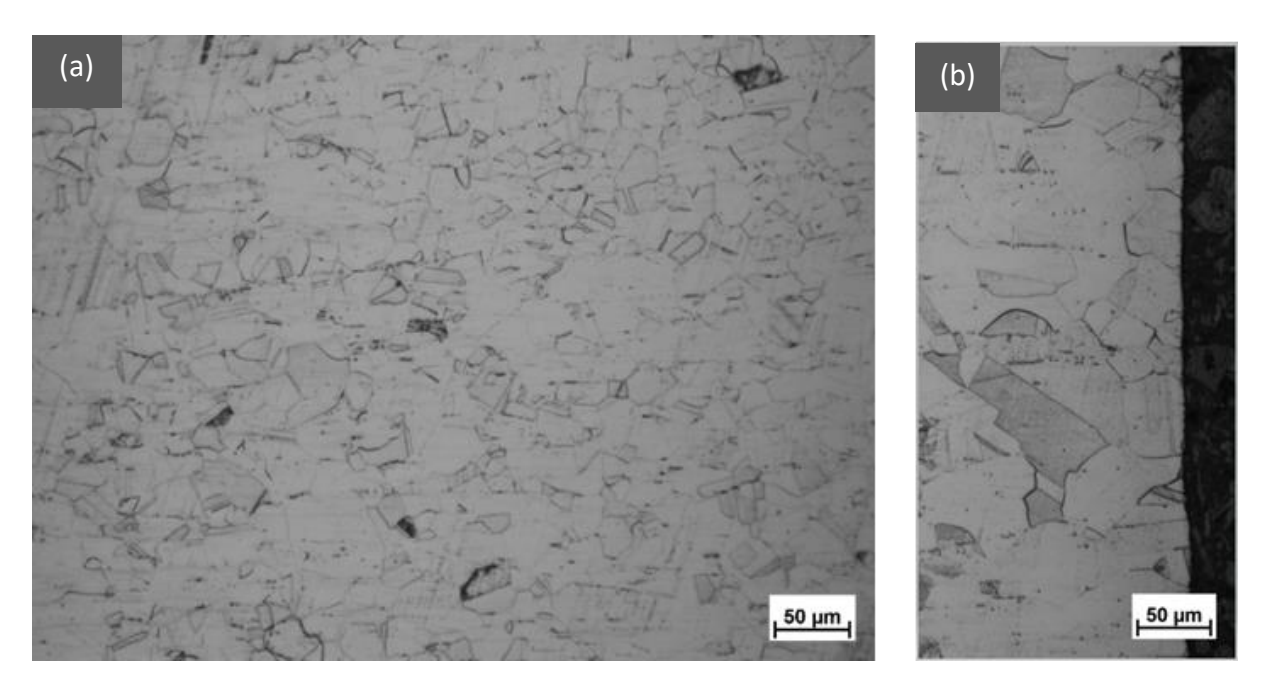


Figure 6-2. Optical microscopy images of the specimen in the annealed condition. (a) Centre of the cross-section; (b) Edge of the cross-section

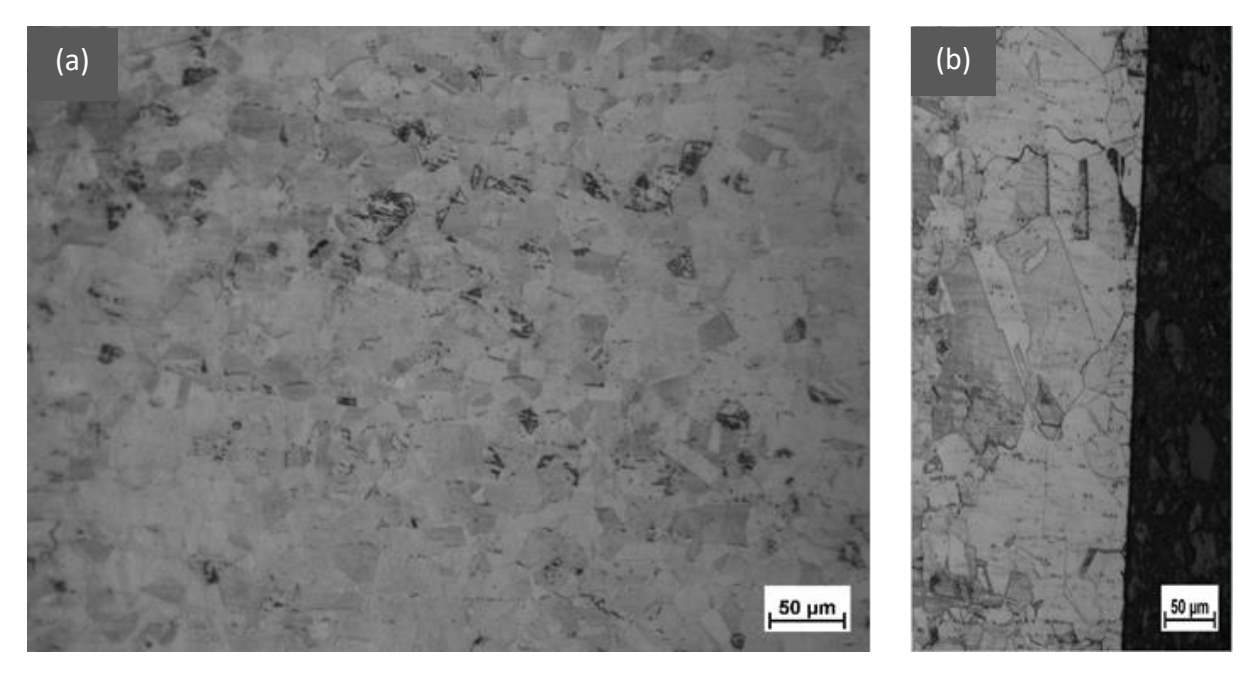


Figure 6-3. Optical microscopy images of the specimen after 2 fatigue cycles. (a) Centre of the cross-section; (b) Edge of the cross-section

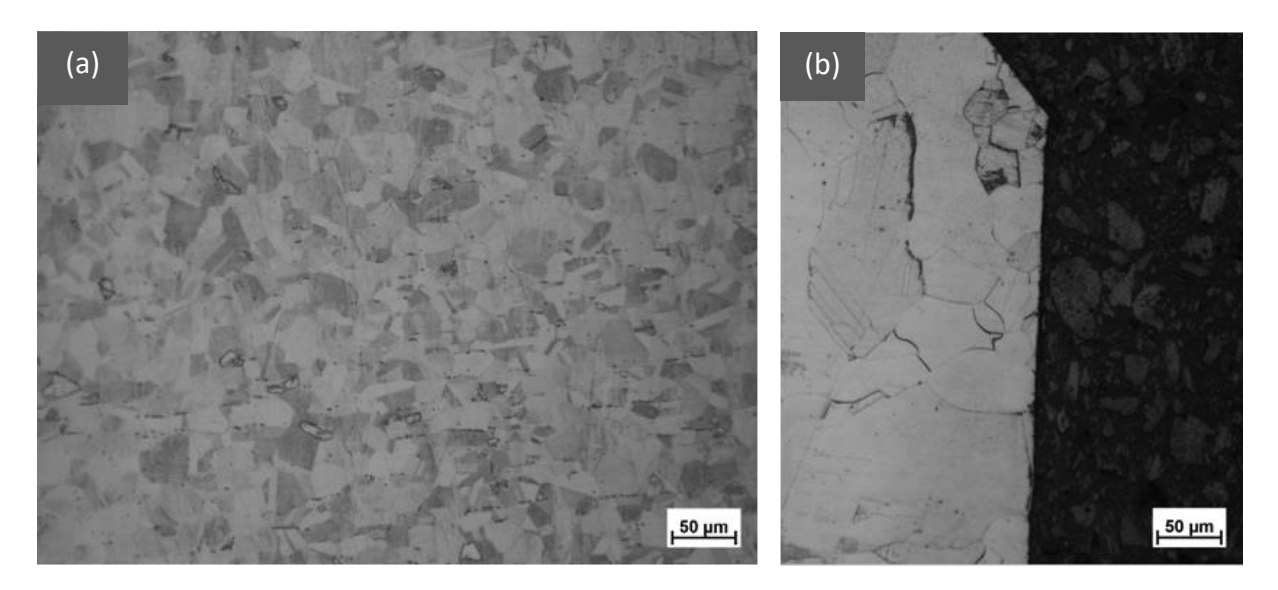


Figure 6-4. Optical microscopy images of the specimen after 5 fatigue cycles. (a) Centre of the cross-section; (b) Edge of the cross-section

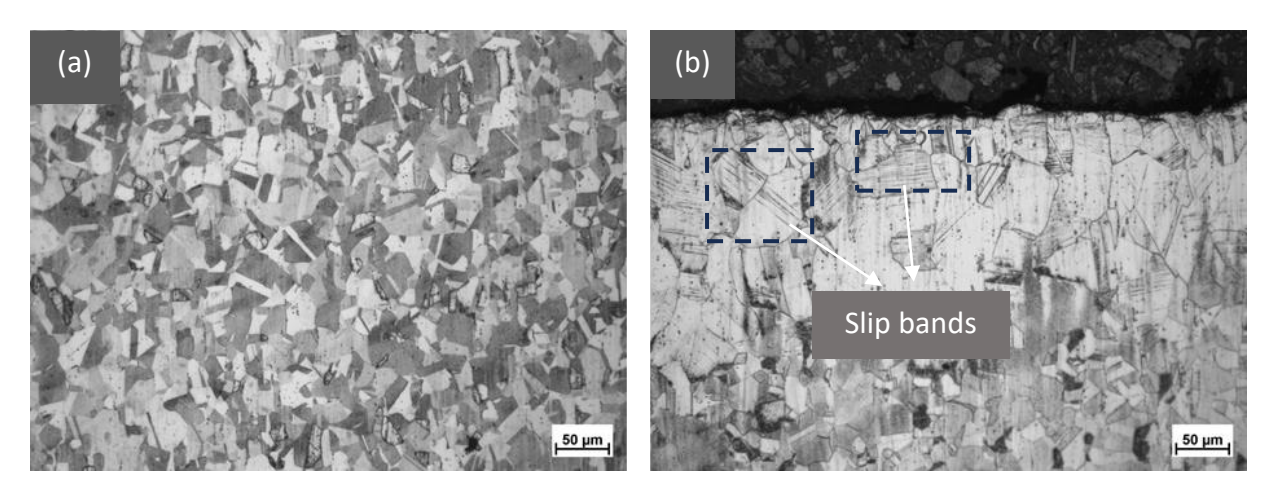


Figure 6-5. Optical microscopy images of the specimen after 10 fatigue cycles. (a) Centre of the cross-section; (b) Edge of the cross-section

Furthermore, optical microscopy images shown in Figure 6-6 and Figure 6-7 corresponding to the sample surface after 50 and 500 fatigue cycles, respectively—demonstrate the presence of well-developed persistent slip bands (PSBs) distributed across multiple grains. These PSBs are indicative of localized plastic deformation resulting from fatigue. The observation of PSBs as early as 50 cycles further validates the selection of high-cycle fatigue for this study.

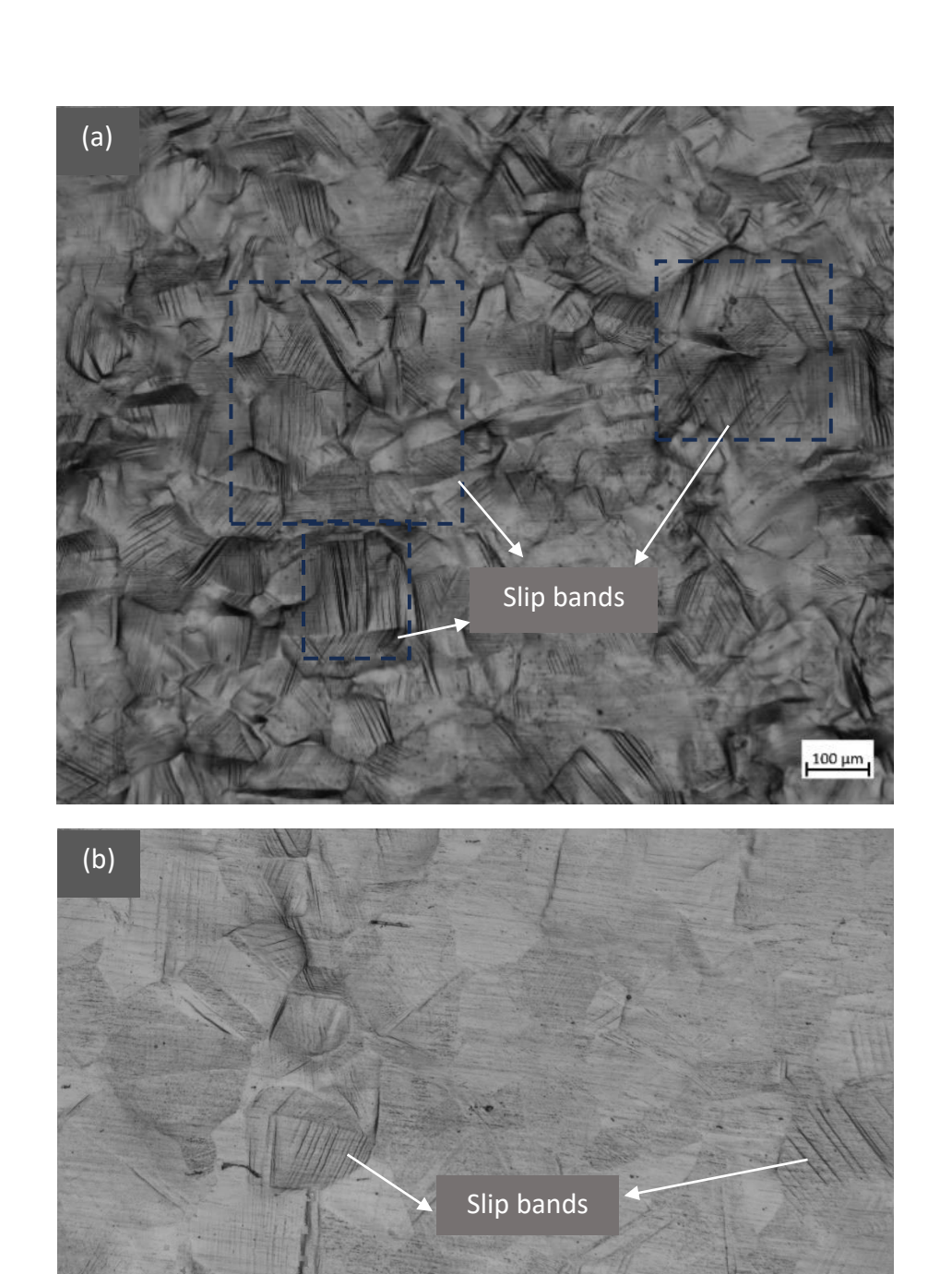
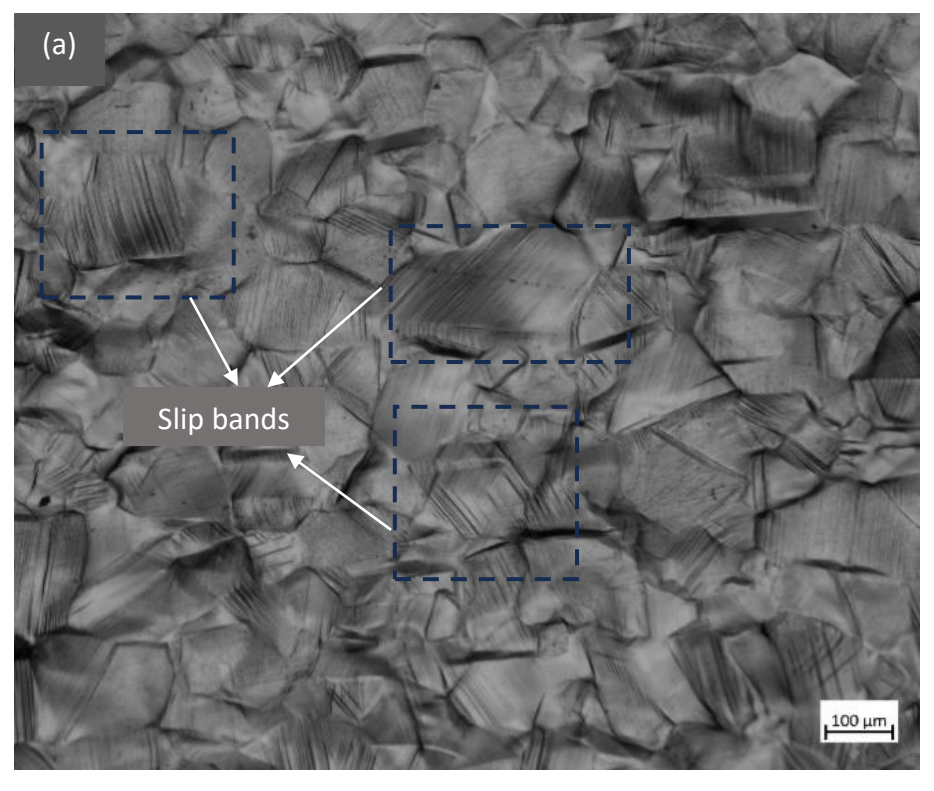


Figure 6-6. Optical microscopy images of the specimen surface after 50 fatigue cycles at two different magnifications. (a)

Lower magnification; (b) Higher magnification



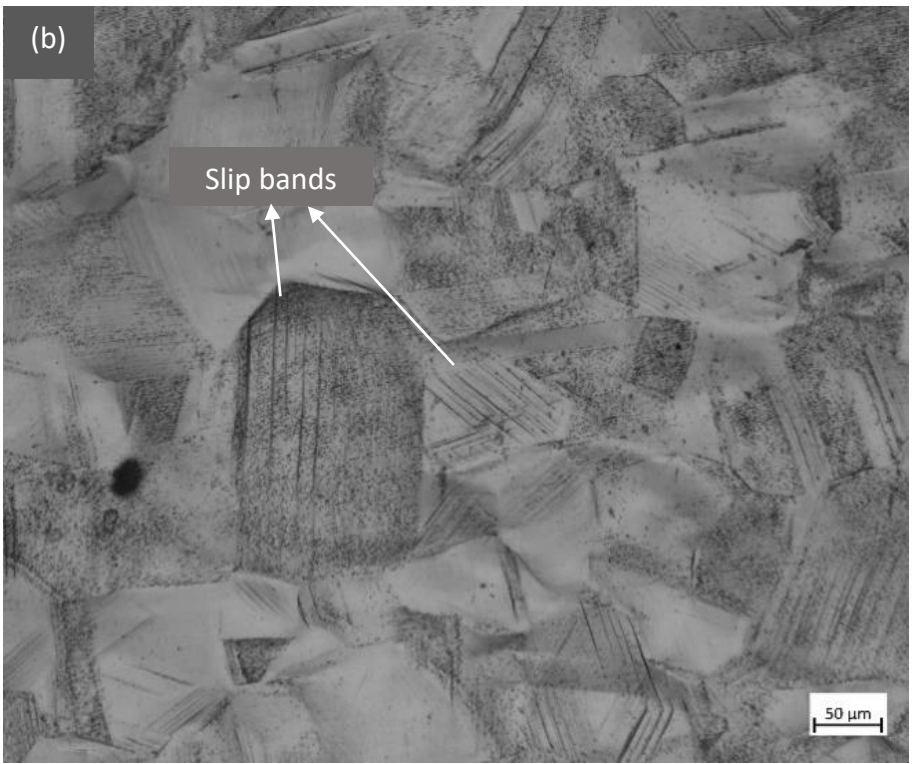


Figure 6-7. Optical microscopy images of the specimen surface after 500 fatigue cycles at two different magnifications. (a)

Lower magnification; (b) Higher magnification

Due to these findings, HCF was selected, as it allows for a more gradual accumulation of dislocations, providing a better opportunity to detect subtle changes in material behavior using non-destructive testing (NDT) methods before the formation of macroscopic features like persistent slip bands on surface.

6.2 Electrical resistance method results

In alignment with Objective 1 of this thesis, an initial experimental evaluation is conducted to assess the repeatability and reliability of electrical resistivity method. Prior to applying this technique for fatigue damage detection, multiple baseline measurements were conducted to ensure the consistency and reliability of the setup. These tests also helped determine optimal parameters such as probe spacing and position, measurement duration, and the influence of surface roughness. This step is essential for verifying that this method could produce stable results across repeated trials, thereby confirming its suitability for detecting microstructural defects associated with early-stage fatigue. Different materials were used in these preliminary evaluations depending on the purpose of each test. For the probe spacing study, a long aluminium bar (AA6082) was used to accommodate variable probe distances and evaluate their influence on measurement stability. For the repeatability test, both 316L stainless steel and aluminium were tested to demonstrate that the method performs consistently across materials with different resistivity values. For the reliability assessment, aluminium (AA6082), copper, and 316L stainless steel were included to verify that the system produces reproducible and accurate readings across materials with a wide range of electrical conductivities.

6.2.1 Effect of probe spacing

This experiment aimed to investigate the influence of varying the spacing between probes on electrical resistivity (ER) measurements using an AA6082 aluminium bar. Understanding the impact of probe spacing is important for evaluating both the sensitivity of the four-probe setup and the consistency of readings under different configurations. Figure 6-8 and Table 6-1 summarize the resistivity measurements recorded at four different probes spacing: 10 mm, 15 mm, 20 mm, and 30 mm. The average resistivity results are 42.21 $\mu\Omega$ ·mm at 10 mm, 42.33 $\mu\Omega$ ·mm at 15 mm, 42.60 $\mu\Omega$ ·mm at 20 mm and 43.07 $\mu\Omega$ ·mm at 30 mm. The differences in mean values across the four configurations are within a $\pm 1~\mu\Omega$ ·mm range, suggesting that probe spacing has minimal influence on the overall resistivity measurement within this scale. In terms of variability, the standard deviation decreased as the probes distance increased from 10.67 $\mu\Omega$ ·mm at 10 mm down to 5.51 $\mu\Omega$ ·mm at 30 mm. Similarly, the standard deviation also decreased with increased spacing, improving the statistical reliability of the measurements. This suggests that while average resistivity remained relatively constant, longer probe distance offered more stable and less noisy readings, likely due to reduced influence of localized surface irregularities and edge effects. Based on these observations, a 20 mm spacing was selected for all subsequent experiments. It is large enough to ensure consistent contact and signal quality, yet small enough to remain fully within the gauge length of the sample, avoiding overlap with clamping regions. In addition, 20 mm spacing makes the probe setup more convenient and reduces the risk of probes making contact or crossing paths, which could introduce error.

For best accuracy in four-probe measurements, probes should remain co-linear and equidistant, as deviations from these conditions can distort current distribution and voltage readings. This study confirms that when these conditions are maintained, moderate variation in probe spacing does not significantly affect the accuracy of electrical resistivity measurements in AA6082 aluminium.

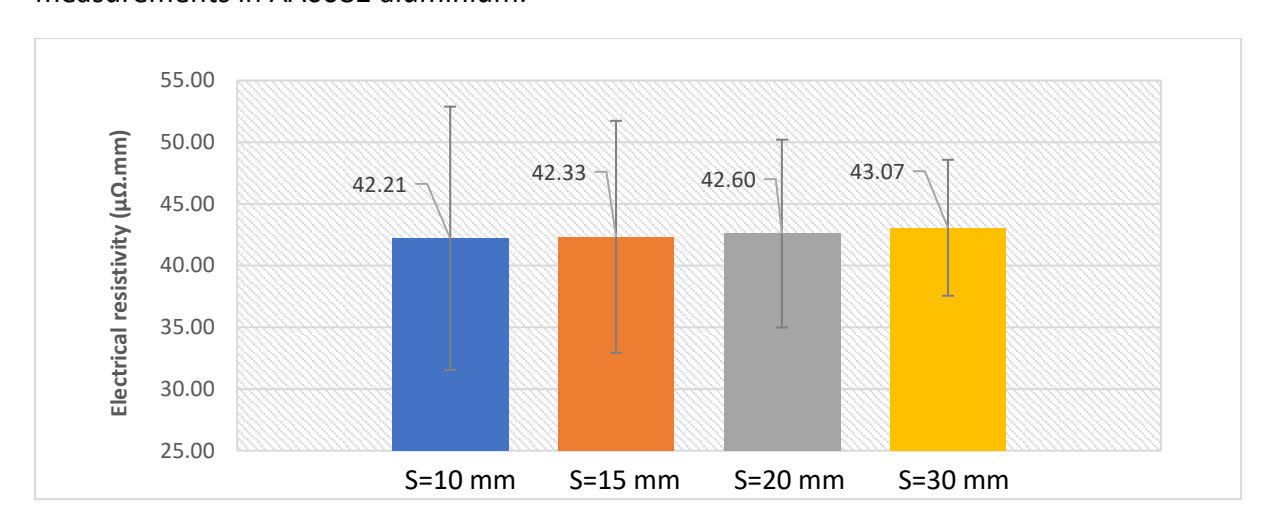


Figure 6-8. Effect of distance between probes on electrical resistivity measurements for aluminium bar AA6082

Probe spacing (mm)	Average (μΩ.mm)	Minimum(μΩ.mm)	Maximum(μΩ.mm)	Standard deviation	Standard deviation
10	42.21	29.24	69.24	10.67	1.25
15	42.33	24.86	69.24	9.40	1.18
20	42.60	24.65	64.19	7.61	0.89
30	43.07	30.29	57.66	5.51	0.64

Table 6-1. Summary of resistivity measurement for different probe spacing

6.2.2 Effect of measurement time on electrical resistivity

The objective of this experiment is to determine the optimal reading time required to obtain stable and accurate measurements of electrical resistivity (ER) using the Keithley 6221 and Keithley 2182A instruments. Given the sensitivity of these devices in the $n\Omega$ scale, fluctuations in the last digits of the readings necessitated careful analysis of measurement duration. The aim was to ensure that there were no significant differences in the ER measurements across different reading times. While the main objective was not to compare material conditions, using two different samples helped confirm the consistency of the measurement results.

Table 6-2 and Figure 6-9 summarize the electrical resistivity measurements for an annealed stainless steel 316L stainless steel specimen measured at 10, 20, and 30 seconds. The average ER values recorded were 781.98 $\mu\Omega$ ·mm, 781.27 $\mu\Omega$ ·mm, and 781.90 $\mu\Omega$ ·mm, respectively. The minimum and maximum values showed slight variation across all durations, with a narrow overall range (733.42 to 827.52 $\mu\Omega$ ·mm). The standard deviations were 17.27, 17.30, and 16.45 $\mu\Omega$ ·mm, indicating consistent dispersion. The standard deviation decreased with

increasing time, from 2.14 $\mu\Omega$ ·mm at 10 seconds to 1.16 $\mu\Omega$ ·mm at 30 seconds, suggesting improved precision with longer measurement duration.

Table 6-3 and Figure 6-10 presents the corresponding data for a non-annealed 316L stainless steel sample. The average ER values recorded were 792.62 $\mu\Omega$ ·mm, 793.21 $\mu\Omega$ ·mm, and 793.46 $\mu\Omega$ ·mm for 10, 20, and 30 seconds, respectively. These values are consistently higher than those of the annealed specimen, as expected. The minimum ER recorded was 737.47 $\mu\Omega$ -mm and the maximum were 842.83 $\mu\Omega$ -mm. The standard deviations ranged from 19.6 to 20.56 μΩ·mm, and the standard deviation improved slightly with longer durations, from 2.45 to 1.55 $\mu\Omega$ ·mm. Both sets of data show that increasing the measurement duration slightly reduces the standard error of the mean, thereby enhancing measurement precision. However, the average ER values remained relatively consistent across different durations, with variations within 1 $\mu\Omega$ ·mm, suggesting that extending measurement time beyond 10 seconds may offer limited additional benefit in terms of accuracy. Additionally, the unannealed sample consistently showed higher ER values compared to the annealed one. This difference can be attributed to the higher dislocation density and internal stresses in the unannealed material, which increase electron scattering and thus resistivity. Overall, the results indicate that 10-second measurements are sufficiently reliable for general ER testing with this setup, although 20 or 30-second intervals may be preferred in cases where slightly greater precision is desired. The setup shows stable and repeatable performance across all time durations, supporting its reliability for fatigue damage assessment application. Therefore, a measurement duration of 10 seconds was selected for all subsequent experiments to ensure efficiency while maintaining sufficient accuracy.

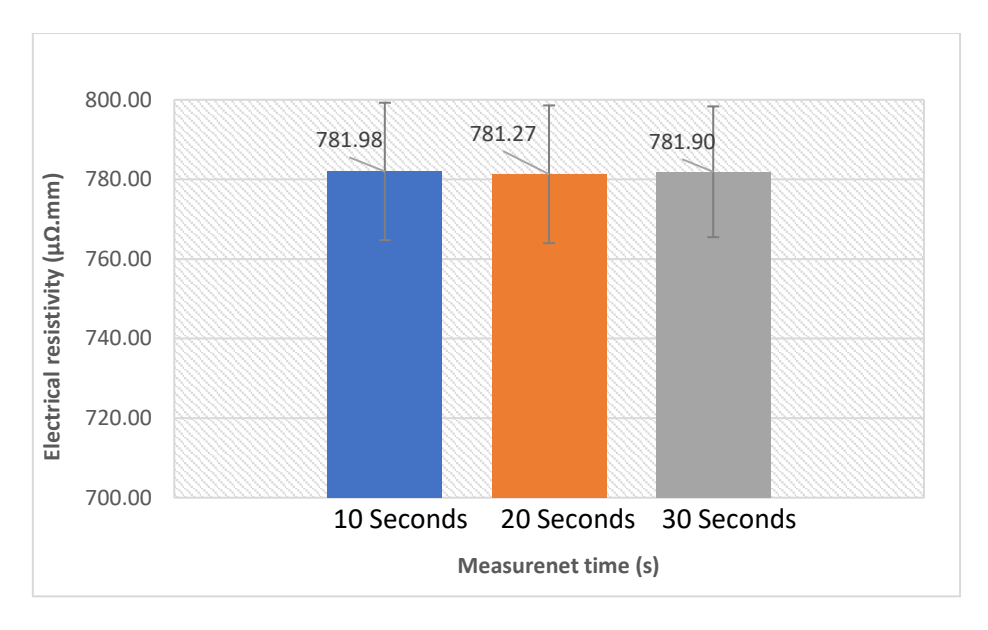


Figure 6-9. Effect of measurement time on electrical resistivity (Flat tensile test 316L stainless steel sample, annealed at 900°C for 1hr in Argon atmosphere with thickness 5mm)

Table 6-2. Summary of resistivity measurements over time

Measurement time (s)	Average (μΩ.mm)	Minimum (μΩ.mm)	Maximum (μΩ.mm)	Standard deviation	Standard error of the mean
10	781.98	733.42	825.62	17.27	2.14
20	781.27	733.43	827.52	17.30	1.51
30	781.9	733.42	827.51	16.45	1.16

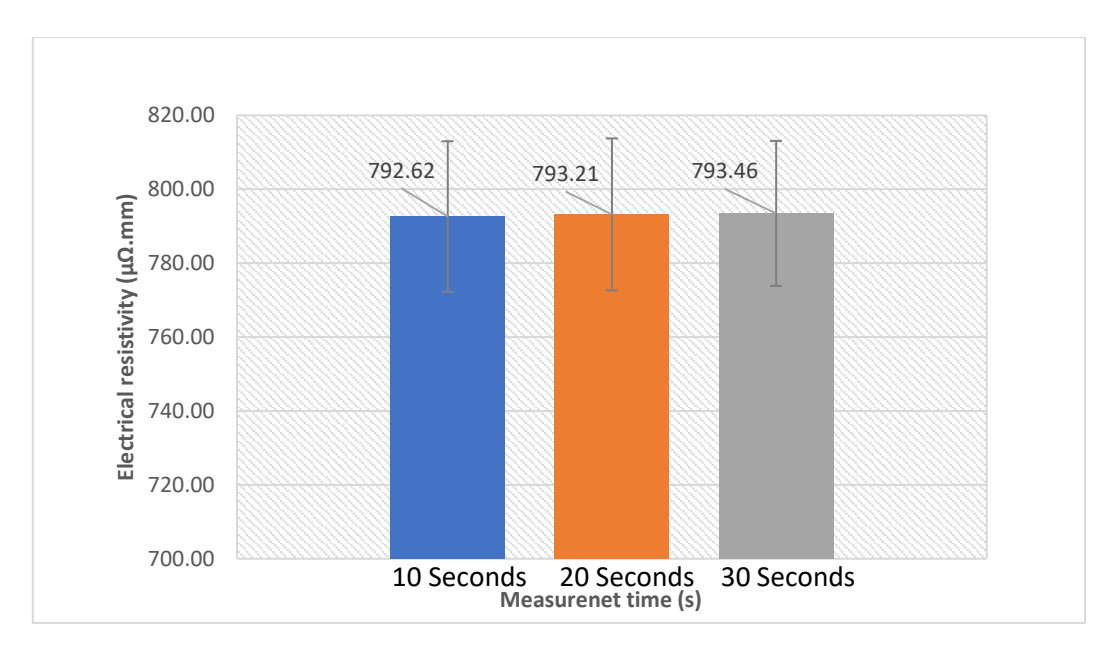


Figure 6-10. Effect of measurement time on electrical resistivity (Flat tensile test 316L stainless steel sample –Not annealed with thickness 5mm)

Measurement time (s)	Average (μΩ.mm)	Minimum (μΩ.mm)	Maximum (μΩ.mm)	Standard deviation	Standard error of the mean
10	792.62	739.92	830.58	20.37	2.45
20	793.21	737.47	842.83	20.56	1.77
30	793 46	737 47	842 83	19.6	1 55

Table 6-3. Summary of resistivity measurements over time

6.2.3 Effect of surface roughness on electrical resistivity

Surface roughness plays a significant role in electrical resistivity measurements, particularly when using precision methods such as the four-probe technique. Rougher surfaces introduce irregularities that can disrupt electron flow by increasing scattering at the material's surface, while smoother surfaces facilitate more uniform current distribution and lower resistivity. This effect becomes especially important in sensitive measurements, where surface condition can substantially influence the accuracy and consistency of results.

Figure 6-11 shows the measured surface roughness and corresponding electrical resistivity values for each surface condition. As shown in Figure 6-11b, surface roughness increased substantially from 0.24 μ m (as-received) to 0.496 μ m after grinding with 80-grit paper — an increase of approximately 107%. However, surface roughness dropped dramatically to 0.0741 μ m after grinding with 1200-grit paper, and further to 0.067 μ m after polishing, representing a 73–86% reduction compared to the roughest condition. Figure 6-11a show the effect of these surface changes on electrical resistivity. Electrical resistivity increased from 757.6 $\mu\Omega$ ·mm (as-received) to 793.1 $\mu\Omega$ ·mm after coarse grinding (80-grit), corresponding to a 4.7% increase. With finer grinding (1200-grit), resistivity decreased to 733.6 $\mu\Omega$ ·mm and further dropped to 709.3 $\mu\Omega$ ·mm after polishing — a 10.6% total reduction compared to the roughest

condition. These results confirm a clear trend: as surface roughness decreases, electrical resistivity also decreases. This is consistent with findings in the literature, where increased surface roughness is known to enhance electron scattering and reduce the number of effective conductive paths. For example, in studies on conductive composites such as gold-coated multi-walled carbon nanotubes (Au/CNTs), a 10–20% increase in contact resistance was observed with greater surface roughness, attributed to fewer real contact points and higher scattering. Similarly, in indium tin oxide (ITO) films, smoother surfaces led to lower resistivity due to reduced surface-level electron disruption. The observed trend in this study aligns well with these findings, confirming that controlling surface roughness is crucial for ensuring reliable resistivity measurements across diverse applications [152, 153, 154].

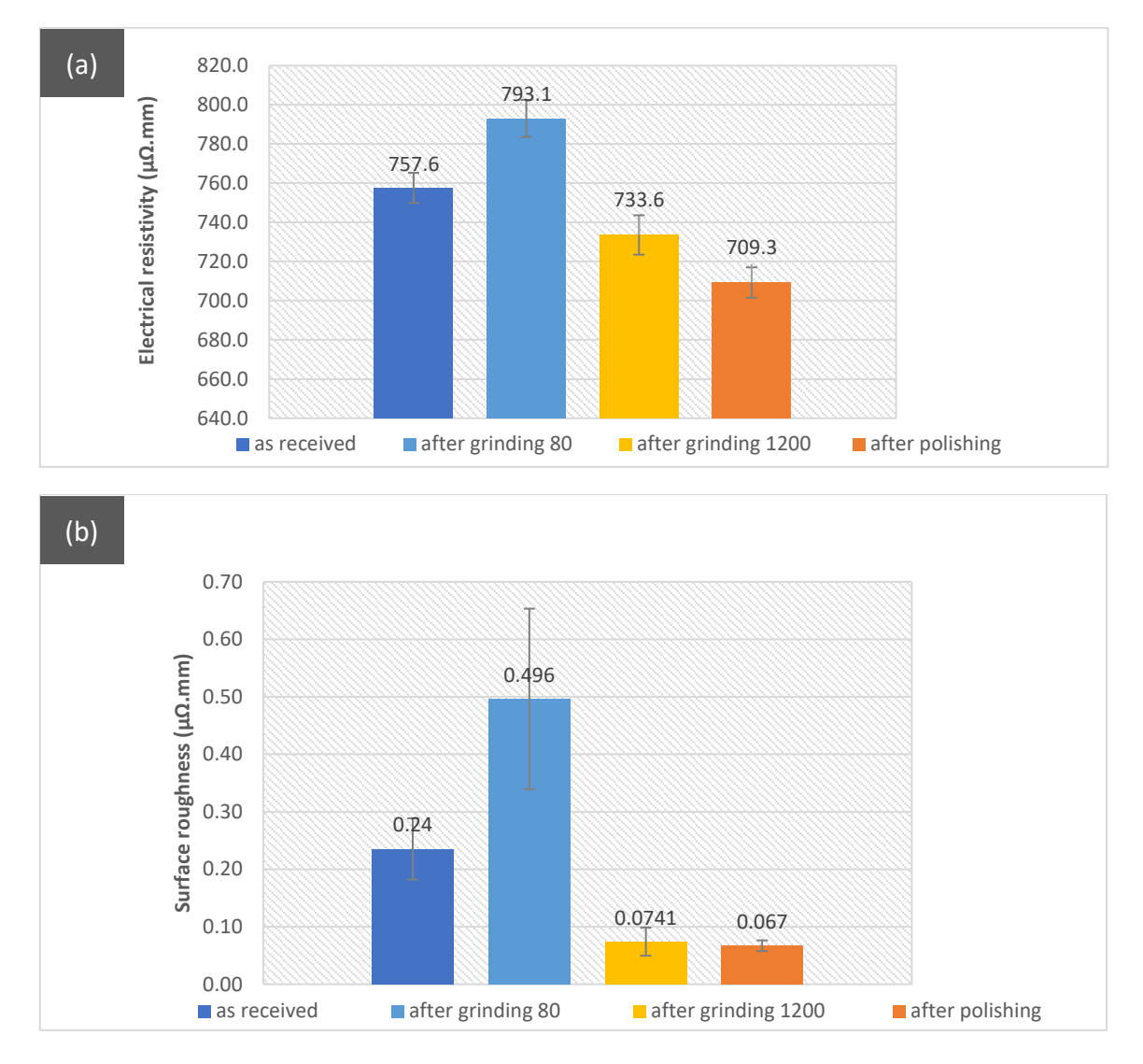


Figure 6-11. Effect of surface roughness on electrical resistivity of flat tensile test 316L stainless steel sample. (a) plot of ER versus various sample preparation and (b) surface roughness versus various sample preparation

6.2.4 Repeatability of the electrical resistivity (ER) measurement setup

Repeatability refers to the ability to produce consistent results when the same measurement is repeated under identical conditions. In this context, it measures how consistently the Keithley 6221 and 2182A set up can capture electrical resistivity (ER) of the same sample over multiple trials, with minimal variation in results. Results of these measurements are in Figure 6-12 and Figure 6-13. To evaluate the repeatability of measurements, several statistical methods from statistical science can be applied, such as the range method, average deviation, variance, standard deviation and pooled standard deviation. Below, each term is briefly explained, followed by an explanation of why the pooled standard deviation and standard deviation methods were chosen for evaluating the device's repeatability.

6.2.4.1 Statistical methods to evaluate repeatability of electrical resistivity measurements

6.2.4.1.1 Range method

This method is the difference between the highest and lowest values in a set of measurements. Provides a simple measure of the spread or variability of measurements. A smaller range indicates that the device is consistently producing similar results across multiple measurements, suggesting good repeatability. However, this method is often less precise than others because it doesn't consider the distribution of data, so it might not capture all sources of variability.

Range=Maximum Value-Minimum Value

6-1

6.2.4.1.2 Variance method

Variance is a measure of how far each data point in a dataset is from the mean, calculated by averaging the squared differences between each data point and the mean. Variance provides a more precise measure of the spread of data than the range or average deviation. Lower variance indicates that repeated measurements are consistently close to each other, thus implying good repeatability. However, the units of variance are squared, which can make interpretation difficult.

6.2.4.1.3 Standard deviation method

The standard deviation is the square root of the variance, providing a measure of the spread of data that is in the same units as the original data. It indicates how much individual measurements deviate from the mean. A lower standard deviation means that the results of repeated measurements are closer to each other and to the mean, indicating high repeatability. It is widely used because it provides a clear and interpretable measure of variability in the same units as the data. Standard deviation is particularly useful when analysing repeatability because it shows how tightly grouped the data is. This method Provides a reliable measure of variability that accounts for both the size and spread of measurements.

6.2.4.1.4 Pooled standard deviation method

The pooled standard deviation is a weighted average of the standard deviations (s) from different groups or sets of measurements. It is used when multiple sets of data are being compared, as it combines their individual variabilities into one overall measure. Like the standard deviation method, but it combines information from multiple observations. When investigating the repeatability of the device across multiple samples, the pooled standard deviation helps to compare the variability between different sets of measurements. If the pooled standard deviation is below 1 in this context, it indicates that the device is consistent across different measurements, regardless of the sample being tested. It is useful for combining multiple datasets (like the two different samples in this experiment) to assess the overall repeatability.6-2 shows the formula for calculating the pooled standard deviation, where $s_1 to s_5$ represent the standard deviations from individual measurement sets.

$$\frac{\sqrt{s_1^2+s_2^2+s_3^2+s_4^2+s_5^2}}{\overline{sqrt(number\ of\ observation)}}$$
 pooled standard deviatio =
$$\frac{\sqrt{number\ of\ measurement\ in\ each\ observation}}{\sqrt{number\ of\ measurement\ in\ each\ observation}}$$

As in this research five measurement is being done for each sample, pooled standard deviation method is ideal because it allows to combine the variability from these repeated measurements into a single, overall measure of spread. This method minimizes the impact of outliers, handles small sample sizes efficiently and gives a balanced view of how consistent the setup is in measuring electrical resistivity across different materials [155, 156]. Results for measuring standard deviation and pooled standard deviation for two samples (AA6082 and 316L stainless steel) are summarized in

Table 6-4, Table 6-5, and Table 6-6 compared results from these measurements for Al 6082 and 316L stainless steel. Al 6082 was included in these measurements to confirm the repeatability of the results and to demonstrate that the applied method shows consistent outcomes across different metallic materials. The pooled standard deviation is low for both metals, indicating that the device setup performs consistent results across multiple measurements, demonstrating good repeatability of the results.

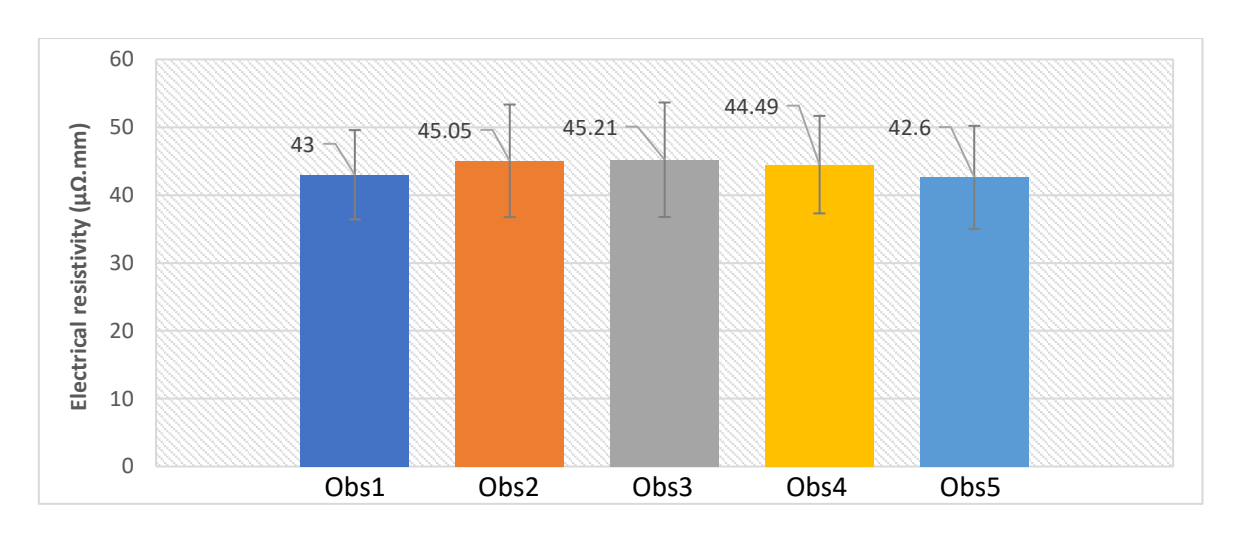


Figure 6-12. Electrical resistivity measurements for AA6082 sample for five observations with the same condition – distance between electrodes =20 mm-flat tensile specimen

Table 6-4. Electrical Resistivity Measurements for AA6082. The table displays the mean, maximum, minimum, and standard deviation values across five observations, highlighting consistent results with minimal variability

	Mean	Maximum	Minimum	Standard
AI680	(μΩ.mm)	(μΩ.mm)	(μΩ.mm)	deviation
Observation 1	43	54.61	25.98	6.58
Observation 2	45.05	65.03	24.86	8.30
Observation 3	45.21	65.2	28.95	8.44
Observation 4	44.49	63.56	30.56	7.19
Observation 5	42.60	64.19	24.86	7.61

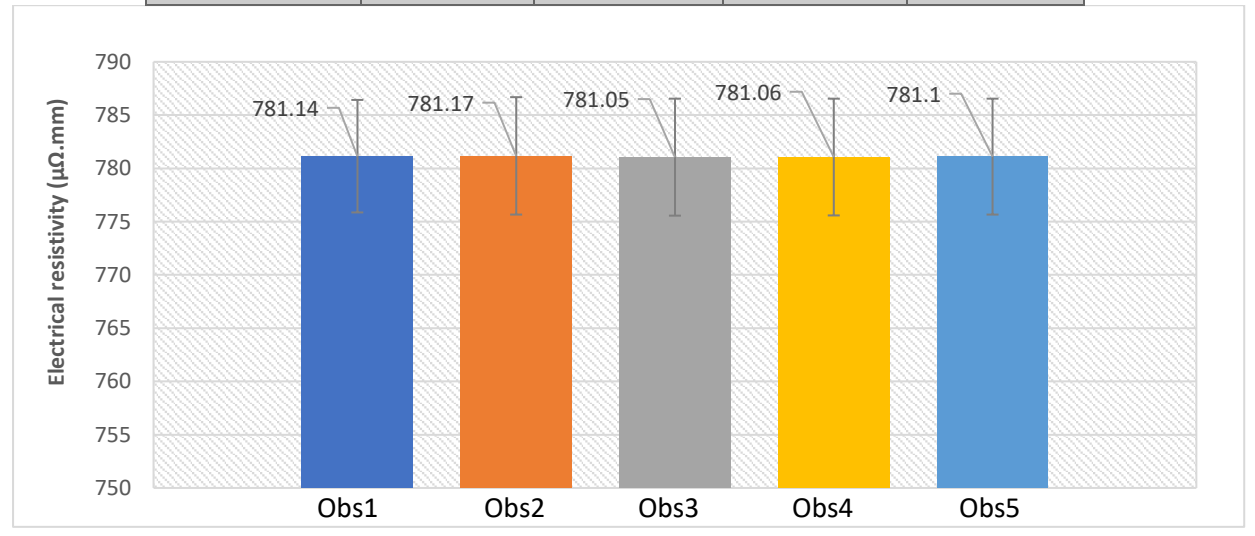


Figure 6-13. Electrical resistivity of flat fatigue sample 316L stainless steel – flat tensile test specimen - thickness=2 mm - distance between electrodes=20mm

Table 6-5. Electrical Resistivity Measurements for Stainless Steel 316L. The table displays the mean, maximum, minimum, and standard deviation values across five observations, highlighting consistent results with minimal variability

316L stainless steel	Mean(μΩ.mm)	Maximum(μΩ.mm)	Minimum(μΩ.mm)	Standard deviation
Observation 1	781.14	792.92	769.28	5.28
Observation 2	781.17	790.95	768.42	5.51
Observation 3	781.05	792.92	768.25	5.49
Observation 4	781.06	792.42	770.27	5.48
Observation 5	781.10	792.52	768.50	5.44

Table 6-6.Comparison of Standard Deviation and Pooled Standard Deviation for Stainless Steel 316L and Al680 Samples.

The results highlight the variability and consistency of measurements for each material

Sample	316L stainless steel	AA6802
Standard deviation	5.44	7.7
Pooled standard deviation	0.65	0.92

The data presented in Table 6-6 highlights the variability and consistency of measurements for Stainless Steel 316L and AA6802. AA6802 shows a higher standard deviation (7.7) compared to Stainless Steel 316L (5.44), indicating greater variability in its individual measurements. This increased variability can be attributed to the inherently lower electrical resistivity of aluminium compared to stainless steel. Materials with lower resistivity, like AA6802, are more susceptible to subtle changes in contact resistance, temperature fluctuations, and setup inconsistencies, which can significantly impact measurement precision. Although both materials demonstrate relatively low pooled standard deviations—0.92 for AA6802 and 0.65 for 316L—suggesting good repeatability within individual trials, the lower pooled deviation in 316L reflects its higher stability under testing conditions.

6.2.5 Reliability of the electrical resistivity (ER) measurement setup

Reliability refers to the ability of a setup to consistently perform its intended function without failure over time. To evaluate the reliability of the measurement system, electrical resistance (ER) values were recorded for multiple metallic specimens, including different alloys. Table 6-7 presents the measured electrical resistance values for various metallic specimens obtained in this study, alongside corresponding values reported in the literature. The materials tested include annealed and non-annealed stainless steel 316L, aluminium alloy AA6082, and pure copper. Table 6-7 demonstrates strong agreement between the measured values and those found in the literature, confirming the reliability of the experimental setup. The measured ER value for annealed stainless steel 316L (770 \pm 7 $\mu\Omega\cdot$ mm) is slightly lower than that of the non-annealed specimen (790 \pm 7 $\mu\Omega\cdot$ mm), which aligns with expectations.

Annealing typically reduces dislocation density and relieves internal stresses, both of which minimize electron scattering and thus reduce electrical resistivity. This observation provides further confidence in the sensitivity and accuracy of the measurement system. It is also worth noting that the relatively wide range of literature values for 316L (690–780 $\mu\Omega$ ·mm) reflects differences in material form, grade, and processing history—such as whether the sample is cast, wrought, cold-worked, or annealed. Additionally, many literature values are obtained using simpler methods such as two-probe measurements, which are more prone to contact resistance and thermoelectric noise. These factors contribute to broader uncertainty in published data.

Table 6-7. Comparison of measured electrical resistivity of various metals with published values in the literatures to validate setup reliability [157]

Samples	Electrical resistivity Keithley (μΩ.mm)	Electrical resistivity literature (μΩ.mm)
Annealed 316L stainless steel	770±7	690 - 780
Not Annealed 316L stainless steel	790±7	690 - 780
AA6802	44±7	37 - 45
Copper bar(pure)	17.1±7	17 - 17.24

As a summary for this section, the reliability and consistency of the experimental setup, using Keithley 6221 and Keithley 2182A instruments, for measuring electrical resistivity was successfully demonstrated. The pooled standard deviation method effectively accounted for variability within repeated measurements, yielding a single, comprehensive measure of spread. Minimal variability observed in the results for both Al680 and 316L stainless steel samples, as evidenced by low pooled standard deviations, indicates high repeatability of the resistivity measurements. Furthermore, analysis revealed that measurement time within the range of 10 to 30 seconds did not significantly affect the measured resistivity values, allowing for a standardized 10-second measurement interval. Similarly, variations in probe spacing within a reasonable range did not produce significant changes in resistivity readings, leading to the selection of 20 mm as the optimal distance for practical considerations. Finally, the influence of surface roughness on resistivity was acknowledged, and for future experiments all samples are polished to achieve a consistent surface finish, minimizing variability attributed to surface conditions.

6.2.6 Study of fatigue process by ER

This section focuses on applying electrical resistivity (ER) measurements to monitor the fatigue process in stainless steel 316L flat tensile test specimens subjected to cyclic loading.

Specifically, the aim is to assess how ER changes during fatigue and to evaluate its sensitivity in detecting early-stage high cycle fatigue damage—particularly in the first 10% of fatigue life.

To ensure accuracy and repeatability of the ER measurements, several experimental controls were implemented. These included maintaining uniform surface roughness across all specimens to reduce variability and isolate the influence of fatigue damage. Maintaining consistent probe positioning throughout the test is also essential. Ensuring co-linear alignment and fixed spacing—was observed to guarantee accurate and reproducible readings.

Initially, a high-cycle fatigue (HCF) regime was applied to cylindrical SS316L specimens with an expected fatigue life of 2 million cycles. The tests were carried out under load-controlled tension—tension loading with a stress ratio (R) of 0.5, a maximum stress of 310 MPa, and a frequency of 10 Hz at room temperature (Details of this fatigue condition are also provided in Table 5-4). Electrical resistivity (ER) measurements were performed ex-situ throughout the fatigue life, meaning the test was paused at specific intervals to record ER and then resumed (Figure 6-14). To further investigate ER behaviour in the early stages of fatigue damage, a more extended fatigue regime was applied to flat SS316L specimen with an expected fatigue life of 5 million cycles. This regime allowed for a more detailed evaluation of ER evolution before 10% of fatigue life, with shorter measurement intervals adopted to enhance sensitivity to early damage detection.

As seen in Figure 6-14 a notable increase in ER is observed during the early cycles, particularly between 0 and approximately 35,000 cycles, where the ER rises from about 770 $\mu\Omega$ ·mm to 900 $\mu\Omega$ ·mm (a ~17% increase). Following this initial phase, ER increases more gradually, reaching around 1020 $\mu\Omega$ ·mm by 1,500,000 cycles, representing a total increase of approximately 32% from the baseline. In the final stage, beyond 1,500,000 cycles (roughly 70% of the fatigue life), there is an abrupt rise in ER, ultimately exceeding 1350 $\mu\Omega$ ·mm, which suggests significant structural degradation.

The changes in ER are hypothesized to be linked to underlying microstructural evolution. The initial rise may be associated with increasing dislocation density, while the sharp increase at later stages is likely related to crack initiation and growth. However, these mechanisms remain hypothetical at this stage and will be further investigated using destructive characterization techniques and microscopy. This graph aligns well with the typical cyclic shear stress-strain curve (CSSE) of FCC metals and alloys that had been shown in Figure 2-2 in 2.2.1 (a three-stage curve). Based on that image, stage A, involves the formation of dislocation cells but no persistent slip bands (PSBs); Stage B, shows the formation of PSBs but no fatigue cracks; and Stage C, marks the formation and growth of fatigue cracks [13].

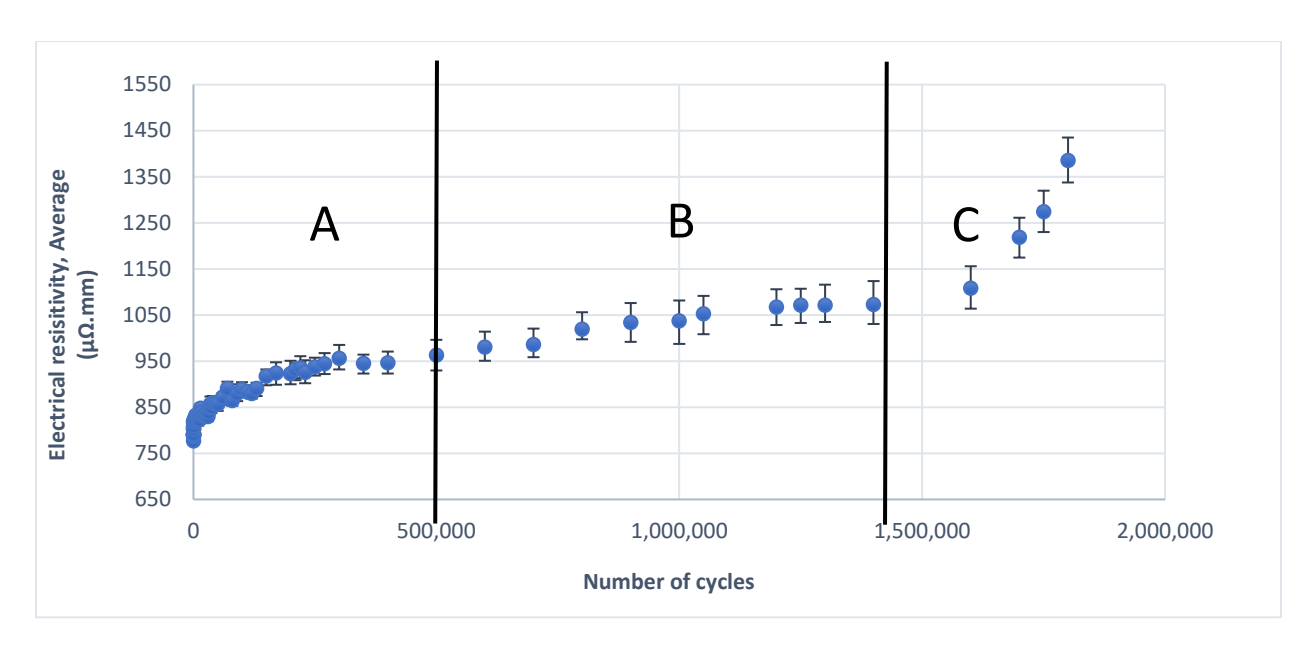


Figure 6-14. Electrical resistivity measurement for high cycle fatigue of 316L stainless steel

Now that the ability of ER to detect the three stages of fatigue is approved, it's crucial to check its ability to detect early stages of fatigue where the change in microstructure is so minor. Figure 6-15 and Figure 6-16 show changes in electrical resistivity (ER) measurements under a high-cycle fatigue (HCF) regime for a flat 316L stainless steel fatigue sample with specifications described in Table 5-4. The fatigue tests were performed under load-controlled tension—compression loading with a stress ratio (R) of -0.4, a maximum stress of 260 MPa, and a frequency of 10 Hz at room temperature, corresponding to a total fatigue life of 5 million cycles. In Figure 6-15 ER was measured ex-situ from 0 cycles up to nearly 350,000 cycles (about 8% of fatigue life). This figure shows the average electrical resistivity (in $\mu\Omega/mm$) as a function of fatigue cycles. Figure 6-16 illustrates the normalized electrical resistivity against the percentage of fatigue life before 10% of fatigue life. Normalized electrical resistivity is a dimensionless measure that represents how the electrical resistivity (ER) of a material changes relative to its initial or baseline value, typically at the start of testing (e.g., before fatigue loading begins). Normalized Electrical Resistivity is usually expressed as:

Normalized ER =
$$\frac{ER_{current \ cycle}}{ER_{refrence \ sample}}$$
 6-3

As observed in both figures two distinct peaks are identified in the electrical resistivity measurements, indicating an increase followed by a drop in the component's resistivity. These peaks occur at approximately 0.01% and 1% of the fatigue life, as highlighted by the green-shaded regions in both Figure 6-15 and Figure 6-16. While two peak regions are identified, it is noted in both figures that only the first peak is distinctly visible, whereas the second peak appears less pronounced. The lower intensity of the second peak will be discussed in more detail in Chapter 8, where higher-magnification analysis and a quantitative evaluation of the percentage increase in electrical resistivity are provided. It is hypothesized that the first peak corresponds to increase in dislocation density, while the second peak may

relate to the formation of slip bands or changes in dislocation structures. The reasons and mechanisms behind these peaks of these two peaks are discussed in the next chapters, using TEM microscopy techniques to examine the structures. In Figure 6-16, normalized electrical resistivity is used instead of average electrical resistivity values ($\mu\Omega\cdot$ mm) to ensure consistency and alignment with other techniques used in this study (nonlinear ultrasound parameter), which are also presented in normalized form. Normalization eliminates variability due to initial sample conditions, such as slight differences in dimensions or material properties, ensuring results are independent of these factors. This approach allows for easier comparison across different samples and test conditions while emphasizing the relative changes in resistivity that correspond to fatigue damage. By focusing on normalized values, the data provides clearer insights into the material's behaviour during early fatigue stages, enabling consistent and interpretable results.

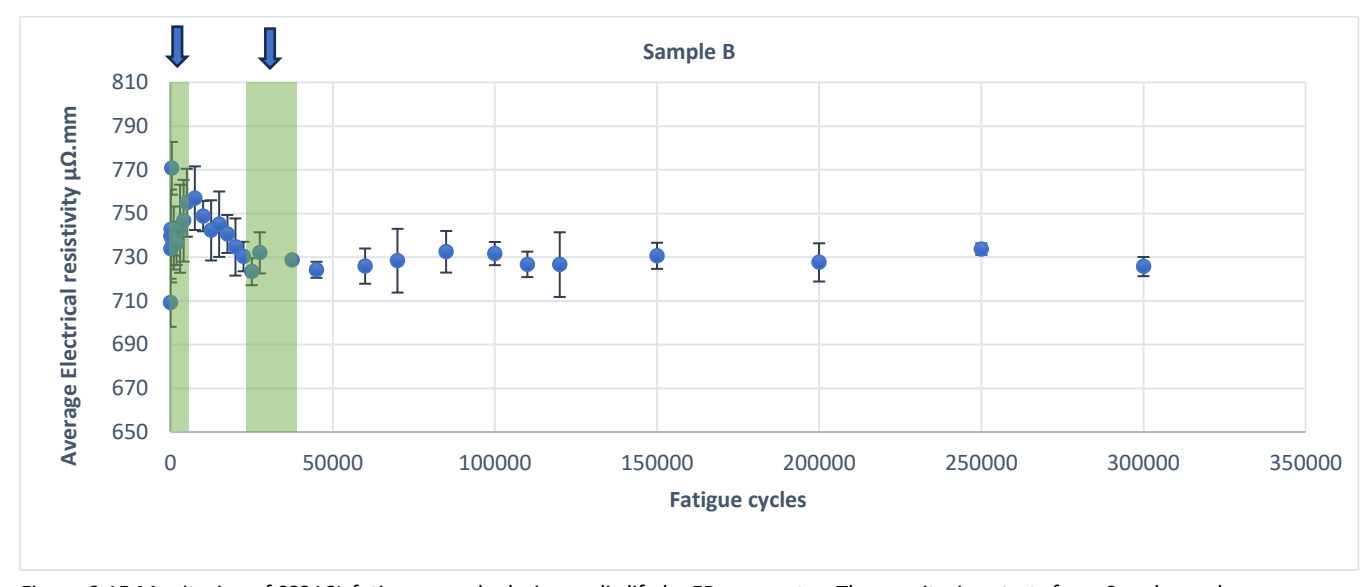


Figure 6-15.Monitoring of SS316L fatigue sample during cyclic life by ER parameter. The monitoring starts from 0 cycles and continues to 350K cycles equal to approximately 8% of the cyclic life

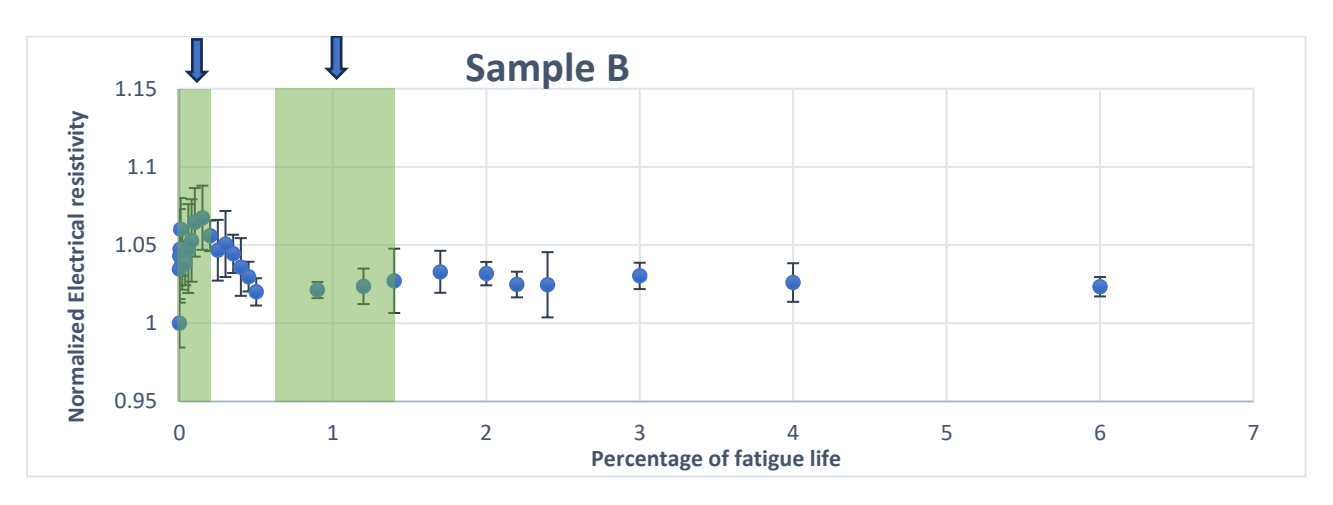


Figure 6-16. Monitoring of SS316L fatigue sample during cyclic life by ER (Normalized ER). The monitoring starts from 0 cycles and continues to 350K cycles equal to approximately 8% of the cyclic life

Based on Figure 6-16 at 0.01% of the fatigue life (200 to 400 cycles), there is a 6-7% increase in electrical resistivity (ER), followed by a subsequent decrease. Even after this drop, the resistivity remains 2-3% higher than the initial (as-received) sample. This elevated resistivity level is maintained up to 0.1% of the fatigue life. At 1% (85k to 120k) fatigue life, the ER increases again by 2%, followed by a drop back to its previous level, where it remains stable until 8% of the fatigue life. This pattern of increase and subsequent stabilization in ER suggests microstructural changes occurring in stages, which may be linked to dislocation density evolution, slip band formation, or other fatigue-related mechanisms. The underlying reasons behind of these peaks will be explored in greater detail in Chapter 8, where Transmission Electron Microscopy (TEM) images taken at, before, and after each identified peak are analysed to provide microstructural evidence supporting these interpretations.

6.3 Nonlinear Ultrasonic testing method

6.3.1 Influence of gain and magnitude on accuracy of measurements

In nonlinear ultrasonic testing, gain and magnitude are crucial parameters that influence the accuracy and reliability of the measurements. Gain refers to the amplification applied to the received signal, which enhances signal strength but can also introduce noise if not properly controlled. Magnitude, on the other hand, represents the actual signal amplitude, which directly affects the generation and detection of harmonic components. Both factors play a significant role in ensuring the consistency and repeatability of nonlinear ultrasonic measurements. Another term is Channel 1 and Channel 2 which refer to the two signal paths used for measuring the fundamental and second harmonic components of the ultrasonic wave. Magnitude in this context represents the amplitude of the signals in each channel, which directly impacts the measurement of nonlinearity. Channel 1 Magnitude corresponds to the amplitude of the fundamental frequency signal (A₁), which is the primary ultrasonic wave transmitted through the material. This signal is crucial as it serves as the reference for measuring nonlinear effects. Channel 2 Magnitude refers to the amplitude of the second harmonic signal (A₂), which is generated due to material nonlinearity.

To determine the optimal criteria for gain and magnitude, a series of tests were conducted using a sample with 0 fatigue cycles, ensuring that the material's response remained stable throughout the measurements.

For first experiment, the magnitude of both Channel 1 (fundamental frequency, A1) and Channel 2 (second harmonic, A2) was kept constant, while the gain values were varied from 38 dB to 24 dB to observe their effect on the nonlinear ultrasonic measurements. Figure 6-17 shows a set of plots of the second harmonic amplitude (A_2) against the square of the fundamental amplitude (A_1^2) for each gain level. Each dataset was fit with a linear regression line, where the slope of the line represents the nonlinear parameter (β), the R^2 value indicates the quality of the fit, with values close to 1.0 suggesting strong linearity and reliable measurements.

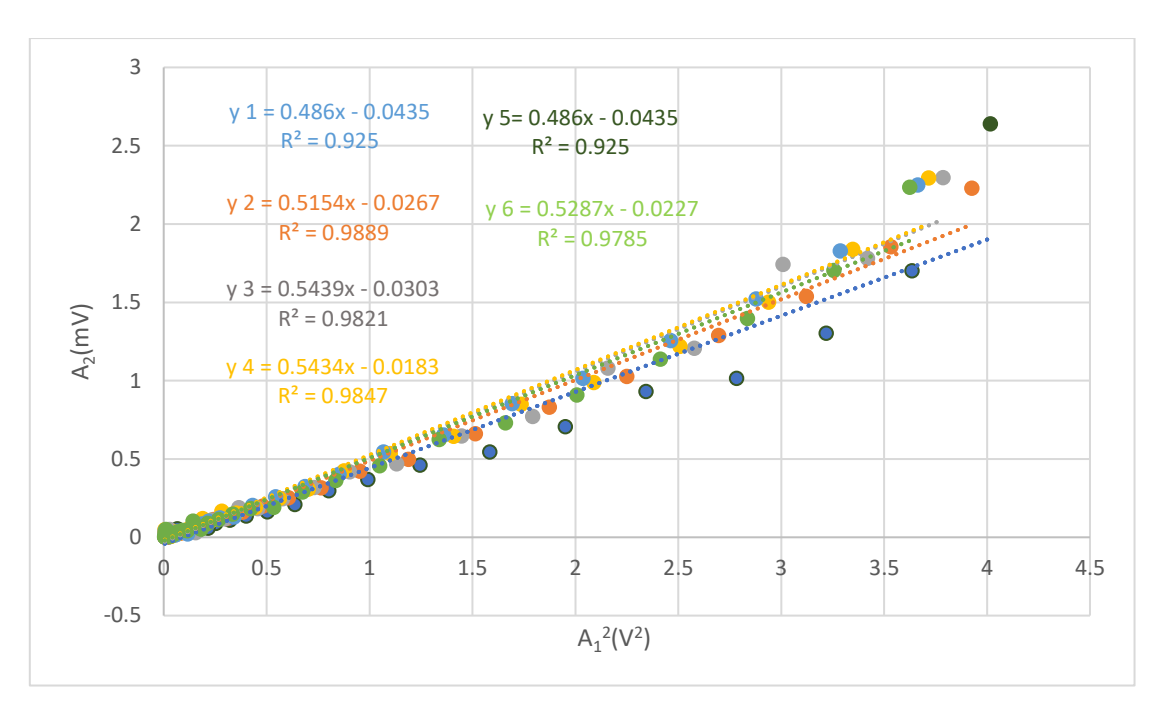


Figure 6-17. A plot of A_2 vs A_1^2 obtained using various gain of: (1)38dB; (2)32dB; (3)30dB; (4)28dB; (5)26dB and (6)24dB for as-received stainless steel 316L sample

Table 6-8 presents the calculated values of β and R^2 for each gain setting. The β values range from 0.486 to 0.551, while R^2 values remain consistently high, between 0.925 and 0.9889, confirming that the second harmonic response maintains strong linearity across all gain levels. From the table and plot, it is evident that while the gain level affects the absolute amplitude of the received signals (as shown by the magnitude ranges in Channels 1 and 2), the β values remain relatively stable, with only minor variation. This suggests that the measurement setup is robust, and gain changes do not introduce significant distortion or nonlinear artefacts. However, there is a slight improvement in the R^2 values within the gain range as shown in Table 6-8 of 28 dB to 32 dB, indicating better linear regression fit in this range. Based on this observation, 30 dB was selected as the optimal gain setting for all subsequent experiments, offering a good balance between signal strength and measurement consistency.

Table 6-8. Table of non-linear coefficient of as-received stainless steel 316L measured using various gain from 32dB to 24dB

Equation	Gain(dB)	Magnitude of	Magnitude of	β	R ²
		channel 1(mV)	channel 2(mV)		
1	38	2.074±0.006	2.300-2.500	0.486	0.925
2	32	2.074±0.006	2.300-2.500	0.5154	0.9889
3	30	2.074±0.006	2.300-2.500	0.5439	0.9821
4	28	2.074±0.006	2.300-2.500	0.5434	0.9847
5	26	2.074±0.006	2.300-2.500	0.486	0.925
6	24	2.074±0.006	2.300-2.500	0.5287	0.9785

This section evaluates how variations in the magnitude of channel 2 effect on nonlinear ultrasonic parameter (β) in an as-received SS316L stainless steel specimen. All measurements were carried out at a fixed gain of 30 dB, and the magnitude of channel 1 was held constant at 2.068 \pm 0.012 mV. Figure 6-18 presents a series of linear regression plots of A₂ (second

harmonic amplitude) versus A_1^2 (square of the fundamental amplitude) across seven different ranges of channel 2 magnitudes. These channel 2 ranges are from 1.253–1.500 mV up to 2.800–2.900 mV, enabling investigation of how signal amplitude affects the sensitivity and stability of nonlinear measurements. Each data series is fit with a linear trend line, where the slope represents the nonlinear coefficient (β), and the R^2 value reflects the accuracy of the linear regression fit.

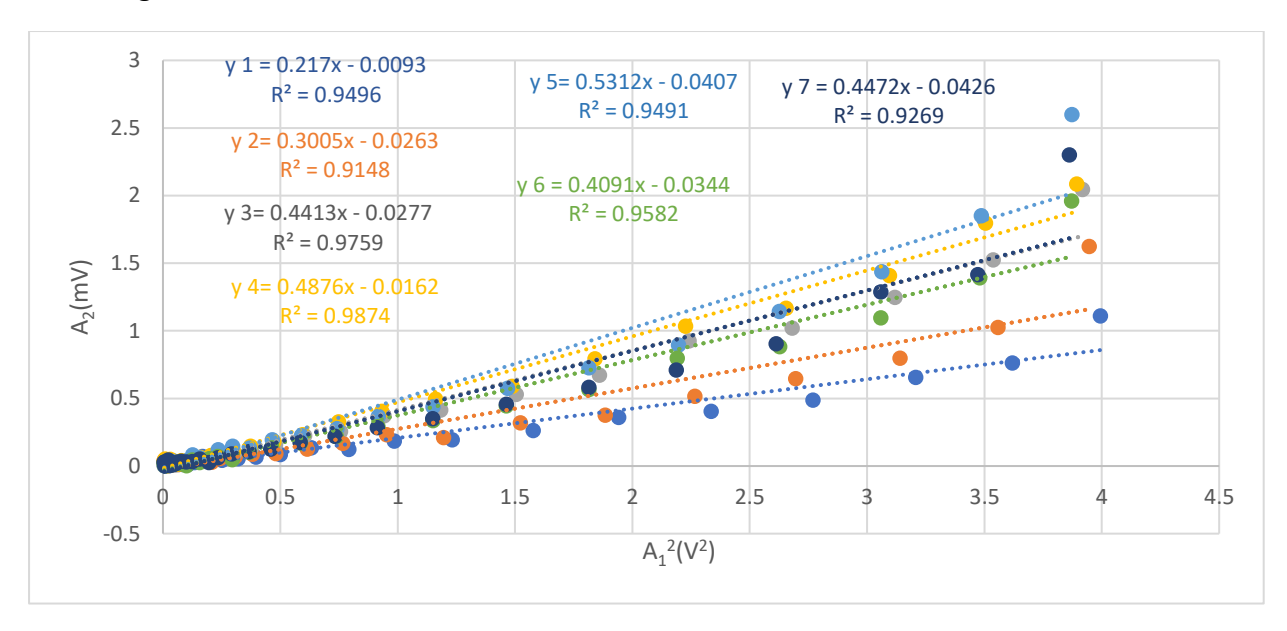


Figure 6-18. a plot of A_2 vs A_1^2 using similar gain of 30db, channel 1 magnitude of 2.068±0.012 as a function of channel 2 magnitude (1) =1.253-1.500 (2) = 1.400-1.600, (3) =2.005-2.356, (4) =2.300-2.556, (5) =2.800-2.900, (6) =2.002-2.200 and (7) =2.200-2.356

Table 6-9 summarizes the β and R^2 values obtained at different Channel 2 magnitudes. The nonlinear coefficient β ranges from 0.217 to 0.531, with lower values observed at smaller signal amplitudes. Specifically, the lowest β values (0.217 and 0.300) were recorded when Channel 2 magnitudes were below 1.6 mV, during which the R² values also fell below 0.95. This behaviour is likely due to the second harmonic signal (A₂) approaching the noise floor of the measurement system at low amplitudes. As a result, A₂ becomes more susceptible to electrical or background noise, weakening the observed nonlinear response and leading to an underestimation of β . Moderate β values (ranging from 0.441 to 0.487) were observed at intermediate Channel 2 magnitudes (2.0-2.5 mV), where the regression fits were strongest, with R² values between 0.97 and 0.98. The highest β value (0.531) was recorded when the Channel 2 magnitude exceeded 2.8 mV, though the corresponding R² dropped below 0.96. While increasing the Channel 2 magnitude enhances the second harmonic signal and raises β, it can also introduce measurement artefacts and system nonlinearities. These effects may cause the data to deviate from the ideal A_2 , A_1^2 relationship, thereby reducing regression accuracy. This highlights the importance of selecting an optimal signal amplitude—high enough to capture nonlinear effects sensitively, but low enough to avoid artefactual distortions—for accurate and reliable nonlinear ultrasonic measurements.

Table 6-9. Variations in Nonlinear Parameter and Measurement accuracy at Different magnitude Levels of channel 2 and constant gain and magnitude of channel 1

Equation	Gain(dB)	Magnitude of	Magnitude of	β	R²
		channel 1(mV)	channel 2(mV)		
1	30	2.068±0.012	1.253 -1.500	0.217	0.9496
2	30	2.068±0.012	1.400-1.600	0.300	0.9148
3	30	2.068±0.012	2.005-2.356	0.441	0.9759
4	30	2.068±0.012	2.300-2.556	0.487	0.9874
5	30	2.068±0.012	2.800-2.900	0.531	0.9491
6	30	2.068±0.012	2.002-2.200	0.409	0.9582
7	30	2.068±0.012	2.200-2.356	0.447	0.9269

Based on these experiments, a gain of 30 dB, a Channel 1 magnitude of approximately 2 mV, and a Channel 2 magnitude between 2 to 2.300 mV were chosen for the remaining experiments in this study. These settings ensure that the collected data can be reliably fitted to a straight line with a linear regression analysis to extract the nonlinear coefficient (β).

6.3.2 Repeatability of NLP measurement setup

An important aspect to consider for nonlinear ultrasound method, like electrical resistivity, is ensuring the repeatability of the setup to guarantee that the experiment can be reliably reproduced. Figure 6-19 shows the results of the four repeated measurements, presented as plots of the second harmonic amplitude (A_2) versus the square of the fundamental amplitude (A_1^2). Each linear regression line represents one test (β_1 to β_4). The slopes of these lines correspond to the nonlinear coefficients (β), which quantify the degree of acoustic nonlinearity in the material. From the figure, it is evident that, all data points follow a strong linear trend. R^2 values for all four curves range from 0.9832 to 0.9964, indicating a very high degree of fit and thus measurement consistency. Visually, the slopes of the lines remain close to each other, showing only minor variation between tests.

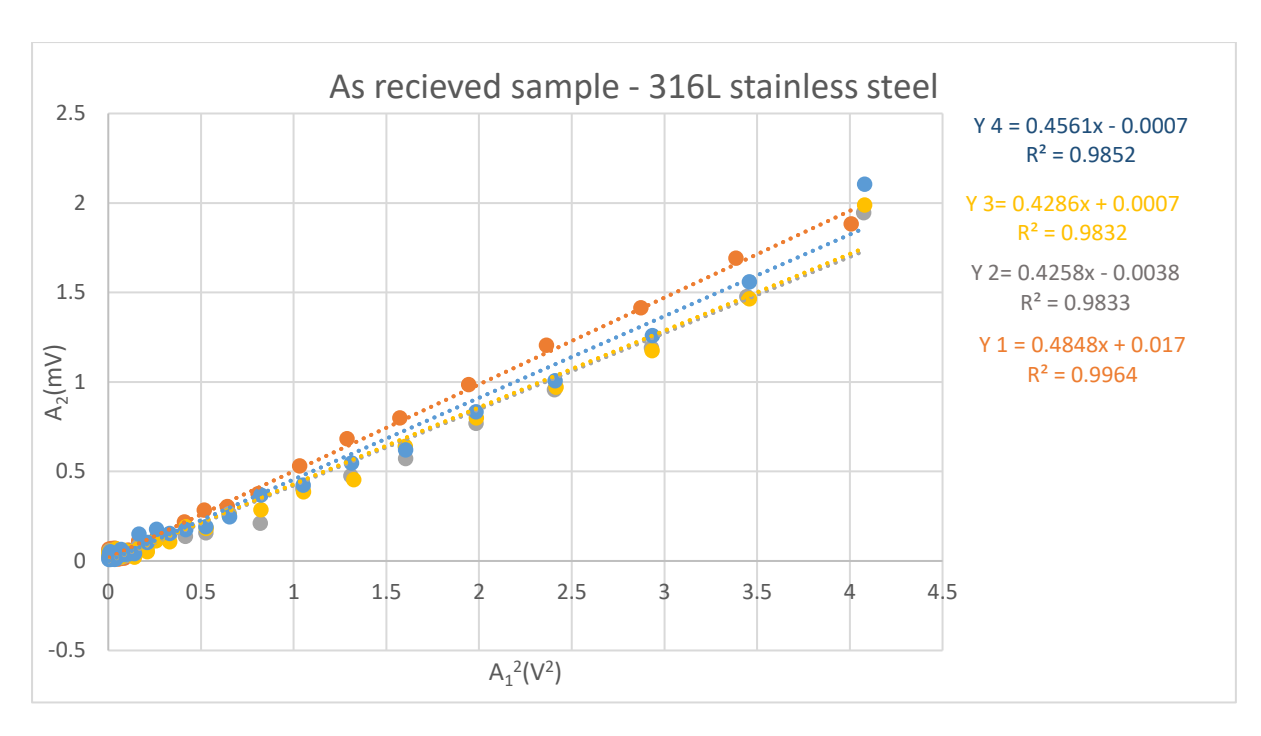


Figure 6-19. Plot of A_2 (2nd harmonic signal amplitude) vs A_1^2 (fundamental frequency signal amplitude) for 4 repeat tests on stainless steel as-received sample

Table 6-10 summarizes the β coefficients obtained from the four measurements. Average β is 0.4488, with a standard deviation of 0.0276. This small standard deviation demonstrates minimal variation across repeated measurements, supporting the method's high repeatability. The low spread in β values—alongside consistently high R² values—confirms that the nonlinear ultrasound setup is both reliable and repeatable for fatigue monitoring in 316L stainless steel.

Table 6-10. Table of non-linear coefficients (β 1 to β 4) obtained from four repeat measurement of stainless steel asreceived sample

β1	β2	β ₃	β4	Average	Standard deviation
0.4848	0.4258	0.4286	0.4561	0.448825	0.027606

6.3.3 Study of fatigue process using NLP

To investigate the progression of fatigue damage using the nonlinear ultrasonic parameter (NLP), a series of tests were performed on a 316L stainless steel sample under high-cycle fatigue loading. The study aimed to evaluate how the NLP evolves throughout the fatigue life—from the as-received condition to mid-life (approximately 50% of fatigue life) and ultimately near failure (at 5 million cycles). To capture this progression, nonlinear ultrasonic measurements were taken at three critical stages: (1) before fatigue cycling (as received), (2) at 50% of the expected fatigue life, and (3) near failure (around 5 million cycles). For each stage, fundamental (A_1) and second harmonic (A_2) amplitudes were recorded, and the

nonlinear parameter (β) was calculated using linear regression of A₂ versus A₁². Table 6-11 presents the number of cycles and the corresponding β values for each fatigue stage. The results are further visualized in Figure 6-20, which shows the trend of the nonlinear parameter as a function of fatigue cycles. As showed in Figure 6-20, the observed mountain-shaped trend reflects three distinct fatigue stages. In the early stage (0 to ~2.6 million cycles, or approximately 52% of fatigue life), the normalized β increases from 1 to 1.266, representing a 26.6% rise. This increase is because of the accumulation of dislocations and the formation of dislocation tangles, which increase the material's acoustic nonlinearity base on this study[108], [158]. During the intermediate stage (~2.6 million cycles), the nonlinear parameter peaks could be correlated to the rearrangement of dislocations into well-defined dislocation walls and cells. This leads to a temporary stabilization in microstructure. In the final stage (2.6 million to 4.985 million cycles, ~52% to ~99.7% of fatigue life), β gradually decreases to 1.033, marking a decrease of about 18.4% from its peak value. This reduction is likely due to the onset of microcrack formation and propagation. As fatigue failure approaches, the dominance of cracks causes a decline in acoustic nonlinearity, signalling the degradation of material integrity. This trend aligns with the findings discussed in Section 2.3.6.3, where nonlinear parameter measurements for selective laser melting (SLM) 316L stainless steel revealed three distinct fatigue stages: (1) an initial rise in dislocation density and tangle formation, (2) evolution of dislocation structures such as walls and cells, and (3) crack propagation and failure. These results confirm the sensitivity of NLP measurements in capturing the underlying microstructural transitions throughout the fatigue process [108, 157].

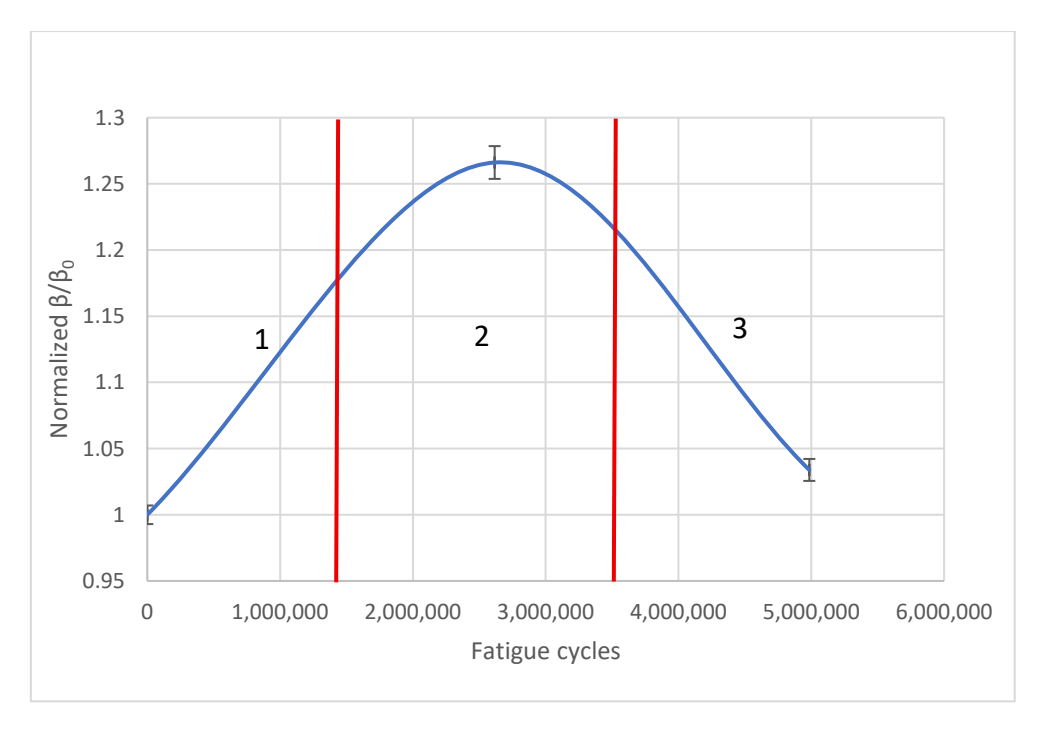


Figure 6-20. Normalized nonlinear parameter (eta) as a function of fatigue cycles in 316L stainless steel

Table 6-11. Summary of Normalized nonlinear parameter (β) in as-recived-50% and 98% fatigue life in 316L stainless steel

Cycle of fatigue life	Percentage of fatigue life	Normalized NLP
0	0	1
2,615,681	52%	1.266
4,985,000	98%	1.033

Now that the three main stages of fatigue damage detection have been confirmed using this method, the next step focuses on applying it to detect early-stage fatigue damage, specifically before 8% of the fatigue life. Figure 6-21 presents the NLP measurement results. The NLP is measured from 0 cycles up to 8% of the component's fatigue life, which corresponds to approximately 0.5 million cycles.

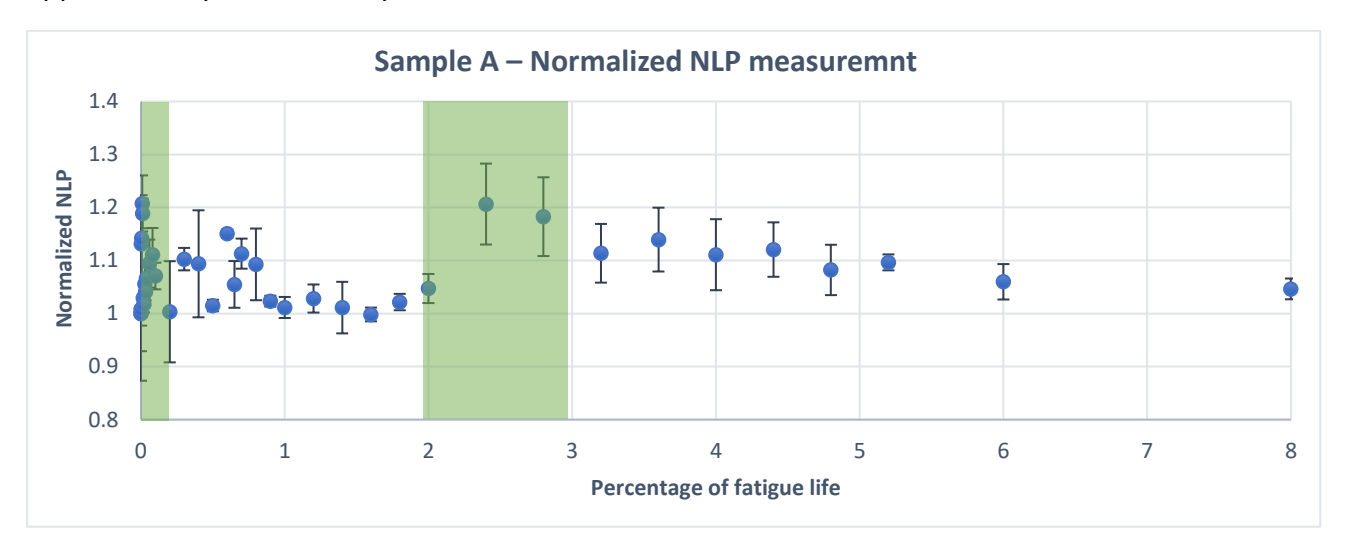


Figure 6-21. Normalised NLP plot vs % of fatigue life of stainless-steel sample A up to give 8% fatigue life equivalent to 400,000 Cycles

Based on this figure, at 0.004% of the fatigue life (200 to 400 cycles), there is a 16% increase in Nonlinear ultrasound parameter (β), followed by a subsequent decrease. Even after this drop, β remains 3% higher than the initial (as-received) sample. This elevated NLP level is maintained up to 2.4% (120K to 150K cycles) of the fatigue life. At 2.4% fatigue life, β increases again by 16%, followed by a drop back to its previous level, where it remains stable until 8% of the fatigue life. This pattern of increase and subsequent stabilization in NLP suggests microstructural changes occurring in stages, which may be linked to dislocation density evolution, slip band formation, or other fatigue-related mechanisms. The same test had been done on another sample with same initial condition as repeatability and reproducibility of results. Results are shown in Figure 6-22:

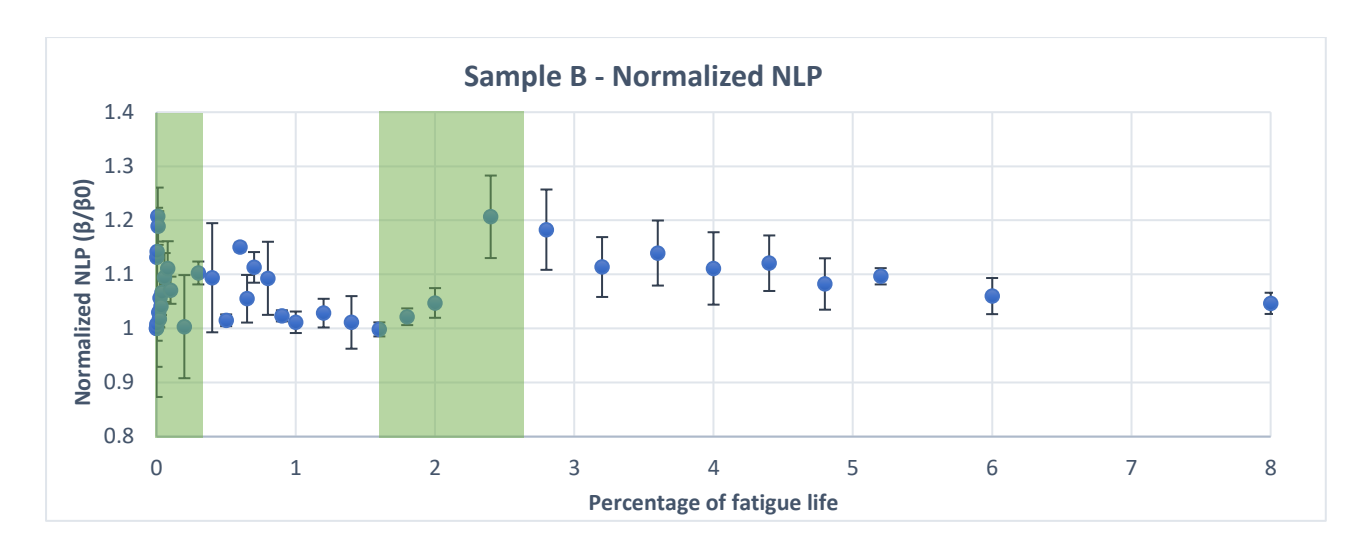


Figure 6-22. Normalised NLP plot vs % of fatigue life of stainless-steel sample B up to give 8% fatigue life equivalent to 400,000 Cycles

Based on Figure 6-22, at 0.004% of the fatigue life (200 to 400 cycles), there is a 15% increase in Nonlinear ultrasound parameter (β), followed by a subsequent decrease. This elevated NLP level is maintained up to 2.4% (120K to 150K cycles) of the fatigue life. At 2.4% fatigue life, β increases again by 16%, followed by a drop back to its previous level, where it remains stable until 8% of the fatigue life. This pattern of increase and subsequent stabilization in NLP is the same in both samples confirms the reliability of the nonlinear ultrasonic method in detecting early-stage fatigue damage. It also confirms the compatibility and reproducibility of the results, thereby validating the effectiveness of β as a sensitive and robust indicator for tracking fatigue-induced microstructural evolution.

6.4 Summary

In this chapter, the application of the nonlinear ultrasonic method (NLP) and electrical resistivity (ER) for early fatigue damage detection in 316L stainless steel was comprehensively investigated. Initial assessments focused on the repeatability and reliability of the measurement setup, confirming high consistency through multiple tests on different samples.

Initial experiments confirmed the high repeatability and reliability of the Keithley 6221/2182A setup through multiple trials, with low standard and pooled standard deviations across both stainless steel and AA6802 metallic specimen. The impact of surface roughness, measurement time and probe spacing on ER accuracy was also evaluated, and standardized procedures were established to ensure consistency. Subsequently, ER monitoring under high-cycle fatigue revealed distinct patterns of early damage evolution. Two notable peaks in ER were observed at approximately 0.01% and 1% of fatigue life, corresponding to early dislocation activity and microstructural rearrangements, respectively.

Further experiments on NLP explored the influence of signal gain and magnitude on measurement accuracy, leading to the identification of optimal operating parameters that ensured both precision and stability. The fatigue monitoring results revealed a characteristic mountain-shaped trend in the nonlinear parameter (β) across the fatigue life, aligning with established microstructural stages such as dislocation accumulation, formation of dislocation structures, and crack initiation. Most notably, detailed monitoring up to 8% of fatigue life showed two distinct increases in β —first at 0.004% and again at 2.4%—followed by periods of stabilization. These trends, consistently observed in two independently tested samples, demonstrate the method's sensitivity to early microstructural changes and confirm the reliability, compatibility and reproducibility of nonlinear ultrasonic testing. The results strongly support the use of NLP as an appropriate non-destructive evaluation technique for tracking fatigue-induced microstructural evolution from the earliest stages. The next chapter (Chapter 7) will present microscopy analyses to investigate the mechanisms underlying the observed β peaks and further assess the sensitivity of NLP and ER methods in detecting microstructural features such as slip bands and dislocation structures.

Chapter 7. Microstructural characterization results

7.1 Introduction

In this chapter, microstructural characterization results are reported. These characterizations were conducted to analyze the effects of early-stage high cycle fatigue on 316L stainless steel, focusing on the structural changes occurring before, at, and after each peak observed in electrical resistivity and nonlinear parameter measurements in Chapters 6. Initial microstructural studies were performed using optical microscopy (OM) and detailed microstructural studies were followed using transmission electron microscopy (TEM), which allowed for a detailed examination of dislocation structures and slip patterns.

7.2 Optical microscopy study

To investigate the microstructural changes associated with fatigue and peaks observed in nonlinear parameter and electrical resistivity measurements, optical microscopy (OM) was initially used on selected samples. The observations were carried out on flat fatigue samples of 316L stainless steel tested under a tension-compression fatigue regime (stress ratio R = -0.4, maximum stress = 260 MPa, frequency = 10 Hz) with a total fatigue life of 5 million cycles. Specifically, samples from the as-received condition, 80,000 cycles, and 120,000 cycles were examined. These cycles correspond to the second peak in the measured data, and the goal was to determine whether any observable microstructural changes could be detected at this scale. Figure 7-1 to Figure 7-3 present optical microscopy (OM) images of SS316L samples at different fatigue stages: the as-received condition (Figure 7-1), 80,000 cycles (Figure 7-2), and 120,000 cycles (Figure 7-3). These conditions were selected to examine the microstructure before and at the second peak observed in both the nonlinear ultrasonic (NLP) and electrical resistivity (ER) measurement. Across all three figures, the grain structure is unchanged. The microstructure shows equiaxed grains typical of austenitic stainless steel, with no visible signs of slip bands, intrusions, or microcrack formation at this magnification. Both the center and edge regions of the specimens demonstrate similar grain size and morphology, and no significant fatigue-related microstructural degradation is observed.

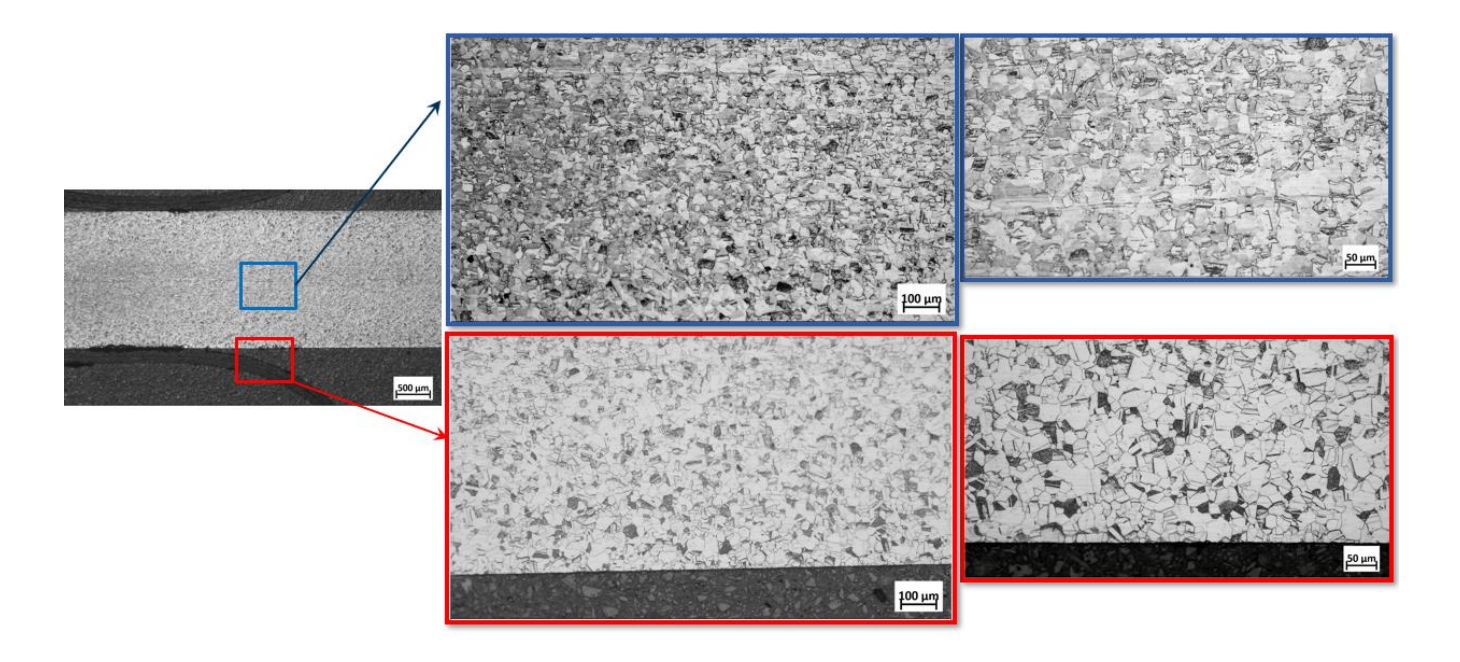


Figure 7-1. Optical microscopy images of as-received sample at two different magnifications, taken at the edge and centre of the sample's cross-section

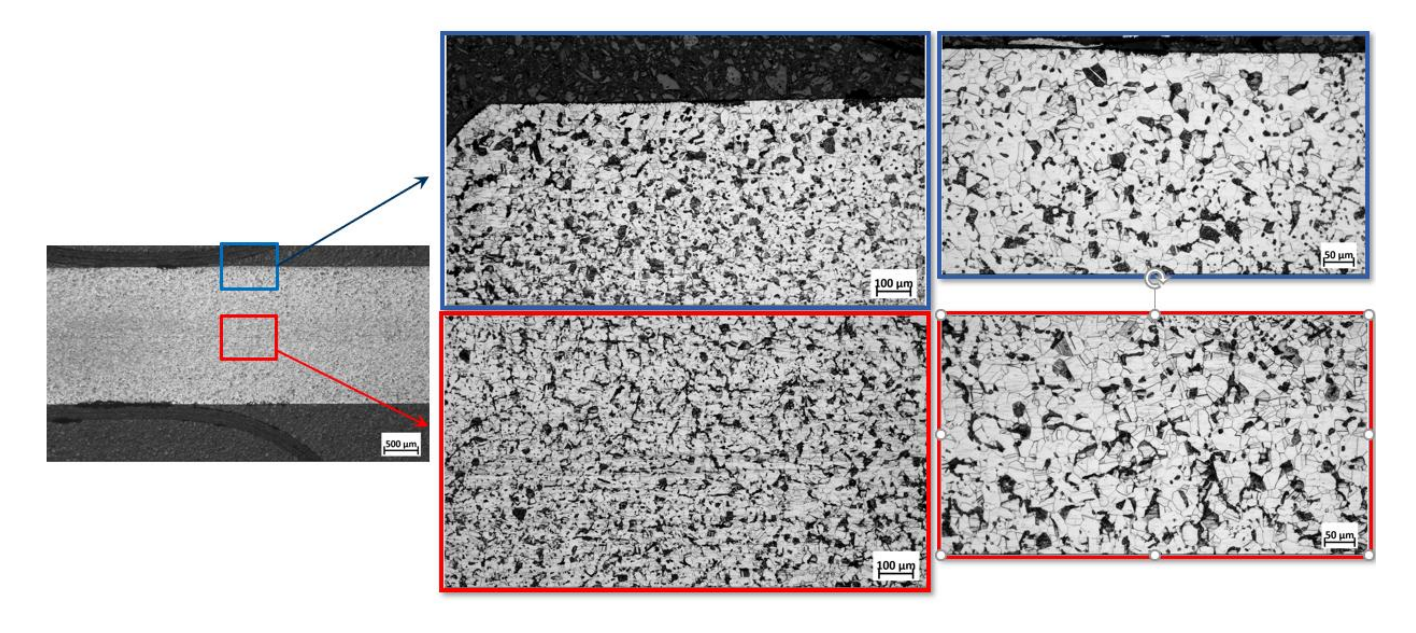


Figure 7-2. Optical microscopy images of the 80,000-cycle fatigue sample at two different magnifications, taken at the edge and centre of the sample's cross-section

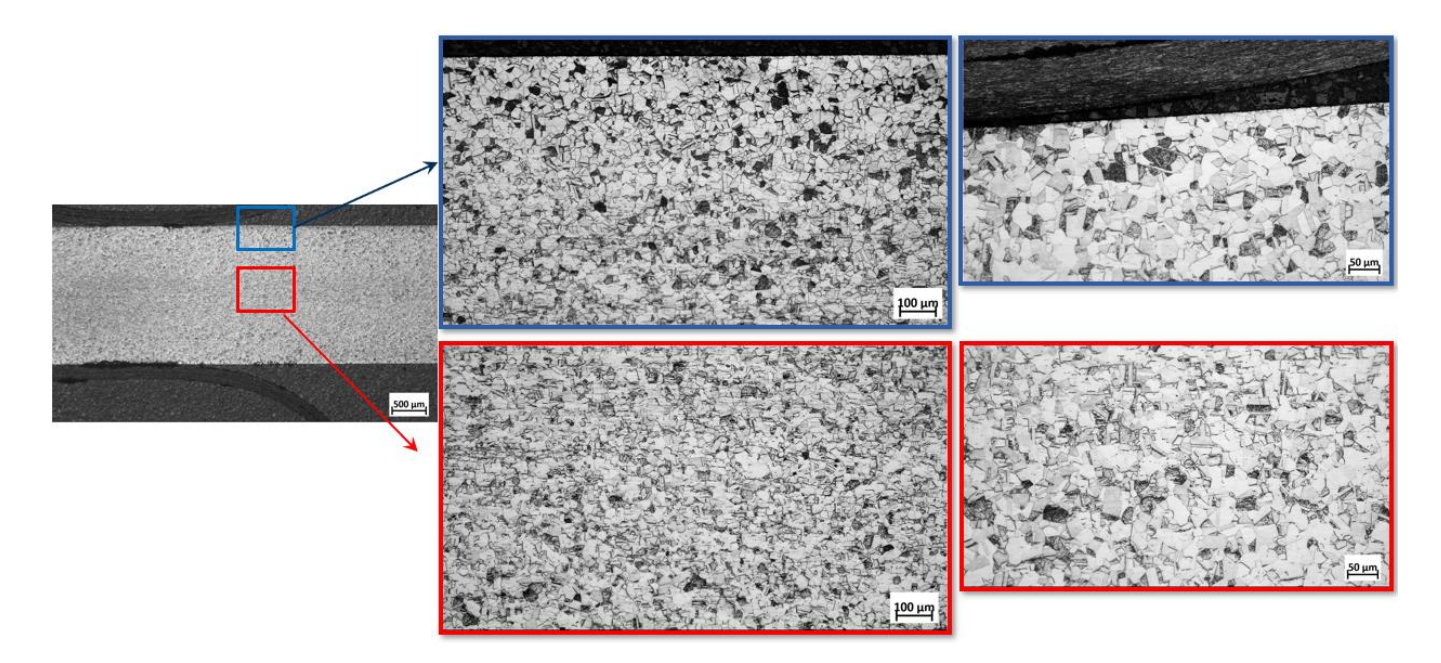


Figure 7-3. Optical microscopy images of the 120,000-cycle fatigue sample at two different magnifications, taken at the edge and centre of the sample's cross-section

OM investigation initially focused on the second peak to assess whether any optical-scale microstructural changes could be detected at these stages of fatigue. The logic was that if no differences were observed near the second peak—where the extent of damage is expected to be more pronounced—then earlier stages such as the first peak would likely also show no discernible changes with OM. Since the results confirmed that OM could not resolve the microstructural evolution even near the second peak, it was deemed unnecessary to proceed with lower-cycle samples using this technique. The resolution limit of OM (in the micrometre range) is insufficient to capture the microstructural changes (e.g., dislocation tangles or early cell formation) believed to occur at the nanometre scale. Therefore, higher-resolution methods such as TEM were adopted in later part of this chapters to investigate these nanoscale phenomena.

7.3 TEM studies

Section 7.3.1 presents the TEM images of 316L stainless steel samples at different cycling stages. These images were captured from the same grain using two techniques: conventional TEM (Bright field TEM imaging) and STEM-HAADF. The latter was employed to validate the discussion in Section 5.6.2.1.3 regarding the advantages of using STEM-HAADF in this study. Following this, TEM images corresponding to various cycling stages, particularly those associated with peak evolution observed in ER and NLP measurements, are reported.

7.3.1 Comparison of conventional TEM and STEM-HAADF images

Figure 7-4 to Figure 7-6 present a comparative microstructure analysis of 316L stainless steel flat fatigue samples tested under the tension–compression fatigue regime (R = -0.4, maximum stress = 260 MPa, frequency = 10 Hz, total fatigue life = 5×10^6 cycles using both conventional Bright Field Transmission Electron Microscopy (BF-TEM) and Scanning

Transmission Electron Microscopy with High-Angle Annular Dark Field (STEM-HAADF) imaging. For each fatigue condition, image (a) represents the Bright Field TEM image, while image (b) corresponds to the STEM-HAADF image. All Bright Field TEM and STEM-HAADF images presented in Figures 7-4 to 7-6 were taken under the two-beam condition using the g = [110] diffraction vector, with the sample oriented along the <110> beam direction to optimize dislocation contrast in FCC 316L stainless steel.

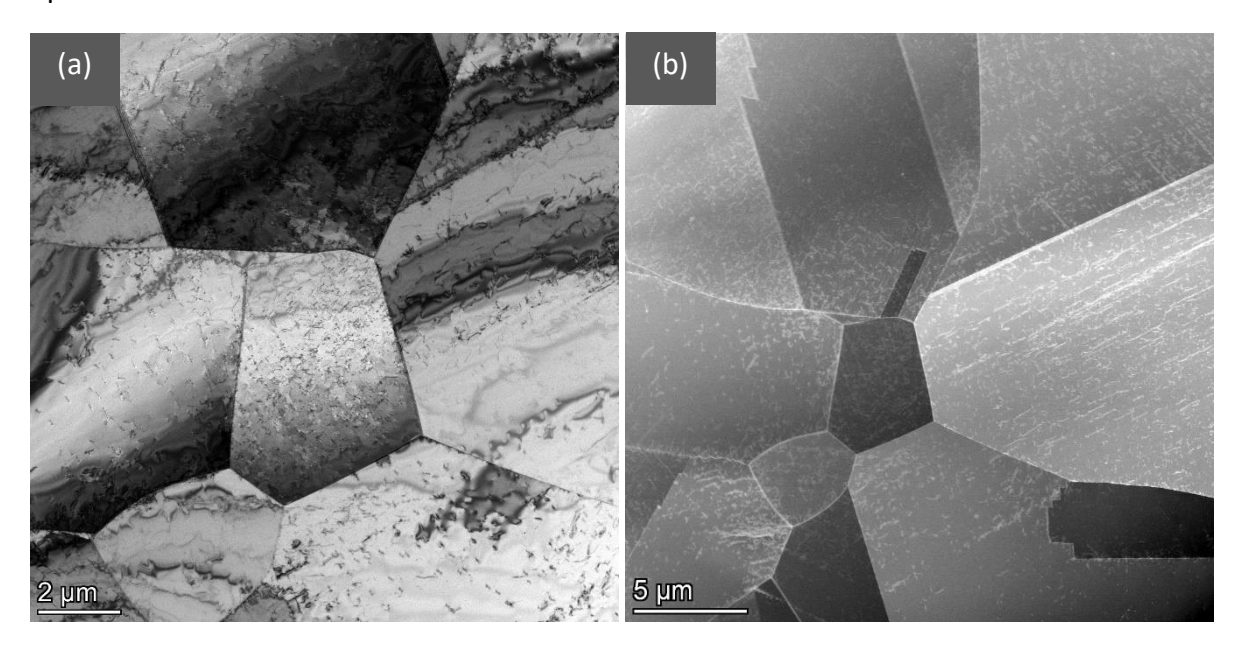


Figure 7-4. St.st 316L as-received flat sample (a) BF-TEM (b) STEM-HAADF from the same grain

Figure 7-4, shows the as-received 316L stainless steel sample imaged using both BF-TEM and STEM-HAADF under the g = [110] two-beam condition. In the BF-TEM image (Figure 7-4a) is dominated by complex contrast effects due to bending contours and thickness variation. These artefacts obscure finer microstructural details and hinder accurate assessment of dislocation configurations. In contrast, the STEM-HAADF image (Figure 7-4b), taken from the same region, provides a clearer view of the grain structure with minimal imaging artefacts. The homogeneous contrast in this mode facilitates the identification of dislocation features and sets a more reliable baseline for tracking microstructural evolution during fatigue.

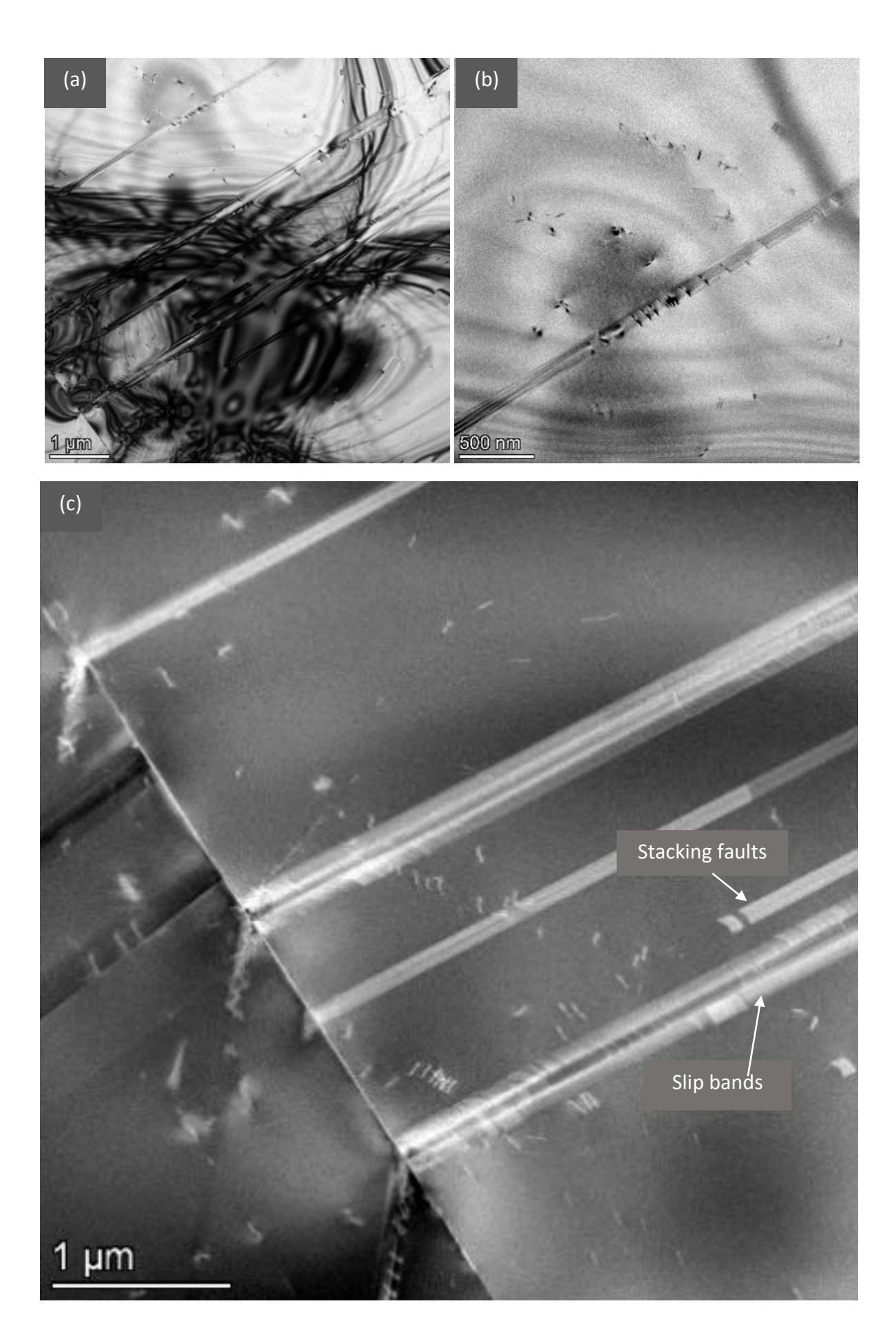


Figure 7-5. St.st 316L St.st at 0.03% fatigue life (a and b) BF-TEM (c) STEM-HAADF from same grain

Figure 7-5 captures the microstructure at an early fatigue stage (approximately 0.03% of fatigue life). The BF-TEM images (Figure 7-5a and b) show the presence of emerging slip activity and potential stacking faults. However, the visibility of these features is significantly reduced due to strong diffraction contrast and bending contours, making precise analysis of dislocation structures and slip bands challenging. In comparison, the STEM-HAADF image (Figure 7-5c) presents a high-contrast view of the same grain area, clearly displaying isolated dislocations and stacking faults. This demonstrates the enhanced capability of STEM-HAADF to resolve early-stage fatigue-induced defects with minimal interference from imaging artefacts.

Figure 7-6 presents the microstructure at approximately 2% fatigue life. The BF-TEM image (Figure 7-6a) again shows significant distortion from bending contours and overlapping contrast effects, which obscure detailed dislocation structures. By contrast, the STEM-HAADF image (Figure 7-6b) of the same region reveals a more defined and continuous dislocation network. The elimination of diffraction-related contrast allows for clearer visualization of dislocation evolution, highlighting the value of STEM-HAADF in characterizing fatigue-induced microstructural changes at early stages of fatigue.

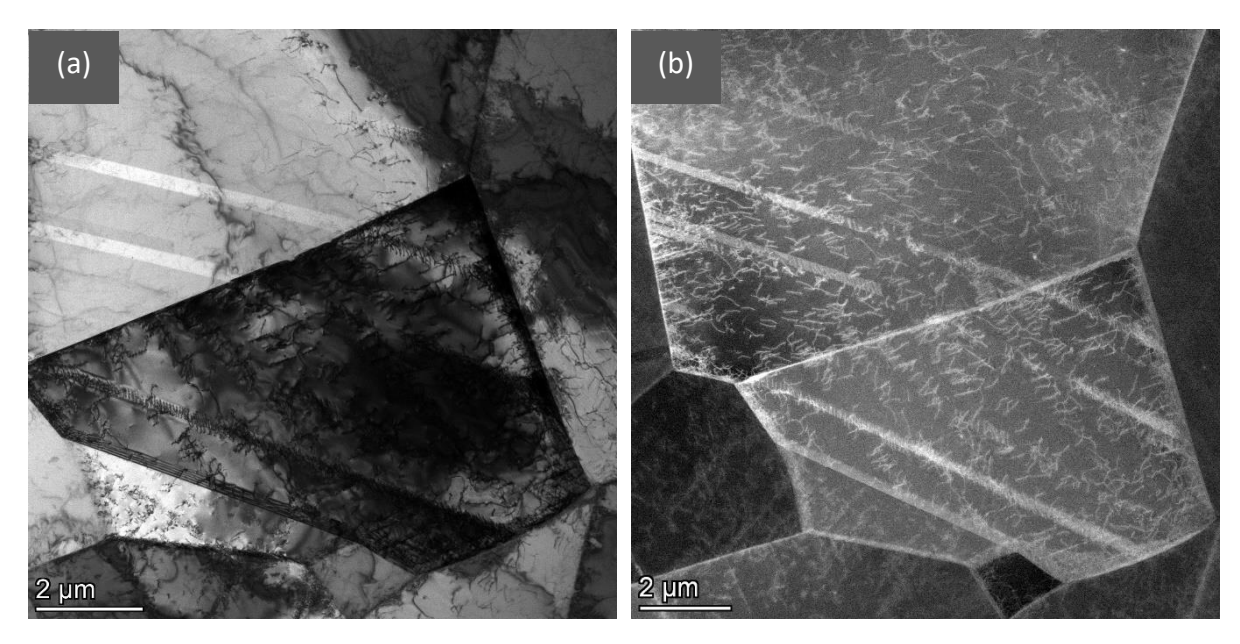


Figure 7-6. St.st 316L at 2% fatigue life (a) BF-TEM (b) STEM-HAADF for the same grain

Based on these results, STEM-HAADF imaging consistently demonstrates better contrast and clarity compared to BF-TEM condition. This advantage enables more accurate visualization of microstructural features such as dislocation structures and slip bands. Given these benefits, all subsequent imaging in the next stages of this research will be taken by using the STEM-HAADF technique to ensure the highest possible image quality and analytical reliability.

7.3.2 STEM-HAADF studies of stainless steel 316L subjected to fatigue

In this section, STEM-HAADF images obtained from samples at different fatigue cycles are presented, and the microstructural features observed at each stage are discussed. The images were taken from 316L stainless steel flat fatigue samples tested under a tension—compression fatigue regime (R = -0.4, maximum stress = 260 MPa, frequency = 10 Hz, total fatigue life = 5×10^6 cycles). The selected fatigue stages include the as-received condition, 200 cycles, 1,500 cycles, 80,000 cycles, and 120,000 cycles. These specific cycles were chosen to capture the microstructural evolution before, during, and after the characteristic peaks observed in the nonlinear parameter (NLP) and electrical resistivity (ER) results. Then in Chapter 8 correlation between these microscopic findings and Non-destructive evaluation results that was reported in Chapter 6 will be discussed.

In the as-received sample the most prominent characteristic across all grains is the presence of individual planar dislocations. Dislocations are primarily distributed along the grains. Moreover, some grains display twin boundaries, which are commonly observed in low-SFE FCC alloys and contribute to strain accommodation. Figure 7-7. shows a STEM-HAADF image of one grain of as received sample oriented along the <110> beam direction, captured at different magnifications. The loading direction (LD) is indicated in all images. After indexing the SAED pattern, it can be observed that these dislocations are aligned along the [220] direction, which corresponds to the $\langle 110 \rangle$ slip direction—the primary slip direction in FCC metals, such as the austenitic phase of 316L stainless steel. This alignment confirms that dislocation motion occurs mainly within the $\{111\}$ $\langle 110 \rangle$ slip system [29].

Figure 7-8 focuses on a twin boundary, highlighting the structural interface within the grain. The SAED pattern shown in Figure 7-8 (a) confirms the presence of a twin boundary through its characteristic mirror symmetry. Like other grains, dislocations observed in this image are aligned along the [220] direction, consistent with the primary $\langle 110 \rangle$ slip direction of the FCC structure. This further supports the dominance of the $\{111\}$ $\langle 110 \rangle$ slip system in the as received 316L stainless steel.

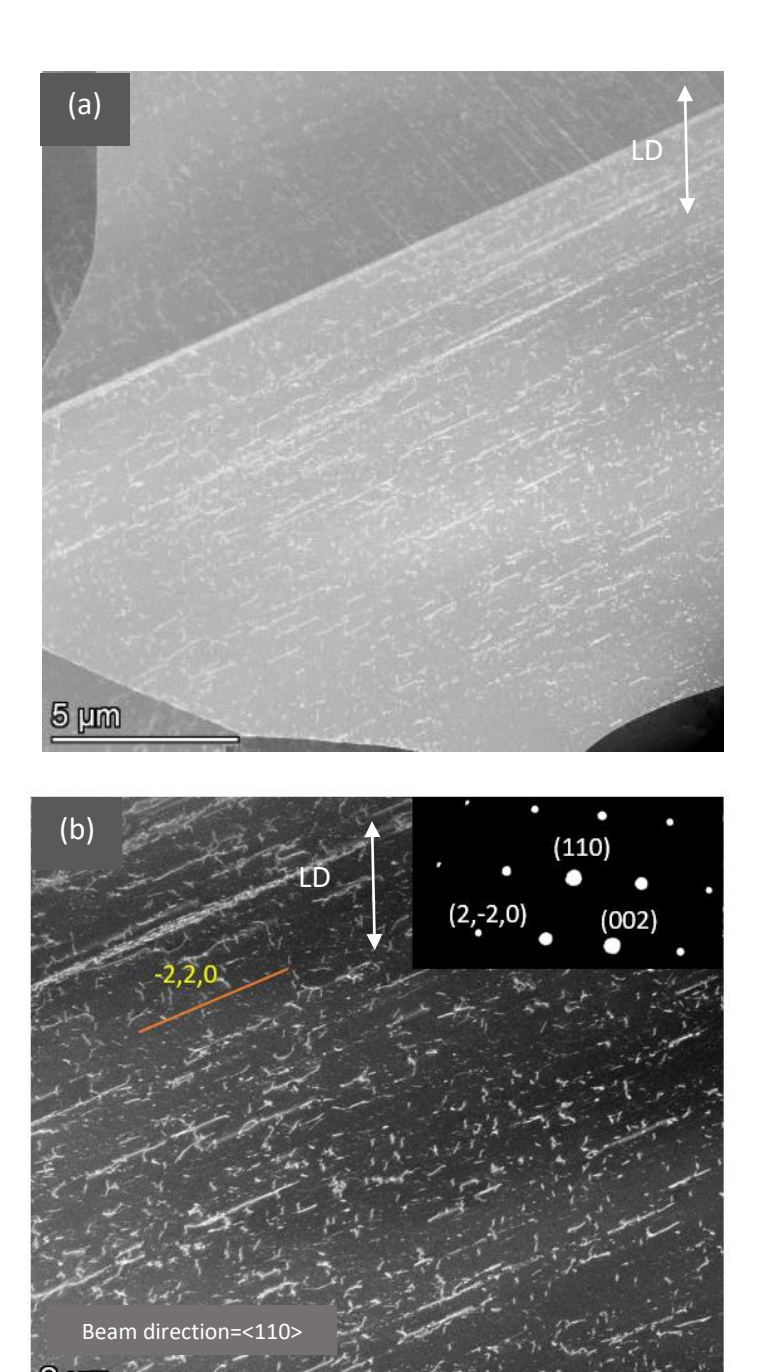
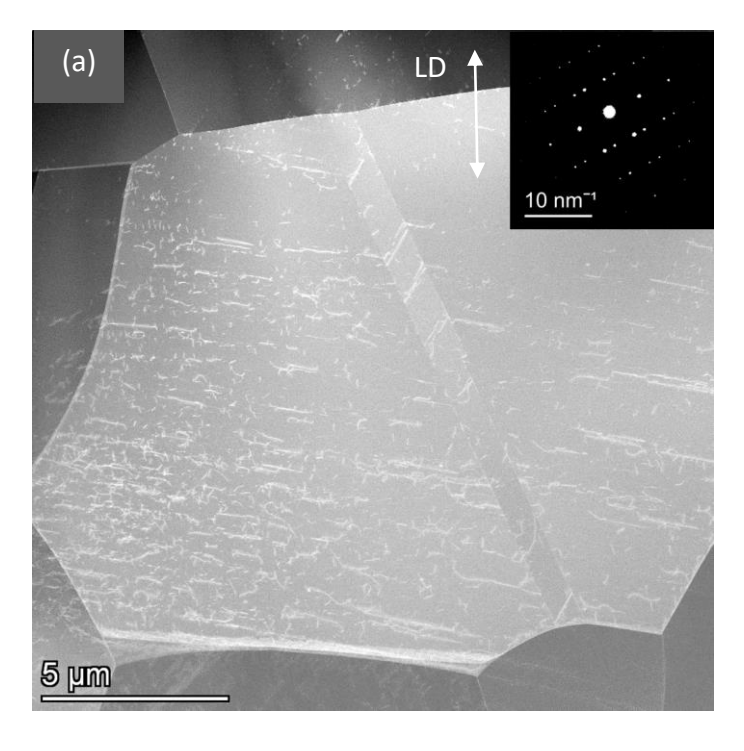


Figure 7-7. Dislocation condition in as- received sample with (a) Lower magnification; (b) Higher magnification. The orange line indicates crystallographic direction [Z20] determined from the SAED pattern, aligned with the <110> beam direction



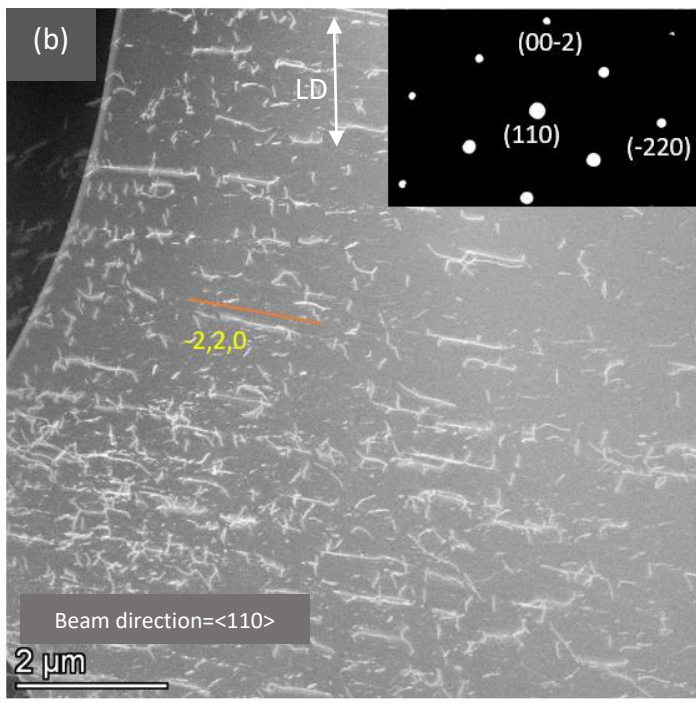


Figure 7-8. Dislocation condition in as- received sample with (a) Lower magnification; (b) Higher magnification. The orange line indicates crystallographic direction [220] determined from the SAED pattern, aligned with the <110> beam direction

At the 200-cycle stage, the main differences observed compared to as received condition is an increase in dislocation density, dislocation tangles near grain boundaries and the onset of dislocation alignment in specific directions indicating the initiation of slip bands. Each of these features is discussed in more detail in the following paragraphs. As shown in Figure 7-9, a notable increase in dislocation density close to grain boundaries is observed, on the other hand, there is a slight increase in dislocation density within the grains and we can see more

tangled planar structures. Also slip bands were observed in some grains as shown in Figure 7-13 . In addition to the slip bands, stacking faults are also observed in some grains like the one in Figure 7-9. Additionally, dislocations accumulate significantly near grain boundaries during cyclic deformation forming pile-up. Across the grain, dislocations intersect in two directions, signalling the activation of multiple slip systems to manage strain. Additionally, TEM images reveal activation of primary and secondary slip systems, though with higher intensity near grain boundaries. The incidence of tangled structures(Figure 7-9a and Figure 7-10a) increases with dislocation density and such structures can act as obstacles for the movement of dislocations, the formation of tangled structures promotes the activation of secondary slip planes near grain boundaries, higher initial dislocation density, such as dislocation pile-up(Figure 7-9a and Figure 7-10b), creates internal stresses that promote the early activation of secondary slip systems. These mechanisms contribute to the evolving microstructure at the 200-cycle stage.

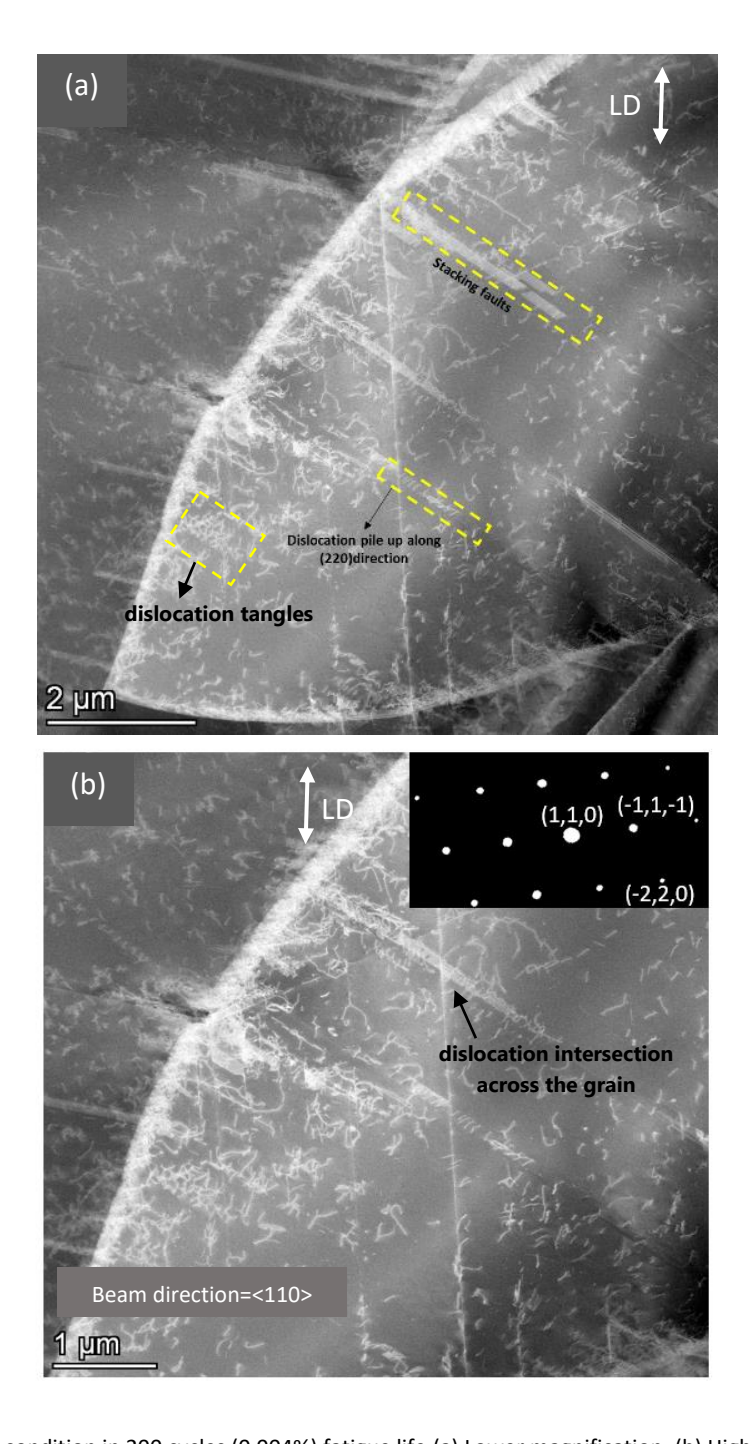


Figure 7-9. Dislocation condition in 200 cycles (0.004%) fatigue life (a) Lower magnification; (b) Higher magnification. The orange lines indicate crystallographic directions [220] and [004] determined from the SAED pattern, aligned with the <110> beam direction.

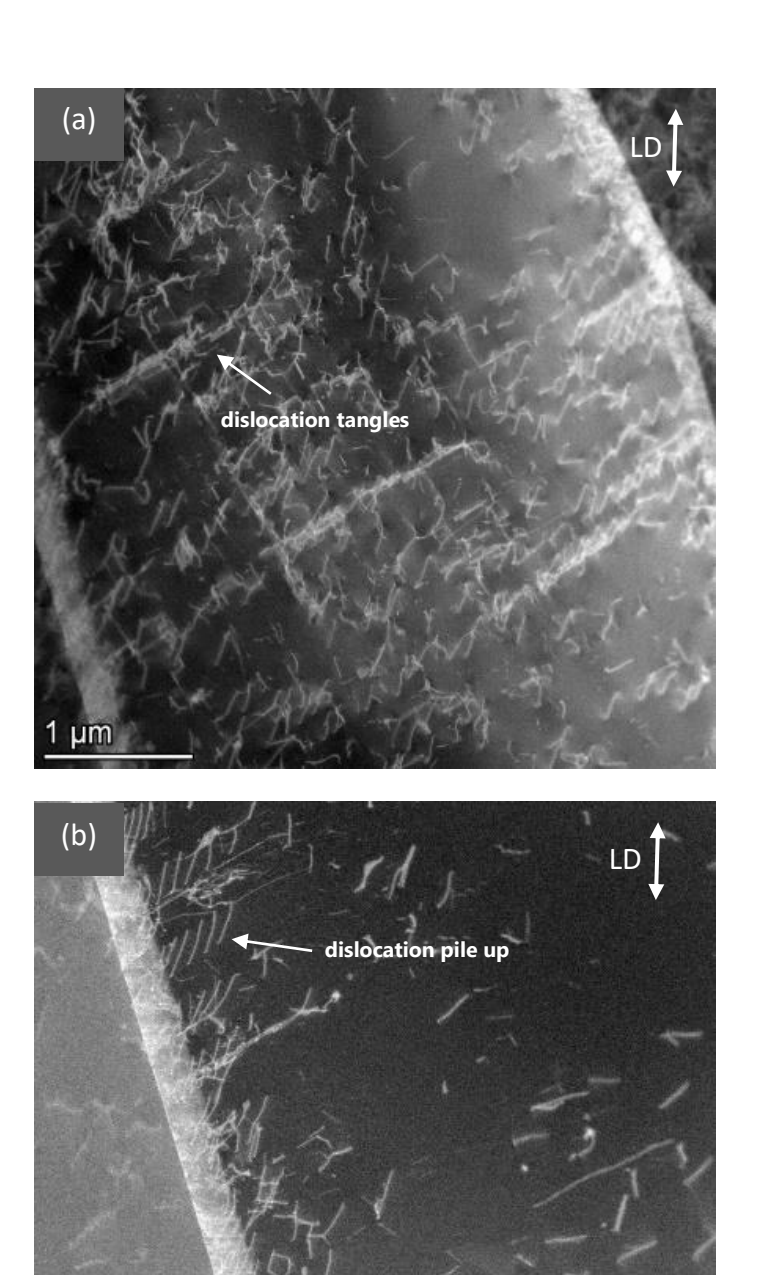


Figure 7-10. Dislocation condition in 200 cycles (0.004%) fatigue life (a) Lower magnification; (b) Higher magnification

500 nm

While <110> beam direction is ideal for FCC structures like 316L stainless steel , images with other beam directions also had been taken. This could give more comprehensive view and details of different grains at this cyclic life. Considering Figure 7-11a in <111> and Figure 7-11b <112> in beam direction same results can be observed across grains showing consistency in results. These observations, demonstrating consistent microstructural evolution regardless of the grain's crystallographic orientation.

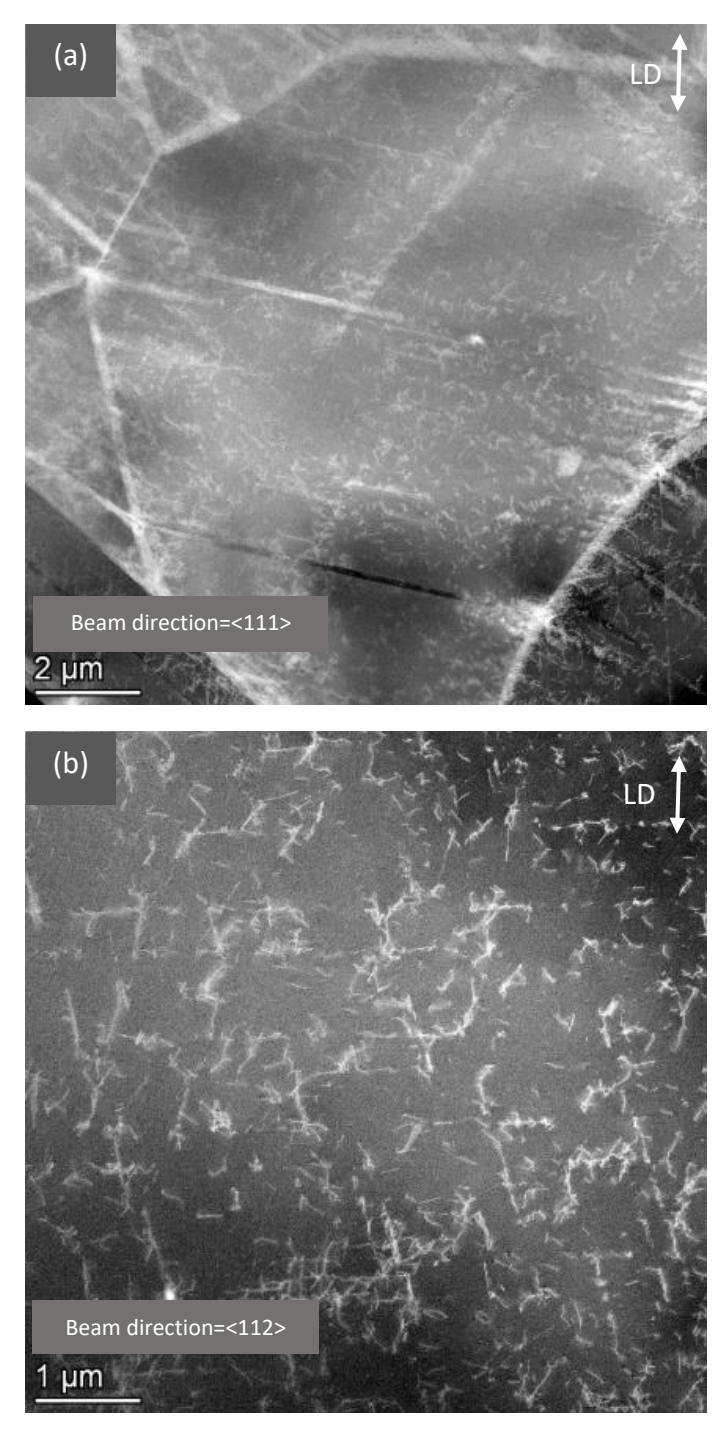


Figure 7-11. Dislocation condition with different beam directions at 200 cycles (0.004%) fatigue life (a) one grain with beam direction <111> and lower magnification; (b) another grain with beam direction <112> and higher magnification

Figure 7-12 presents not only the similar dislocation structure as other grains, but also the diffraction pattern of this grain reveals the presence of a twin. Dislocations are observed to accumulate along the twin boundary, indicating that it serves as both a barrier to dislocation motion and a site for stress concentration.

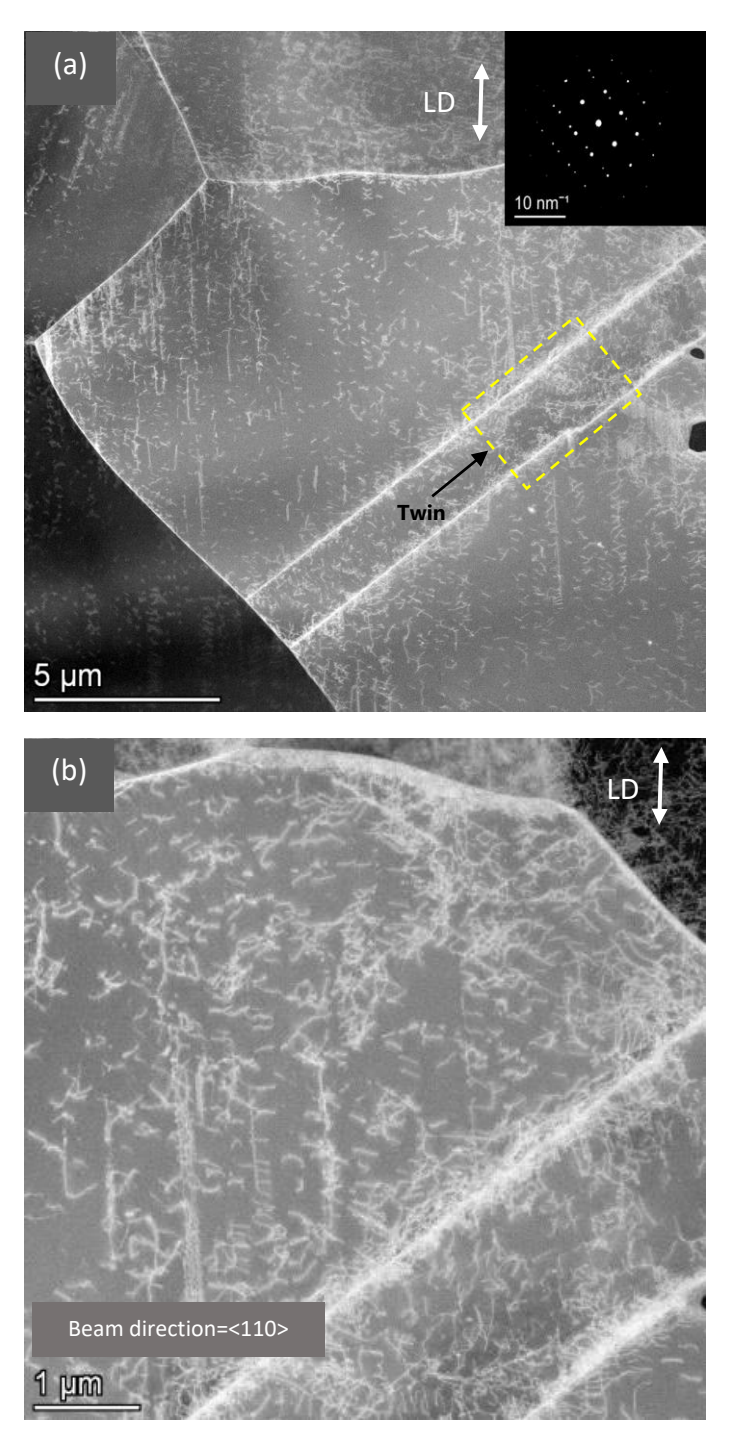


Figure 7-12. Presence of twin at 200 cycles (0.004%) fatigue life (a) Lower magnification; (b) Higher magnification

Slip band is a visible result of deformation caused by the motion of dislocations along specific planes in a crystal structure, known as slip planes. When shear stress is applied, dislocations move step-by-step across the crystal, causing localized deformation. This movement creates permanent, microscopic deformations in the material which manifest as slip bands indicating regions where atoms have been displaced due to the dislocation activity. Figure 7-13 captured with the electron beam oriented along the [112] direction, reveal the presence of slip bands distributed throughout the grain in 200 cycles. These bands are regions of concentrated dislocation activity, where dislocations are organized in a regular and parallel arrangement.

In the higher magnification image in Figure 7-13 b, slip bands shows evidence of intense dislocation interactions.

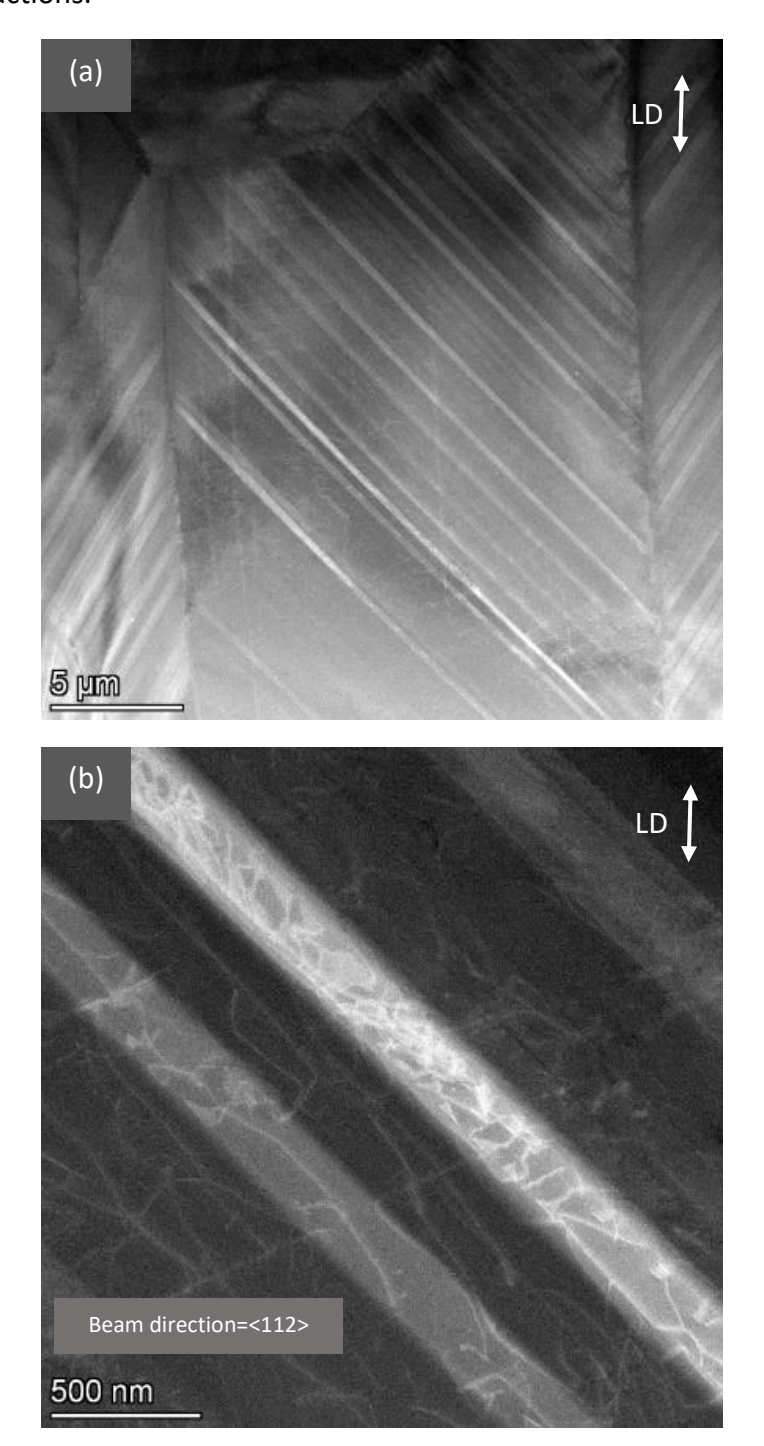


Figure 7-13.Presence of slip bands at 200 cycles (0.004%) fatigue life (a) Lower magnification; (b) Higher magnification

Next cycle that had been investigated is 1500 cycles which is around 0.03% fatigue life. As shown in Figure 7-14 at 1500 cycles, dislocations form more organized structures such as partial dislocation walls or aligned structure in specific directions. Grain boundaries become more defined again compared to the 200-cycle stage, reflecting a transition to a more stable structure.

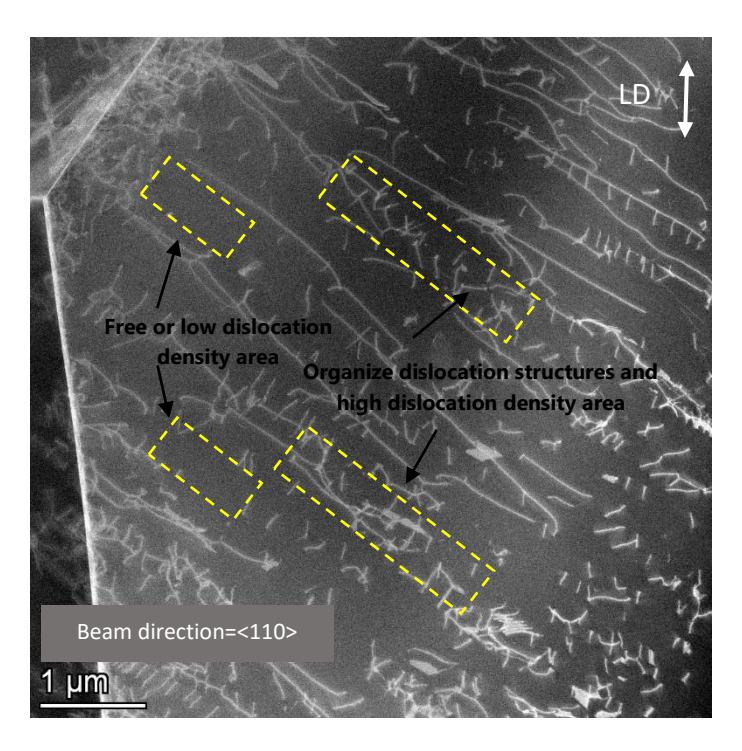


Figure 7-14. Dislocation condition at 1500 cycles (0.03%) fatigue life with beam direction <110>

Figure 7-15 clearly reveals the formation of slip bands aligned along the $[-1\ 1\ 1]$ direction, indicating active slip along the (111) plane—part of the dominant $\{111\}\$ $\langle 110\rangle$ slip system in FCC metals. In addition to slip bands, the presence of stacking faults is also evident.

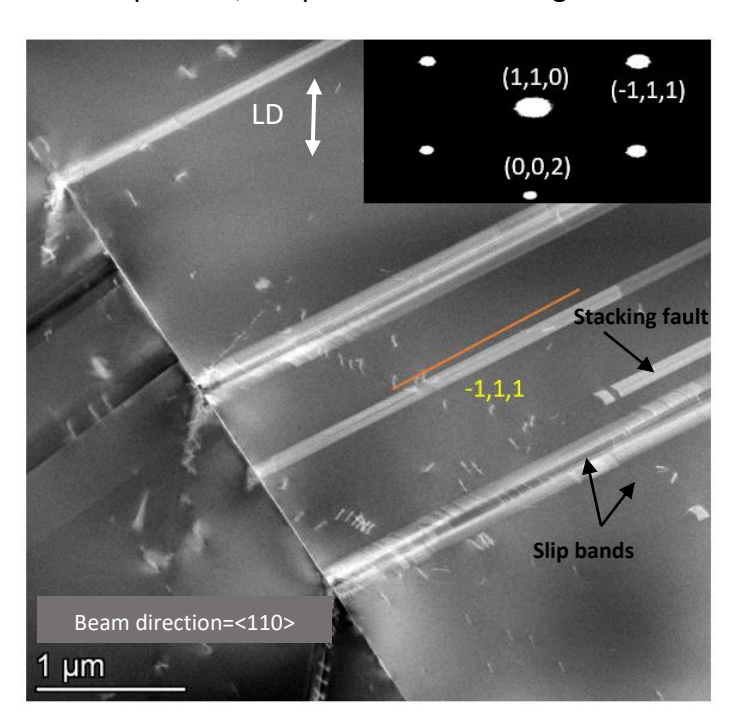


Figure 7-15. Dislocation structure at 1500 cycles (0.03%) fatigue life with beam direction <110>. The orange line indicates crystallographic direction [T1T] determined from the SAED pattern, aligned with the <110> beam direction

In some grains as shown in Figure 7-16 dislocation arrangements show characteristics like the wall—channel pattern. These tangled regions may evolve into cellular or sub-grain structures over continued cycling. The key observation compared to the 200-cycle stage is the

emergence of aligned dislocations forming slip bands in most grains. Furthermore, some grains show dislocation-free areas in their interiors, likely resulting from the annihilation or rearrangement of mobile dislocations.

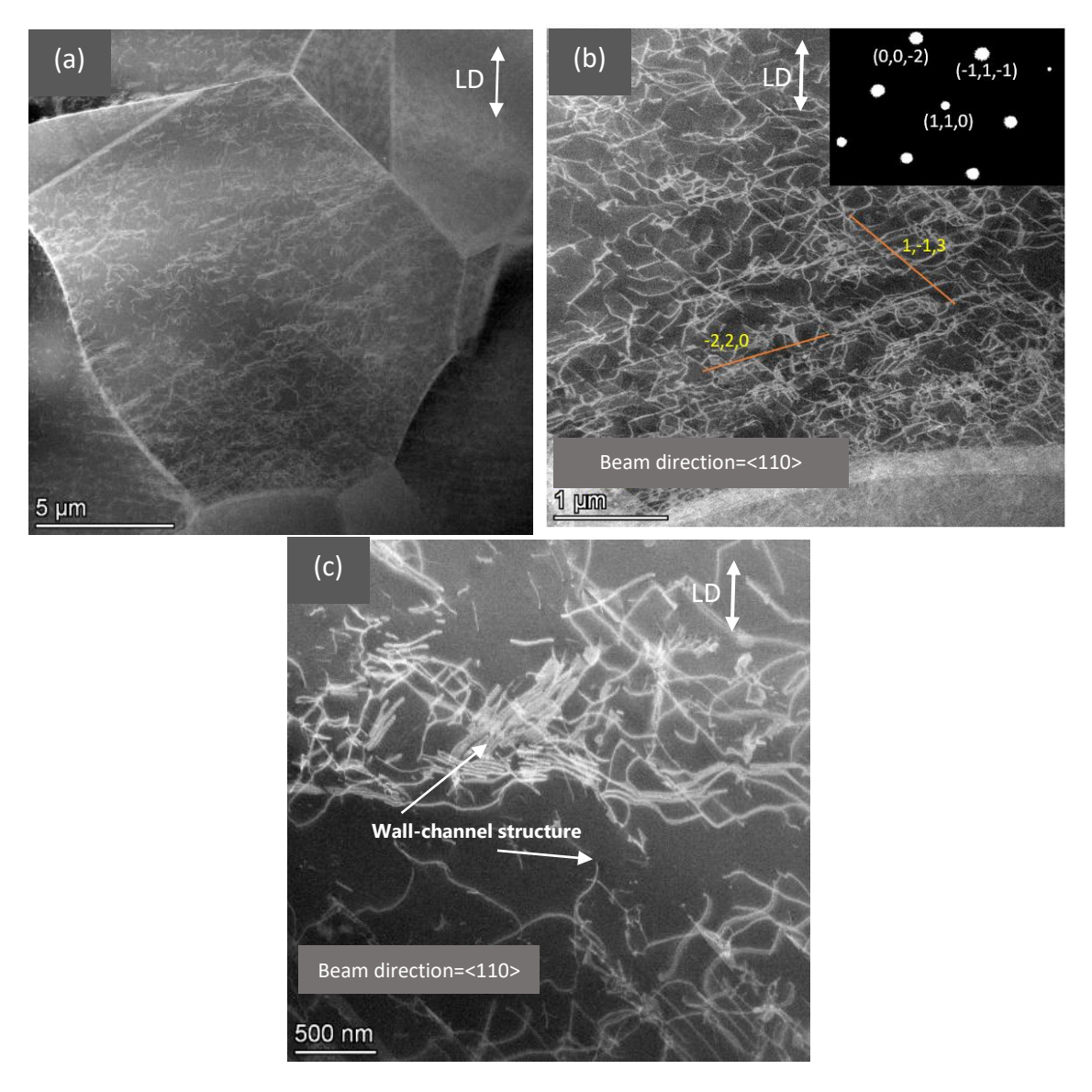
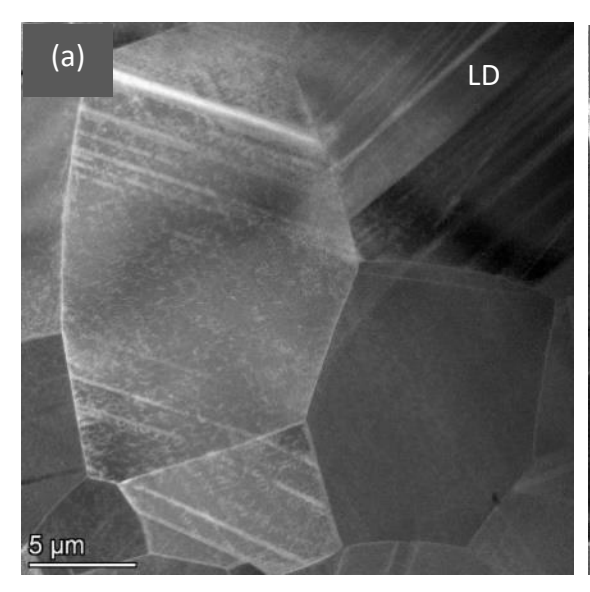


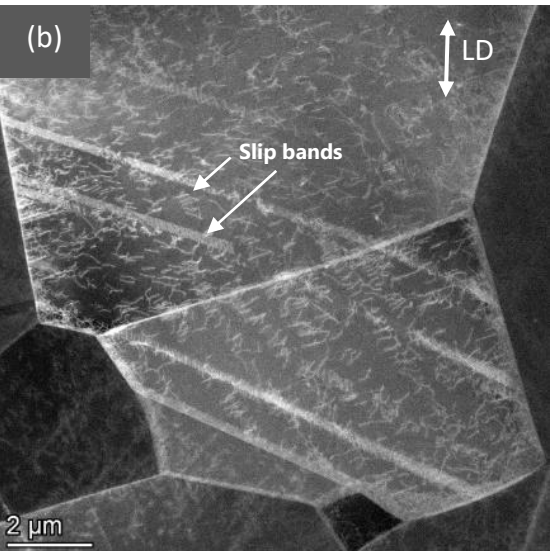
Figure 7-16. Dislocation condition at 1500 cycles (0.03%) fatigue life with beam direction <110> in a grain with different magnifications (a) Lower magnification; (b and c) higher magnification images of the bottom region of the grain shown in (a). The orange lines indicate crystallographic directions [T13]and [Z20]as determined from the SAED pattern, aligned with the <110> beam direction

At 80,000 cycles—corresponding to approximately 2% of the total fatigue life—the dislocation structures in 316L stainless steel show clear progression from earlier stages. While some features resemble those observed at 1,500 cycles, the microstructure becomes more evolved and complex, particularly in terms of slip band formation and interactions between active slip systems.

In Figure 7-17a (low magnification), broad slip bands are visible across the grain, along with regions where dislocations accumulate into more compact structures. Moving to Figure 7-17b, a higher magnification image reveals that the dislocation activity is increasingly

localized within well-defined slip bands. These bands are more pronounced compared to earlier cycles, such as at 1,500 cycles. Dislocations inside these bands appear dense and aligned, while the regions between them are relatively dislocation-free. In Figure 7-17c, another high-magnification view of the same grain shows a more detailed structure of these bands. Compared to 1500 cycle, more and wider slip bands is observed within the grains (Figure 7-17b and Figure 7-18). However, it seems that there is no significant increase in overall dislocation density. Instead, slip bands dominate the deformation behaviour with dislocation activity becoming more localized within these bands (Figure 7-18). Between slip bands areas free of dislocations existed, as the dislocations have either annihilated or are entirely concentrated within the bands. In Figure 7-18a multiple slip bands are observed within the grain, with several intersecting at different angles. This indicates the activation of both primary and secondary slip systems.





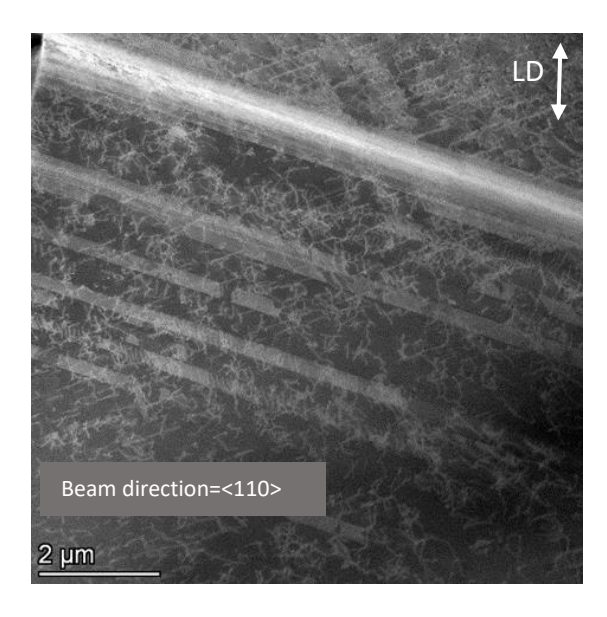


Figure 7-17. Dislocation condition at 80,000 cycles (1.6% fatigue life) (a) Lower magnification; (b) Higher magnification image of the bottom region of the grain shown in (a); (c) Higher magnification image of the upper region of the grain shown in (a)

Figure 7-18b, captured at higher magnification, reveals localized regions of intense dislocation activity at the intersection of multiple slip bands. The bright regions correspond to areas of high dislocation density, where dislocations from different systems interact and form tangles or pile-ups. The aligned dislocation lines within the slip bands and their intersection geometry suggest slip band interaction and cross-slip activity. This indicates that multiple slip systems are active, leading to localized stress concentrations and microstructural refinement characteristic of intermediate fatigue stages in 316L stainless steel.

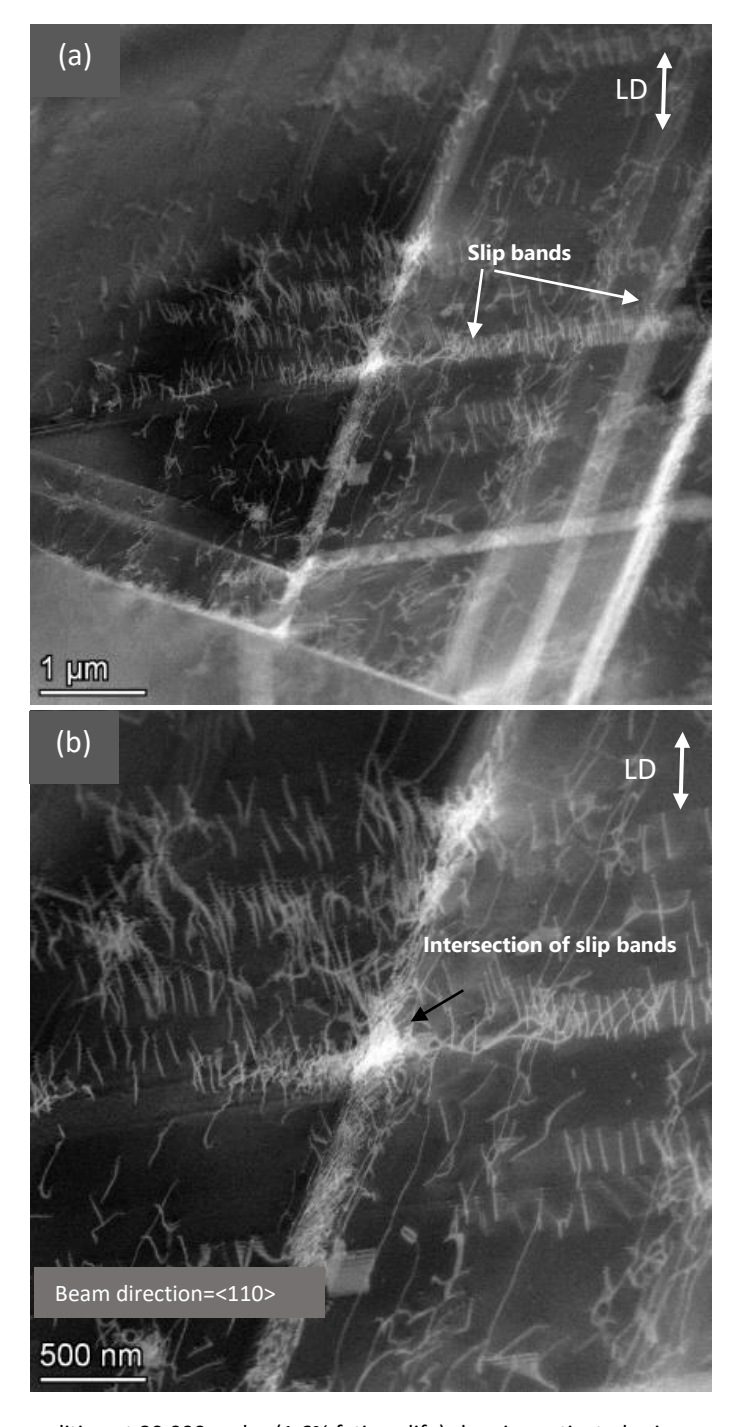


Figure 7-18. Dislocation condition at 80,000 cycles (1.6% fatigue life) showing activated primary and secondary slip bands (a) Lower magnification; (b) Higher magnification

Figure 7-19 provides further confirmation of multiple slip system activity at 80,000 cycles (1.6% of fatigue life). Multiple sets of slip traces intersect at various angles, clearly indicating dislocation motion occurring on more than one slip plane.

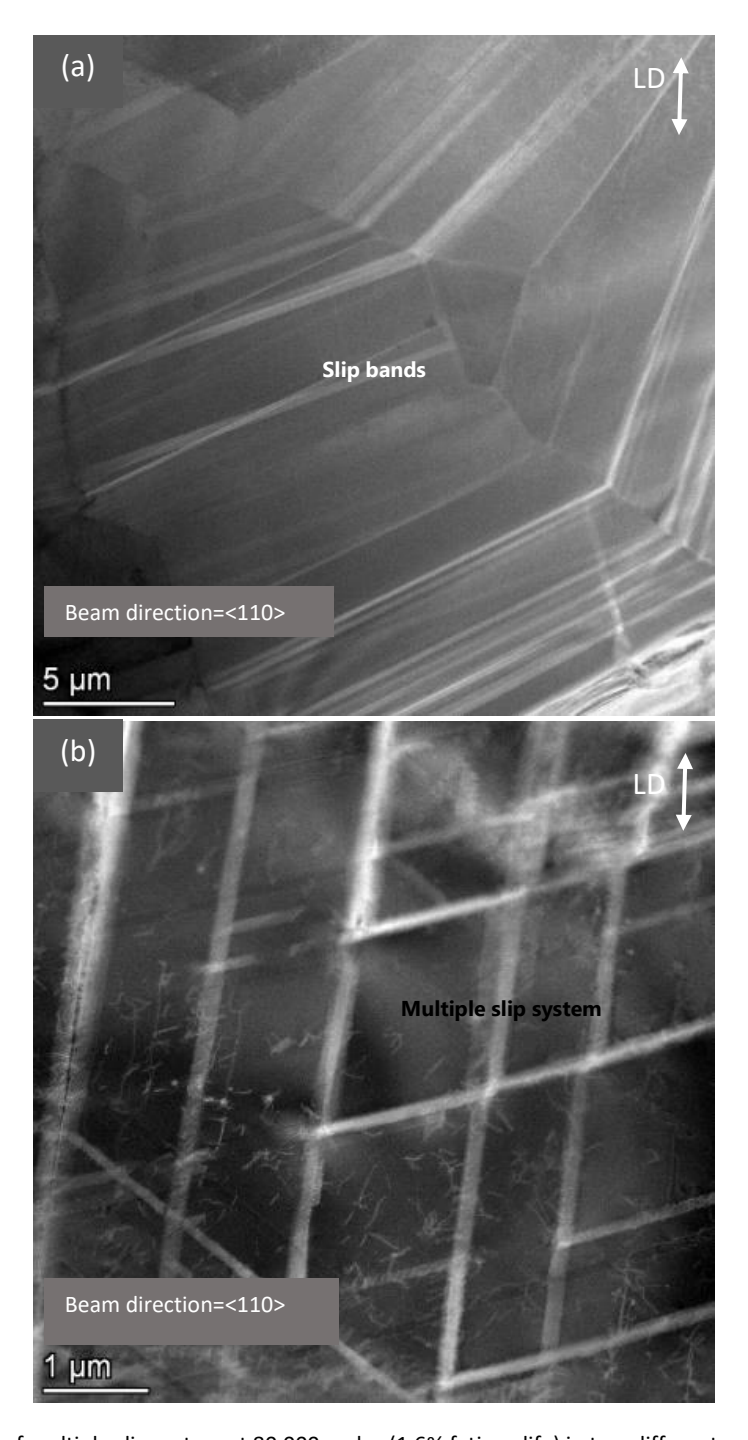


Figure 7-19. Presence of multiple slip system at 80,000 cycles (1.6% fatigue life) in two different grains (a) grain one with <110> beam direction (b) grain two with <110> beam direction

To summarize, at 80000 cycles, the microstructure is dominated by thicker and more numerous slip bands. The crossing of slip bands and the activation of multiple slip systems result in increased localization of deformation. Additionally, dislocation-free areas become prominent in the regions between slip bands. At 120,000 cycles, as shown in Figure 7-20 the microstructure reveals thick tangles of dislocations, an overall higher dislocation density, reduced dislocation mobility and possibly of formation of cell structures. A key observation at this stage is the presence of thicker slip bands and the reappearance of dislocations between them. Figure 7-21 shows a grain where secondary slip system activation is still clearly visible.

Multiple slip bands intersect at sharp angles, showing continued deformation via multiple active slip systems.

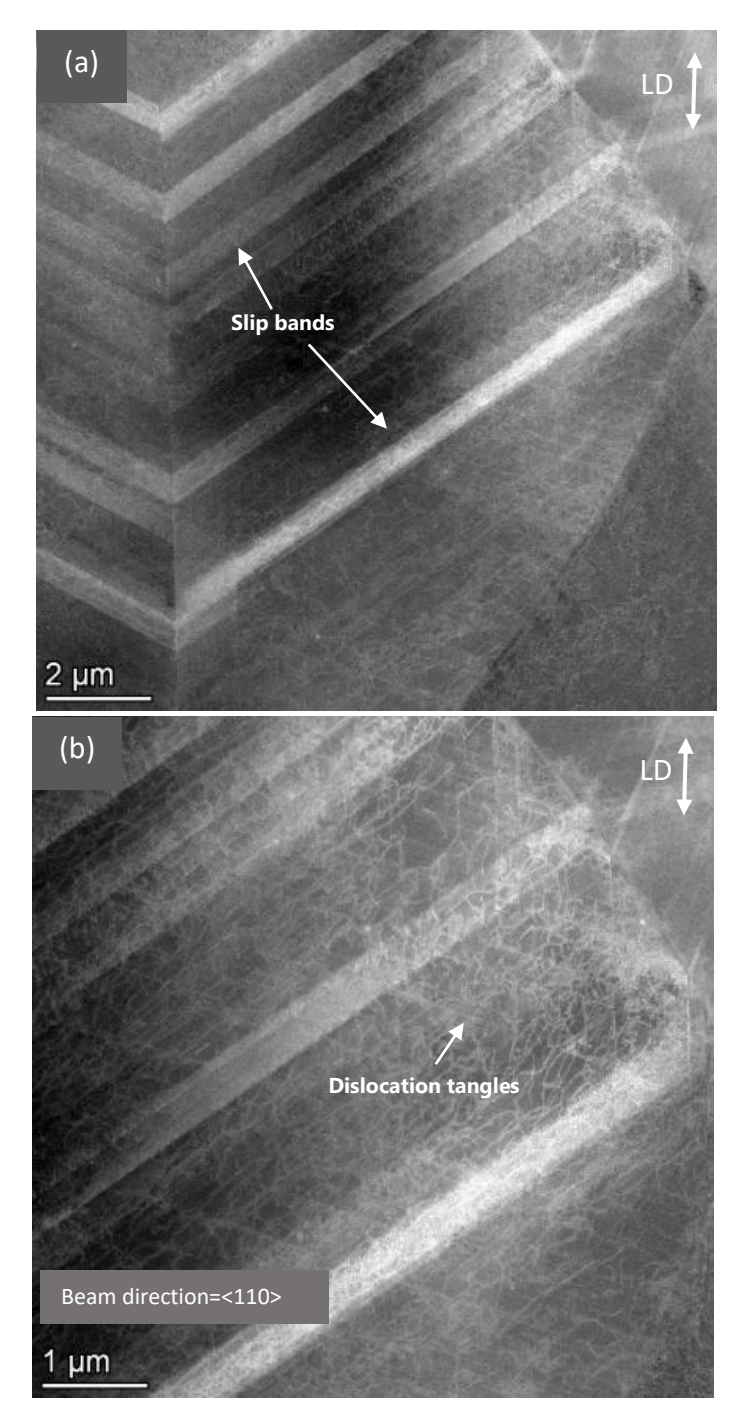


Figure 7-20. Slip bands and dislocation structure at 120,000 cycles (2.5% fatigue life) in one grain (a) Lower magnification; (b) Higher magnification

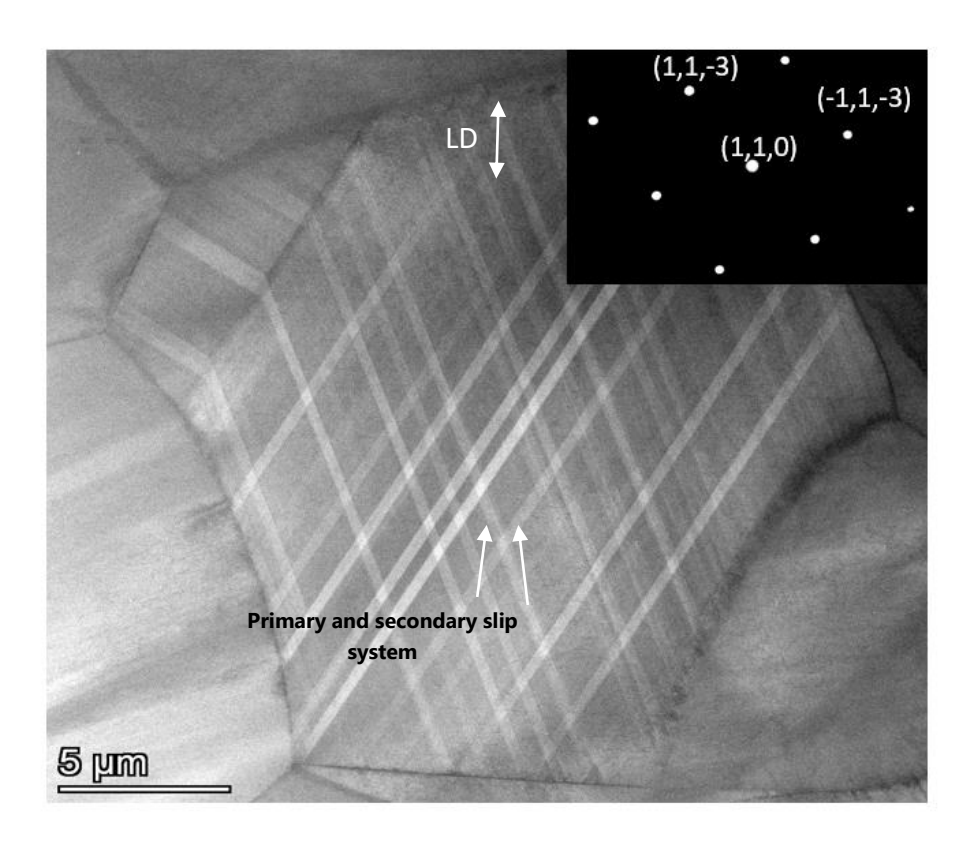


Figure 7-21. Activation of secondary slip systems at 120,000 cycles (2.5% fatigue life). The orange lines indicate crystallographic directions [1T3] and [TT3]as determined from the SAED pattern, aligned with the <110> beam direction

Figure 7-22 reveals a significant increase in dislocation density compared to 80k. Dislocations appear densely tangled and uniformly distributed across the grain. This image clearly contrasts with earlier fatigue stages where dislocations were mostly localized within slip bands. The SAED pattern remains consistent with previous imaging along the [110] direction, and indexed planes further confirm that the deformation is still occurring along expected slip systems. The absence of clear stacking faults in this image, which were common in early fatigue stages, is notable.

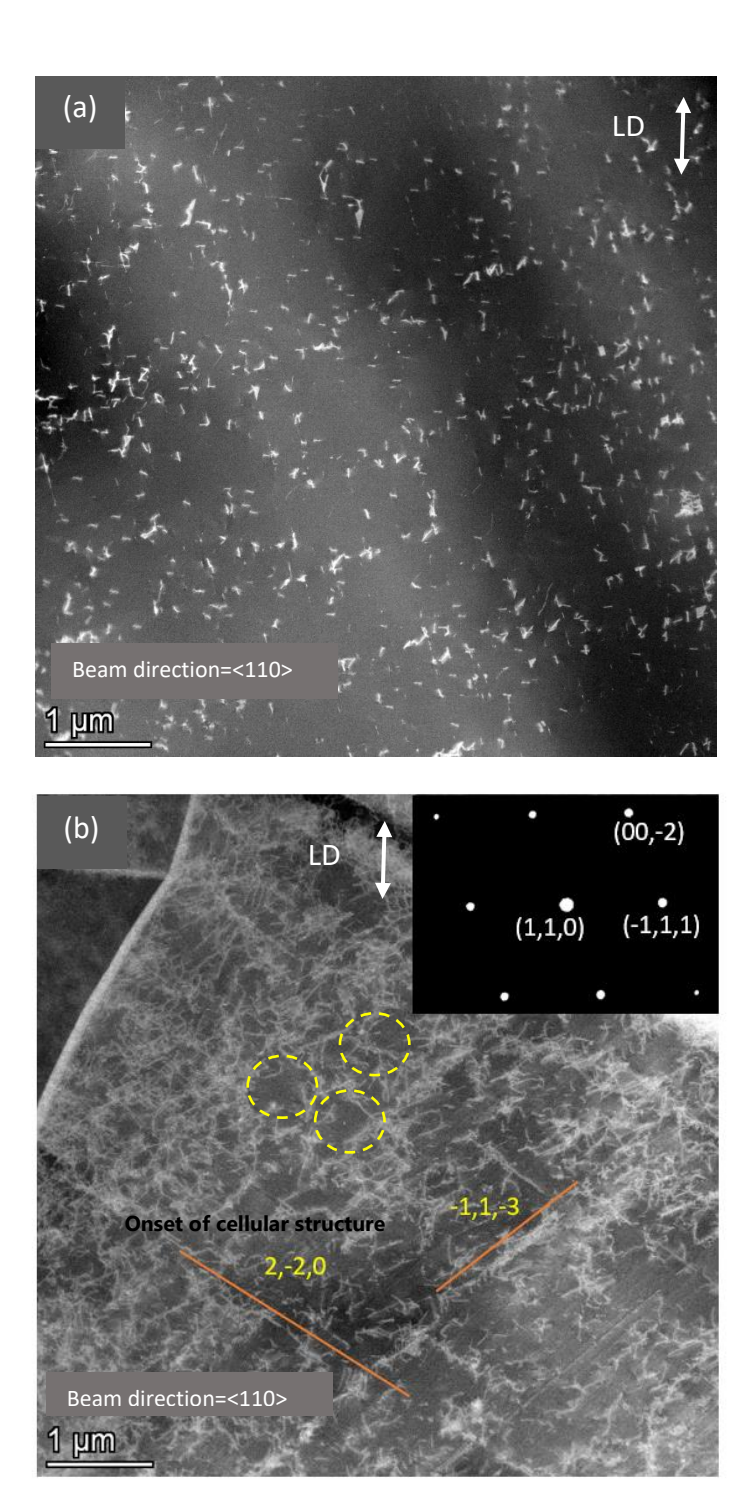


Figure 7-22. STEM-HAADF images comparing dislocation densities at two fatigue stages: (a) 80,000 cycles (~1.6% fatigue life) (b) 120,000 cycles (~2.4% fatigue life). The orange lines indicate crystallographic directions [220] and [113] as determined from the SAED pattern, aligned with the <110> beam direction

When comparing the microstructure at 120,000 cycles to that at 80,000 cycles, several important differences become apparent, reflecting the ongoing evolution of the material under cyclic loading. One of the most noticeable changes is the increase in overall dislocation density. At 80,000 cycles, dislocations were primarily concentrated within well-formed slip bands, and regions between these bands were often relatively free of dislocations. However, by 120,000 cycles, dislocations are more evenly distributed throughout the grains, and

entangled dislocation networks are commonly observed. This can be clearly seen in Figure 7-20 and Figure 7-21, where dislocation activity extends beyond slip bands and fills much of the grain interior. Another key difference is related to the slip bands themselves. At 80,000 cycles, the bands were sharp and narrow while at 120,000 cycles, slip bands become more diffuse, often containing dense clusters of dislocations. This suggests that slip bands have reached a saturation point, where they can no longer store additional dislocations efficiently. A significant microstructural shift is the disappearance of stacking faults, which were commonly observed at earlier stages. Their absence at 120,000 cycles indicates a change in slip behaviour from primarily planar to wavy slip mode. Despite the more advanced stage of deformation, secondary slip systems continue to be active in certain grains. As shown in Figure 7-21, intersecting slip bands still appear, similar to those seen at 80,000 cycles (e.g., in Figure 7-19).

Finally, at 120,000 cycles, there are early signs of cell structure formation within the grains. The tangled and dense dislocation networks seen in Figure 7-22 suggest the beginning of dislocation rearrangement into more stable substructures, such as sub-grain boundaries or dislocation cells. This marks a key transition in the material's fatigue response and points toward the onset of more permanent structural changes as the material approaches crack initiation.

7.4 Summary

This chapter presented a detailed transmission electron microscopy (TEM) analysis of the dislocation evolution in 316L stainless steel under cyclic loading in HCF regime. Using STEM-HAADF imaging, microstructural changes were characterized across different fatigue stages, from the as-received condition up to 120,000 cycles. Early stages revealed planar slip dominated by individual dislocations and stacking faults, while mid-life fatigue cycles (e.g., 80,000 cycles) were marked by well-developed slip bands, secondary slip system activity, and the formation of dislocation walls and pile-up. At 120,000 cycles, microstructure showed higher dislocation density, saturation of slip bands, and early signs of dislocation cell formation. The key contribution of this chapter lies in the TEM/STEM-HAADF investigation that captures the progressive transition of dislocation structures across different stages of fatigue. This provides direct microstructural evidence linking distinct dislocation configurations to specific stages of fatigue life — information that has rarely been documented for 316L stainless steel under identical loading conditions, particularly in the high-cycle fatigue (HCF) regime. The observations generate new knowledge on how slip localization and dislocation cell formation precede measurable nonlinear and electrical responses, offering a mechanistic foundation for interpreting NDE signals. In the following chapter, the focus will shift toward correlating these microstructural findings with nondestructive (NDT) techniques results. By linking TEM observations with electrical resistivity and nonlinear ultrasonic results, the goal is to establish reliable indicators of fatigue damage progression that can be used for early detection in engineering components.

Chapter 8. Discussion

8.1 Introduction

This chapter provides a comprehensive discussion of the findings presented in previous chapters (Chapter 6 and Chapter 7), focusing on the effectiveness of non-destructive testing (NDT) methods, namely Electrical Resistivity (ER) measurement and Nonlinear Ultrasonic Parameter (NLP), for early-stage fatigue damage detection in 316L stainless steel. The discussion is organized around four main aspects: (1) The evolution of dislocation structures during early-stage high-cycle fatigue, (2) Changes in ER and NLP in response to dislocation activity, (3) A comparison of ER and NLP performance during early-stage HCF, and (4) The correlation between ER/NLP measurements and TEM/HAADF microstructural observations.

8.2 Evolution of dislocation during early-stage high cycle fatigue

Based on the TEM and HAADF-STEM results presented in previous chapter, it is evident that both dislocation density and dislocation structures evolve progressively with the number of cycles in high-cycle fatigue (HCF) regime. Therefore, this section discusses the development of various types of dislocation structures during the early stages of fatigue, drawing on both experimental observations from this study and relevant findings from the literatures. The focus is on the transformation of dislocations from planar to more complex configurations, such as slip bands, persistent slip bands (PSBs), dislocation tangles, substructures, and secondary dislocation systems.

The initial dislocation structure in 316L stainless steel is strongly influenced by its low stacking fault energy (SFE), which promotes dislocation motion confined to specific crystallographic planes. This planar slip behaviour is further reinforced by the presence of nitrogen, which induces short-range order (SRO), such as Cr-N clusters, that act as barriers to dislocation movement [159, 160]. As a result, dislocations tend to align along the {111} slip planes in the (110) direction, producing a highly organized configuration. In the as-received condition (0 cycles), TEM and HAADF-STEM imaging reveal individual, well-defined planar dislocations distributed along grain interiors, often near twin boundaries (Figure 7-7. and Figure 7-8). These boundaries, commonly found in low-SFE FCC alloys, contribute to strain accommodation and serve as obstacles that influence dislocation arrangement. The selected area electron diffraction (SAED) patterns, particularly in grains imaged along the <110> beam direction, confirm that dislocations are aligned with the (220) planes, reinforcing the activation of the dominant {111}(110) slip system typical of FCC metals like austenitic 316L (Figure 7-8). These observations are consistent with prior studies, such as those by Pham et al.[22], and emphasize the role of crystallography and alloy chemistry, including nitrogeninduced SRO, in defining the initial microstructural state prior to cyclic loading.

At the 200-cycle stage, corresponding to approximately 0.004% of the total fatigue life, significant microstructural changes become evident in 316L stainless steel compared to the as-received condition. A clear increase in dislocation density is observed, particularly near grain boundaries, where dislocations begin to tangle and form dense networks (Figure 7-9a and Figure 7-10a). These tangled structures, characteristic of early fatigue response in low-SFE materials, emerge as individual dislocations accumulate and interact under cyclic loading. The restricted cross-slip behaviour in 316L—further intensified by nitrogen-induced shortrange order—leads to localized dislocation motion limited to specific slip planes. As dislocation density increases, the rising internal stress within the material encourages dislocations to rearrange into more organized, aligned patterns—marking the onset of slip band formation (Figure 7-13). These slip bands are planar regions of concentrated dislocation activity that evolve to relieve local internal stresses created by tangles and pile-up. Their development is especially pronounced near grain boundaries, which act as effective barriers to dislocation motion and sites of stress concentration, further promoting dislocation accumulation and pile-up formation. Such structural evolution—from planar dislocations to tangles, pile-up, and organized slip bands—clearly demonstrates the early-stage hardening response of 316L under cyclic loading. These findings align well with previous studies, including those by Pham et al.[23], [25], and other works characterizing the early cyclic behaviour of low-SFE stainless steels further validating the mechanisms observed in this study.

Microstructure at this stage also reveals stacking faults—linear interruptions in the atomic stacking sequence—formed because of partial dislocation activity, visible in some grains such as the one in Figure 7-9. These faults are indicative of the planar slip behaviour dominant in low-SFE FCC alloys and contribute to strain localization. In certain grains, dislocations intersect along two directions, reflecting the activation of multiple slip systems and indicating the material's adaptation to cyclic strain through more complex deformation modes. TEM observations also show that primary and secondary slip systems are active, especially near grain boundaries, and their interaction divides grains into sub-domains with distinct dislocation densities. These patterns suggest the initial activation of secondary slip in highly stressed regions [25, 161].

The formation of tangled dislocation structures plays a dual role: while they initially obstruct further dislocation motion, they also promote the activation of secondary slip systems, contributing to the evolution of the microstructure. Near grain boundaries, where dislocation pile-up are more prominent, internal stresses are sufficient to trigger these secondary deformation mechanisms, leading to more complex sub-domains and the early signs of microstructural instability. The overall arrangement is not limited to specific grain orientations. TEM images captured under various beam directions, including <111> and <112> (Figure 7-11a and Figure 7-11b), show consistent dislocation behaviour across differently oriented grains, highlighting the universal nature of fatigue-induced dislocation evolution in 316L stainless steel. Further evidence of this consistency is seen in Figure 7-12,

where a twin boundary acts simultaneously as a barrier and a site of dislocation accumulation, reinforcing its role in strain accommodation and microstructural evolution.

At 1500 cycles, which corresponds to approximately 0.03% of the total fatigue life, the microstructure of 316L stainless steel reveals a notable transition from the disordered tangle-dominated state observed at 200 cycles to more organized and stable dislocation configurations. As shown in Figure 7-14, dislocations begin to align into more orderly structures, including partial dislocation walls and well-oriented slip bands. The increased alignments and interaction between dislocations lead to a higher rate of dislocation annihilation, thereby slightly reducing the overall dislocation density. This evolution results in a more heterogeneous dislocation distribution, with some regions showing high dislocation concentration—typically along active slip bands—while others, particularly grain interiors, appear largely dislocation-free.

The emergence of these dislocation-free zones can be attributed to two mechanisms happening at the same time. First, the redistribution of strain into localized slip bands naturally leads to regions of concentrated dislocation activity and, by contrast, areas of lower dislocations. Second, the annihilation of dislocations with opposite Burgers vectors becomes more prominent as cyclic loading progresses, especially in grains where dislocation saturation has already occurred. Together, these mechanisms promote a microstructure characterized by alternating bands of high and low dislocation density, effectively relieving internal stress and contributing to structural stabilization. This is reflected in the clearer grain boundary definition observed at this stage, compared to the more chaotic arrangement at 200 cycles.

Figure 7-14 supports these observations by showing distinct dislocation pile-ups aligned along the $[-1\ 1\ 1]$ direction, confirming active slip on the (111) plane of the dominant $\{111\}\langle110\rangle$ slip system in the FCC structure. Stacking faults are also visible, indicating limited cross-slip behaviour typical of low—stacking-fault-energy (SFE) alloys such as 316L stainless steel. These faults reflect persistent planar slip and contribute to cyclic strain localization, thereby enhancing the material's hardening response.

Of particular interest at this stage is the appearance of wall—channel-type dislocation patterns in some grains, as seen in Figure 7-16. Similar configurations have been reported in the literature. For example, Mughrabi and Essmann [27], describe the formation of wall—channel microstructures during cyclic hardening in low-SFE FCC metals, where high-density walls confine regions of lower dislocation activity—a pattern consistent with this study observations at this stage.

The transition to these organized patterns signals a shift from early-stage, chaotic dislocation interactions to more stable deformation modes. The presence of well-aligned slip bands across most grains, alongside large dislocation-free areas in others, suggests that the material is approaching a stabilized cyclic state. This behaviour is often associated with the onset of persistent slip band structures and sub-grain boundary development under continued fatigue loading.

At 80,000 cycles (~2% fatigue life), the dislocation structure in 316L stainless steel shows a distinct transition toward a more localized and organized deformation mode. Compared to 1,500 cycles, the microstructure is now dominated by thicker, more numerous slip bands (Figure 7-17b and Figure 7-18), with most dislocation activity concentrated within them. These bands appear dense and well-aligned, while areas between them are nearly dislocation-free—an effect attributed to dislocation annihilation and the redistribution of strain into preferred slip paths.

The existence of intersecting slip bands (Figure 7-18a and Figure 7-19) indicates the activation of both primary and secondary slip systems. This suggests that the material accommodates cyclic strain through more complex mechanisms, including multiple slip system, which becomes more active at this stage. The interaction of dislocations along intersecting slip bands (Figure 7-18b) produces regions of intense tangling and localized strain accumulation, indicating slip band interaction and cross-slip activity. This suggests that multiple slip systems are active, contributing to local stress concentration and dislocation multiplication at this fatigue stage. These observations align with studies shows dislocation structures evolve from planar slip to well-defined slip bands and substructures due to activation of multiple slip systems and the need to reduce internal energy. The transition to more stable and confined deformation patterns reflects the material's adaptation to prolonged cyclic loading [22, 27].

At 120,000 cycles, corresponding to the later stage of high-cycle fatigue, the dislocation structure in 316L stainless steel undergoes a significant transformation. As seen in Figure 7-20, the overall dislocation density increases noticeably compared to earlier stages. Dislocations are no longer limited to slip bands—they are now spread throughout the grain, including between the slip bands. This marks a shift away from localized deformation toward a more widespread, complex internal structure. The appearance of thick dislocation tangles and the re-emergence of dislocations between previously clear slip bands indicate that the bands have reached their saturation limit and can no longer accommodate additional dislocations efficiently. As a result, excess dislocations accumulate in surrounding areas, leading to a more disordered arrangement (Figure 7-21).

A key microstructural change at this stage is the disappearance of stacking faults, which were frequently observed during earlier cycles. Their absence suggests a transition from planar to wavy slip—a hallmark of increased slip activity and a more three-dimensional pattern of dislocation movement. This behaviour is typical of FCC alloys under prolonged cyclic loading and aligns with findings from Mughrabi [27], who reported similar transitions in low-SFE metals under fatigue. The continued activation of secondary slip systems is evident from the intersecting slip bands in Figure 7-21, further confirming that multiple slip planes remain active even at advanced fatigue stages [27].

In summary, at 120,000 cycles, the material shows a clear progression from localized, band-dominated deformation to a more diffuse, tangled dislocation network. The shift from planar to wavy slip, loss of stacking faults, and signs of cell formation all point to an advanced fatigue

stage driven by cross-slip, dislocation saturation, and strain redistribution. These observations align with Zhang et al. [28], who reported dislocation wall and cell formation under cyclic loading in additively manufactured 316L shows similar tendencies, where retained cellular microstructures significantly influence fatigue resistance and dislocation evolution [162]. Figure 8-1 illustrates this progression, summarizing the key stages in dislocation and slip band evolution during early fatigue damage.

Evolution of dislocation structure and slip bands during early fatigue cycles.

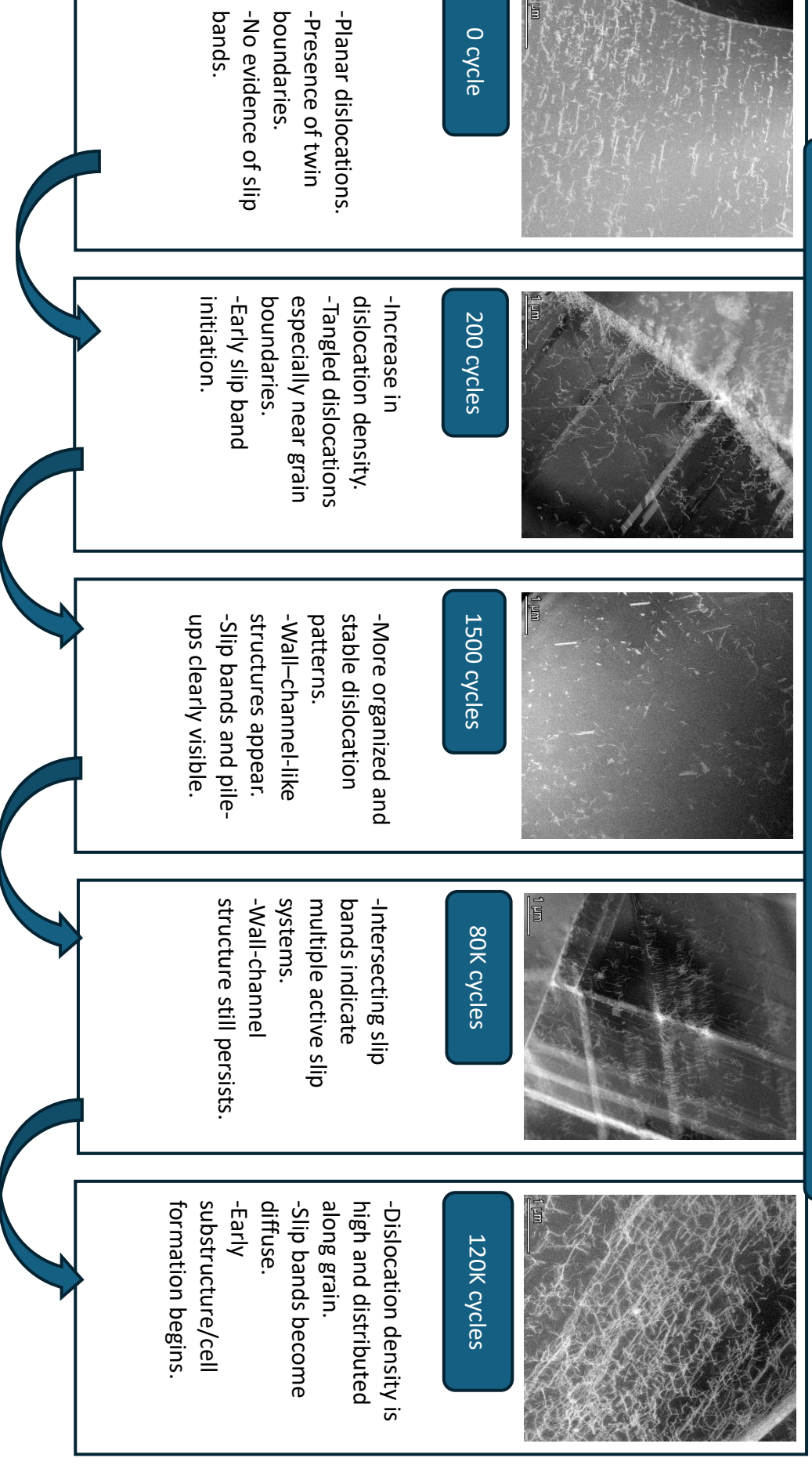


Figure 8-1. Flowchart illustrating the microstructural evolution of dislocations and slip bands in 316L stainless steel during early high-cycle fatigue

8.3 Changes in ER and NLP in response to dislocation

As discussed in literature review section (4.1) the nonlinear parameter β is influenced by the crystalline structure of the material as well as the localized strain present within it. This strain originates from microstructural features such as dislocations and precipitates, which both contribute to the nonlinear parameter β , but dislocations often have a much larger impact than precipitates This is because dislocations introduce highly localized, mobile stress—strain fields — especially when they bow, unpin, or form dipoles — which strongly distort ultrasonic wave propagation, producing more substantial harmonic distortion than the more static and spatially limited strain fields associated with precipitates[163]. This section provides a detailed review of various microstructural factors that affect the magnitude of the acoustic nonlinearity parameter. Theoretical and experimental analyses of different mechanisms, including dislocation pinning, dislocation dipoles, precipitate-pinned dislocations and cracks are discussed in detail. This section provides a theoretical framework explaining how different dislocation-based features contribute to nonlinear wave behaviour, with an emphasis on quantifying their effects through mathematical formulation.

8.3.1 Effect of dislocation pinning on nonlinear acoustic response

Dislocation pinning plays a significant role in influencing the nonlinear acoustic response of materials subjected to ultrasonic waves. When dislocations are restricted from free movement due to interactions with obstacles such as grain boundaries, precipitates, or other dislocations, they create localized stress—strain fields that contribute to material nonlinearity. This behaviour primarily leads to an increase in the amplitude of the second harmonic component of the ultrasonic signal, which is quantified by the nonlinear parameter β . As a result, dislocation pinning is a key mechanism underlying the sensitivity of nonlinear ultrasonic techniques to early-stage fatigue damage.

The dislocation monopole model, originally developed by Hikata and Elbaum [93], and later refined by Cantrell[164], describes dislocation pinning based on the dislocation string vibration theory, where dislocations are represented as bowed segments pinned between two fixed points a distance apart Figure 8-2a. When a small external stress is applied, it induces a shear component that acts on the dislocation segment, causing it to bow between the pinning points (Figure 8-2b). The curvature of the bowed dislocation depends on the applied stress and governs the material's nonlinear response. When an ultrasonic wave is introduced, it sets the pinned dislocation into vibrational motion, which modifies the stress-strain behaviour and enhances the nonlinear parameter [165, 166].

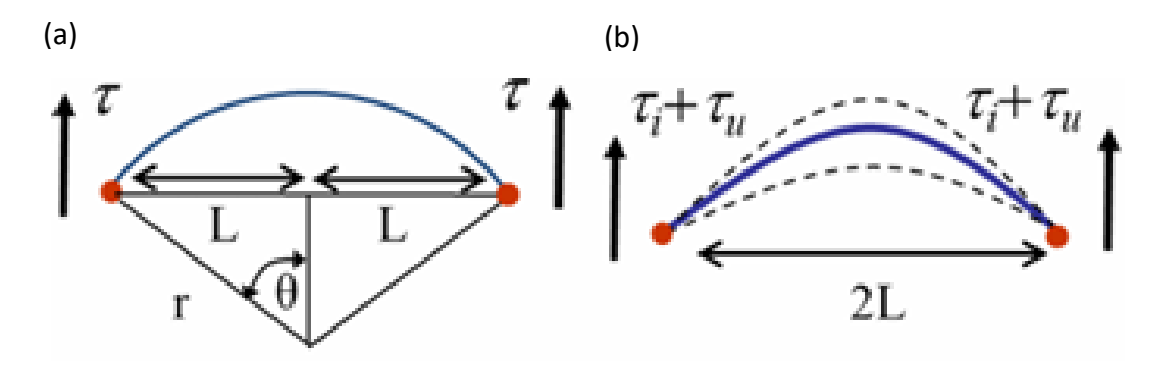


Figure 8-2 (a) Diagram showing geometry of bowed dislocation segment of length 2L between two pinning points and under an applied shear stress τ i, in terms of radius of curvature r and angle θ . B) Diagram showing movement of dislocation segment with superimposed ultrasonic stress on top of initial stress τ [167]

The total strain in a material consists of contributions from both the lattice strain and the strain induced by dislocation motion. The latter, particularly in the case of dislocation pinning, is characterized by higher-order stress terms that directly influence the nonlinear ultrasonic parameter β . The relationship between the change in the nonlinear parameter due to dislocation pinning and various material properties is given by Equation 8-1 [167].

$$\Delta\beta_{pd} = \frac{24}{5} \frac{\Omega \Lambda L^4 R^3 C_{11}^2}{\mu^3 b_2} \sigma_1 \label{eq:delta-beta}$$
 8-1

Here, $\Delta\beta_{pd}$ represents the change in the nonlinear parameter due to dislocation pinning, Λ is the dislocation density, L is the dislocation loop length, R is the radius of curvature, and σ_1 is the applied shear stress acting on the pinned dislocation segment. Ω , C_{11} , μ , and b are material constants related to volume, stiffness, shear modulus, and Burgers vector, respectively. An increase in dislocation density leads to a corresponding increase in nonlinearity, as more dislocations interact with the propagating wave and contribute to harmonic generation. The loop length L is also critical: longer pinned dislocation segments generate greater strain gradients and amplify nonlinear effects. Additionally, the curvature and bowing of dislocations are influenced by the applied stress, which modulates the strength of higher harmonic generation during ultrasonic testing. As fatigue progresses, the number of pinned dislocations increases, resulting in a gradual rise in the nonlinear parameter. This makes second harmonic generation especially sensitive to early-stage fatigue damage, as changes in β often occur before the appearance of macroscopic cracks. Therefore, dislocation pinning is a key mechanism that underlies the sensitivity of nonlinear ultrasonic techniques for early damage detection and structural health monitoring.

However, it is important to recognize a key limitation of Equation 8-1. While it establishes a theoretical relationship between β and dislocation-related parameters, it does not explicitly include the amplitude of the incident acoustic wave. In nonlinear ultrasonic testing, β results from the interaction between ultrasonic waves and dislocation structures, meaning the acoustic wave's stress field should be explicitly represented. If σ_1 in this equation is interpreted purely as mechanical stress (e.g., from cyclic loading), it overlooks the dynamic

stress field generated by the acoustic wave, which is responsible for exciting dislocation motion during testing.

To address this gap, more advanced models—such as those developed by Cantrell [164]0, and refined by Chen and Qu [168]—integrate the acoustic wave field directly into the dislocation motion framework. These models account for the orientation dependence of line energy and dislocation configuration and more accurately describe the amplitude-dependent nonlinear response in anisotropic materials. As such, while Equation 8-1 provides a valuable approximation of how pinned dislocations contribute to nonlinearity, it should be viewed as a structurally focused model, not a complete dynamic representation of ultrasonic wave—dislocation interaction.

Later work by Cantrell et al. [169], extended the Hikata et al. [93], model by incorporating orientation-dependent line energy, which was further validated through dislocation dynamics simulations. Their findings demonstrated that the Hikata model accurately predicts β for materials with low Poisson's ratios and applies to both screw and edge dislocations. However, at Poisson's ratios above 0.2—which includes most metals—their simulations, based on monotonic mechanical loading (e.g., tensile stress), indicated that the relationship between β and applied stress is not strictly linear. It should be noted that this finding does not directly reflect cyclic loading conditions typical of fatigue but rather highlights the complexity of dislocation-induced nonlinearity even under static loading scenarios. Notably, their simulations showed that under certain conditions, edge dislocations can produce negative values of β , a phenomenon difficult to capture experimentally due to phase-related measurement limitations. This finding underscores the need for more advanced experimental techniques to measure β over a wider stress range and better resolve the complexity of dislocation-induced nonlinearity.

Chen and Qu [168], further developed this modelling approach by incorporating both pure and mixed dislocation types in anisotropic crystals. Their framework, validated through molecular dynamics simulations, showed that dislocation orientation has a significant effect on acoustic nonlinearity—especially in materials with directionally dependent elastic properties. While their model effectively describes the behaviour of screw dislocations, it does not fully account for the nonlinear response of edge dislocations, indicating the need for additional experimental validation. Overall, these extended models enhance our understanding of dislocation-induced nonlinearity and emphasize the importance of refining both theoretical and experimental methods to accurately characterize β across a range of material systems.

8.3.2 Effect of dislocation dipoles on nonlinear acoustic response

Dislocation dipoles are formed when two dislocations with opposite burgers vectors move within a small distance of each other and become mutually trapped. This interaction creates a localized stress field that modifies the force-displacement relationship of the dipole, making it inherently nonlinear. When an ultrasonic wave excites the dipole, it generates a measurable

nonlinear response, contributing to the second harmonic generation and, consequently, changing the nonlinear parameter β . The nonlinearity arising from dislocation dipoles has been theoretically derived and is expressed as equation 8-2 [170]:

$$\Delta \beta_{pd} = \; \frac{16 \pi^2 \Omega R^2 \Lambda_{dp} h^3 (1-v)^2 C_{11}^2}{u^2 b} \label{eq:delta-beta} \qquad \qquad \text{8-2}$$

where Λ represents the density of dislocation dipoles, h is the dipole height, v is Poisson's ratio, and C_{11} , μ and b are material-dependent elastic constants.

In fatigue-damaged materials, cyclic loading promotes the formation of complex dislocation substructures, with dislocation dipoles playing a crucial role in the evolution of nonlinearity [106, 171]. Dipoles commonly form when segments of two dislocation loops, expanding on parallel slip planes in proximity, pass over one another. These segments can reorient into a stable configuration, two parallel dislocation lines with opposite Burgers vectors (i.e., antiparallel segments with the same Burgers vector), forming what is known as a dislocation dipole. This process is particularly happening in the early stages of plastic deformation when numerous dislocation loops are generated. Dipoles are more likely to form from edge dislocations, as screw segments can easily annihilate through cross-slip—especially in metals with high stacking fault energy—reducing their contribution to dipole formation [172].

In metals showing wavy-slip behaviour, such as polycrystalline nickel, aluminium alloys, and copper single crystals, these dislocation substructures emerge as vein structures, regions of high dislocation density that eventually saturate with dislocation dipoles. The surrounding regions, known as channels, exhibit significantly lower dislocation density. As cyclic deformation progresses, the redistribution and accumulation of dislocations drive the transition to persistent slip band (PSB) structures. These structures develop through a self-organizing mechanism in which cyclic strain localization causes the alternating arrangement of veins and channels into a ladder-like morphology.

In contrast, planar slip metals deform predominantly along specific crystallographic planes, forming planar slip bands. These may intermittently evolve into persistent Lüders bands (PLBs) due to fluctuations in local stress and strain. PLBs form when local stress exceeds a critical threshold, triggering localized plastic flow in a band that propagates until the stress relaxes. This transition from planar slip to PLBs involves the intermittent activation of slip bands governed by the interplay between dislocation mobility, strain hardening, and dynamic recovery processes. This transition from initial slip bands to persistent slip bands (PSBs) occurs progressively under cyclic loading. At the onset of deformation, slip bands appear randomly and transiently across grains, driven by dislocation glide along preferred crystallographic planes. With continued cyclic strain, certain bands become repeatedly activated due to favourable orientation and stress concentration. These bands begin to accumulate and rearrange dislocations more efficiently than others, forming stable vein-channel structures. Over time, the repeated plastic strain in these favoured regions lead to a steady-state

configuration of high dislocation density in the "veins" (walls), separated by low-density "channels," giving rise to the characteristic ladder-like PSB structure [173].

The contribution of dislocation dipoles to nonlinearity is particularly significant in materials subjected to high cyclic loading. The force interactions between dipoles lead to nonlinear strain accumulation, which modifies the acoustic wave propagation in the material. Cantrell [169, 174], developed a formulation describing the total nonlinearity parameter β for wavy-slip metals, accounting for the contributions from dislocation monopoles, dipoles, and different substructures [175]:

$$\beta = \frac{B^e + f^{m_p}\Gamma^{m_p} + f^dp\Gamma^dp}{(1 + f^{m_p}\Gamma^{m_p} + f^dp\Gamma^dp)^2}$$
 8-3

where f^{m_P} and f^dp are the total volume fractions of dislocation monopoles and dipoles, respectively, and Γ represents parameters that depend on specific β and dipole strain fields in the veins, channels, and PSBs. Also B^e is the material elastic nonlinearity. These gamma factors are material and dislocation-dependent, further reinforcing the role of microstructural characteristics in determining the nonlinear response [176].

From a physical perspective, dislocation dipoles contribute to nonlinearity by creating localized residual stress fields, which disrupt the uniform propagation of ultrasonic waves. As dipoles interact with the applied acoustic stress, they introduce higher harmonic components into the transmitted wave, which can be detected and quantified to assess material fatigue. Their increasing density with fatigue cycles makes them a key contributor to the early-stage evolution of material degradation, reinforcing the value of nonlinear ultrasonic techniques for early fatigue damage detection.

Since in this study, the primary focus is on understanding the sensitivity of the nonlinear parameter (β) to dislocation structures, as dislocations play a crucial role in the early stages of fatigue damage. The interaction of dislocations, including dislocation pinning, dipoles and their evolution under cyclic loading, directly influences the nonlinear acoustic response, making them a key factor in nonlinear ultrasonic evaluation. While other microstructural features such as precipitates and microcracks also contribute to nonlinearity, their effects are beyond the scope of this research. Precipitates influence β through dislocation-precipitate interactions, modifying the stress field and altering wave propagation. Microcracks, on the other hand, contribute to contact acoustic nonlinearity (CAN), which dominates in later fatigue stages when cracks open and close under applied stress. For a detailed discussion on how precipitates and microcracks affect nonlinear ultrasonic, following references can be useful[177].

8.3.3 Effect of dislocation features on electrical resistivity

Electrical resistivity in metals increases as dislocations are introduced and evolve during plastic deformation[176]. Dislocations serve as electron scattering centres, disrupting the movement of electrons and decreasing their mean free path. The degree of this scattering

and the resulting increase in resistivity depends not only on the dislocation density but also on the type and distribution of those dislocations. The classical framework for this phenomenon is provided by Matthiessen's Rule, which assumes that each scattering mechanism (phonons, impurities, dislocations) contributes linearly and independently to the total resistivity (8-4)[178].

$$p_{total} = p_{thermal} + \rho_{impurities} + p_{dislocations} + \cdots$$
 8-4

In this equation ρ_{th} is the resistivity due to temperature, ρ_{imp} is the resistivity due to impurities and ρ_{def} is the the resistivity due to defects. In terms of dislocation-specific contributions, early theoretical and experimental work (e.g., Basinski et al. [176]) confirmed a linear relationship between dislocation density N and the corresponding resistivity increase:

$$\Delta p_{\rm D} \propto N$$
 8-5

where $\Delta \rho_D$ is the dislocation-induced resistivity and N is the dislocation density. Despite its simplicity, Matthiessen's Rule remains widely used and provides a consistent first approximation in metals undergoing plastic deformation. However, more advanced models, such as those proposed by Watts [179], and Gaal et al.[180], show that this relationship becomes more complex when dislocations form structures such as walls, tangles or slip bands. These microstructural arrangements lead to anisotropic regions of high internal strain and localized atomic distortion, which could enhance electron scattering. Consequently, even materials with the same average dislocation density can show different resistivity responses depending on how those dislocations are distributed and oriented. To date, no studies have quantified an additional resistivity change (in %) due solely to structure or orientation at constant density. This highlights the importance of considering not just dislocation quantity but also their morphology and evolution in any resistivity-based damage assessment. Recent experimental studies have expanded this understanding by exploring the quantitative impact of dislocation evolution on electrical resistivity during cyclic and creep deformation. For instance, in a study on fatigue-loaded ICE R7 railway wheels, Starke et al. [181], demonstrated a clear correlation between the increase in electrical resistance and the accumulation of dislocation density over fatigue life. Their findings showed that as dislocations multiplied and began forming more complex substructures, such as tangles and cell walls, the electrical resistance increased at an accelerating rate and factor of approximately 16. These dislocation configurations create more pronounced barriers to electron flow compared to uniformly distributed or isolated dislocations. This work confirms the view that not only the amount but also the morphology of dislocations significantly influences the resistivity response, especially in materials subjected to cyclic mechanical loading. Similarly, Malki et al. [182], in an in-situ creep study of n-type PbTe, highlighted the differing roles of mobile and immobile dislocations in influencing electrical resistivity. Their findings revealed that it is primarily the immobile dislocations, particularly those that accumulate at sub grain boundaries, that have a lasting and measurable impact on resistivity. These immobile dislocations become fixed within the microstructure and serve as persistent scattering centres for electrons, thereby contributing to a steady increase in resistivity over time. In contrast, mobile dislocations, which are actively involved in deformation and glide through the crystal structure, have a transient influence. Although they momentarily disrupt the lattice, their short-lived presence means they do not significantly affect the long-term electron scatter behaviour of the material. As deformation continues, many of these mobile dislocations either annihilate, pinned or are absorbed into sub grain boundaries, gradually becoming immobile and thereby enhancing their contribution to resistivity. This distinction is especially important in processes such as creep or cyclic fatigue, where microstructural rearrangement over time leads to the progressive accumulation of immobile dislocations, which dominate the observed resistivity increase. Also, regarding the rate of increase in electrical resistivity, their result suggests that a ~40% increase in electrical resistivity can be caused by dislocation accumulation alone over 20% compressive strain under creep conditions [182].

8.4 Comparison of ER and NLP method

8.4.1 Comparison of ER and NLP results during the early-stage HCF

To evaluate and compare the sensitivity of nonlinear parameter (NLP) and electrical resistivity (ER) techniques for early fatigue damage detection, measurements were performed concurrently on the same sample (sample B) following the identification of two prominent peaks during fatigue monitoring. The results were presented in Figure 6-22 and Figure 6-21 for NLP and Figure 6-16 for ER measurement. In both NLP and ER measurements, two distinct peaks are observed within the early stage of fatigue life, specifically before 10% of total fatigue life. These peaks suggest that both methods can detect early-stage damage and possibly correlate with microstructural changes occurring during initial fatigue cycling. To facilitate a more direct comparison of the magnitude and behaviour of these changes, both parameters are plotted together in Figure 8-3. This visualization reveals a notable difference in sensitivity between the two techniques. The normalized NLP shows more pronounced changes, with sharper and higher peaks compared to the ER. This suggests that the nonlinear parameter is more responsive to early fatigue damage, potentially offering higher resolution in identifying microstructural changes such as dislocation movement or early crack nucleation. Conversely, while ER also captures early damage, the changes are more gradual, and the peaks are less sharp compared to NLP. The sharper and more pronounced peaks observed in the NLP measurements, compared to the relatively gradual changes in ER, can be attributed to the underlying mechanisms each technique is sensitive to as explained in section 8.3.1, 8.3.2, and 8.3.3. Electrical resistivity is governed primarily by electron scattering, which increases with dislocation density, as described by Matthiessen's rule and supported by early work such as Basinski et al. [176]. While resistivity is indeed influenced by dislocation structures (e.g., walls, tangles, and sub grain boundaries), its response is generally smoother and less sensitive to localized dislocation arrangements unless the density is sufficiently high or the structures become persistent, as seen in the studies by Malki et al.[182]. In contrast, the nonlinear ultrasonic parameter β is not only sensitive to dislocation density but also highly responsive to dislocation configuration, pinning, and interaction mechanisms. As detailed in

the dislocation monopole and dipole models developed by Hikata and refined by Cantrell [93, 164, 169, 175], β increases significantly when dislocations become pinned or form dipole structures under cyclic stress. These localized and highly nonlinear features—such as pinned dislocation segments and dipole interactions—generate strong second harmonic components in ultrasonic wave propagation, leading to a sharper and more immediate increase in β even at early stages of fatigue. Because of this multi-mechanism sensitivity, NLP detects not only dislocation accumulation but also dynamic rearrangements, local pinning, and substructure evolution such as the formation of persistent slip bands (PSBs). These features often precede significant dislocation density changes and are thus picked up earlier and more strongly in the NLP signal. This explains why, in Figure 8-3, the NLP response shows sharper, higher peaks compared to the relatively lower ER variations. However, despite this difference in sensitivity, the literature to date does not provide a direct quantitative comparison of the relative percent change in ER versus β for equivalent microstructural states—highlighting the importance of this study.

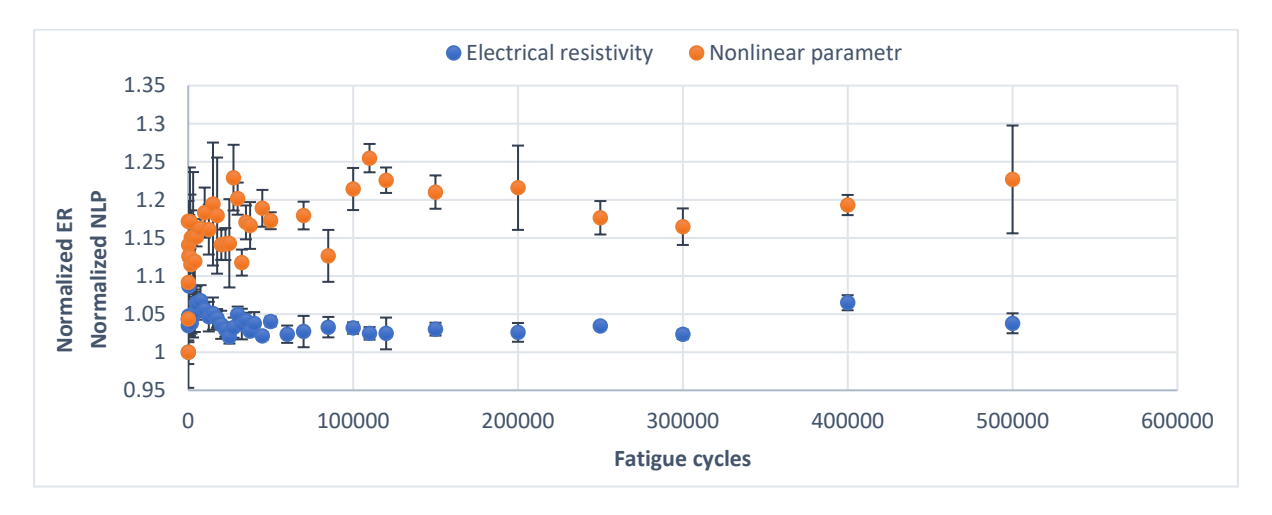


Figure 8-3. Comparison of normalized nonlinear parameter (NLP) and Normalized electrical resistivity (ER) measurements for the same sample (sample B) during early fatigue life cycles.

Figure 8-4 and Figure 8-5 focus on the localized behaviour of the first and second peaks observed in the normalized nonlinear parameter (NLP) and electrical resistivity (ER) measurements during the early fatigue life of Sample B, respectively. Both NLP and ER show a similar trend around each peak which starts with an initial increase followed by a decrease. This trend is consistent across both the first and second peaks. However, the location of the peaks slightly different for second peak in NLP and ER. The first peak occurs at a very early stage of fatigue life for both methods —below 0.015%—while the second peak appears earlier for ER at 1.3 to 2.3%, and for NLP around 2.4–2.5% of fatigue. This shift may indicate distinct stages of dislocation evolution or different mechanisms dominating damage progression at different fatigue phases. A potential hypothesis for the earlier and less pronounced appearance of the second peak in the electrical resistivity (ER) signal—observed between approximately 1.3% and 2.3% of fatigue life (around 82k to 85k cycles)—relates to the differing sensitivities of ER and NLP to dislocation behaviour. It is well-established that ER is primarily sensitive to dislocation density, particularly to immobile (persistent) dislocations

that act as long-term electron scattering centres. In contrast, mobile dislocations, which are actively gliding or rearranging, have a much weaker or negligible effect on ER.

During the fatigue stage associated with the second ER peak, there is likely a slight increase in dislocation density, possibly due to the activation of Frank-Read sources and limited cross-slip. Additionally, some wider slip bands begin to evolve, which contribute modestly to overall resistivity. This limited increase in dislocation density, combined with the presence of only partially stabilized or non-persistent dislocation structures, can explain why the ER peak forms earlier than the corresponding NLP peak, yet appears much less sharp or intense.

In contrast, the NLP (nonlinear ultrasonic parameter) is highly sensitive not only to dislocation density but also to the configuration, interaction, and mobility restriction of dislocations. The mechanisms of dislocation pinning, dipole formation, and the development of substructures such as veins or onset of cell formation significantly enhance acoustic nonlinearity and thus lead to a delayed but sharper peak in NLP. At the fatigue stage corresponding to the second NLP peak (around 2.4% to 2.5%), the microstructure likely shows a higher degree of dislocation organization and pinning, which enhances the second harmonic generation in the ultrasonic response.

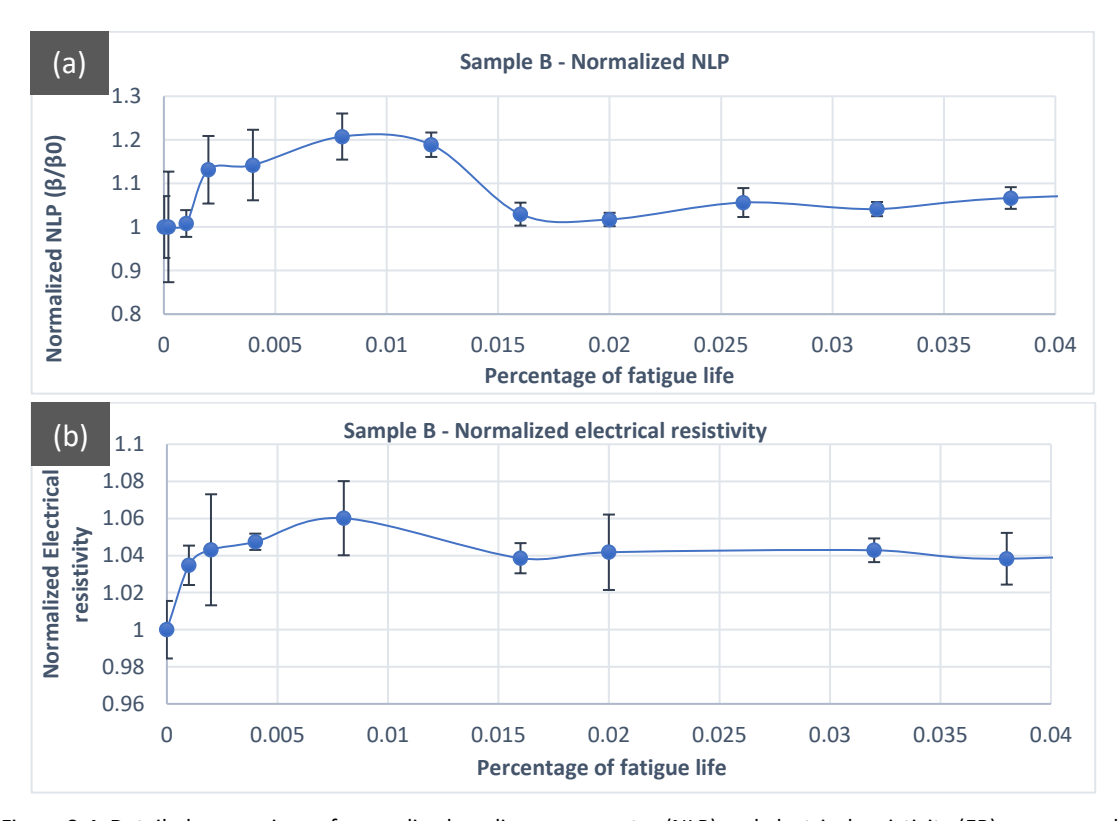


Figure 8-4. Detailed comparison of normalized nonlinear parameter (NLP) and electrical resistivity (ER) responses during the first peak of Sample B

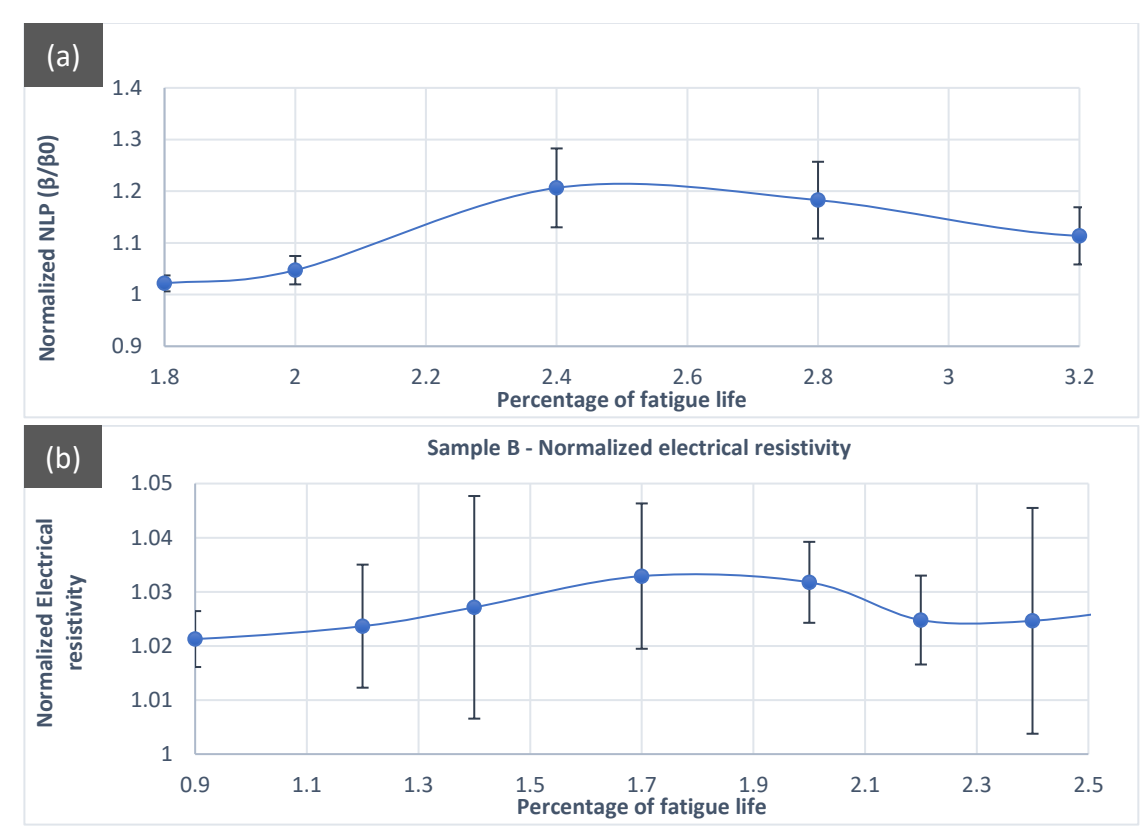


Figure 8-5. Detailed comparison of normalized nonlinear parameter (NLP) and electrical resistivity (ER) responses during the second peak of Sample B

8.4.2 Comparison of NLP results during the early-stage HCF for both sample A and B

Figure 6-21andFigure 6-22 illustrates normalized nonlinear ultrasonic parameter (NLP), β/β_0 , plotted against fatigue cycles for Sample A and Sample B. In both samples, two distinct regions are highlighted in green, representing early fatigue stages detected by this method. These regions show a sharp increase followed by a decrease in the NLP values at approximately the same fatigue cycle range in both datasets. This similarity in the trend particularly the rise and fall of NLP within the same fatigue interval strongly supports the repeatability and consistency of the nonlinear ultrasonic measurements across different specimens. It suggests that the nonlinear response of the material to early fatigue damage is repeatable under similar test conditions. Figure 8-6 presents the evolution of the normalized nonlinear ultrasonic parameter (NLP, β/β_0) as a function of fatigue cycles for Sample A and Sample B in first and second peak. The figure demonstrates the sensitivity and repeatability of NLP measurements in capturing early fatigue damage in 316L stainless steel. In the early fatigue regime (Figure 8-6 a), both samples show comparable trends, with NLP rising to values above 1.2, suggesting a consistent nonlinear acoustic response to incipient damage. Sample B shows a slightly higher and more stable peak, whereas Sample A shows a similar but slightly noisier pattern. This consistency between samples supports the repeatability of the nonlinear ultrasonic technique for early-stage fatigue monitoring. Beyond the early stage (100K to 300K cycles) shows in Figure 8-6b, Sample B maintains relatively steady NLP values with slight gradual decline, while Sample A demonstrates a more pronounced downward trend. By 400,000 cycles, Sample A's normalized NLP falls to around 1.05, whereas Sample B sustains higher normalized NLP levels close to 1.18. Since the initial normalized NLP values (as received) for both samples were the same, this divergence indicates that the difference arises from a relative change in the nonlinear parameter during cycling. Observed increase in normalized NLP for Sample B likely reflects a higher NLP parameter compared to Sample A at this stage. This could be attributed to microstructural factors such as differing fatigue damage accumulation or local inhomogeneities between the two samples, which affect how nonlinearity evolves during loading. Nevertheless, the consistent trends between the datasets support the utility of the NLP as a robust, non-destructive indicator of fatigue progression.





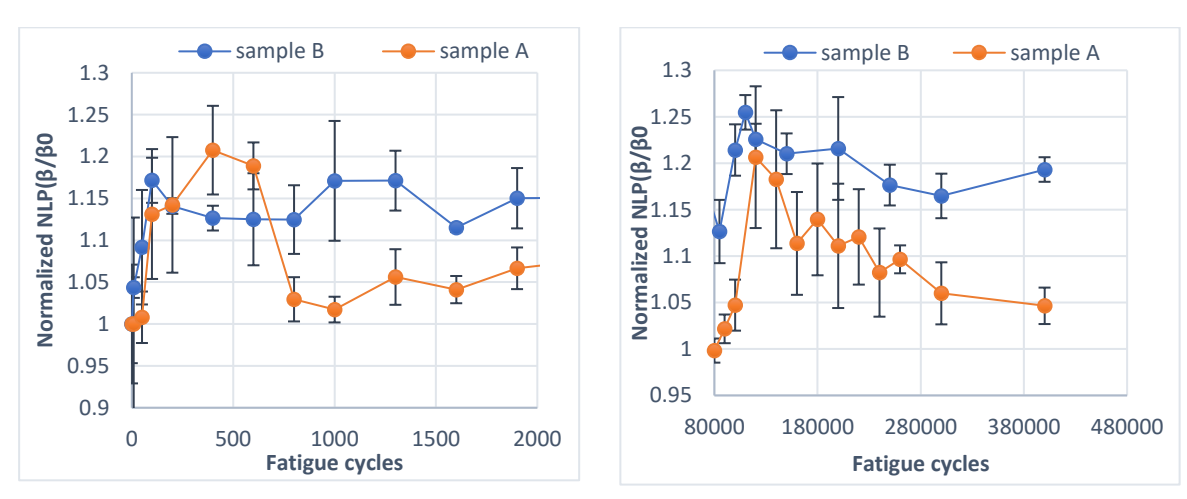
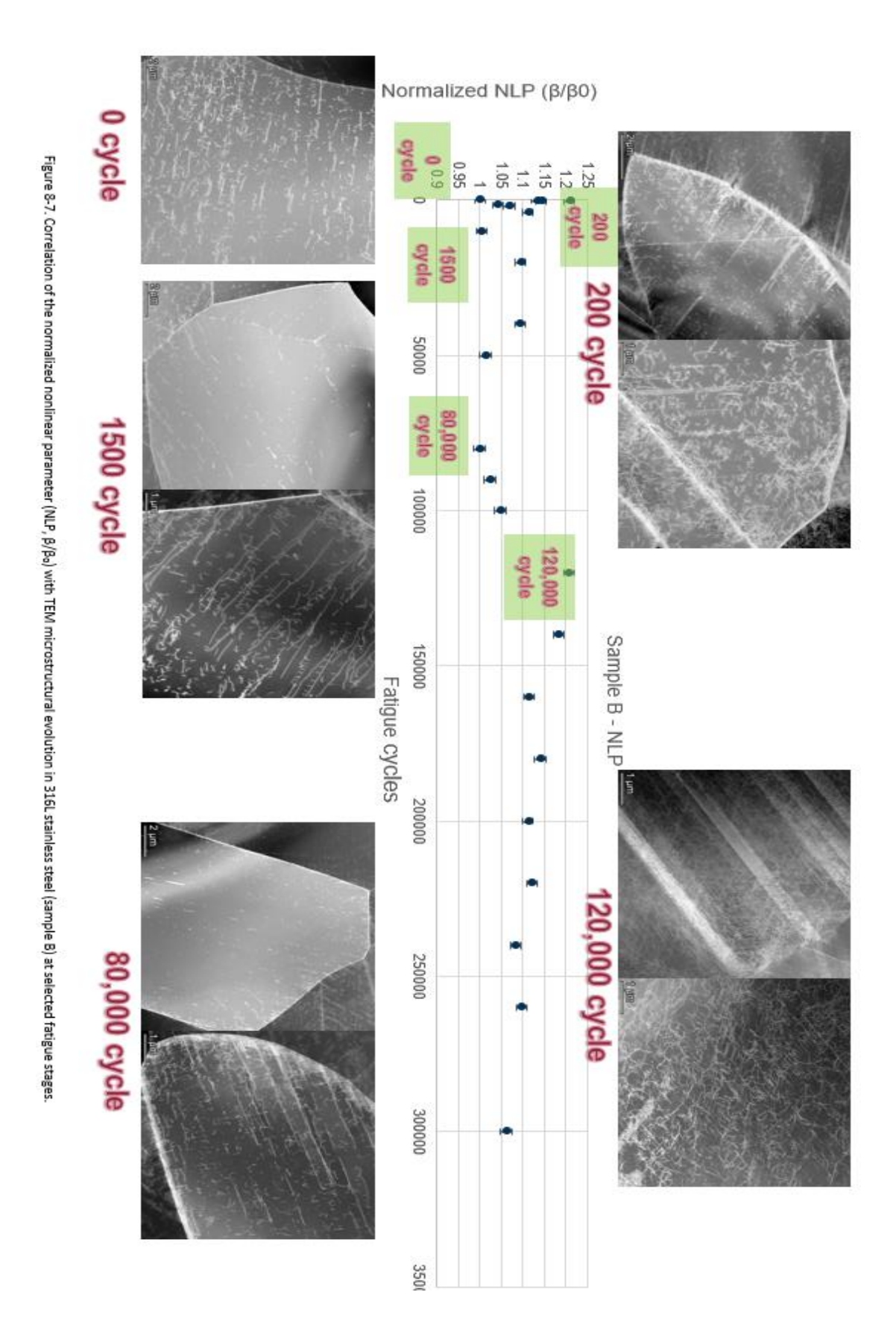


Figure 8-6. Normalized nonlinear ultrasonic parameter (NLP, β/β_0) versus fatigue cycles a) first and b) second peak for both samples A and B

8.5 Correlation between ER/NLP and TEM/HDDF observations

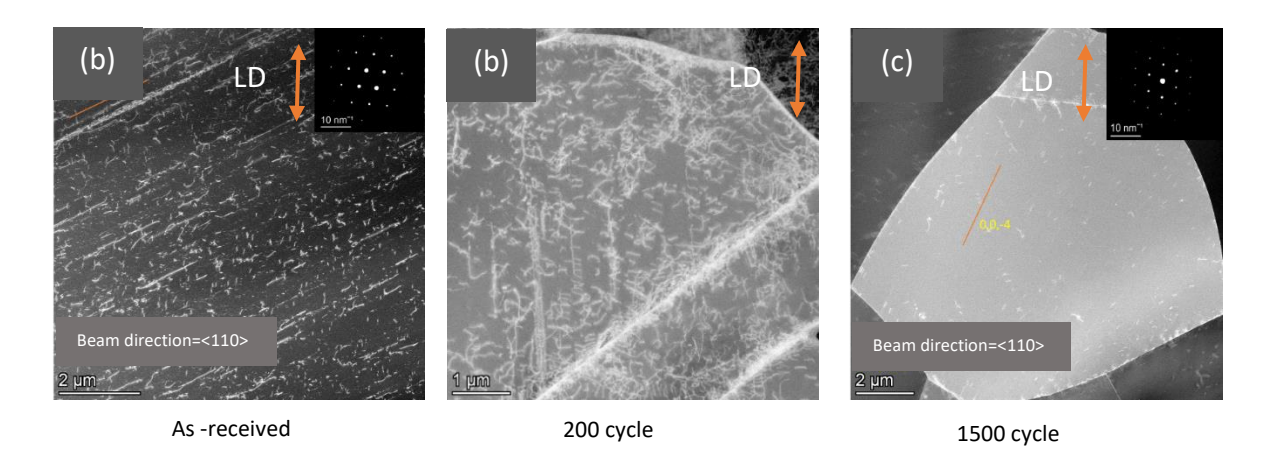
As explained in 7.3, five specific fatigue cycles were selected for STEM-HAADF imaging, primarily based on the peaks observed in the nonlinear parameter (NLP), which appeared more reliable due to higher intensity and consistency across two samples. However, these selected cycles can also be correlated with the electrical resistivity (ER) results. For instance, the first peak appears at a similar location in both NLP and ER measurements. Regarding the second peak, although there is a slight discrepancy in its location between the two methods—occurring between approximately 50,000 and 100,000 cycles in ER (corresponding to 1.1% to 2.4% of fatigue life)—the selected cycles for imaging at 85,000 (before the second ER peak) and 120,000 (after the second ER peak) still effectively capture the relevant changes. Therefore, while the selection was primarily driven by NLP observations, the chosen samples remain valid for drawing correlations with ER behavior as well. Figure 8-7 presents a visual correlation between normalized nonlinear ultrasonic parameter (NLP) and STEM-HAADF

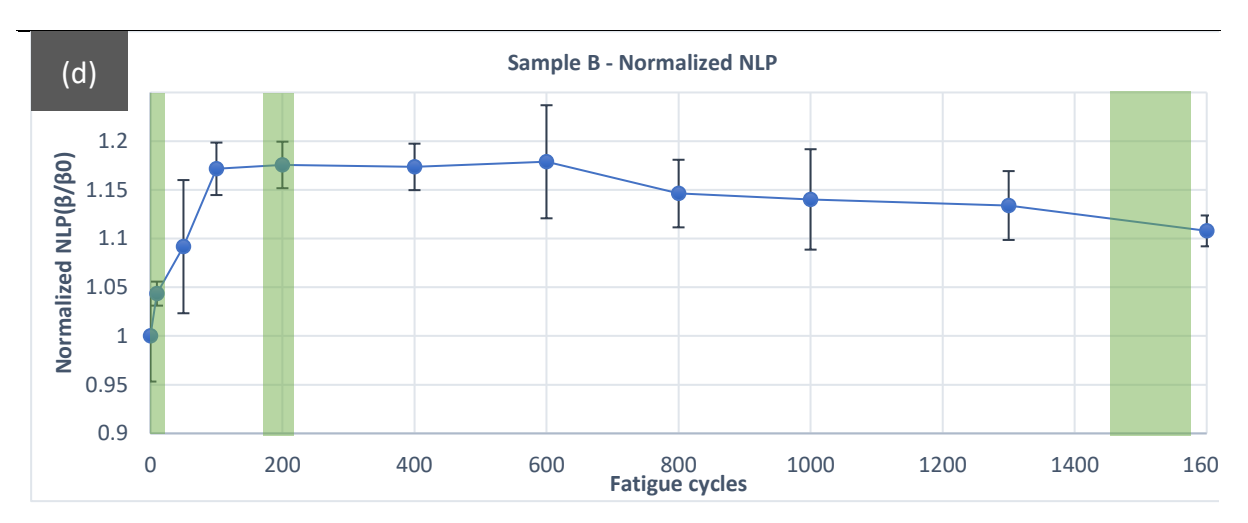
images taken at five critical fatigue cycles: 0, 200, and 1500 cycles—corresponding to before, at, and after the first peak, respectively—as well as 80,000 and 120,000 cycles, representing the points before and at the second peak. Based on Figure 8-7a, which represents the asreceived condition, microstructure shows an evenly distributed planar dislocation low interaction all along grains. By 200 cycles as shown in Figure 8-7b there is a marked increase in dislocation density and the emergence of dislocation tangling and alignment near grain boundaries. Slip bands begin to appear, indicating the onset of cyclic plastic deformation. These microstructural changes are consistent with observations reported in the literature, where early-stage fatigue leads to increase in dislocation density and the development of localized slip in low cycle fatigue 316L and copper alloys [23, 25, 27]. These changes coincide with the first significant peak in the NLP and ER curve, showing the sensitivity of both electrical resistivity and nonlinear parameter to dislocation density and dislocation tangles. This correlation highlights the sensitivity of NLP and ER to microstructural features such as dislocation density and tangling, as supported by studies showing that dislocation interactions influence nonlinear acoustic response and increase electron scattering, thereby raising electrical resistivity [183, 184]. At 1500 cycles, Figure 8-7c, the dislocation structures evolve into more defined bands and partial dislocation walls. Grains show reduced dislocation density due to annihilation or dynamic recovery. This stage appears as a plateau in the NLP and ER signal, reflecting a temporary stabilization in microstructural evolution. Similar dislocation rearrangement and partial recovery behaviour have been reported in early fatigue stages in low-cycle fatigue (LCF) of copper single crystals and in aluminium alloys under cyclic loading [27, 185]. By 80,000 cycles (Figure 8-7d), which is within the high-cycle fatigue (HCF) regime in this study, the microstructure reveals more advanced features, including thicker slip bands, intersecting patterns, and localized cyclic deformation. There is also evidence of crossslip and the activation of secondary slip systems, which typically mark the transition from planar to wavy slip — a well-known phenomenon observed in HCF studies of aluminium and nickel-based alloys [186, 187]. Despite these structural developments, the NLP and ER signals remain relatively stable, suggesting that the accumulated damage, while microstructurally significant, has not yet reached a threshold to alter the global acoustic or electrical response. This observation contrasts with studies such as the one for cyclic loading LCF of aluminiumlithium alloys led to clear correlations between dislocation evolution and harmonic generation. However, in another study in HCF of nickel-based alloys, the sensitivity of nonlinear ultrasonic measurements may be subtler or delayed until dislocation structures become more complex. At 120,000 cycles (Figure 7-8e), dense dislocation networks and saturated slip bands appear, along with dislocation cells between bands. This suggests the material has reached a microstructural saturation point, losing its ability to accommodate strain solely through localized slip. Studies on HCF of nickel superalloys, similarly, report that increases in nonlinear acoustic parameters precede or coincide with the onset of fatigue damage accumulation, even before macroscopic cracking becomes apparent [188, 189].



The next step is to discuss the images related to each peak in more detail and discuss the reason behind NLP and ER fluctuations as a function of fatigue life, focusing on Dislocation structure patterns and dislocation density. Before proceeding with the correlation between nonlinear ultrasonic parameters (NLP), Electrical resistivity (ER) and TEM observations, the theoretical foundations explaining the sensitivity of them to various dislocation structures are discussed. This includes how different dislocation configurations such as planar dislocations, tangles, pile-up and slip bands affect acoustic nonlinearity and electron scattering contribute to variations in the measured nonlinear parameter and electrical resistivity. The response of both electrical resistivity (ER) and the nonlinear ultrasonic parameter (NLP or β) to dislocation structures stems from their inherent dependence on the microstructural state of the material. Dislocations, through their density, configuration, and interaction mechanisms, significantly influence these two parameters. In nonlinear ultrasonic, the formation of dislocation pinning sites, dipoles, and evolving substructures (e.g., slip bands, persistent slip bands) alters the local stress-strain response, enhancing second harmonic generation and thereby increasing the nonlinear parameter β. Dislocation pinning restricts dislocation mobility and contributes to localized nonlinearity, while dislocation dipoles and complex arrangements further amplify acoustic nonlinear effects due to their interaction with ultrasonic waves. Similarly, ER increases with dislocation density as dislocations serve as electron scattering centres, disrupting electron flow. However, it is not merely the quantity but the morphology and distribution of dislocations—such as walls, tangles, and sub grain boundaries—that critically modulate ER, especially in cyclic and creep-loaded materials. Collectively, these observations confirm that both ER and NLP are highly sensitive to dislocation behaviour, making them powerful indicators of microstructural evolution and early-stage fatigue damage. Notably, findings from the literature suggest that NLP is highly responsive to a variety of dislocation structures and may serve as a more sensitive tool for detecting subtle changes in dislocation configurations. In the next part of this chapter, STEM-HAADF images corresponding to selected fatigue cycles are analysed in correlation with their respective NLP and ER measurements, providing a more detailed discussion on the relationship between microstructural evolution and signal response. At the as-received condition (0 cycles), STEM-HAADF images (Figure 8-8a) show grains with a relatively clean, planar dislocation structure, representing the undeformed reference state. At this stage, both the nonlinear ultrasonic parameter (NLP) and electrical resistivity (ER) serve as baseline measurements. Under cyclic loading, dislocations within the crystal lattice undergo repeated back-and-forth motion as the material is subjected to alternating stress. During this process, dislocations interact with obstacles such as grain boundaries, impurities, and other dislocations. These interactions contribute to an increase in overall dislocation density and promote the formation of more complex microstructural configurations. This behaviour is evident in the STEM-HAADF images at 200 cycles, where planar dislocations can be observed across multiple grains. This peak corresponding to the first distinct peak in the NLP (Figure 8-8d) and ER (Figure 8-8e) curve, the STEM-HAADF image (Figure 8-8b) reveals a significant increase in dislocation density, with dislocations beginning to form tangles and interact actively within the grains. These evolving

microstructural features produce strong localized stress fields that interact with ultrasonic waves, enhancing second harmonic generation and leading to a sharp rise in the nonlinear parameter. This demonstrates the high sensitivity of NLP to early-stage dislocation activity, particularly dynamic configurations such as pinned dislocations and dipoles. ER also shows an increase at this point, though its magnitude is more moderate implying that while dislocation activity has begun, the formation of long-range or densely packed immobile dislocation networks—needed for significant electron scattering—has not yet fully developed and the microstructure is still transitioning from disordered dislocation interactions to more stabilized features such as sub grain boundaries or wall-like structures, which are more efficient at scattering electrons. Hence, although ER responds to the increased presence of dislocations, its sensitivity at this stage is less pronounced compared to NLP. By 1500 cycles (Figure 8-8c), both NLP and ER values begin to decline. The STEM-HAADF image at this stage reveals that the dislocation network is less dense and more heterogeneous, with areas partially or entirely free of dislocations. This suggests that a significant proportion of dislocations have undergone annihilation or have been absorbed into grain or sub grain boundaries. As the number of dynamically interacting dislocations decreases, the localized stress fields responsible for second harmonic generation are reduced, leading to a drop in the nonlinear parameter. At the same time, ER also decreases, though more gradually, due to the gradual reduction in dislocation density and the diminishing number of effective electrons scattering sites. The decline in both parameters at this stage underscores the different sensitivities of the two techniques, NLP is more responsive to dynamic, stress-generating dislocation interactions, while ER reflects more stable, long-range structural features. This stage underscores the differing sensitivities of NLP and ER: while both respond to dislocation evolution, NLP reacts more sharply to changes in dynamic interactions, whereas ER integrates the cumulative effect of more stable, long-range dislocation structures.





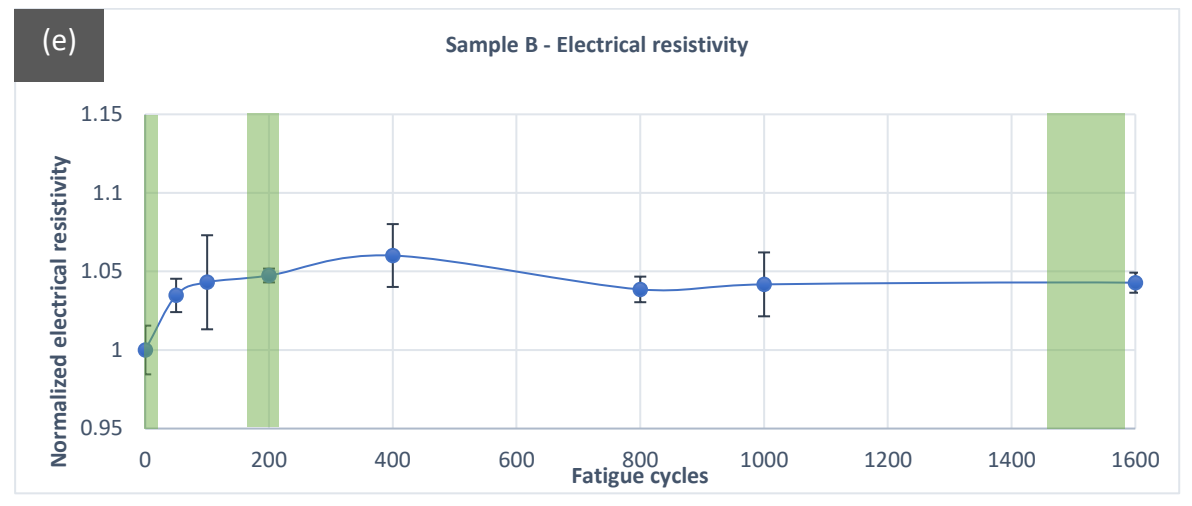
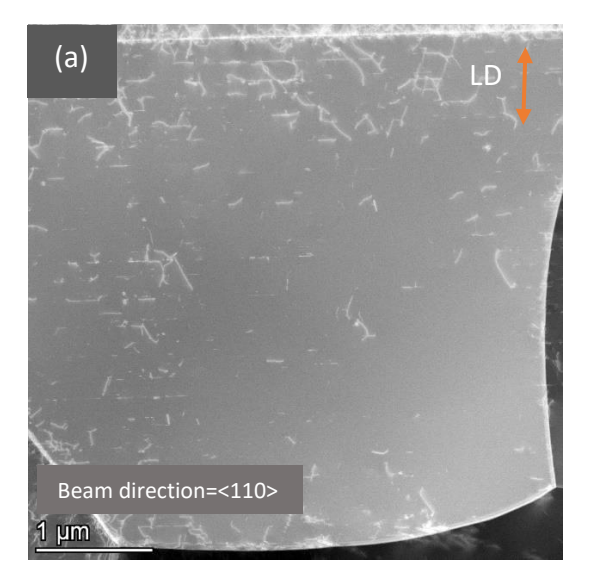
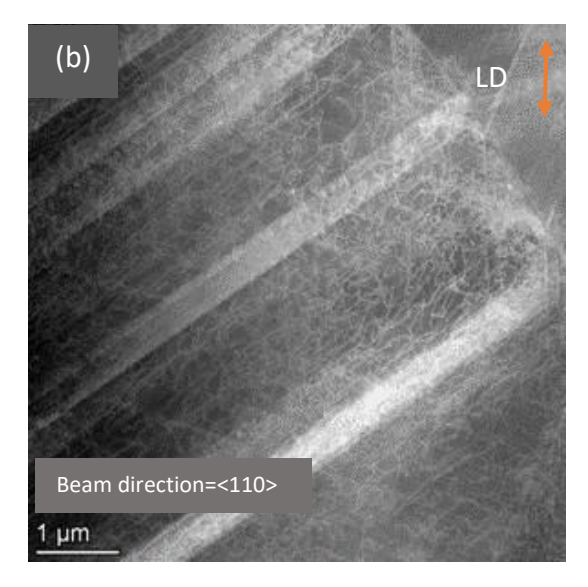


Figure 8-8. (a–c) STEM-HAADF images showing dislocation structures at three different fatigue stages in Sample B: (a) Asreceived condition (Reference point for ER and NLP), (b) 200 cycles (at the first NLP and ER peak), and (c) 1500 cycles (after the NLP and ER peak). LD denotes the loading direction. (d) Plot of normalized nonlinear ultrasonic parameter (NLP, β/β_0) versus fatigue cycles (e) Plot of normalized electrical resistivity versus fatigue cycles

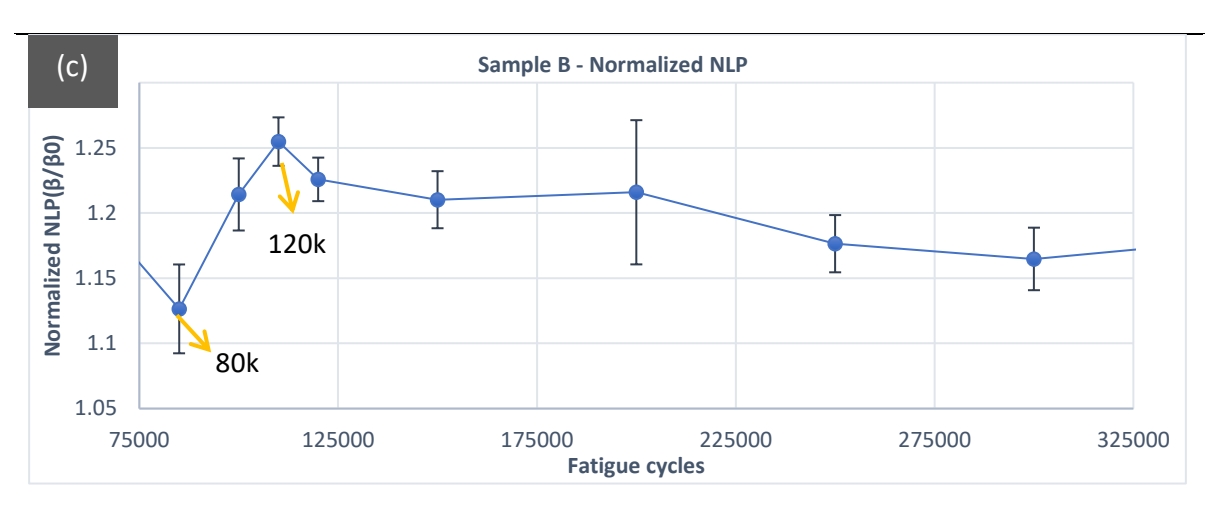
Between 1500 and 80,000 fatigue cycles, both the nonlinear ultrasonic parameter (NLP) and electrical resistivity (ER) plots show a plateau, suggesting either minimal microstructural evolution or changes that fall below the detection threshold of these techniques. This is supported by STEM-HAADF observations at these two stages, which show largely similar dislocation structures in most grains. However, by 80,000 cycles, a greater number of grains

have slip bands and signs of cross-slip activity, indicating the beginning of localized dislocation reorganization The second peak in the NLP plot (Figure 8-9 c) and ER (Figure 8-9b) plot occurs at approximately 120,000 fatigue cycles. This trend suggests renewed microstructural activity within the material, specifically involving dislocation interactions that enhance acoustic nonlinearity. The STEM-HAADF image at 80,000 cycles (Figure 8-9a), taken prior to the peak, reveals a moderately developed dislocation network with disordered, spread-out structures—consistent with a phase of relatively low dynamic interaction and lower nonlinear response. In contrast, by 120,000 cycles (Figure 8-9b), the image shows intensified dislocation activity, with dense tangles and possible wall-like formations across multiple grains. These features introduce high internal stress fields and energy gradients, which are known to interact strongly with ultrasonic waves and generate higher harmonic components, thereby increasing the NLP signal. From a microstructural standpoint, this peak likely reflects a secondary phase of dislocation multiplication and interaction triggered by prolonged cyclic loading. As the material endures additional cycles, accumulated damage leads to rearrangement and reactivation of previously stabilized dislocation segments. This results in the emergence of new tangles or partial localization of plasticity, particularly along preferred slip planes, as observed in the clear banded contrast in Figure 8-9b. Such rearrangements significantly contribute to nonlinear acoustic behaviour by altering the stress-strain response locally. The ER curve (Figure 8-9d), while following a generally increasing trend up to this point, displays only a moderate response at 120,000 cycles compared to the distinct NLP peak. This again underscores the greater response of NLP to dislocation dynamics and evolving local stress environments, whereas ER reflects longer-term and more static features such as the formation of dense, immobile dislocation structures like walls or sub grain boundaries. Hypothetically, the larger fluctuations and error bars in the ER data suggest that dislocations are unevenly distributed, which causes electron scattering to vary more from place to place compared to the more consistent way ultrasonic waves interact with the material.





80,000 cycle 120,000 cycle



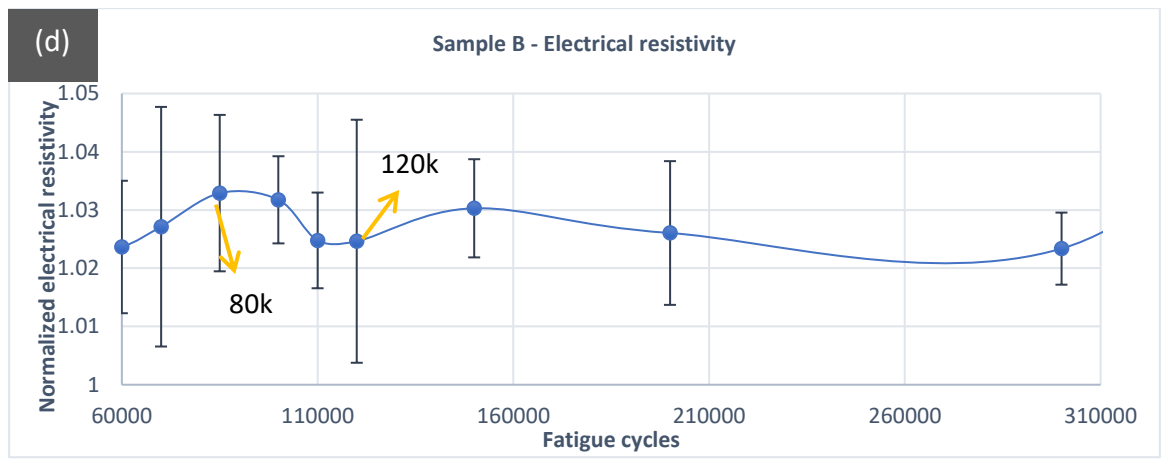


Figure 8-9. (a–b) STEM-HAADF images showing dislocation structures at (a) 80,000 cycles and (b) 120,000 cycles in Sample B, illustrating the microstructural evolution under high-cycle fatigue loading. The loading direction (LD) is indicated by orange arrows. (c) Normalized NLP (β/β_0) as a function of fatigue cycles. (d) Normalized electrical resistivity (ER) as a function of fatigue cycles

8.6 Summary

In summary, this chapter provided a comprehensive discussion integrating the findings from nonlinear ultrasonic parameter (NLP), electrical resistivity (ER), and transmission electron microscopy (TEM/STEM-HAADF) analyses to establish an understanding of early-stage high-cycle fatigue (HCF) behaviour in 316L stainless steel. The results demonstrated that both NLP and ER are effective indicators of fatigue-induced microstructural changes, with each responding to different aspects of dislocation evolution. While ER primarily reflects changes in dislocation density and the formation of stable, immobile dislocation structures that act as electron scattering centres, NLP is more sensitive to dynamic dislocation mechanisms, such as pinning, dipole formation, and the emergence of persistent slip bands.

The key contribution of this chapter lies in establishing a qualitative correlation between nondestructive testing signals and the underlying microstructural features observed through TEM and STEM-HAADF imaging. This correlation provides direct experimental evidence that variations in the nonlinear acoustic parameter (β) and electrical resistivity are governed by distinct but complementary dislocation mechanisms. Specifically, the first peaks in both NLP and ER were linked to rapid dislocation multiplication and tangling during early cyclic loading, whereas the second peaks corresponded to the reorganization and saturation of dislocations into well-defined walls and cell structures. These relationships reveal that the evolution of fatigue damage in 316L stainless steel follows a two-stage dislocation process, which can be effectively tracked by combining NLP and ER monitoring. This study also offers new insights into the complementary behaviour of acoustic and electrical NDE techniques, showing that NLP responds more sharply to reversible and transient dislocation configurations, while ER captures the cumulative effect of stable, long-term structural changes. The integration of both techniques therefore provides a more complete and physically grounded assessment of fatigue damage evolution than either method alone. Overall, the work presented in this chapter contributes new knowledge by directly linking the evolution of dislocation structures with measurable NDE responses, bridging the gap between microscopic mechanisms and macroscopic signal behaviour. This integrated framework advances the current understanding of how nonlinear acoustic and electrical properties evolve under cyclic loading, paving the way for mechanism-based early fatigue damage assessment in structural health monitoring of austenitic stainless steels.

Chapter 9. Conclusion and prospects

9.1 Conclusion

Base on the two main objectives of this study which were 1- evaluation of responsive and reliable NDT techniques for early-stage fatigue damage detection and 2- microstructural evolution and its correlation with NDT responses in early fatigue damage, the following conclusions have been drawn:

- 1. Electrical resistivity (ER) and nonlinear ultrasonic (NLU) methods were selected from the currently available non-destructive testing techniques based on their ability to detect fatigue damage through microstructural indicators such as dislocation density and slip band development. Unlike surface-confined methods or those requiring extensive specimen preparation, ER and NLU techniques offer both depth sensitivity and non-invasiveness, making them well-suited for detecting subsurface damage prior to crack initiation. Their proven sensitivity to nanoscale changes, validated in both experimental and literature contexts, along with their potential for future in-situ and real-time monitoring applications, positions them as the most promising tools for this study. These operating parameters of these methods were optimised to minimise errors, variability, while maintaining repeatability.
- 2. Both methods were successfully demonstrated for monitoring early-stage fatigue damage under high-cycle fatigue (HCF) conditions using 316L stainless steel samples subjected to 5 million cycles. Each technique detected two distinct peaks before 10% of the total fatigue life, fulfilling Objective 1 of this study.
- 3. ER study showed a two-peak trend in the normalized electrical resistivity response, with the first distinct peak occurring at approximately 0.01% of the fatigue life and the second, less pronounced peak appearing around 1%. The first peak corresponds to a sharp increase of approximately 8% in resistivity, followed by a gradual decrease of about 5%, indicating a transient rise likely due to increase in dislocation density in the early fatigue phase. The second peak shows a smaller increase of around 4%, followed by a subtle drop of approximately 2%, reflecting slower or more localized microstructural changes suggesting slower or more complex microstructural evolution, potentially related to slip band formation or dislocation structure reorganization.
- 4. NLP study showed a distinct two-peak trend in the normalized nonlinear ultrasonic parameter (β), with the first sharp increase of approximately 16% occurring at 0.004% of the fatigue life (between 200 and 400 cycles), followed by a gradual decrease and stabilization at a level 3% above the as-received sample ER. The second peak, also showing a 16% increase, appears at 2.4% of the fatigue life (around 120,000 to 150,000 cycles), after which the parameter returns to the previously stabilized level

and remains constant up to 8% of the fatigue life. The first peak shows a steep gradient, indicating a rapid onset of early microstructural changes, likely due to increase in dislocation density, whereas the second peak presents a more gradual rise and fall, suggesting more complex or distributed microstructural evolution such as slip band formation. The repeatability of this trend across two independently tested samples confirms β as a responsive early-stage fatigue damage indicator.

5. During the early-stage HCF prior to crack formation, it was found that dislocation density and structural complexity evolved progressively with increasing fatigue cycles. Initially (0 cycles), the microstructure showed planar dislocations with no slip bands and the presence of twin boundaries. By 200 cycles, a notable increase in dislocation density was observed, with the formation of tangled dislocations—particularly near grain boundaries—and the initiation of early slip bands. At 1,500 cycles, dislocations became more organized, forming stable wall—channel-like structures, and slip bands with clear pile-up emerged, indicating advanced slip localization. At 80,000 cycles, intersecting slip bands appeared, suggesting the activation of multiple slip systems, whilepersistent wall-channel structures indicated ongoing microstructural rearrangement. Finally, by 120,000 cycles, dislocation density was significantly elevated and distributed throughout the grains, with slip bands becoming diffuse and the early formation of substructure or dislocation cells commencing.

9.2 Future work

9.2.1 Extending NDT monitoring further within pre-crack fatigue life

The current study focused on early fatigue monitoring using ER and NLP techniques. Future work should continue to apply these methods throughout the entire pre-crack phase to further characterise the damage progression window before crack initiation.

9.2.2 Apply TEM/HDDF to study the development of microstructural change up to 20% HCF lifetime of 316L stainless steel

In this study, scanning transmission electron microscopy (STEM) with high-angle annular dark-field (HAADF) imaging was primarily used to qualitatively validate the signal peaks observed in the NLP and ER data. These observations confirmed changes in dislocation density and structures at specific stages of fatigue life. Future work should expand on this by discussing more quantitative analysis techniques, such as measuring Schmid factors, numerically evaluating dislocation density, and quantifying slip band width and depth.

9.2.3 Integration of NDT Techniques for In-Situ Fatigue Monitoring

Currently, ER and NLP methods have been applied in an ex-situ manner. A logical next step is to integrate both techniques into a real-time fatigue testing setup, enabling continuous insitu monitoring of microstructural evolution and damage accumulation.

9.2.4 Use of ECCI for dislocation mapping over larger areas

Electron channelling contrast imaging (ECCI) provides a technique to characterise dislocation type and arrangement over larger areas and bulk samples. Future work should include ECCI as a complementary method to TEM, especially for surface and near-surface studies in HCF regimes.

9.2.5 Applying these NDT methods to other engineering alloys

The effectiveness of ER and NLP for early fatigue damage detection in 316L stainless steel suggests strong potential for broader application. Future studies should test these methods on other advanced alloys such as Ni-based superalloys, Ti-based alloys, and high-entropy alloys, where early fatigue damage detection is equally critical.

9.2.6 Implementation for complex-shaped components

To evaluate real-world applicability, ER and NLP techniques should be adapted for use on large, complex-shaped components commonly found in aerospace, energy, and biomedical industries. This would demonstrate the scalability and robustness of these methods in realistic structural configurations.

Appendix A

In the following the explanation of using three step delta mode to cancel thermoelectric voltage is provided with an example following section 3.3.1.3, Three step delta mode (Three-point current reversal technique). Let's assume the temperature is linearly increasing over the short term in such a way that it produces a voltage profile like that shown in Figure 0-1 [120].

Test current = $\pm 5nA$

Device = 500Ω resistance

Disregarding errors caused by thermoelectric voltage, the measured voltages at each step are as follows:

$$V1 = 2.5\mu V$$
; $V2 = -2.5\mu V$; $V3 = 2.5\mu V$

Assume the temperature is increasing linearly over the short term, resulting in a voltage profile similar to that shown in Figure 0-2, where Vt rises by 100 nV with each successive reading.

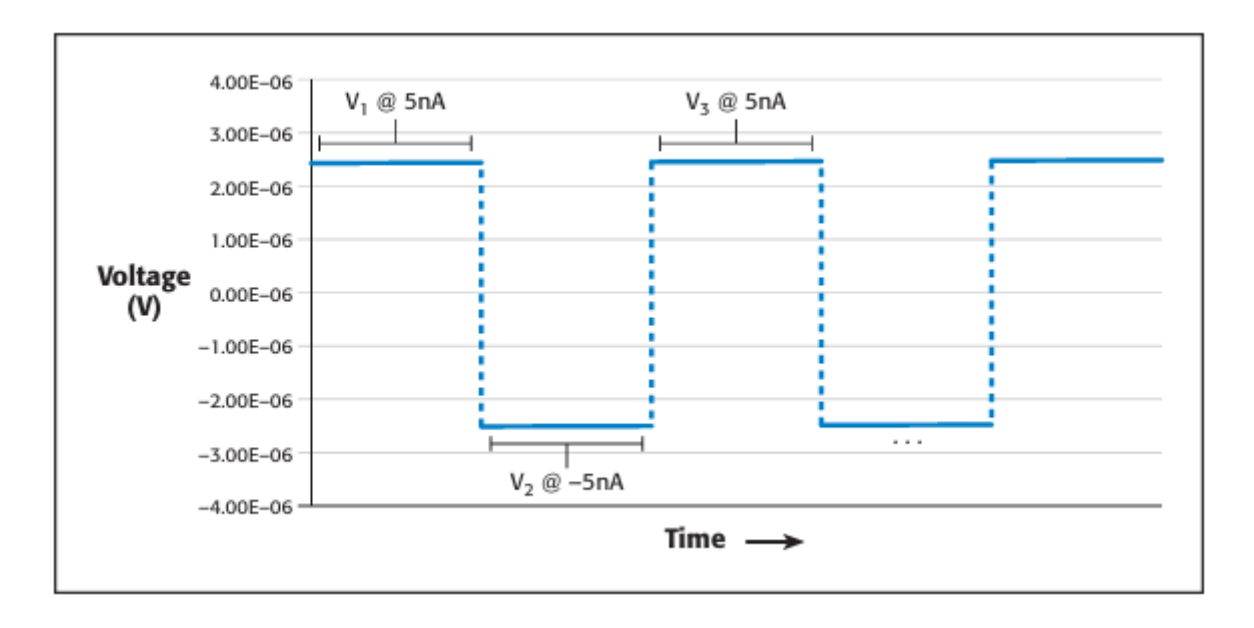


Figure 0-1. The graph depicts an alternating, three-point delta method of measuring voltage with no thermoelectric voltage error [120]

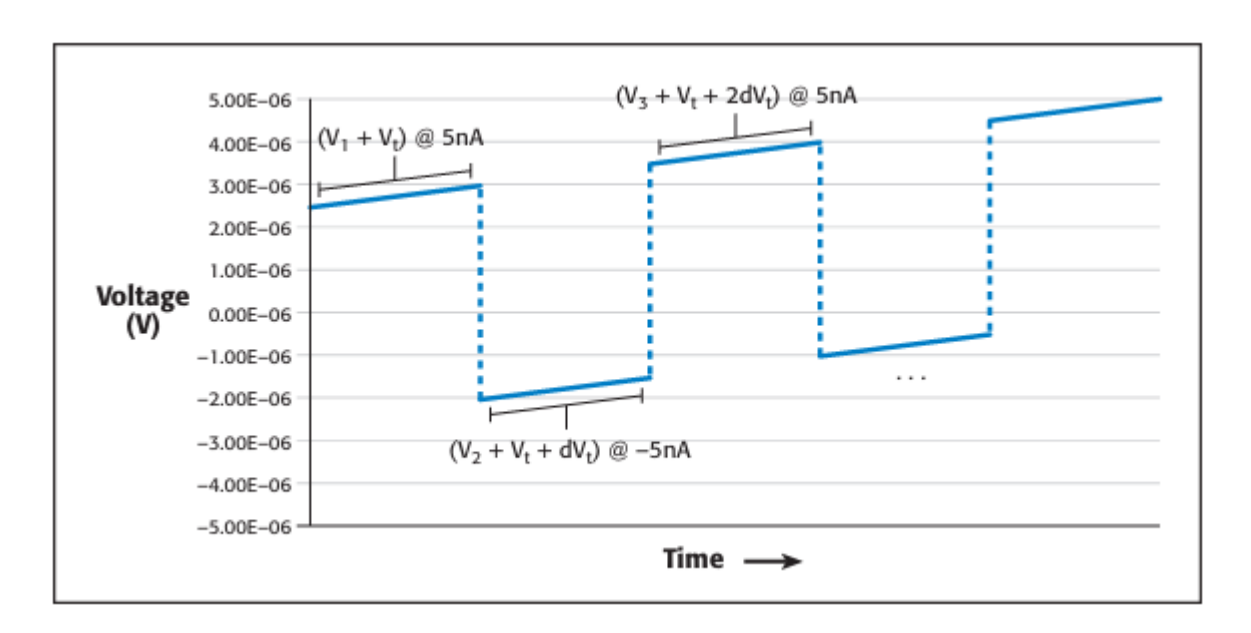


Figure 0-2. A linearly increasing temperature generates a changing thermoelectric voltage error, which is eliminated by the three-point delta method [120]

As Figure 0-2 shows, the voltages now measured by the voltmeter include error due to the increasing thermoelectric voltage in the circuit; therefore, they are no longer of equal magnitude. However, the absolute difference between the measurements is in error by a constant 100nV, so it's possible to cancel this term. The first step is to calculate the delta voltages. The first delta voltage (V_a) is equal to:

The second delta voltage (Vb) is equal to:

The thermoelectric voltage adds a negative error term in V_a and a positive error term in the calculation of Vb. When the thermal drift is a linear function, these error terms are equal in magnitude. Thus, we can cancel the error by taking the average of V_a and $V_b[120]$

$$V_f = final \ voltage \ reading = \frac{(V_a + V_b)}{2} = 2.5 \ V$$

References

- [1] L.P. Pook, Metal Fatigue: What It Is, Why It Matters. Springer, 2007.
- [2] S. Suresh, Fatigue of Materials. Cambridge University Press., 1998.
- [3] T. L. Anderson, Fracture Mechanics: Fundamentals and Applications. CRC Press, 2017.
- [4] D. K. Bhattacharya, "Non-Destructive Techniques for Microstructural and Structural Characterisation," in Recent Trends in Structural Integrity Assessment, National Metallurgical Laboratory, Jamshedpur, India, Jan. 2001, pp. 185–202.
- [5] F. Bjørheim, S. C. Siriwardane, and D. Pavlou, "A review of fatigue damage detection and measurement techniques," Int J Fatigue, vol. 154, Jan. 2022, doi: 10.1016/j.ijfatigue.2021.106556.
- [6] Š. Miroslav, C. Vladimír, and M. Kepka, "Possibility of fatigue damage detection by non-destructive measurement of the surface hardness," Procedia Structural Integrity, Elsevier B.V., 2017, pp. 262–267. doi: 10.1016/j.prostr.2017.11.087.
- [7] A. F. R. S. H. O. F. Ralph I. Stephens, Metal Fatigue in Engineering. John Wiley & Sons, 2000.
- [8] J. Schijve, Fatigue of Structures and Materials. Springer, 2009.
- [9] J. Ewing, J.; Humfrey, "The Fracture of Metals under Repeated Alternations of Stress," Philosophical Transactions of the Royal Society of London. Series A, 1934, doi: 10.1098/rsta.1903.0006.
- [10] M. Asif Kattimani et al., "Design and Fabrication of Fatigue Testing Machine," Int J Sci Res Sci Eng. Techno, pp. 295–304, Feb. 2020, doi: 10.32628/ijsrset20728.
- [11] J. Schijve, "Fatigue of structures and materials in the 20th century and the state of the art" vol. 25, no. September 2002, pp. 679–702, 2003, doi: 10.1016/S0142-1123(03)00051-3.
- [12] M. D. Sangid, "The physics of fatigue crack initiation," Int J Fatigue, vol. 57, pp. 58–72, 2013, doi: 10.1016/j.ijfatigue.2012.10.009.
- [13] P. Peralta and C. Laird, Cyclic Plasticity and Dislocation Structures, no. May. 2016. doi: 10.1016/b978-0-12-803581-8.02917-9.
- [14] H. Mughrabi, "Revisiting 'Steady-State' Monotonic and Cyclic Deformation: Emphasizing the Quasi-Stationary State of Deformation," Metal Mater Trans A Phys Metal Mater Sci, vol. 51, no. 4, pp. 1441–1456, Apr. 2020, doi: 10.1007/s11661-019-05618-x.
- [15] J. Polák and J. Man, "Materials Science & Engineering A Mechanisms of extrusion and intrusion formation in fatigued crystalline materials," Materials Science & Engineering A, vol. 596, pp. 15–24, 2014, doi: 10.1016/j.msea.2013.12.005.
- [16] J. Man, K. Obrtlík, and J. Polák, "Study of surface relief evolution in fatigued 316L austenitic stainless steel by AFM," Materials Science and Engineering A, vol. 351, no. 1–2, pp. 123–132, Jun. 2003, doi: 10.1016/S0921-5093(02)00846-8.

- [17] J. Man, M. Petrenec, K. Obrtlík, and J. Polák, "AFM and TEM study of cyclic slip localization in fatigued ferritic X10CrAl24 stainless steel," Acta Materialia, vol. 52, no. 19, pp. 5551–5561, Nov. 2004, doi: 10.1016/j.actamat.2004.08.014.
- [18] J. Man, P. Klapetek, O. Man, A. Weidner, K. Obrtlík, and J. Polák, "Extrusions and intrusions in fatigued metals. Part 2. AFM and EBSD study of the early growth of extrusions and intrusions in 316L steel fatigued at room temperature," Philosophical Magazine, vol. 89, no. 16, pp. 1337-1372, June. 2009, doi: 10.1080/14786430902917624.
- [19] Y. Murakami, M. Takada, and T. Toriyama, "Super-long-life tension-compression fatigue properties of quenched and tempered 0.46% carbon steel, 1998.
- [20] K. O. Findley, R. Cryderman, A. B. Nissan, and D. Matlock, "The effects of inclusions on fatigue performance of steel alloys," *Iron Steel Technol.*, vol. 10, pp. 234–243, Oct. 2013.
- [21] P. C. Paris and F. Erdogan, "A critical analysis of crack propagation laws," *Journal of Basic Engineering*, vol. 85, no. 4, pp. 528–533, Dec. 1963.
- [22] M.-S. Pham, "Fatigue behaviour of AISI 316L: Mechanical response, microstructural evolution, fatigue crack propagation, & physically based constitutive modelling," Ph.D. dissertation, ETH Zurich, 2011. doi: 10.3929/ethz-a-009757628.
- [23] M. S. Pham, C. Solenthaler, K. G. F. Janssens, and S. R. Holdsworth, "Dislocation structure evolution and its effects on cyclic deformation response of AISI 316L stainless steel," *Materials Science and Engineering: A*, vol. 528, no. 7–8, pp. 3261–3269, Mar. 2011, doi: 10.1016/j.msea.2011.01.015.
- [24] L. Boulanger, "Labyrinth structure and persistent slip bands in fatigued 316 stainless steels," *Philosophical Magazine A*, vol. 51, no. 2, pp. 163–181, 1985,
- [25] M.-S. Pham and S. R. Holdsworth, "Evolution of relationships between dislocation microstructures and internal stresses of AISI 316L during cyclic loading at 293 K and 573 K (20°C and 300°C)," *Metallurgical and Materials Transactions A*, vol. 44, no. 1, pp. 47–60, 2013.
- [26] M. S. Pham and S. R. Holdsworth, "Role of microstructural condition on fatigue damage development of AISI 316L at 20 and 300 °C," *International Journal of Fatigue*, vol. 51, pp. 36–48, 2013, doi: 10.1016/j.ijfatigue.2013.02.005.
- [27] U. Essmann and H. Mughrabi, "Annihilation of dislocations during tensile and cyclic deformation and limits of dislocation densities," *Philosophical Magazine A*, vol. 40, no. 6, pp. 731–756, 1979, doi: 10.1080/01418617908234871.
- [28] L. Li, Z. Zhang, P. Zhang, C. Li, and Z. Zhang, "Dislocation arrangements within slip bands during fatigue cracking," Mater Charact, vol. 145, pp. 96–100, Nov. 2018, doi: 10.1016/j.matchar.2018.08.039.
- [29] D. G. R. William D. Callister Jr., Materials Science and Engineering: An Introduction. 2011. doi: 10.1142/9789814374064 0002.

- [30] W. Yun, H. Kimura, Y. Akiniwa, and K. Tanaka, "EBSD-AFM hybrid analysis of crack initiation in stainless steel under fatigue loading," Key Eng Mater, vol. 340-341 I, pp. 531–536, 2007, doi: 10.4028/www.scientific.net/kem.340-341.531.
- [31] M. Mohin, Fatigue Crack Growth Assessment and Fatigue Resistance Enhancement of Aluminium Alloys, M.Sc. thesis, 2018. https://www.researchgate.net/publication/329094003.
- [32] M. A. Tafti, Experimental High Cycle Fatigue Testing and Shape Optimization of Turbine Blades, M.Sc. thesis, Concordia University, 2013.
- [33] T. Nicholas, *High Cycle Fatigue: A Mechanics of Materials Perspective*. Oxford, UK Elsevier, 2006, doi: 10.1016/B978-0-08-044691-2.X5000-0.
- [34] A. Ghosh, "Low cycle fatigue behaviour of engineering metallic materials: Review on cyclic deformation micro-mechanism," Mechanics of Materials, vol. 188, Jan. 2024, doi: 10.1016/j.mechmat.2023.104852.
- [35] D. Ye, "Investigation of cyclic deformation behaviour in the surface layer of 18Cr-8Ni austenitic stainless steel based on Vickers microhardness measurement," Mater Chem Phys, vol. 93, no. 2–3, pp. 495–503, Oct. 2005, doi: 10.1016/j.matchemphys.2005.03.031.
- [36] D. Ye, X. Tong, L. Yao, and X. Yin, "Fatigue hardening/softening behaviour investigated through Vickers microhardness measurement during high-cycle fatigue," Mater Chem Phys, vol. 56, no. 3, pp. 199–204, 1998, doi: 10.1016/S0254-0584(98)00135-7.
- [37] D. Ye and Z. Wang, "An approach to investigate pre-nucleation fatigue damage of cyclically loaded metals using Vickers microhardness tests," Int. J. Fatigue, 2001. Available: https://www.elsevier.com/locate/ijfatigue.
- [38] D. G. Pavlou, "A phenomenological fatigue damage accumulation rule based on hardness increasing, for the 2024-T42 aluminum," Eng Struct, vol. 24, no. 11, pp. 1363–1368, 2002, doi: 10.1016/S0141-0296(02)00055-X.
- [39] G. Drumond, F. Roudet, D. Chicot, B. Pinheiro, and I. Pasqualino, "A Damage Criterion to Predict the Fatigue Life of Steel Pipelines Based on Indentation Measurements," Journal of Offshore Mechanics and Arctic Engineering, vol. 143, no. 1, Feb. 2021, doi: 10.1115/1.4047203.
- [40] Š. Miroslav, C. Vladimír, and M. Kepka, "Possibility of fatigue damage detection by non-destructive measurement of the surface hardness," Procedia Structural Integrity, Elsevier B.V., 2017, pp. 262–267. doi: 10.1016/j.prostr.2017.11.087.
- [41] B. Pinheiro, J. Lesage, I. Pasqualino, N. Benseddiq, and E. Bemporad, "X-ray diffraction study of microstructural changes during fatigue damage initiation in steel pipes," Materials Science and Engineering: A, vol. 532, pp. 158–166, 2012, doi: 10.1016/j.msea.2011.10.077.

- [42] B. Pinheiro, J. Lesage, I. Pasqualino, E. Bemporad, and N. Benseddiq, "X-ray diffraction study of microstructural changes during fatigue damage initiation in pipe steels: Role of the initial dislocation structure," Materials Science and Engineering: A, vol. 580, pp. 1–12, Sep. 2013, doi: 10.1016/j.msea.2013.05.042.
- [43] Nagao, M., and Weiss, V. "X-Ray Diffraction Study of Low Cycle Fatigue Damage in Plain Carbon Steel." ASME. J. Eng. Mater. Technol. April 1977; 99(2): 110-113, https://doi.org/10.1115/1.3443418
- [44] Taira, S. X-ray-diffraction approach for studies on fatigue and creep. Experimental Mechanics 13, 449–463 (1973). https://doi.org/10.1007/BF02322729
- [45] M. P. Luong, "Infrared thermographic scanning of fatigue in metals," Nuclear Engineering and Design, vol. 158, no. 2–3, pp. 363–376, 1995, doi: 10.1016/0029-5493(95)01043-H.
- [46] G. La Rosa and A. Risitano, "Thermographic methodology for rapid determination of the fatigue limit of materials and mechanical components," Int. J. Fatigue, vol. 22, no. 1, pp. 65–73, 2000. doi: 10.1016/S0142-1123(99)00088-2.
- [47] M. Amiri and M. M. Khonsari, "Rapid determination of fatigue failure based on temperature evolution: Fully reversed bending load," Int J Fatigue, vol. 32, no. 2, pp. 382–389, Feb. 2010, doi: 10.1016/j.ijfatigue.2009.07.015.
- [48] Z. Teng, H. Wu, C. Boller, and P. Starke, "A unified fatigue life calculation based on intrinsic thermal dissipation and microplasticity evolution," Int J Fatigue, vol. 131, Feb. 2020, doi: 10.1016/j.ijfatigue.2019.105370.
- [49] A. Dupasquier, G. Kögel, and A. Somoza, "Studies of light alloys by positron annihilation techniques," Acta Mater, vol. 52, no. 16, pp. 4707–4726, Sep. 2004, doi: 10.1016/j.actamat.2004.07.004.
- [50] J. Čížek, "Characterization of lattice defects in metallic materials by positron annihilation spectroscopy: A review," J Mater Sci Technol, vol. 34, no. 4, pp. 577–598, Apr. 2018, doi: 10.1016/j.jmst.2017.11.050.
- [51] J. Čížek, "Characterization of lattice defects in metallic materials by positron annihilation spectroscopy: A review," J Mater Sci Technol, vol. 34, no. 4, pp. 577–598, Apr. 2018, doi: 10.1016/j.jmst.2017.11.050.
- [52] Y. Uematsu, T. Kakiuchi, K. Hattori, N. Uesugi, and F. Nakao, "Non-destructive evaluation of fatigue damage and fatigue crack initiation in type 316 stainless steel by positron annihilation line-shape and lifetime analyses," Fatigue Fract Eng Mater Struct, vol. 40, no. 7, pp. 1143–1153, Jul. 2017, doi: 10.1111/ffe.12572.
- [53] Y. Kawaguchi, N. Nakamura, and S. Yusa, "Non-destructive evaluation of fatigue damage in type 316 stainless steel using positron annihilation line shape analysis," Materials Transactions, vol. 43, no. 4, pp. 727–734, 2002, doi: 10.2320/matertrans.43.727.

- [54] Y. Kawaguchi and Y. Shirai, "Fatigue Evaluation of type 316 stainless steel using positron annihilation line shape analysis and β +- γ coincidence positron lifetime measurement," J Nucl Sci Technol, vol. 39, no. 10, pp. 1033–1040, 2002, doi: 10.1080/18811248.2002.9715291.
- [55] U. Holzwarth and P. Schaaff, "On the non-destructive detection of fatigue damage in industrial aluminium alloys by positron annihilation," J Mater Sci, vol. 42, no. 14, pp. 5620–5628, Jul. 2007, doi: 10.1007/s10853-006-0993-8.
- [56] M. Chai, J. Zhang, Z. Zhang, Q. Duan, and G. Cheng, "Acoustic emission studies for characterization of fatigue crack growth in 316LN stainless steel and welds," Applied Acoustics, vol. 126, pp. 101–113, Nov. 2017, doi: 10.1016/j.apacoust.2017.05. 014.
- [57] M. Chai, X. Hou, Z. Zhang, and Q. Duan, "Identification and prediction of fatigue crack growth under different stress ratios using acoustic emission data," Int J Fatigue, vol. 160, Jul. 2022, doi: 10.1016/j.ijfatigue.2022.106860.
- [58] M. Chai, Z. Zhang, Q. Duan, and Y. Song, "Assessment of fatigue crack growth in 316LN stainless steel based on acoustic emission entropy," Int J Fatigue, vol. 109, pp. 145–156, Apr. 2018, doi: 10.1016/j.ijfatigue.2017.12.017.
- [59] M. Chai, C. Lai, W. Xu, Q. Duan, Z. Zhang, and Y. Song, "Characterization of Fatigue Crack Growth Based on Acoustic Emission Multi-Parameter Analysis," Materials, vol. 15, no. 19, Oct. 2022, doi: 10.3390/ma15196665.
- [60] P. A. Vanniamparambil, U. Guclu, and A. Kontsos, "Identification of Crack Initiation in Aluminium Alloys using Acoustic Emission," Exp Mech, vol. 55, no. 5, pp. 837–850, Jun. 2015, doi: 10.1007/s11340-015-9984-5.
- [61] M. Seleznev, A. Weidner, H. Biermann, and A. Vinogradov, "Novel method for in situ damage monitoring during ultrasonic fatigue testing by the advanced acoustic emission technique," Int J Fatigue, vol. 142, Jan. 2021, doi: 10.1016/j.ijfatigue.2020.105918.
- [62] F. Vlasic, P. Mazal, and F. Hort, "Comparison of Acoustic Emission Signal and X-ray Diffraction at Initial Stages of Fatigue Damage," Proc. 30th European Conference on Acoustic Emission Testing (EWGAE), Vienna, Austria, Sep. 2010. Available: https://www.ndt.net/article/ewgae2010/papers/61_Vlasic.pdf.
- [63] H. Kikuchi, K. Ara, Y. Kamada, and S. Kobayashi, "Effect of microstructure changes on barkhausen noise properties and hysteresis loop in cold rolled low carbon steel," IEEE Trans Magn, vol. 45, no. 6, pp. 2744–2747, 2009, doi: 10.1109/TMAG.2009.2020545.
- [64] N. Kasai, H. Koshino, K. Sekine, H. Kihira, and M. Takahashi, "Study on the effect of elastic stress and microstructure of low carbon steels on barkhausen noise," J Non -destructive Eval, vol. 32, no. 3, pp. 277–285, Sep. 2013, doi: 10.1007/s10921-013-0180-1.
- [65] M. Teschke, J. R. Vasquez, L. Lücker, and F. Walther, "Characterization of damage evolution on hot flat rolled mild steel sheets by means of micromagnetic parameters and fatigue strength determination," Materials, vol. 13, no. 11, Jun. 2020, doi: 10.3390/ma13112486.

- [66] S. Yamaura, Y. Furuya, and T. Watanabe, "The effect of grain boundary microstructure on Barkhausen noise in ferromagnetic materials," Acta Materialia, vol. 49, pp. 3019–3027, Sep. 2001, doi: 10.1016/S1359-6454(01)00189-6.
- [67] J. C. Brice, "The effect of inclusions on the domain coercive force of thin ferromagnetic films," Br. J. Appl. Phys., vol. 16, no. 10, pp. 1523–1527, 1965, doi: 10.1088/0508-3443/16/10/315.
- [68] B. Astié, J. Degauque, J. L. Porteseil, and R. Vergne, "Influence of the dislocation structures on the magnetic and magneto mechanical properties of high-purity iron," IEEE Trans. Magn, vol. 17, no. 6, Nov. 1981,
- [69] Scherpereel, D.E., Kazmerski, L.L. & Allen, C.W. The magnetoelastic interaction of dislocations and ferromagnetic domain walls in iron and nickel. Metall Trans 1, 517–524 (1970). https://doi.org/10.1007/BF02811563
- [70] M. Lindgren and T. Lepistö, "Application of a novel type Barkhausen noise sensor to continuous fatigue monitoring," NDT & E Int., vol. 33, no. 6, pp. 423–428, Sep. 2000. doi: 10.1016/S0963-8695(00)00011-6.
- [71] M. Soultan, X. Kleber, J. Chicois, and A. Vincent, "Mechanical Barkhausen noise during fatigue of iron," NDT and E International, vol. 39, no. 6, pp. 493–498, 2006, doi: 10.1016/j.ndteint.2006.03.003.
- [72] E. S. Palma, T. R. Mansur, S. F. Silva, and A. Alvarenga, "Fatigue damage assessment in AISI 8620 steel using Barkhausen noise," Int J Fatigue, vol. 27, no. 6, pp. 659–665, Jun. 2005, doi: 10.1016/j.ijfatigue.2004.11.005.
- [73] S. P. Sagar, N. Parida, S. Das, G. Dobmann, and D. K. Bhattacharya, "Magnetic Barkhausen emission to evaluate fatigue damage in a low carbon structural steel," Int J Fatigue, vol. 27, no. 3, pp. 317–322, Mar. 2005, doi: 10.1016/j.ijfatigue.2004.06.015.
- [74] L. Pantleon et al., "Simultaneous dual configuration van der Pauw measurements of gated graphene devices," Measurement, vol. 225, p. 113954, 2024. doi: 10.1016/j.measurement.2023.113954.
- [75] Y. Singh, "Electrical resistivity measurements: A review," International Journal of Modern Physics: Conference Series, vol. 22, pp. 745–756, Jan. 2013, doi: 10.1142/S2010194513010970.
- [76] J. Polák, "Electrical resistivity of cyclically deformed copper," Czechoslovak Journal of Physics, vol. 19, no. 3, pp. 315–322, 1969, doi: 10.1007/BF01712868.
- [77] Z. Stanković and O. T. Bruhns, "Fatigue life investigation using non-destructive testing methods," PAMM, vol. 7, no. 1, pp. 4030027–4030028, Dec. 2007, doi: 10.1002/pamm.200700811.
- [78] P. Charsley and B.A. Robins, "Electrical resistance changes of cyclically deformed copper," Materials Science and Engineering, vol. 14, pp. 189–196, 1974.

- [79] P. Wang, T. Takagi, T. Takeno, and H. Miki, "Early fatigue damage detecting sensors—A review and prospects," Sensors and Actuators A: Physical, vol. 198, pp. 46–60, Aug. 2013, doi: 10.1016/j.sna.2013.05.017.
- [80] P. Starke, M. Klein, and D. Eifler, "Resistivity A characteristic fingerprint of fatigue induced changes in the microstructure of metallic materials," Procedia Engineering, Elsevier Ltd, 2011, pp. 698–703. doi: 10.1016/j.proeng.2011.04.116.
- [81] P. Starke, D. Eifler, and C. Boller, "Fatigue assessment of metallic materials beyond strain measurement," International Journal of Fatigue, Elsevier Ltd, Jan. 2016, pp. 274–279. doi: 10.1016/j.ijfatigue.2015.03.018.
- [82] H. Germann, P. Starke, and D. Eifler, "Resistivity-based evaluation of the fatigue behavior of cast irons," Metallurgical and Materials Transactions A: Physical Metallurgy and Materials Science, Aug. 2012, pp. 2792–2798. doi: 10.1007/s11661-011-0852-3.
- [83] Starke, P., Klein, M., & Eifler, D. (2011). Resistivity A characteristic fingerprint of fatigue induced changes in the microstructure of metallic materials. *Procedia Engineering, 10*, 698–703. https://doi.org/10.1016/j.proeng.2011.04.118
- [84] M. Smaga, F. Hahnenberger, A. Sorich, and D. Eifler, "Cyclic deformation behaviour of austenitic steels in the temperature range -60°C ≤ T ≤ 550°C," in Key Engineering Materials, Trans Tech Publications Ltd, 2011, pp. 439–442. doi: 10.4028/www.scientific.net/KEM.465.439.
- [85] B. Sun and Y. Guo, "High-cycle fatigue damage measurement based on electrical resistance change considering variable electrical resistivity and uneven damage," Int J Fatigue, vol. 26, no. 5, pp. 457–462, May 2004, doi: 10.1016/j.ijfatigue.2003.10.004.
- [86] B. Sun, L. Yang, and Y. Guo, "A high-cycle fatigue accumulation model based on electrical resistance for structural steels," Fatigue Fract Eng Mater Struct, vol. 30, no. 11, pp. 1052–1062, 2007, doi: 10.1111/j.1460-2695.2007.01175. x.
- [87] M. A. Omari and I. Sevostianov, "Evaluation of the growth of dislocations density in fatigue loading process via electrical resistivity measurements," Int J Fract, vol. 179, no. 1–2, pp. 229–235, Jan. 2013, doi: 10.1007/s10704-012-9780-5.
- [88] H. Wu et al., "Characterization of the fatigue behaviour for SAE 1045 steel without and with load-free sequences based on non-destructive, X-ray diffraction and transmission electron microscopic investigations," Materials Science and Engineering: A, vol. 794, Sep. 2020, doi: 10.1016/j.msea.2020.139597.
- [89] R. Nobile and A. Saponaro, "Electrical Resistance measurements for fatigue damage prediction of AISI 316L stainless steel," Procedia Structural Integrity, Elsevier B.V., 2022, pp. 421–429. doi: 10.1016/j.prostr.2022.05.048.
- [90] R. Nobile and A. Saponaro, "Real-time monitoring of fatigue damage by electrical resistance change method," Int J Fatigue, vol. 151, Oct. 2021, doi: 10.1016/j.ijfatigue.2021.106404.

- [91] S. Saberi et al., "A new development of four-point method to measure the electrical resistivity in situ during plastic deformation," Measurement (Lond), vol. 180, Aug. 2021, doi: 10.1016/j.measurement.2021.109547.
- [92] M. G. Silk, "Defect detection and sizing in metals using ultrasound," International Metals Reviews, vol. 27, no. 1, pp. 28–50, 1982, doi: 10.1179/imr.1982.27.1.28.
- [93] A. Hikata, B. B. Chick, and C. Elbaum, "Dislocation contribution to the second harmonic generation of ultrasonic waves," J Appl Phys, vol. 36, no. 1, pp. 229–236, 1965, doi: 10.1063/1.1713881.
- [94] J. Zheng, Z. Li, J. He, J. Teng, and L. Zheng, "Axial stress measurement of concrete with nonlinear ultrasonic harmonic method," e-Journal of Non-destructive Testing (eJNDT), vol. 23, no. 11, July 10–13, 2018. ISSN 1435-4934. Available: https://www.ndt.net/article/ewshm2018/papers/ewshm-1115.pdf.
- [95] K. H. Matlack, J. Y. Kim, L. J. Jacobs, and J. Qu, "Review of Second Harmonic Generation Measurement Techniques for Material State Determination in Metals," J Nondestr Eval, vol. 34, no. 1, Mar. 2015, doi: 10.1007/s10921-014-0273-5.
- [96] S. K. Chakrapani, "Multiscale model to study dislocation dynamics in nonlinear resonance spectroscopy of crystalline solids," Ultrasonics, vol. 96, no. January, pp. 220–223, 2019, doi: 10.1016/j.ultras.2019.01.003.
- [97] J. N. Potter, A. J. Croxford, and P. D. Wilcox, "Nonlinear ultrasonic phased array imaging," Phys. Rev. Lett., vol. 113, no. 14, p. 144301, Oct. 2014. doi: 10.1103/PhysRevLett.113.144301.
- [98] M. Yalçın, "Comparison of the flaw detection abilities of phased array and conventional ultrasonic testing methods in various steels" M.S. Master of Science, Middle East Technical University, 2014.
- [99] H. Yun, R. Rayhana, S. Pant, M. Genest, and Z. Liu, "Nonlinear ultrasonic testing and data analytics for damage characterization: A review," Measurement (Lond), vol. 186, no. 943411, p. 110155, 2021, doi: 10.1016/j.measurement.2021.110155.
- [100] K. Y. Jhang, "Nonlinear ultrasonic techniques for non-destructive assessment of micro damage in material: A Review," International Journal of Precision Engineering and Manufacturing, vol. 10, no. 1, pp. 123–135, 2009, doi: 10.1007/s12541-009-0019-y.
- [101] K. Y. Jhang, "Applications of nonlinear ultrasonics to the NDE of material degradation," IEEE Trans Ultrason Ferroelectr Freq Control, vol. 47, no. 3, pp. 540–548, 2000, doi: 10.1109/58.842040.
- [102] S. Palit Sagar, S. Das, N. Parida, and D. K. Bhattacharya, "Non-linear ultrasonic technique to assess fatigue damage in structural steel," Scr Mater, vol. 55, no. 2, pp. 199–202, Jul. 2006, doi: 10.1016/j.scriptamat.2006.03.037.
- [103] S. Palit Sagar, A. K. Metya, M. Ghosh, and S. Sivaprasad, "Effect of microstructure on non-linear behavior of ultrasound during low cycle fatigue of pearlitic steels," Materials Science and Engineering A, vol. 528, no. 6, pp. 2895–2898, 2011, doi: 10.1016/j.msea.2010.12.078.

- [104] J.-Y. Kim, L. J. Jacobs, J. Qu, and J. W. Littles, "Experimental characterization of fatigue damage in a nickel-base superalloy using nonlinear ultrasonic waves," J Acoust Soc Am, vol. 120, no. 3, pp. 1266–1273, Sep. 2006, doi: 10.1121/1.2221557.
- [105] Y. qing Cai, J. zhong Sun, C. jie Liu, S. wei Ma, and X. cheng Wei, "Relationship between Dislocation Density in P91 Steel and Its Nonlinear Ultrasonic Parameter," Journal of Iron and Steel Research International, vol. 22, no. 11, pp. 1024–1030, Nov. 2015, doi: 10.1016/S1006-706X (15)30107-2.
- [106] Y. Xiang, M. Deng, C. J. Liu, and F. Z. Xuan, "Contribution of mixed dislocations to the acoustic nonlinearity in plastically deformed materials," J Appl Phys, vol. 117, no. 21, Jun. 2015, doi: 10.1063/1.4922176.
- [107] J. Zhang and F. Z. Xuan, "Fatigue damage evaluation of austenitic stainless steel using nonlinear ultrasonic waves in low cycle regime," J Appl Phys, vol. 115, no. 20, May 2014, doi: 10.1063/1.4879415.
- [108] R. Qiao and X. Yan, "The Characterization of Fatigue Damage of 316L Stainless Steel Parts Formed by Selective Laser Melting with Harmonic Generation Technique," Materials, vol. 15, no. 3, 2022, doi: 10.3390/ma15030718.
- [109] M. Inês Silva, E. Malitckii, T. G. Santos, and P. Vilaça, "Review of conventional and advanced non-destructive testing techniques for detection and characterization of small-scale defects," Sep. 01, 2023, Elsevier Ltd. doi: 10.1016/j.pmatsci.2023.101155.
- [110] B. Wisner, K. Mazur, and A. Kontsos, "The use of non-destructive evaluation methods in fatigue: A review," Procedia Structural Integrity, vol. 34, pp. 268–275, 2021, doi: 10.1016/j.prostr.2021.10.031.
- [111] P. Bayer, L. Singher, and A. Notea, "Ultrasonic evaluation of fatigue damage," in Quantitative Nondestructive Evaluation, AIP Conf. Proc., vol. 700, pp. 1240–1247, Feb. 2004. doi: 10.1063/1.1711759.
- [112] Y. Kong, C. J. Bennett, and C. J. Hyde, "A review of non-destructive testing techniques for the in-situ investigation of fretting fatigue cracks," Nov. 01, 2020, Elsevier Ltd. doi: 10.1016/j.matdes.2020.109093.
- [113] S. Dwivedi, M. Vishwakarma, and A. Soni, "Advances and research on non-destructive testing: A review," Materials Today: Proceedings, vol. 5, no. 1, pp. 3690–3698, 2018, doi: 10.1016/j.matpr.2017.11.620.
- [114] B. Raeisinia and W. J. Poole, "Electrical resistivity measurements: A sensitive tool for studying aluminum alloys," Materials Science Forum, vol. 519–521, no. PART 2, pp. 1391–1396, 2006, doi: 10.4028/www.scientific.net/MSF.519-521.1391.
- [115] D. Cigoy, "Accurate Low-Resistance Measurements Start with Identifying Sources of Error," vol. 44139, no. 440, pp. 1–14, 2010.
- [116] Tektronix. Expert, "Low Resistance Measurement with a Source Meter: Do I use Current Reversal, Offset Compensation or Delta Mode measurement methods?" January 15, [online].

- Available: https://www.tek.com/en/blog/low-resistance-measurement-sourcemeter-do-i-use-current-reversal-offset-compensation-or-delta-m
- [117] Tektronix, Achieving Accurate and Reliable Resistance Measurements in Low Power and Low Voltage Circuits, Available: https://www.tek.com/en/documents/whitepaper/achieving-accurate-and-reliable-resistance-measurements-low-power-and-low-voltag
- [118] Y. Singh, "Electrical resistivity measurements: A review," International Journal of Modern Physics: Conference Series, vol. 22, pp. 745–756, 2013, doi: 10.1142/S2010194513010970.
- [119] D. Cigoy, "Accurate Low-Resistance Measurements Start with Identifying Sources of Error," vol. 44139, no. 440, pp. 1–14, 2010.
- [120] Tektronix, Low Voltage Measurement Techniques, Technical Article, Available: https://www.tek.com/en/documents/technical-article/low-voltage-measurement-techniques.
- [121] Tektronix, 2-Wire vs. 4-Wire Resistance Measurements, Tektronix, Inc., Available: https://download.tek.com/document/2Wire_4Wire%20Resistance%20Article.pdf.
- [122] Keithley Instruments, Model 6220 DC Current Source / Model 6221 AC and DC Current Source User's Manual, Document No. 622x-900-01 Rev. B, June 2005. Available: www.keithley.com.
- [123] Tektronix, "Techniques for Measuring Resistivity for Materials Characterization," Application Note, [online]. Available: https://www.tek.com/en/documents/application-note/materials-char_apps_guide [Accessed: May. 20, 2025].
- [124] H. Nyquist, "Thermal agitation of electric charge in conductors," Phys. Rev., vol. 32, no. 1, pp. 110–113, 1928. doi: 10.1103/PhysRev.32.110.
- [125] A. Rafefi, "Development and evaluation of thin film electrical resistance sensors for monitoring CO2 top of the line corrosion," Sens Actuators B Chem, vol. 346, March 2021, doi: 10.1016/j.snb.2021.130492.
- [126] S. Saberi et al., "A new development of four-point method to measure the electrical resistivity in situ during plastic deformation," Measurement (Lond), vol. 180, no. April, p. 109547, 2021, doi: 10.1016/j.measurement.2021.109547.
- [127] R. Nobile and A. Saponaro, "Real-time monitoring of fatigue damage by electrical resistance change method," Int J Fatigue, vol. 151, no. January, p. 106404, 2021, doi: 10.1016/j.ijfatigue.2021.106404.
- [128] C. Bermes, "Generation and detection of nonlinear Lamb waves for the characterization of material nonlinearities," M.S. thesis, School of Civil and Environmental Engineering, Georgia Institute of Technology, Atlanta, GA, USA, 2007.
- [129] J. D, Achenbach, Wave Propagation in Elastic Solids., First edition, 1975.
- [130] C. Prüll, L. J. Jacobs, J.-Y. Kim, J. Qu, and G. W. Woodruff, "Generation and Detection of Lamb Waves for the Characterization of Plastic Deformation," 2007.

- [131] C. Ehrlich, J.-Y. Kim, L. J. Jacobs, J. Qu, and J. Wall, "Experimental characterization of creep damage in a welded steel pipe section using a nonlinear ultrasonic technique," AIP Conf. Proc., vol. 1430, pp. 292–298, May 2012. doi: 10.1063/1.4716242.
- [132] Mitutoyo, *Surftest SJ-210: User guide*, Andover, UK: Mitutoyo UK Ltd., 2012. Available: https://www.mitutoyo.co.uk.
- [133] Mitutoyo, SJ-201 Surface Roughness Tester: User's manual, No. 99MBB079A5, Series No. 178, Mitutoyo Corp.
- [134] Polytec GmbH, TopMap Micro.View®+ Next Generation Optical Surface Profiler, Datasheet, 2021. Available: https://www.polytec.com
- [135] Keithley Instruments, Model 2182A Nanovoltmeter Product Page. Available: https://www.tek.com/en/products/keithley/low-level-sensitive-and-specialty-instruments/nanovoltmeter-model-2182a.
- [136] Keithley Instruments, Precision, Low Current Sources: Model 6220 DC Current Source, Model 6221 AC and DC Current Source User Manual. Available: www.keithley.com.
- [137] K. Instruments Inc, "Model 6220 DC Current Source Model 6221 AC and DC Current Source Reference Manual," 2008. [Online]. Available: www.keithley.com
- [138] K. Instruments LLC, "Model 2182 and 2182A Nanovoltmeter Service Manual," 2022.
- [139] Keithley Instruments, 6220/6221 Reference Manual, Cleveland, Ohio, USA, Keithley Instruments Inc., Available: https://www.scribd.com/document/208118341/622x-Keithely-reference-manual. Accessed April 2025.
- [140] Daire, A. Improving the Repeatability of Ultra-High Resistance and Resistivity Measurements. Keithley Instruments. Available: https://www.techonline.com/tech-papers/improving-the-repeatability-of-ultra-high-resistance-and-resistivity-measurements/.
- [141] Ritec Inc. SNAP System Specifications. Sonemat Ltd., 2024. Available: https://www.sonemat.co.uk/app/uploads/2024/10/Ritec-SNAP-Specifications.pdf.
- [142] Ritec Inc. Advanced Measurement System RAM-5000-SNAP: User Guide. Available: https://www.ritecinc.com/uploads/5/2/3/3/5233467/snap.pdf.
- [143] J.-Y. Kim, L. J. Jacobs, J. Qu, and J. W. Littles, "Experimental characterization of fatigue damage in a nickel-base superalloy using nonlinear ultrasonic waves," J Acoust Soc Am, vol. 120, no. 3, pp. 1266–1273, Sep. 2006, doi: 10.1121/1.2221557.
- [144] S. Park, L. J. Jacobs, J.-Y. Kim, J. Qu, and G. W. Woodruff, "Measurements of acoustic nonlinearity in cold-rolled and heat-treated 304 austenitic stainless steel using nonlinear ultrasound," Journal of Non-destructive Evaluation, vol. 38, no. 1, 2019, doi: 10.1007/s10921-019-0574-5.
- [145] Pu Sun, Comparison of STFT and Wavelet Transform in Time-Frequency Analysis, Bachelor's Thesis in Electronics, University of Gävle, Sweden, December 2014. Available: https://www.diva-portal.org/smash/get/diva2:793176/FULLTEXT01.pdf.

- [146] B. Fultz and J. Howe, Transmission Electron Microscopy and Diffractometry of Materials, 3rd ed. Berlin, Germany: Springer, 2013.
- [147] C. Y. Chen, S. F. Chen, J. R. Yang, and C. C. Chen, "Precipitation of Nano-Sized Carbides in a Ti-Mo Bearing Steel at a Low Transformation Temperature," Atlas Journal of Materials Science, vol. 2, no. 1, pp. 48–53, Jul. 2015, doi: 10.5147/ajms.2015.0164.
- [148] S. Zaefferer, "A critical review of orientation microscopy in SEM and TEM," in Crystal Research and Technology, Jun. 2011, pp. 607–628. doi: 10.1002/crat.201100125.
- [149] C. Sun, E. Müller, M. Meffert, and D. Gerthsen, "Analysis of crystal defects by scanning transmission electron microscopy (STEM) in a modern scanning electron microscope," Adv Struct Chem Imaging, vol. 5, no. 1, Dec. 2019, doi: 10.1186/s40679-019-0065-1.
- [150] Q. Chen et al., "Imaging Beam-Sensitive Materials by Electron Microscopy," Apr. 01, 2020, Wiley-VCH Verlag. doi: 10.1002/adma.201907619.
- [151] Microscopy Australia, "Transmission Electron Microscopy." Accessed: Mar. 13, 2025. [Online]. Available: https://myscope.training/TEM_Beam_sample_interactions.
- [152] Y. Fargier, L. Dore, and A. Ihamouten, "Surface variations effect on electrical resistivity measurement: Aroughness based approach," J Appl Geophy, vol. 159, pp. 341–349, Dec. 2018, doi: 10.1016/j.jappgeo.2018.08.016.
- [153] J. W. McBride and H. Liu, "The relationship between contact resistance and roughness (Sq) of a bi-layered surface using a finite element model," Proc. 2020 IEEE 66th Holm Conf. Electrical Contacts and Intensive Course (HLM), San Antonio, TX, USA, 2020, pp. 176–181, doi: 10.1109/HLM49214.2020.9307833.
- [154] W. Tang, Y. Chao, X. Weng, L. Deng, and K. Xu, "Optical Property and the Relationship between Resistivity and Surface Roughness of Indium Tin Oxide Thin Films," in Physics Procedia, Elsevier B.V., 2012, pp. 680–686. doi: 10.1016/j.phpro.2012.03.618.
- [155] Technology Networks, "Repeatability vs. Reproducibility," Technology Networks, Oct. 1, 2018.

 Available: https://www.technologynetworks.com/informatics/articles/repeatability-vs-reproducibility-317157.
- [156] Richard Hogan, "How to Perform a Repeatability Test for Estimating Uncertainty in Measurement." Accessed: Oct. 02, 2024. [Online]. Available: https://www.isobudgets.com/how-to-perform-a-repeatability-test/
- [157] Iowa State University Centre for Non-destructive Evaluation, "Non-destructive Evaluation Techniques," Available: https://www.nde-ed.org/NDETechniques/index.xhtml
- [158] Z. Wang, S. Yang, Y. Huang, C. Fan, Z. Peng, and Z. Gao, "Microstructure and fatigue damage of 316l stainless steel manufactured by selective laser melting (Slm)," Materials, vol. 14, no. 24, Dec. 2021, doi: 10.3390/ma14247544.

- [159] Y. Wang, Z. Wang, W. Wang, and B. Ma, "Effect of nitrogen content on mechanical properties of 316L(N) austenitic stainless steel," Materials Science and Engineering: A, vol. 884, no. August, p. 145549, 2023, doi: 10.1016/j.msea.2023.145549.
- [160] G. V. Prasad Reddy, R. Kannan, K. Mariappan, R. Sandhya, S. Sankaran, and K. Bhanu Sankara Rao, "Effect of strain rate on low cycle fatigue of 316LN stainless steel with varying nitrogen content: Part-I cyclic deformation behaviour," Int J Fatigue, vol. 81, pp. 299–308, 2015, doi: 10.1016/j.ijfatigue.2015.07.033.
- [161] M. S. Pham and S. R. Holdsworth, "Change of stress-strain hysteresis loop and its links with microstructural evolution in AISI 316L during cyclic loading," Procedia Eng, vol. 10, pp. 1069–1074, 2011, doi: 10.1016/j.proeng.2011.04.176.
- [162] L. Cui et al., "Superior low cycle fatigue property from cell structures in additively manufactured 316L stainless steel," J Mater Sci Technol, vol. 111, pp. 268–278, 2022, doi: 10.1016/j.jmst.2021.10.006.
- [163] K. H. Matlack, "Nonlinear ultrasound for radiation damage detection," Ph.D. dissertation, G. W. Woodruff School of Mechanical Engineering, Georgia Institute of Technology, Atlanta, GA, USA, May 2014.
- [164] J. H. Cantrell, "Fundamentals and applications of nonlinear ultrasonic non-destructive evaluation," Ultrasonic Non-destructive Evaluation: Engineering and Biological Material Characterization, pp. 363–434, 2003, doi: 10.1201/b12268-10.
- [165] Y. Xiang, M. Deng, C. J. Liu, and F. Z. Xuan, "Contribution of mixed dislocations to the acoustic nonlinearity in plastically deformed materials," J Appl Phys, vol. 117, no. 21, Jun. 2015, doi: 10.1063/1.4922176.
- [166] X. Yan, H. Wang, and X. Fan, "Research Progress in Nonlinear Ultrasonic Testing for Early Damage in Metal Materials," Mar. 01, 2023, MDPI. doi: 10.3390/ma16062161.
- [167] K. H. Matlack, J. Y. Kim, L. J. Jacobs, and J. Qu, "Review of Second Harmonic Generation Measurement Techniques for Material State Determination in Metals," J Nondestr Eval, vol. 34, no. 1, Mar. 2015, doi: 10.1007/s10921-014-0273-5.
- [168] Z. Chen and J. Qu, "Dislocation-induced acoustic nonlinearity parameter in crystalline solids," J Appl Phys, vol. 114, no. 16, 2013, doi: 10.1063/1.4826523.
- [169] J. H. Cantrell, "Nonlinear dislocation dynamics at ultrasonic frequencies," J Appl Phys, vol. 105, no. 4, 2009, doi: 10.1063/1.3081972.
- [170] C. L. Williams, M. H. Lear, and P. Shokouhi, "A review of the microstructural contributions to the acoustic nonlinearity parameter measured with longitudinal and Rayleigh wave second harmonic generation in metals," NDT and E International, vol. 142, no. December 2023, 2024, doi: 10.1016/j.ndteint.2023.103027.
- [171] C. S. Kim, S. I. Kwun, and C. J. Lissenden, "Influence of Precipitates and Dislocations on the Acoustic Nonlinearity in Metallic Materials," 2009.

- [172] F. Kroupa. Dislocation dipoles and dislocation loops. Journal de Physique Colloques, 1966, 27 (C3), pp.C3-154-C3-167.doi: 10.1051/jphyscol:1966320ff.
- [173] J. Polák, "Role of Persistent Slip Bands and Persistent Slip Markings in Fatigue Crack Initiation in Polycrystals," Crystals (Basel), vol. 13, no. 2, 2023, doi: 10.3390/cryst13020220.
- [174] J. H. Cantrell and K. Salama, "Acoustoelastic characterisation of materials," International Materials Reviews, vol. 36, no. 1, pp. 125–145, 1991, doi: 10.1179/imr.1991.36.1.125.
- [175] J. H. Cantrell, "Quantitative assessment of fatigue damage accumulation in wavy slip metals from acoustic harmonic generation," Philosophical Magazine, vol. 86, no. 11, pp. 1539–1554, Apr. 2006, doi: 10.1080/14786430500365358.
- [176] Z. S. Basinski, J. S. Dugdale, and A. Howie, "The electrical resistivity of dislocations," Philosophical Magazine, vol. 8, no. 96, pp. 1989–1997, 1963, doi: 10.1080/14786436308209092.
- [177] J. H. Cantrell and W. T. Yost, "Nonlinear ultrasonic characterization of fatigue microstructures," Int J Fatigue, vol. 23, no. SUPPL. 1, pp. 487–490, 2001, doi: 10.1016/s0142-1123(01)00162-1.
- [178] A. B. Bhatia and O. P. Gupta, "Electrical Resistivity due to Dislocations," American Physical Society, vol. 1.
- [179] S. R. Dugasani, T. Hwang, J. A. Kim, and B. R. Watts, "Calculation of electrical resistivity produced by dislocations in various metals," 1988.
- [180] I. Gaal, L. Uray, and T. Vicsek, "The Effect of the Dislocation Distribution on the Electrical Resistivity in Deformed Metals," 1975.
- [181] P. Starke, F. Walther, and D. Eifler, "Model-based correlation between change of electrical resistance and change of dislocation density of fatigued-loaded ICE R7 wheel steel specimens," Materialpruefung/Materials Testing, vol. 60, no. 7–8, pp. 669–677, Jul. 2018, doi: 10.3139/120.111202.
- [182] M. Al Malki, Y. Liu, J. Male, V. P. Dravid, D. C. Dunand, and G. J. Snyder, "In situ observation of electrical resistivity increase via creep-induced dislocations in n-type PbTe," Acta Mater, vol. 266, Mar. 2024, doi: 10.1016/j.actamat.2024.119652.
- [183] A. Hikata, B. B. Chick, and C. Elbaum, "Dislocation contribution to the second harmonic generation of ultrasonic waves," J Appl Phys, vol. 36, no. 1, pp. 229–236, 1965, doi: 10.1063/1.1713881.
- [184] J.-Y. Huang, J.-J. Yeh, S.-L. Jeng, C.-Y. Chen, and R.-C. Kuo, "High-cycle fatigue behavior of type 316L stainless steel," Mater. Trans., vol. 47, no. 2, pp. 409–417, 2006. doi: 10.2320/matertrans.47.409.
- [185] H. Mughrabi, "Cyclic Slip irreversibility's and the Evolution of Fatigue Damage.," Metall Mater Trans A, vol. 40, pp. 1257–1279, 2009, [Online]. Available: https://doi.org/10.1007/s11661-009-9839-8

- [186] K. Tanaka and M. T. Tanaka, "A dislocation model for fatigue crack initiation," ASME J. Appl. Mech., vol. 48, no. 1, pp. 97–103, 1981.
- [187] H. Mughrabi, "Dislocation clustering and long-range internal stresses in monotonically and cyclically deformed metal crystals," Revue de Physique Appliquée, vol. 23, no. 4, pp. 367–379, 1988, doi: 10.1051/rphysap:01988002304036700.
- [188] William. Cantrell, John & Yost, "Nonlinear ultrasonic characterization of fatigue microstructures.," Int J Fatigue, vol. 23, pp. 487–490, 2001, [Online]. Available: 10.1016/S0142-1123(01)00162-1.
- [189] J. Frouin, S. Sathish, T. E. Matikas, and J. K. Na, "Ultrasonic linear and nonlinear behavior of fatigued Ti-6Al-4V," J Mater Res, vol. 14, no. 4, pp. 1295–1298, 1999, doi: 10.1557/JMR.1999.0176.